THE UNIVERSITY OF CHICAGO

DEVELOPMENT OF TRUE THERANOSTIC RADIOPHARMACEUTICALS FOR METASTATIC CASTRATION RESISTANT PROSTATE CANCER WITH RADIOSCANDIUM LABELED PSMA-617

A DISSERTATION SUBMITTED TO
THE FACULTY OF THE DIVISION OF THE BIOLOGICAL SCIENCES
AND THE PRITZKER SCHOOL OF MEDICINE
IN CANDIDACY FOR THE DEGREE OF
DOCTOR OF PHILOSOPHY

COMMITTEE ON MEDICAL PHYSICS

BY
JASON PATRICK MEIER

CHICAGO, ILLINOIS
AUGUST 2025

Copyright © 2025 by Jason Patrick Meier

All Rights Reserved

TABLE OF CONTENTS

LIST OF FIGURES vi

LIST OF TABLES viii

ACKNOWLEDGMENTS ix

ABSTRACT xii

1 INTRODUCTION 1
1.1 History of Radiotheranostic Development 1
1.2 Motivation for True Theranostic Development 4
1.3 Innovation of Radioscandiums in Metastatic Castration Resistant Prostate Cancer 6
1.3.1 Limitations in the Current Standards of Metastatic Castration Resistant Prostate Cancer Management 6
1.3.2 Potential Improvements in Metastatic Castration Resistant Prostate Cancer Management with Radioscandium PSMA-617 11
1.4 Dissertation Objectives 12
1.5 Dissertation Organization 13

2 BACKGROUND 15
2.1 Principles of Nuclear Medicine and Molecular Imaging 15
2.1.1 Radiopharmaceuticals 15
2.1.2 PET Imaging 17
2.1.3 SPECT Imaging 20
2.1.4 Targeted Radionuclide Therapy 23
2.2 Decay Properties of Radioscandiums 26
2.2.1 Scandium-43 26
2.2.2 Scandium-44 28
2.2.3 Scandium-47 30
2.3 PSMA-617 32

3 NUCLEAR PRODUCTION OF RADIOSCANDIUMS 36
3.1 Introduction 36
3.1.1 Scandium-43 37
3.1.2 Scandium-44 38
3.1.3 Scandium-47 40
3.2 Methods 42
3.2.1 Development of a Solid Target Holder for a Biomedical Cyclotrons . . 42
3.2.2 Scandium-43 46
3.2.3 Scandium-44 51
3.2.4 Scandium-47 53

3.3 Results . . . 56
3.3.1 Scandium-43 . . . 56
3.3.2 Scandium-44 . . . 60
3.3.3 Scandium-47 . . . 60
3.4 Recovery of Enriched Calcium Materials . . . 61
3.5 Discussion . . . 63
3.6 Conclusion . . . 66

4 CHEMICAL SYNTHESIS OF RADIOSCANDIUM PSMA-617 FROM IRRADIATED TARGET MATERIALS . . . 68
4.1 Introduction . . . 68
4.2 Methods . . . 70
4.2.1 Separation of Radioscandium from Calcium Targetry . . . 71
4.2.2 Radiosynthesis of Radioscandium PSMA-617 . . . 71
4.2.3 Purification and Quality Control of Radioscandium PSMA-617 . . . 73
4.2.4 Reformulation of Radioscandium PSMA-617 . . . 74
4.3 Results . . . 75
4.3.1 Separation of Radioscandium from Calcium Targetry . . . 75
4.3.2 Radiosynthesis of Radioscandium PSMA-617 . . . 76
4.3.3 Purification and Quality Control of Radioscandium PSMA-617 . . . 78
4.4 Discussion . . . 79
4.5 Conclusion . . . 81

5 *IN VITRO* AND *IN VIVO* ANALYSIS OF RADIOSCANDIUM CONJUGATED PSMA-617 . . . 83
5.1 Introduction . . . 83
5.2 Methods . . . 84
5.2.1 Enzalutamide Resistant Cellular and Animal Models . . . 84
5.2.2 *In Vitro* Specificity . . . 85
5.2.3 *In Vivo* Imaging . . . 88
5.2.4 *Ex Vivo* Biodistribution . . . 92
5.2.5 Scandium-47 Radionuclide Therapy . . . 94
5.3 Results . . . 94
5.3.1 *In Vitro* Specificity . . . 94
5.3.2 *In Vivo* Imaging . . . 101
5.3.3 *Ex Vivo* Biodistribution . . . 111
5.3.4 Scandium-47 Radionuclide Therapy . . . 114
5.4 Discussion . . . 115
5.5 Conclusion . . . 118

6 DOSIMETRIC AND RADIOBIOLOGICAL CHARACTERIZATION OF RADIOSCANDIUMS WITH TOPAS . . . 120
6.1 Introduction . . . 120
6.1.1 Radially-Varying Radiation Dosimetry . . . 121

6.1.2 Cellular S-Values . . . 122
6.1.3 DNA Double Strand Breaks . . . 124
6.2 Methods . . . 125
6.2.1 Radially-Varying Radiation Dosimetry . . . 125
6.2.2 Cellular S-Values . . . 133
6.2.3 DNA Double Strand Breaks . . . 137
6.3 Results . . . 140
6.3.1 Radially-Varying Radiation Dosimetry . . . 140
6.3.2 Cellular S-Values . . . 148
6.3.3 DNA Double Strand Breaks . . . 152
6.4 Discussion . . . 156
6.5 Conclusion . . . 159

7 CONCLUSIONS AND FUTURE DIRECTIONS . . . 161
7.1 Summary of Work . . . 161
7.2 Conclusions . . . 164
7.3 Future Directions . . . 167
7.3.1 Production of Radioscandiums . . . 167
7.3.2 Further Refinement of Radiochemistry . . . 169
7.3.3 Radioscandium PET and SPECT Imaging . . . 170
7.3.4 Murine Metastases Model . . . 171
7.3.5 Multicellular S-Values . . . 172
7.3.6 Radiobiology in TOPAS Monte Carlo . . . 172
7.3.7 Translation to the Clinical Space . . . 173
7.3.8 Translation to other Cancer Targets . . . 174

REFERENCES . . . 177

LIST OF FIGURES

1.1 Structural components of PSMA-617 and PSMA-11 10

2.1 Graphical depiction of a radiopharmaceutical 16
2.2 Graphical depiction of PET imaging 18
2.3 Graphical depiction of scatter and random coincidence events in PET 19
2.4 Graphical depiction of SPECT imaging with a parallel hole collimator 22
2.5 Chemical structure of PSMA-617 33
2.6 Chemical structure of occupied DOTA chelate 34

3.1 Schematic of the target holder used as a beam-stop conversion system 43
3.2 Beam-stop conversion solid target holder 44
3.3 ^{42}CaO target 49
3.4 CZT spectrum of ^{43}Sc produced with the ^{42}Ca(d,n)^{43}Sc reaction 50
3.5 $^{48}CaCO_3$ and graphite target 54
3.6 Yield of ^{43}Sc produced with the ^{42}Ca(d,n)^{43}Sc reaction 57
3.7 Experimental and theoretical yield of ^{43}Sc produced with the ^{42}Ca(d,n)^{43}Sc reaction 58
3.8 Percent difference of experimental and theoretical yield of ^{43}Sc produced with the ^{42}Ca(d,n)^{43}Sc reaction as a function of target mass 59

4.1 Chemical separation and radiolabeling of radioscandiums 70
4.2 DGA activity elution curve 76
4.3 Molar activity of radiolabeled scandium PSMA-617 77
4.4 Radio iTLC chromatograms before and after purification 78

5.1 ^{43}Sc-PSMA-617 blocking assay 95
5.2 ^{43}Sc-PSMA-617 uptake assay 96
5.3 ^{43}Sc-PSMA-617 internalization assay 97
5.4 ^{47}Sc-PSMA-617 blocking assay 99
5.5 ^{47}Sc-PSMA-617 uptake assay 100
5.6 ^{47}Sc-PSMA-617 internalization assay 101
5.7 ^{43}Sc-PSMA-617 static PET/CT 102
5.8 ^{43}Sc-PSMA-617 multi-timepoint static PET/CT 103
5.9 ^{43}Sc-PSMA-617 dynamic imaging 105
5.10 ^{43}Sc-PSMA-617 SUV curves 106
5.11 ^{43}Sc-PSMA-617 multi-tumor SUV curve 107
5.12 ^{47}Sc-PSMA-617 SPECT/CT 108
5.13 $^{43/47}$Sc-PSMA-617 PET/SPECT serial imaging (low molar activity) 109
5.14 $^{43/47}$Sc-PSMA-617 PET/SPECT serial imaging (high molar activity) 110
5.15 ^{43}Sc-PSMA-617 *ex vivo* biodistribution (2 h post-injection) 111
5.16 ^{43}Sc-PSMA-617 *ex vivo* biodistribution (4 h post-injection) 112
5.17 ^{43}Sc-PSMA-617 *ex vivo* biodistribution (6 h post-injection) 112
5.18 ^{44}Sc-PSMA-617 *ex vivo* biodistribution 114

5.19 DNA DSB immunohistochemical staining 115

6.1 Radial energy deposition simulation geometry 126
6.2 Energy deposition in radially scored bins of various fractional spheres of water with r = 100 cm. 130
6.3 Summed energy deposition in radially scored bins of various fractional spheres of water with r = 100 cm. 131
6.4 Percent error of summed energy deposition in radially scored bins of various fractional spheres of water with r = 100 cm. 132
6.5 S-value simulation geometry 134
6.6 Radiobiological S-Values of ^{47}Sc calculated with TOPAS and MIRDcell 136
6.7 Radiobiological S-Values of ^{68}Ga calculated with TOPAS and MIRDcell 136
6.8 Radiobiological S-Values of ^{177}Lu calculated with TOPAS and MIRDcell 136
6.9 TSSolenoidFiber DNA model in TOPAS-nBio 138
6.10 Cellular DNA damage simulation geometry 139
6.11 Energy deposited by ^{43}Sc, ^{44}Sc, and ^{68}Ga decay 142
6.12 Energy deposited by ^{43}Sc, ^{44}Sc, and ^{68}Ga at subcellular scales 144
6.13 Energy deposited by ^{47}Sc and ^{177}Lu 145
6.14 Energy deposited by ^{47}Sc and ^{177}Lu at subcellular scales 147
6.15 Radiobiological S-values of diagnostic radioscandiums 149
6.16 Radiobiological S-values of ^{47}Sc and ^{177}Lu 150
6.17 Simulated DNA DSBs of the diagnostic radioscandiums per radioactive decay . 152
6.18 Simulated DNA DSBs induced by therapeutic ^{47}Sc and ^{177}Lu per radioactive decay 154
6.19 Simulated DNA DSBs of therapeutic radioscandiums per radioactive decay in non-nuclear uptake and internalization 155

7.1 Improved solid target holder design 168

LIST OF TABLES

2.1 Decay information for PET radionuclides 26
2.2 Decay information for TRT radionuclides 31

3.1 Potential radioactive byproducts produced in titanium screws 46
3.2 Isotopic composition and nuclear reactions of enriched ^{42}Ca target material . . . 48
3.3 Isotopic composition and nuclear reactions of enriched ^{44}Ca target material . . . 52
3.4 Isotopic composition and nuclear reactions of enriched ^{48}Ca target material . . . 56

6.1 Polar and azimuthal angle ranges for the partial volume approximation 129
6.2 Computational accuracy of spherical fractions in TOPAS 133
6.3 Radiobiological S-Values calculated with TOPAS and MIRDcell 137
6.4 Radiobiological S-values of the diagnostic radioscandiums 149
6.5 Radiobiological S-values of ^{47}Sc and ^{177}Lu 151
6.6 Simulated direct DNA damage induced by the diagnostic radioscandiums per radioactive decay 153
6.7 Simulated DNA damage induced by therapeutic ^{47}Sc and ^{177}Lu per radioactive decay 155

ACKNOWLEDGMENTS

Throughout my time at the University of Chicago, there have been countless people who have left a lasting impact on me both in my professional development and beyond it. First and foremost, I would like to thank my advisor, Dr. Chin-Tu Chen, for his unwavering support and mentorship. Dr. Chen has not only helped me grow as a scientist, but also provided me guidance and support in trying times. I will never forget the encouragement he showed me when, less than one year into the program, I told him that I wanted to pursue medical school after my PhD. Even though the additional requirements I had to fulfill undoubtedly took away from some of the research time I would have otherwise had, Dr. Chen was always fully supportive and understanding of my career goals, and for that I owe him my utmost gratitude. It has been an honor to train under an esteemed scientist who is not only knowledgeable and reputable, but also kind-hearted and compassionate.

I would of course like to thank my committee members for providing their guidance and expertise throughout the formulation of this dissertation. Dr. Satish Chitneni has provided his immense expertise and experience in radiopharmaceutical development, helping to refine the accelerator production and radiochemical aspects of this work. Dr. Russell Szmulewitz's clinical expertise as an oncologist specializing in genitourinary cancers has been instrumental in the conceptualization of this work and has ensured that the overall research scope remain relevant and practical to the clinical realities of prostate cancer. Dr. Howard Halpern has also provided his clinical expertise as a radiation oncologist whilst offering valuable insights into the simulation-based aspects of this work. Dr. Chien-Min Kao has contributed his technical expertise in nuclear medicine imaging and mathematical modeling. Ultimately, the expertise of these committee members permeates throughout this work, and this dissertation would not have been possible without them.

I would also like to thank the University of Chicago Cyclotron Facility for their persistent dedication to radioscandium production and the synthesis of radioscandium PSMA-617.

Dr. Richard Freifelder and Lucas Gonzalez spent countless nights running the cyclotron to produce ^{43}Sc, even when they also had the responsibility of routine radiopharmaceutical production the following day. Dr. Freifelder also played a major role in the creation of the solid-target holder system which enabled the production of radioscandiums necessary to complete this work. Dr. Mohammed Bhuiyan and Dr. Kaustab Ghosh greatly assisted in the development and execution of the radiochemical and calcium target recovery procedures utilized throughout this dissertation.

Similarly, this dissertation would not have been possible without the help of the University of Chicago Integrated Small Animal Imaging Research Resource (iSAIRR). Dr. Lara Leoni, Dr. Hsiu-Ming Tsai, Dr. Brian Roman, and Erica Markiewicz all provided assistance and guidance in conducting animal imaging studies and performing PET/SPECT/CT image analysis. Dr. Hannah Zhang played a major role in the development and execution of the cellular study protocols utilized in this work. Beyond their laboratory contributions, all of these individuals were pivotal in the development of my understanding of pre-clinical study design.

Our collaborators at Argonne National Laboratory (ANL) and the University of Alabama at Birmingham (UAB) were also instrumental in the completion of this work as they provided ^{47}Sc for the overwhelming majority of this project. Dr. Jerry Nolen (ANL) and Dr. David Rotsch (ANL) also played a fundamental role in establishing this project and developing the accelerator production and radiochemical methods. Dr. Claus Mueller Gatermann (ANL) provided ^{48}Ca for the production of ^{47}Sc at the University of Chicago Cyclotron Facility. Dr. Suzi Lapi (UAB) and Dr. Shelbie Cingoranelli (UAB) also provided us great support by continually producing and radiolabeling ^{47}Sc-PSMA-617 for us at a time where we could not obtain ^{47}Sc anywhere else.

I deeply appreciate the lasting bonds I have forged with my peers in the Graduate Program in Medical Physics, particularly my classmates Joel Toledo, Joseph Cozzi, and Geneva

Anderberg. Within that scope, I must give special mention to the lasting friendship I have developed with Joel over these last 5 years. Whether it was justifying our procrastination over a game of Counter-Strike, driving over an hour to watch *Bleach* together, or heading to the Korean spa in hopes of alleviating our chronic back pain, the brotherhood I developed with Joel will undoubtedly last a lifetime. I truly would not have made it through this program without his companionship.

I would like to thank my family for their support throughout these last 5 years. I am sure that it was not easy having me miss family functions or isolate myself whenever I had an exam coming up or an experiment that needed to be done (especially now that I decided to tack another 4-years of medical school onto that). In that regard, I am so thankful for the understanding, patience, and love you have shown me throughout this process. Your encouragement, sacrifices, and the upbringing you provided for me, have laid the foundation for everything I have accomplished.

Finally, I would like to give the biggest thanks to my wife, Nishi, who has been my strongest beacon of support. Even when she was facing her own challenges as a medical student and resident, Nishi was always there to provide a shoulder to lean on when I was struggling, reinvigorate me when I felt discouraged, and celebrate our successes on the rare occasion that things were going according to plan. Simply being able to sit down and share a meal after a long-day in the lab was truly the greatest reprieve from my work, especially when that meal happened to consist of homemade dosa and fresh coconut chutney. Ever since we were in high school, Nishi has also been a much needed source of inspiration for me, constantly pushing me reach my fullest potential while leading by example in her own career. In that regard, I owe both my aspirations and tenacity to her, and I hope to continue to live by her example as I transition into the next phase of my career.

ABSTRACT

The development of peptide based radiopharmaceuticals has rapidly expanded the role of nuclear medicine in the oncology space to include synergistic diagnostic and therapeutic components. The current rendition of this theranostic approach is built upon the idea that, by utilizing diagnostic and therapeutic radiopharmaceuticals with similar pharmacokinetics, the diagnostic agent can be used as a screening tool in treatment planning. Under this context, uptake patterns observed on PET or SPECT imaging can probe treatment effectiveness prior to the actual administration of any therapeutic, thus mitigating ineffective and burdensome treatments.

The most convincing evidence for the utility of theranostics can be seen in the increasingly widespread clinical implementation of ^{68}Ga-PSMA-11 (LOCAMETZ) and ^{177}Lu-PSMA-617 (PLUVICTO) for the visualization and treatment of metastatic castration resistant prostate cancer (mCRPC). This combination of prostate-specific membrane antigen (PSMA) targeting agents have been instrumental in increasing progression-free survival and overall survival times in cases of mCRPC; however, as pseudo theranostics, ^{68}Ga-PSMA-11 and ^{177}Lu-PSMA-617 do not embody a full realization of the potential of theranostics.

Because ^{68}Ga-PSMA-11 and ^{177}Lu-PSMA-617 utilize different targeting ligands and radioactive elements, they only share similar rather than identical pharmacokinetics. While this is sufficient for the theranostic implementation described above, pseudo theranostics are unsuitable for the application of diagnostic imaging as a predictor of therapeutic dosimetry in treatment planning, often considered to be the penultimate goal of nuclear medicine theranostics.

The development of predictive dosimetry would instead require a true theranostic pair, two radiopharmaceuticals which utilize the same targeting ligand and two different radioisotopes of the same element for diagnostic imaging and targeted radionuclide therapy. In this regard, the radioscandiums are optimal for true theranostic use as they consist of two

potential PET imaging agents, ^{43}Sc and ^{44}Sc, as well as a beta electron emitting isotope well suited for therapy, ^{47}Sc. As a group 3 trivalent cation, the radioscandiums can also conjugate with DOTA, the chelator which connects the radionuclide to the targeting ligand in PSMA-617. Consequently, radioscandium PSMA-617 has the potential to have applications in mCRPC which overlap with ^{68}Ga-PSMA-11 and ^{177}Lu-PSMA-617 in addition to the potential for predictive dosimetry as a true theranostic pair.

Before these potential applications can be tested, however, significant strides need to be made in the development of radioscandium pharmaceuticals with regards to accelerator-based production, radiochemistry, pre-clinical evaluation, and dosimetric simulation. These aspects of radioscandium development are therefore the focus of this work.

The first objective of this work is therefore to **develop radioscandium production methods using a compact medical cyclotron**. This was accomplished through the production of ^{43}Sc, ^{44}Sc, and ^{47}Sc with a novel solid target holder that slots into the beam-stop of a standard biomedical cyclotron. A procedure was also developed for the dissolution of the irradiated target materials and subsequent radiolabeling with PSMA-617.

Utilizing the radiolabeled radioscandium materials, the second objective is to **characterize the diagnostic and therapeutic efficacy of radioscandium PSMA-617 *in vitro* and *in vivo***. This was accomplished through an analysis of uptake and internalization *in vitro*, PET and SPECT imaging, and DNA double strand break immunohistrochemistry *in vivo*. All *in vitro* and *in vivo* models utilized a PSMA expressing enzalutamide resistant LNCaP cell line and a non-PSMA expressing DU145 cell lines for the negative control.

The final objective is to **define the dosimetric properties and radiobiological effect of the radioscandiums using Monte Carlo dosimetry simulations**. Utilizing the Monte Carlo program TOPAS, simulations were devised to generate radially-varying energy deposition curves, cellular S-values, and DNA double strand break data for the radioscandiums and their clinical analogues, ^{177}Lu and ^{68}Ga.

CHAPTER 1

INTRODUCTION

1.1 History of Radiotheranostic Development

While the origin of the term "theranostics" (or the less commonly used "theragnostics")—a hybridization of the words therapy and diagnostics—is somewhat contested, it was likely first used in 1998 by US consultant John Funkhouser to describe an approach to the early stages of disease management which utilizes medical imaging to probe treatment efficacy and guide therapeutic decision making [1–3]. As the CEO of PharmaNetics, Funkhouser would go on to further popularize the term in the early 2000's when describing his company's vision for novel pharmaceuticals as singular selectively targeting materials which could hybridize the diagnosis, treatment, and monitoring of cardiovascular disease [2, 4–6].

While Funkhouser's vision for theranostic pharmaceuticals is still largely congruent with the utilization of the term today, the scope of theranostics has expanded beyond cardiovascular thrombolytics and anticoagulants and is now also associated with fluorescent markers, MRI contrast agents, and nuclear imaging agents [7]. Among these, theranostics is most commonly associated with nuclear imaging agents, or radiopharmaceuticals, particularly those utilized in the diagnosis and treatment of oncologic disease. The scope of theranostics has also expanded beyond the development of singular pharmaceuticals for both diagnosis and therapy. Rather, in nuclear medicine, the term theranostics is now more commonly utilized to describe select pairs of diagnostic and therapeutic radiopharmaceuticals which share the same biological target and targeting moiety and therefore have highly similar pharmacokinetics. Within this context, theranostics have been hypothesized to improve patient outcomes by utilizing tandem pairs of radiopharmaceuticals in which the diagnostic radiopharmaceutical probes the underlying pathology of a patient's disease to inform clinical decision making when treatment planning with the therapeutic radiopharmaceutical [8–13].

In nuclear medicine, the implementation of radiopharmaceuticals as hybridized diagnostic and therapeutic agents occurred long before the term theranostics was ever utilized. The first implementation of theranostics spans back to the 1940's when Massachusetts General Hospital physician Saul Hertz first utilized radioiodine for the detection and treatment of hyperthyroidism and thyroid cancer, predating Funkhouser by over 50 years [14–16]. Shortly thereafter, in 1951, the U.S. Food and Drug Administration (FDA) would approve ^{131}I as the first FDA approved radiopharmaceutical, a standard which has persisted to this day with ^{123}I and ^{131}I sodium iodide still being utilized for theranostic applications in both malignant and benign thyroid disease [14–16]. In the time following the FDA approval of ^{131}I, many other predominantly diagnostic radiopharmaceuticals gained FDA approval, including the highly notable approval of ^{99m}Tc-exametazime (Ceretec) for the SPECT imaging of stroke in 1988 and ^{18}F fluorodeoxyglucose (FDG) for the PET imaging of glucose metabolism associated with epileptic seizures in 1989 [17, 18]. However, there was a lull in therapeutic radiopharmaceutical development up until the FDA approval of ^{89}Sr-chloride (Metastron) and ^{153}Sm lexidronam (Quadramet) for the palliative treatment of bone pain associated with osseous metastases in prostate cancer (as well as osteosarcoma in the case of Quadramet) in 1993 and 1997 respectively [19–21]. Shortly thereafter, the radioimmunotherapies ^{90}Y-ibritumomab tiuxetan (Zevalin) and ^{131}I-tositumomab (Bexxar) were approved in 2002 and 2003 for the treatment of non-Hodgkin's lymphoma [22–24]. Approximately one decade later in 2013, $^{223}RaCl_2$ (Xofigo) was FDA approved for the treatment of bone metastases in metastatic castration resistant prostate cancer (mCRPC) [25–27]. While $^{223}RaCl_2$ itself was not marketed as a theranostic, it has since been hypothesized to be a viable therapeutic counterpart to ^{18}F NaF bone scintigraphy thus yielding theranostic applications in bone metastasis stemming from mCRPC [28]. More critically, the approval of $^{223}RaCl_2$ also marked a significant turning point in radiopharmaceutical development as it signified the successful marketing of a therapeutic radiopharmaceutical by a large pharmaceutical company, likely generating

confidence that the development of therapeutic nuclear medicine drugs was a marketable investment [25].

Shortly after the approval of $^{223}RaCl_2$, the field of nuclear medicine witnessed the FDA approval of the first tandem pair of diagnostic and therapeutic radiopharmaceuticals deliberately developed for theranostic use. Novartis' (formerly Advanced Accelerator Applications) ^{68}Ga-DOTATATE (NETSPOT) was approved for the PET imaging of somatostatin receptor positive neuroendocrine tumors (NETs) in 2016 and, two short years later in 2018, its counterpart ^{177}Lu-DOTATATE (LUTATHERA) was approved for the therapeutic targeting of NETs [25]. The approval of these two radiopharmaceuticals is often cited as a paradigm shift after which the development and progression of theranostics, especially peptide based theranostics, became an accelerated focus of the field of nuclear medicine [25, 29, 30].

While the development of novel radioisotopes and targeting ligands have always garnered scientific intrigue, especially by pharmaceutical companies, under this new era of theranostic prowess, advancements in theranostic radiopharmaceuticals are now also being developed in step-wise fashion in both the industrial and academic spaces with significant interest in developing analogues to existing radiopharmaceuticals (e.g. using the same radioisotope pairings with a different ligand or vice-versa), as well making modifications in ligand or chelation chemistry to optimize pharmacokinetics [25, 31]. This is most clearly evidenced by the fact that in 2022, just four years after the approval of ^{177}Lu-DOTATATE, Novartis secured FDA approval for both ^{68}Ga-PSMA-11 (LOCAMETZ) and ^{177}Lu-PSMA-617 (PLUVICTO) for theranostic applications in mCRPC [32]. Similarly, ITM Isotope Technologies' ^{177}Lu-edotreotide (ITM-11), a radiopharmaceutical developed with similar applications to ^{177}Lu-DOTATATE in the treatment of NETs, is currently being tested against ^{177}Lu-DOTATATE in a Phase III clinical trial and is fast tracked for FDA approval [33, 34].

Ultimately, the recent boom in scientific interest and competition within radiotheranostic development are reflective of the improvement in patient outcomes observed in both the ap-

plication of ^{68}Ga-DOTATATE/^{177}Lu-DOTATATE and ^{68}Ga-PSMA-11/^{177}Lu-PSMA-617, as well as the vast amount of innovative potential still remaining within the theranostic space [25, 29]. One facet of innovation that is of particular intrigue is the expansion of the "theranostic toolbox" to include novel radiopharmaceuticals which utilize different isotopes of the same element for the diagnostic and therapeutic components of a theranostic pair. There are several of these true theranostic candidates which are currently under development including select isotopes within the radioscandiums, radiocoppers, radioterbiums, and radioyttriums [12, 35–38]. Among these, we have designated the radioscandiums to be of particular interest due to their rapid translatability to imaging and treating mCRPC as analogues to the presently utilized pair of ^{68}Ga-PSMA-11/^{177}Lu-PSMA-617. This translatability, as well as the clinical advantages of true theranostics, will be discussed extensively in Sections 1.2-1.3 below.

1.2 Motivation for True Theranostic Development

As described in the previous section, the implementation of theranostic nuclear medicine has been pivotal in developing new standards for the diagnosis and treatment of oncologic disease. The use of PET or SPECT imaging to inform clinical decision making in the planning of radionuclide therapy treatments has been shown to screen out ineffective treatments and improve patient outcomes as one of the first implementations of precision or personalized oncology [39]. Simultaneously, the present implementation of theranostics still only involves the use of molecular imaging to predict general responses to a therapeutic treatment in opposition to a more advanced correlation between diagnostic and therapeutic radiopharmaceuticals in predictive dosimetry [12]. Under this expanded application of theranostic nuclear medicine, any diagnostic imaging taken for tumor staging would also provide information about potential therapeutic tumor dosing and the dose to organs at risk prior to the administration of the therapeutic radiopharmaceutical. This precise characterization of

downstream dosimetry would not only improve patient selection for therapeutic intervention, minimizing unnecessary treatments and reducing the overall burden on the patient and broader healthcare system, but it would also enable individualized dose optimization thus yielding better prognosis and patient outcomes [8–13].

The use of molecular imaging for predictive dosimetry has undoubtedly been one of the primary aims of theranostic development since its inception; however, because most theranostic radiopharmaceuticals are actually "pseudo" theranostics, this concept has remained out of reach [12]. These pseudo theranostics are pairs of diagnostic and therapeutic drugs which share the same biological target (e.g. prostate-specific membrane antigen) and targeting moiety, but vary in the linker, chelation complex, or elemental base of the radionuclide. The slightest variation in these chemical components results in pharmacokinetic differences between the diagnostic and therapeutic agents, even when the affinity for the target receptor is unchanged [12, 40, 41]. As the precision necessitated by predictive dosimetry demands nearly perfect correlations between the biological distribution of both the diagnostic and therapeutic radiopharmaceutical, pseudo theranostics are simply unsuitable.

Ultimately, this predicates the necessity of the development of true theranostics in nuclear medicine, tandem pairs of diagnostic and therapeutic radiopharmaceuticals which are composed of the same targeting moiety, linker molecule, and chelator whilst also utilizing a single element base for the radioactive portion of the pharmaceutical varying only in radioisotope. Within this scope, both the diagnostic and therapeutic radiopharmaceuticals would have nearly identical pharmacokinetics as isotopic variation does not yield any appreciable differences in chemical or physiological behavior. At most, the difference in atomic mass between two true theranostic radiopharmaceuticals may induce a minuscule variation in kinetics; however, these effects are most likely negligible, especially relative to the variance in the kinetics of pseudo theranostics [12].

While theranostic development has been extensive within nuclear medicine with a par-

ticularly notable boom in the last decade, the implementation of true theranostics into the clinical space is immensely underdeveloped. Despite the continually increasing number of hypothesized true theranostic pairs, the FDA approval of true theranostic radiopharmaceuticals has been limited to a single true theranostic pair in ^{123}I and ^{131}I sodium iodide for the SPECT imaging and targeted radionuclide therapy (TRT) of thyroid cancer and neuroblastoma [42, 43].

Even in the preclinical space, while many true theranostics have been investigated, the scope of investigation is often limited and focuses only on singular aspects of radiopharmaceutical development as opposed to a comprehensive evaluation of proposed radiopharmaceuticals across the entire development pipeline. In order to accelerate the development of true theranostics, and thus predictive dosimetry, it is imperative that extreme focus be placed on the holistic investigation and evaluation of proposed true theranostic pairs from the perspectives of radioactive production, radiochemistry, diagnostic capabilities, and therapeutic efficacy.

1.3 Innovation of Radioscandiums in Metastatic Castration Resistant Prostate Cancer

1.3.1 Limitations in the Current Standards of Metastatic Castration Resistant Prostate Cancer Management

As a result of the underdevelopment of true theranostics, there is an absence of data which explicitly illustrates the hypothesized improvements in dose correlation from diagnostic imaging to radionuclide therapy when utilizing a true theranostic pair relative to a pseudo theranostic pair. In this regard, it has become increasingly clear that the rapid development of true theranostics with presently utilized clinical analogues would be immensely beneficial in the evaluation of true theranostics as oncology trends towards precision medicine.

Within this context, metastatic castration resistant prostate cancer (mCRPC)—an advanced form of metastatic prostate cancer which no longer responds to androgen deprivation therapy—is an optimal target for rapid true theranostic development given the prevalence of prostate cancer as the cancer with the second highest incidence and mortality among cancers in the American male population [44]. Although pseudo theranostics already exist for mCRPC, the further refinement of staging and treatment strategies is still highly valuable as mCRPC is also increasing in prevalence in accordance with an aging population demographic [45]. The great strides that the pseudo theranostic pair of ^{68}Ga and ^{177}Lu have made in diagnosing, staging, and treating mCRPC when conjugated with PSMA targeting ligands are critical context for just how transformative theranostic can be; however, it is also clear that the foundation of ^{177}Lu-PSMA-617 (PLUVICTO) therapeutics and ^{68}Ga-PSMA-11 (LOCAMETZ) diagnostics can be further improved upon with a true theranostic analogue.

In the realm of therapeutics, ^{177}Lu-PSMA-617 has greatly increased median progression-free survival time and overall survival time when used to treat mCRPC, and has also shown potential as a neoadjuvant therapy prior to radical prostatectomy in high risk localized prostate cancers [46, 47]. At the time of writing this thesis, the FDA approved usage of ^{177}Lu-PSMA-617 has also just been expanded to include mCRPC patients that have not yet received chemotherapy, further broadening its impact [48]. That being said, the patient prognosis for mCRPC is still objectively poor with a median progression-free survival time of 8.7 months and overall median survival time of 15.3 months when given ^{177}Lu-PSMA-617 therapy [46]. However, as the dosing of ^{177}Lu-PSMA-617 mandates a conservative approach to ensure the sparing of organs at risk, it is feasible that with the predictive dosimetry afforded by a true theranostic analogue, treatment aggressiveness could be amplified thus yielding improved patient outcomes.

In the scope of diagnostics, ^{68}Ga-PSMA-11 has proven to be an effective agent for the

diagnosis and staging of prostate cancer, particularly in cases with intermediate to high Gleason scores and elevated PSA levels [49, 50]. Moreover, increased standardized uptake values observed in ^{68}Ga-PSMA-11 PET have been shown to be moderately to strongly associated with positive outcomes in ^{177}Lu-PSMA-617 TRT [51–53]. Nevertheless, prostate cancer molecular imaging has become increasingly dominated by ^{18}F based radiopharmaceuticals such as the PSMA targeting ^{18}F piflufolastat (PYLARIFY) and ^{18}F flotufolastat (POSLUMA) [12, 54, 55]. There is even some indication that the non-PSMA targeted ^{18}F fluorodeoxyglucose (FDG) may have added utility in prostate cancer applications [56]. This is because the more accessible production and longer half-life of ^{18}F, which enables more widespread transport and the ability to image at longer time-points, and the superior imaging resolution of ^{18}F due to its lower initial positron kinetic energy outweighs the benefits of a marginally closer kinetic match in ^{68}Ga-PSMA-11 [12, 57]. In essence, because none of the above diagnostic radiopharmaceuticals are capable of providing precise dose estimation for ^{177}Lu-PSMA-617, any loss in kinetic similarity between the diagnostic and therapeutic agents does not yield a loss in function.

Even when utilizing ^{68}Ga-PSMA-11 to correlate dose to its therapeutic counterpart, the ratio of absorbed dose estimated from ^{68}Ga-PSMA-11 PET and the true absorbed dose calculated from ^{177}Lu-PSMA-617 SPECT was shown by Peters et al. to vary by $\pm$20.8% in the kidneys, $\pm$28.3% in the submandibular glands, $\pm$26.1% in the parotid glands, and $\pm$53.8% in lesions [58]. This is of particular concern as the kidneys, parotid glands, and submandibular glands are all organs at risk in ^{177}Lu-PSMA-617 therapy [59]. Moreover, while the high variance in dose correlation in lesions was partially dependent on lesion size, it is still indicative of the limitations of pseudo theranostic dose correlation, even more so when one considers that the dose to bone marrow from adjacent metastases is often a limiting factor in TRT [58–62].

The incongruence between the dosimetric distributions of ^{68}Ga-PSMA-11 and ^{177}Lu-

PSMA-617 is unsurprising given the structural differences between the two radiopharmaceuticals. While both PSMA-11 and PSMA-617 utilize the same Lys-urea-Glu tail as a binding motif, the linker molecule and chelator of these two ligands are radically different. As is shown in Figure 1.1, PSMA-617 utilizes a cyclical DOTA chelator and a hybrid naphthylic and cyclohexyl linker structure. Conversely, PSMA-11 utilizes an acyclical HBED-CC chelator and a hydrocarbon linker. In this regard, it has been shown by Banerjee et al. that the modification of chelating agents in PSMA targeted radiopharmaceuticals greatly influences their pharmacokinetics, likely as a result of changes in lipophilicity and charge [63]. Similarly, linker lipophilicity contributes to the binding of the radiopharmaceutical to the hydrophobic pocket of the PSMA active site and also increases non-specific binding to non-target cells [64–66]. This is further compounded by the fact that these two radiopharmaceuticals utilize different elemental bases for the radionuclide portion of their structure which can alter radiopharmaceutical lipophillicity, charge, and conjugation as a consequence of complexation geometry [67].

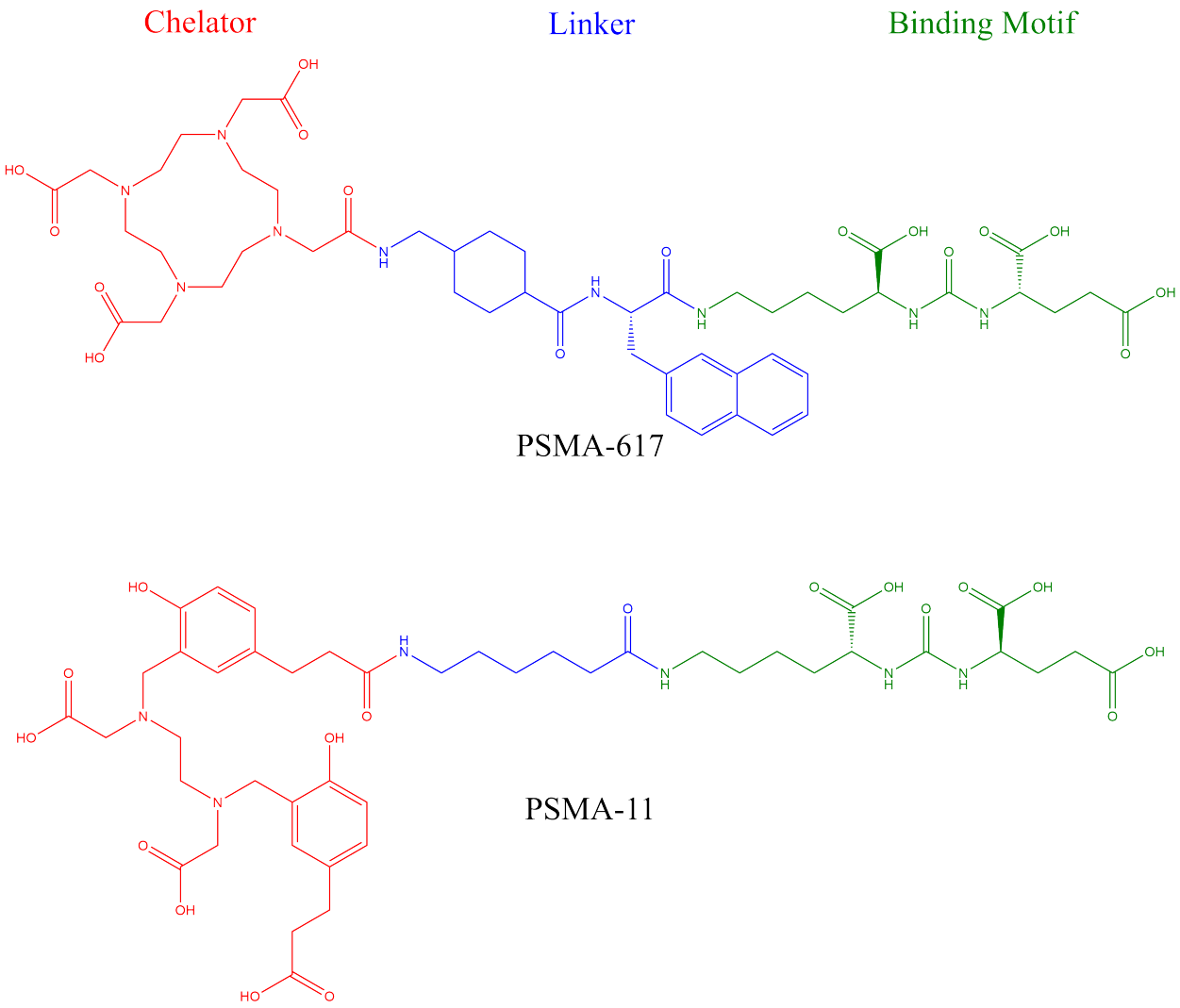

Figure 1.1: Structural componenets of PSMA-617 and PSMA-11.

The clear basis for pharmacokinetic variance between ^{68}Ga-PSMA-11 and ^{177}Lu-PSMA-617 suggests that, for the implementation of a complete theranostic approach to disease management in mCRPC, new radiopharmaceuticals must be devised which utilize analogueous chemical structures beyond just the binding moiety. Only through the development of true theranostic radiopharmaceuticals will it be truly possible to approach mCRPC from the lens of precision medicine as is the penultimate vision of this newfound era in theranostics. With the enhancements brought forth by predictive dosimetry, the true theranostic approach may also alleviate the most pressing shortcomings of the current treatment standards in mCRPC

including the inability to accurately predict dose to organs at risk as well as the short progression-free and overall survival times.

1.3.2 Potential Improvements in Metastatic Castration Resistant Prostate Cancer Management with Radioscandium PSMA-617

Given the vast improvements brought forth by ^{68}Ga-PSMA-11 and ^{177}Lu-PSMA-617 in the management of mCRPC, along with the clear limitations of their tandem use as theranostics, it is unquestionable that the further refinement of mCRPC theranostics through a true theranostic analogue would be of great benefit. In this regard, the radioscandiums are an optimal choice for true theranostic development as radioscandium analogues exist both for the diagnostic component of ^{68}Ga (^{43}Sc and ^{44}Sc) and the therapeutic component of ^{177}Lu (^{47}Sc) with all three of these radioscandiums having accessible nuclear production routes [68].

Scandium also has similar coordination chemistry to lutetium as a lanthanide-like trivalent group 3 element [69]. Consequently, the radioscandiums can be rapidly tailored to mCRPC applications as they readily conjugate with the PSMA-617 ligand [35, 69]. As such, ^{43}Sc-PSMA-617 and ^{44}Sc-PSMA-617 can be readily synthesized for the PET-based diagnosis and staging of mCRPC, and ^{47}Sc-PSMA-617 can be utilized for TRT.

Because they share the same ligand, linker, chelator, and elemental radionuclide base, the radioscandium PSMA-617 analogues would offer significant improvements to the relative pharmacokinetics of the diagnostic and therapeutic agents utilized for mCRPC in comparison to the clinically utilized pair of ^{68}Ga-PSMA-11 and ^{177}Lu-PSMA-617. As predictive dosimetry also relies on the maximization of the time points at which diagnostic imaging is taken, the hypothesized improvements in correlational accuracy are further compounded by the fact that both diagnostic radioscandiums have a half-life that is approximately four times that of ^{68}Ga. As such, the radioscandiums have the optimal decay and chemical properties

to facilitate predictive dosimetry in mCRPC for the very first time.

1.4 Dissertation Objectives

This complete development of radiopharmaceuticals is highly multidisciplinary and involves aspects of radioisotope production, radiochemistry, *in vitro* evaluation, *in vivo* evaluation, and simulation-based analyses of dosimetry and radiobiological effect. This already robust development pipeline is even more expansive than typical radiopharmaceutical development because we aim to further the development of an entire group of radiopharmaceuticals in the radioscandiums as opposed to the development of a singular drug. Under this broad scope, the specific objectives of this thesis are as follows:

1. **Develop Radioscandium Production Methods Using a Compact Medical Cyclotron.** In order to bolster accessibility of the radioscandium production methods, a conversion system will be developed to enable the beamstop of a biomedical cyclotron to be used as a solid target holder. This conversion system will be used to produce ^{43}Sc, ^{44}Sc, and ^{47}Sc from calcium-based targets. Chemical methods for the separation of the radioscandiums from the calcium target material and the radiolabeling of radioscandiums with PSMA-617 will also be developed.

2. **Characterize the Diagnostic and Therapeutic Efficacy of Radioscandium PSMA-617 *in vitro* and *in vivo*.** Enzalutamide resistant and luciferase expressing LNCaP (LNCaP-EnzaR-Luc) and luciferase expressing DU145 (DU145-Luc) cell lines will be used to produce *in vitro* models and *in vivo* murine xenografts to assess the theranostic capabilities of radioscandium PSMA-617. Uptake, internalization, and blocking assays will be performed to assess specificity of radioscandium PSMA-617 to PSMA expression. Murine models will be imaged with radioscandium PSMA-617 PET and SPECT to assess diagnostic efficacy. Therapeutic efficacy will be probed

by using immunohistochemistry to detect DNA doubles strand breaks following the administration of therapeutic ^{47}Sc-PSMA-617 relative to a control group which did not receive any treatment.

3. **Define the Dosimetric Properties and Radiobiological Effect of the Radioscandiums using Monte Carlo Dosimetry Simulations.** Monte Carlo simulations will be conducted in TOPAS to evaluate the micro and macro dosimetric profiles of the radioscandiums decay utilizing energy deposition curves. The geometry and source to target configurations of the MIRD cellular S-value formalism will also be utilized to assess cellular dosimetry at different levels of cellular localization. Additional simulations will be conducted to evaluate the DNA damage directly induced by the ionizing radiation produced in radioscandium decay as a probe for therapeutic efficacy.

1.5 Dissertation Organization

This dissertation spans the entire pipeline of radiopharmaceutical development up through the pre-clinical phase and, as such, explores elements of radioisotope production, radiochemistry, *in vitro* and *in vivo* evaluation, as well as Monte Carlo based characterizations of dosimetry and radiobiological effect.

Chapter 2 provides fundamental context and background knowledge for the design and utilization of radiopharmaceuticals within the contexts of molecular imaging, radionuclide therapy, and their tandem use in theranostics; describes the intrinsic chemical and radioactive properties of ^{43}Sc, ^{44}Sc, and ^{47}Sc within the context of other radioisotopes presently implemented in the clinical diagnosis, staging, and treatment of mCRPC; and finally provides an overview of the structure of the PSMA-617 ligand as it relates to the radioscandiums and the targeting of prostate-specific membrane antigen (PSMA).

Chapter 3 describes the production of ^{43}Sc, ^{44}Sc, and ^{47}Sc from calcium based targets utilizing a standard biomedical cyclotron including the creation of a novel conversion system

which enables the use of the beam-stop as a solid target holder. Chapter 3 also explores the estimation of ^{43}Sc production yields with a mathematical methodology.

Chapter 4 describes the development of a chemical procedure for the separation of radioscandiums from their calcium starting material, radiolabeling of the radioscandiums with PSMA-617, and the reformulation of the final radiopharmaceutical to facilitate *in vivo* use.

Chapter 5 describes the pre-clinical evaluation of ^{43}Sc-PSMA-617 and ^{47}Sc-PSMA-617 within the contexts of specific uptake in PSMA-expressing cell lines and molecular imaging in mice with PSMA-expressing xenografts. Chapter 5 also provides an analysis of the correlation between ^{43}Sc-PSMA-617 PET and ^{47}Sc-PSMA-617 SPECT when used to image the same specimen. The therapeutic efficacy of ^{47}Sc-PSMA-617 TRT is also examined in this chapter by evaluating the presence of DNA double strand breaks induced in PSMA-expressing tumors excised from mice after intravenous ^{47}Sc-PSMA-617 injection relative to a control group which did not receive treatment.

Chapter 6 utilizes the Monte Carlo program TOPAS to characterize the individual decay physics and radiobiological effect of the radioscandiums within the context of radioisotopes clinically utilized for mCRPC. This Monte Carlo based evaluation is multi-faceted including the generation of energy deposition curves, calculation of cellular S-values, and the simulation of DNA damage in a complete nucleus model.

Chapter 7 summarizes the results of this dissertation and proposes future points of innovation for the development of radioscandium theranostics both within the context of mCRPC and beyond it.

CHAPTER 2

BACKGROUND

2.1 Principles of Nuclear Medicine and Molecular Imaging

2.1.1 Radiopharmaceuticals

In the most basic terms, a radiopharmaceutical consists of a radioactive isotope which is bound to a biological molecule that targets specific biological pathways or receptors that are overactive or over-expressed in cases of disease. An easy to conceptualize and prominent example of this would be FDG which enables the functional imaging of glucose metabolism as a positron-emitting ^{18}F-labeled glucose analogue which is taken up by metabolically active cells where it remains trapped due to its lack of the C2 hydroxyl group necessary to proceed with glycolysis after phosphorylation.

Within the context of radiometals, most radiometal-based radiopharmaceuticals consist of four critical parts: a targeting moiety, radioisotope, chelator, and linker molecule. These components are illustrated in Figure 2.1. The targeting moiety is the portion of the radiopharmaceutical which actually complexes with the biological molecule that is being targeted. Typically, the targeting moiety selectively binds to a cell-surface receptor or transmembrane protein that is overexpressed in the target disease. As such, the targeting moiety is carefully selected based upon the intended disease or pathway that is being targeted. Within the context of prostate cancer, a targeting moiety that selectively binds to prostate-specific membrane antigen (PSMA) is often selected because PSMA is a transmembrane protein which is both over-expressed in prostate cancers and contains an enzymatic site which facilitate surface uptake and internalization into the cell [70].

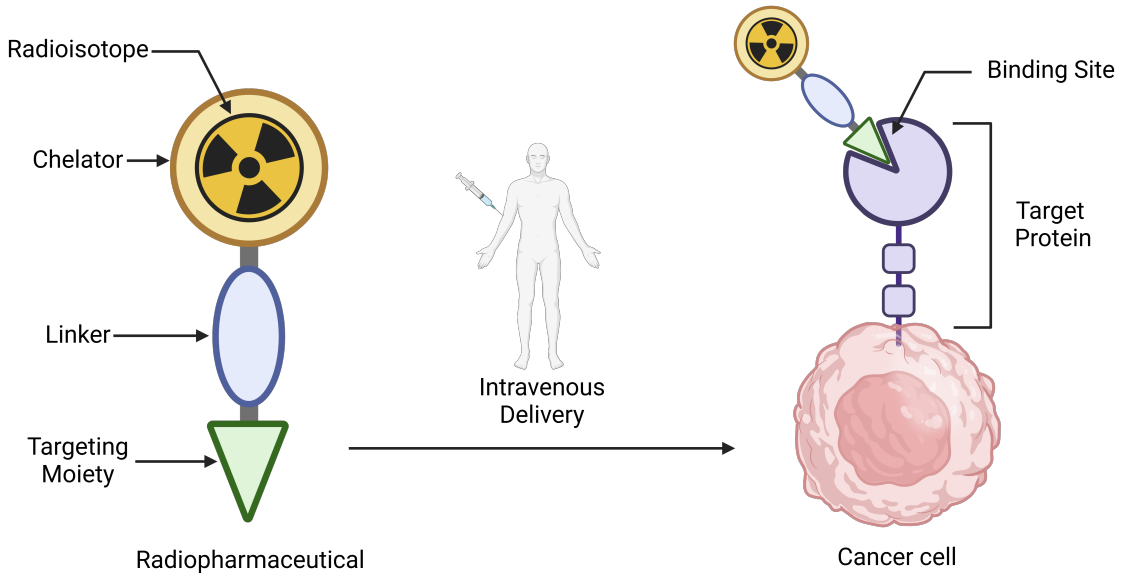

Figure 2.1: Graphical depiction of a radiopharmaceutical with a targeting moiety, linker molecule, and occupied chelation complex. Radiopharmaceutical binding to a target cancer cell is also depicted [71].

Beyond the targeting moiety, the radioisotope is the other portion of a radiopharmaceutical which necessitates careful selection based upon the usage case. This component consists of the actual radioactive atom which will decay and emit the radiation that is necessary for either nuclear molecular imaging or radionuclide therapy. As the decay scheme of a radioisotope dictates which radiative particles are emitted, the frequency at which radioactive particles are emitted, the range of those particles, and the interactions those particles will have with matter along their path of travel, the choice of radioisotope has both functional and dosimetric implications. While PET naturally requires a positron-emitting isotope, and SPECT requires an isotope which emits gamma-rays within a suitable energy range, isotope selection is less straightforward in radionuclide therapy where not only are electron emitting and alpha particle emitting isotopes viable, but administered doses are typically higher and cytotoxic effects to non-target tissues are of significant concern.

For radiometal-based pharmaceuticals, the chelator is then the portion of the radiophar-

maceutical which complexes with the metal radioisotope, ensuring that it cannot dissociate from the radiopharmaceutical and interact with the biological system in unintended ways. Chelators accomplish this by forming chelation complexes which consist of networks of bonds with the radioisotope. Naturally, as the base element of a radioisotope will define its chemical properties, the selected chelator must be well-suited to a given radioisotope's valency and size among other chemical properties to ensure stable bonding.

Finally, the linker molecule is simply the portion of the radiopharmaceutical which connects the targeting moiety and the chelator. That being said, the choice of linker molecule influences the stereochemistry and conformation (spatial arrangement) of the overall radiopharmaceutical, as well as the chemical properties of the overall ligand such as hydrophobicity and lipophilicity. Consequently, the linker molecule can still have significant effects on the kinetics of a radiopharmaceutical potentially influencing both its biological distribution and ability to internalize within a cell [70, 72].

2.1.2 PET Imaging

One of the primary imaging modalities utilized in nuclear medicine is positron emission tomography (PET) which utilizes radiopharmaceuticals labeled with positron (β^+) emitting radioisotopes for functional imaging. Essentially, when the radioisotope decays and a positron is emitted, the positron traverses the local medium continually interacting and losing kinetic energy until it collides with an electron and annihilates. Upon annihilation, two 511 keV gamma rays are emitted approximately 180 degrees apart with some small variance in angular range due to the conservation of the kinetic energy and momentum of the parent positron [73, 74].

If these 511 keV gamma rays interact with two detectors, the coupled scintillation crystal and silicon photomultiplier system which composes each individual PET detector, a line of response can be drawn between the two detections. These detection events are called coin-

cidence events and are gated by energy and timing windows to minimize image degradation from false coincidence events. The culmination of these lines of response ultimately produces the final PET image. A broad depiction of the positron annihilation and a subsequent true coincidence event in the PET detector ring is presented in Figure 2.2.

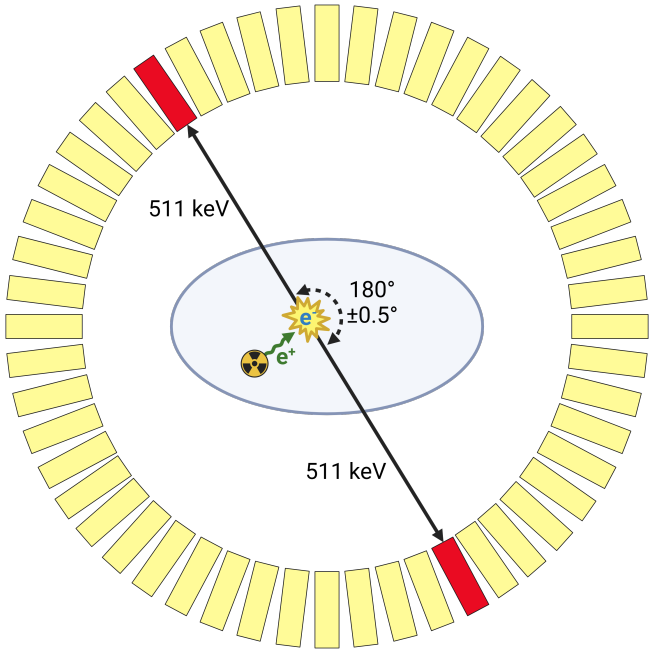

Figure 2.2: Graphical depiction of PET imaging [75].

In addition to true coincidence events as depicted above, it is also possible to detect scatter coincidence and random coincidence events. Scatter coincidences occur when one or both 511 keV gamma rays interact with the tissue they are traversing causing them to scatter and deviate from their original path prior to detection. Random coincidences occur when the 511 keV gamma rays of two separate events are detected simultaneously within the present timing window. These false coincidences produce a line of response which does not pass through the radioactive source degrading overall image quality. These two types of false coincidences are illustrated in Figure 2.3.

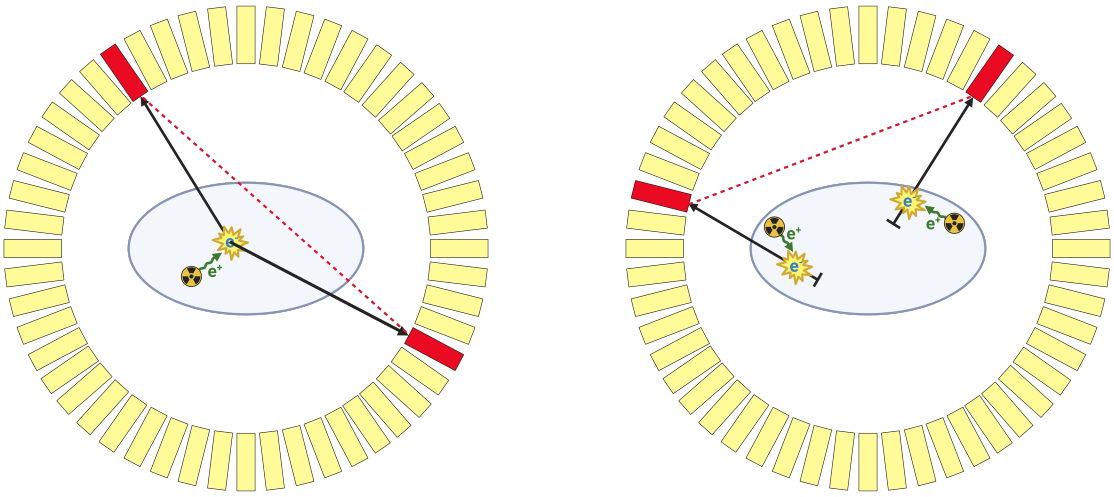

(a) Scatter coincidence (b) Random coincidence

Figure 2.3: Scatter and random coincidence events in PET. The false line of response is demonstrated as the red dashed line between detection events [76, 77].

It is also worth noting that the interaction of single photon emissions (e.g. gamma rays emitted during internal conversion or isomeric transition) with the detector elements contributes to random coincidence detection, detector saturation, and detector dead time, so the energy and frequency of additional gamma ray emissions should be considered in PET isotope selection [78, 79].

The overall spatial resolution of PET is dependent on a myriad of factors originating from the detector system such as detector width, detector separation, reconstruction algorithm, and the ability to measure gamma ray penetration depth into the detector crystal; however, factors intrinsic to the mechanism of positron emission and annihilation such as positron range and accolinearity, small deviations in the separation angle of the annihilation gamma rays due to the conservation of residual momentum at annihilation, are also major factors [80].

Of these factors, resolution degradation due to the positron range is of particular note in

radiopharmaceutical development as it is dependent on radioisotope selection. The kinetic energy of a radioisotope's emitted positron is directly correlated to its average range in tissue given that the cross-section for positron annihilation is inversely related to positron kinetic energy [81]. Consequently, positrons interact with matter continuously thus losing energy and increasing the probability of interaction with an electron up until the point of annihilation [82]. Because positrons do not annihilate at the exact location where they are omitted, the positron range introduces uncertainty in the source location of the radiopharmaceutical [73, 74, 82].

Conversely, image blurring due to accolinearity is mostly independent of isotope selection as annihilation only occurs after an emitted positron has lost most of its kinetic energy. Therefore, the angle between the emitted annihilation gamma-rays is independent of the initial positron kinetic energy.

Naturally, the degrading effects of positron range blurring become greater with greater positron ranges, and thus greater positron kinetic energy, as more uncertainty in the true origin of the positron emissions is introduced [82]. In this sense, even with a perfect detector system; the intrinsic resolution limit of PET imaging is confined to a combination of the positron range and accolinearity of the annihilation gamma rays thus emphasizing the importance of radionuclide selection in PET imaging [80].

2.1.3 SPECT Imaging

In addition to PET, single photon emission computed tomography (SPECT) can also be utilized for functional imaging in nuclear medicine, albeit at lower resolutions for large fields of view such as those used in metastases detection. Typical SPECT systems utilize a pair of gamma camera on a rotating gantry to detect the emission of gamma rays from radiopharmaceuticals at multiple, equally spaced angular positions. Through tomographic reconstruction methods, the 2-D projection images obtained at each camera position are then reconstructed

into a stack of 2-D images which form a 3-D image volume [83].

Ultimately, it is the design of the gamma camera which makes image formation possible without the utilization of coincidence detection as is necessary for PET. Most notably, while SPECT also classically utilizes scintillating crystals to convert incident gamma rays into visible light, a collimator is used to block incident gamma rays which are not coming from a specified direction as defined by the collimator [83]. The information provided by the chosen collimator about the directional origin of any detected gamma-rays at each camera position enables the drawing of a back projection, much like a line of response in PET [83]. When an incident gamma ray does interact with the scintillator, optical photons are produced and collected by a 2-D array of photomultiplier tubes which amplify the optical signal and convert it into a measurable electrical signal [83]. It is worth mentioning, however, that in more contemporary SPECT systems which utilize CZT or cadmium telluride (CdTe) semiconductors rather than scintillating crystals, gamma camera instrumentation is less modular as semiconductor-based detectors directly convert incident photons into an electrical signal [84, 85]. A simplified version of a standard gamma camera is exhibited in Figure 2.4 along with a representation of gamma ray detection in a standard two-detector SPECT system.

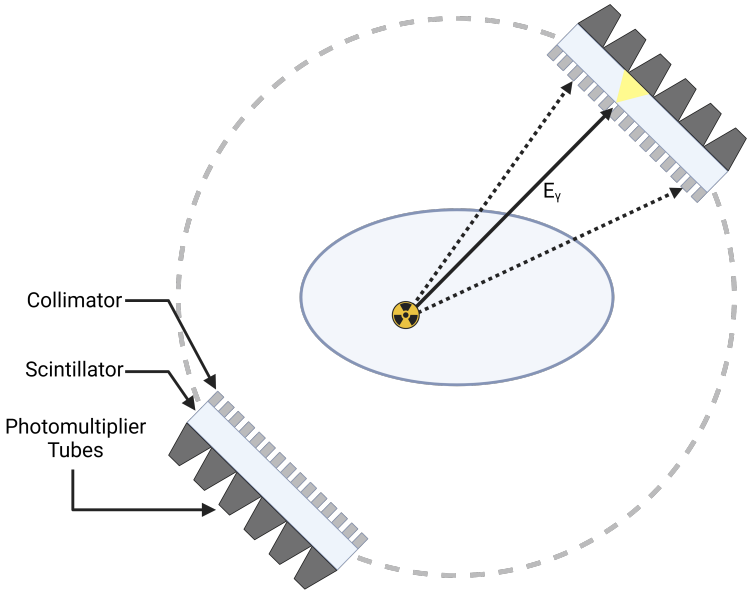

Figure 2.4: Graphical depiction of SPECT imaging with a parallel hole collimator. Dashed lines indicate incident gamma rays that were rejected through collimation. The solid line represents an incident gamma ray which passes through the collimator and interacts with the scintillator as is indicated by the yellow of cone of produced optical photons [86].

SPECT resolution is highly dependent on collimator selection with some of the most prominent collimator geometries being parallel hole, converging-hole, diverging-hole, and pinhole. Each collimator type strikes a unique balance between spatial resolution and sensitivity, so collimator selection is not quite as simple as just choosing which collimator provides the greatest spatial resolution [83]. The number of angular views that the 2D projections are obtained at is also a major factor in SPECT image quality as having less acquisitions than the matrix size of the projection image results in artifacts [87, 88]. However, patient motion also induces imaging artifacts, so the number of views is often practically limited [87].

It is also worth noting that quantitative SPECT imaging—the determination of precise radioactivity concentrations within an imaged volume through SPECT imaging—is relatively underdeveloped compared to quantitative PET which is currently a clinical standard [89, 90]. This is because technical advancements in the minimization of uncertainties in SPECT

imaging such as photon scatter, photon attenuation, and partial volume effects have been considerably slower than with PET [89]. Moreover, the necessitated use of collimators in SPECT imaging also reduces the number of detected events substantially thus resulting in significantly worse sensitivity and counting statistics relative to those characteristic of PET imaging [91]. This could prove an important challenge in the development of theranostic radiopharmaceuticals as accurate dose correlation between PET and SPECT imaging is critical for the development of predictive dosimetry.

2.1.4 Targeted Radionuclide Therapy

TRT broadly involves the applications of radiopharmaceuticals which have decay properties conducive to inducing damage to cancerous cells or the tumor microenvironment. This requires the conjugation of a ligand with a radioisotope which emits ionizing radiations that are capable of depositing sufficient energy to directly or indirectly induce DNA damage. As cancerous cells often exhibit mutations that induce dysfunction in DNA repair pathways, it is possible to utilize ionizing radiation to overload their repair capacity thus inducing apoptosis [92, 93].

The capacity of a radioisotope to induce DNA damage can ultimately be probed through two related quantities, linear energy transfer (LET) and relative biological effectiveness (RBE). The LET describes the energy loss per unit length of distance traveled by an ionizing particle and is often closely associated with the particle range [94]. The RBE describes the ratio of the dose necessary to achieve the same biological end point (often a cellular survival fraction) for two different types of ionizing radiation. Within this construct, the reference radiation type is typically chosen to be gamma rays or beta electrons such that the RBE of a beta electron emitter is approximately equal to one.

RBE increases rapidly with LET up until approximately an LET of 100 keV/μm corresponding to a 2 nm average separation of ionizing events which correlates to the approximate

width of the DNA double helix [95]. Beyond this point, the RBE decreases due to overkill effects in which the mean number of ionizations occurring along a given length of an ionizing particle's track is greater than that necessary to induce cell death [95].

Typically, radioisotopes selected for use in TRT are beta electron (β^-), alpha particle (α), or Auger electron emitters as those particles all exhibit ranges which are on the relevant scale of cancerous lesions [96]. Among these, beta electron emitters are the most commonly utilized in TRT in spite of their relatively lower LET ($\sim$0.1-2 keV/μm) because they are the most forgiving with regards to radiopharmaceutical specificity, offer a range of viable radionuclides with varying chelation chemistry and radiation energies enabling tailored radionuclide selection to more tumor sizes and types, and are the most widely producible and thus commercially available [94]. Because beta electrons interact continuously and have millimeter to sub-millimeter ranges, beta electron emitters are also the most appropriate class of radionuclide for utilization in large tumors and tumors which exhibit a heterogeneous uptake of the radiopharmaceutical as a significant portion of the radiation dose is deposited outside of the accumulating cell and thus into neighboring cancerous tissues, a phenomenon known as the cross-fire effect [94, 97].

Alpha-emitting radioisotopes have extremely large LETs ($\sim$50-300 keV/μm), the highest RBE among the relevant ionizing radiations (anywhere from 2-15 depending on the chosen biological metric), and ranges on the order of tens of microns with a Bragg peak near the end of their tracks [94, 98]. Consequently, alpha-emitting radionuclides induce ionizations in very small volumes which, with proper specificity, yields highly-targeted DNA damage while sparing non-cancerous cells [94]. In accordance with this, alpha particles are mostly suitable for applications in small tumors, tumors which exhibit a homogeneous expression of the targeted protein, and tumors that are proximal to radiosensitive organs such as bone metastases [94, 99]. However, alpha emitting radionuclides also tend to be heavy atoms with cascading decay chains that also produce radioactive daughter nuclei further complicating

assessments of radiopharmaceutical stability, toxicity, and dosimetry [100, 101]. Moreover, radiopharmaceutical specificity becomes increasingly critical in targeted alpha therapy as the highly localized energy deposition of alpha emissions can yield highly toxic effects in healthy tissues in cases of non-specific uptake and biological clearance [94].

Auger electrons have an extremely low kinetic energy (on the order of 1-10 keV) and thus very short ranges on the order of less than a micron. Moreover, Auger electrons can exhibit a variable LET which is only slightly greater than beta electrons with cytoplasmic uptake, but is as high as 26 keV/μm with nuclear uptake [102]. Unsurprisingly, this implies that Auger electrons are also capable of having variable RBEs depending on their degree of localization, with RBE increasing with greater proximity to the nucleus [94]. As such, Auger therapy is regarded as being highly targeted and tissue sparing with the appropriate specificity. However, relative to both beta electron and alpha therapies, intracellular positioning is critical and can be seen as a major practical limitation as it is immensely challenging to design radiopharmaceuticals which are both selectively internalized and undergo nuclear localization [102, 103].

While not widely implemented in the clinical or pre-clinical spaces, positron-emitting isotopes also have immense unrealized potential for TRT due to having a slightly greater linear energy transfer than electrons and a unique radiation track structure which results in an excess deposition of energy just prior to annihilation [104]. Therefore, positron emitters should also be considered when designing radiopharmaceuticals for TRT, especially in true theranostics where the number of viable radioisotopes is limited [104].

2.2 Decay Properties of Radioscandiums

2.2.1 Scandium-43

The radioactive decay of Scandium-43 (^{43}Sc) primarily consists of positron emission with a high frequency (88.1%) and a relatively long half-life of 3.891 h making it a strong candidate for PET imaging applications. ^{43}Sc's positron emissions can be further broken down into two separate initial kinetic energies: 344.46 keV (17.2% intensity) and 508.10 keV (70.9% intensity) yielding an average initial kinetic energy of 476.20 keV. The remaining 11.9% of the ^{43}Sc decay scheme is through electron capture and thus is not relevant with regards to radiopharmaceutical application. These decay characteristics, as well as those for ^{43}Sc's sister radioisotope ^{44}Sc, and other clinically utilized radionuclides for PSMA-targeted PET, are summarized in Table 2.1.

Radionuclide	$t_{1/2}$	β^+ Intensity	$< E_{\beta^+} >$	r^*_{CSDA}	E_γ	E_γ intensity
^{43}Sc	3.891 h	88.1%	476.2 keV	0.163 cm	372.9 keV	22.1%
^{44}Sc	4.042 h	94.3%	630.2 keV	0.241 cm	1157.0 keV	99.9%
^{68}Ga	1.128 h	88.9%	829.5 keV	0.347 cm		
^{18}F	1.829 h	96.7%	249.8 keV	0.062 cm		

Table 2.1: Radioactive decay information for positron-emitting radioscandiums and other radioisotopes used clinically for PSMA PET imaging. Gamma emissions below an energy of 100 keV or an intensity of 1% have been omitted for readability. *Positron range was linearly interpolated from the NIST published values for the energy dependent positron range in water according to the CSDA [105–109].

With reference to the other radionuclides utilized clinically for PSMA PET imaging, ^{43}Sc has a 3.45x longer half-life than ^{68}Ga, a 2.13x longer half-life than ^{18}F, and a half-life that is approximately equal to that of ^{44}Sc. The half-life of ^{43}Sc should therefore facilitate

imaging at longer time-points than are currently feasible with ^{68}Ga and ^{18}F [110, 111]. As PSMA-617 radiopharmaceuticals are rapidly excreted from the renal system after injection, these longer imaging time-points should enable PSMA PET imaging with improved tumor to background ratios, yielding improved visualization of PSMA expressing tumors [112, 113]. Because therapeutic radiopharmaceuticals (including ^{47}Sc and ^{177}Lu) tend to have longer half-lives, these extended time points are especially critical in theranostic applications as PET imaging is utilized as a probe for downstream therapeutic dosimetry [58, 114]. The additional time points possible with ^{43}Sc PET should therefore allow for characterizations of PSMA-617 based treatment kinetics beyond what is currently possible with ^{68}Ga and ^{18}F [115]. This kinetic analysis can then be utilized to correlate the localization of ^{43}Sc-PSMA-617 in PET to an estimate of dosimetry in ^{47}Sc-PSMA-617 TRT thus improving the accuracy of treatment planning and the capacity for highly individualized, aggressive treatments for mCRPC [115].

From the perspective of radiopharmaceutical transport, the longer half-life of ^{43}Sc should also make it significantly more accessible to PET centers without dedicated or local cyclotron facilities relative to ^{18}F [116, 117]. The same is true when comparing ^{43}Sc to pre-conjugated ^{68}Ga radiopharmaceuticals; however the ^{68}Ge/^{68}Ga generator (Galli Eo) still provides distinct advantages in facilities which can perform their own radiolabeling with a generator source [118, 119]. Per Carzaniga et al., the half life of ^{43}Sc should be sufficient to enable transport as far as 500 km (approximately 370 miles) thus opening up the prospects of both intrastate and interstate delivery from dedicated production centers [117].

^{43}Sc has a significantly lower average positron energy than ^{68}Ga and a higher average positron energy than ^{18}F. With regards to its sister isotope, ^{43}Sc also has a lower average positron energy than ^{44}Sc. As positrons continually interact with the media they traverse until annihilation, following the continuous slowing down approximation (CSDA), the average positron energy is directly proportional to its range which contributes to image blur

and is a limiting factor in achievable PET resolution [82, 120]. Consequently, the positron range of ^{43}Sc should yield better PET imaging resolution than ^{68}Ga and ^{44}Sc, but slightly worse imaging resolution than ^{18}F. However, the influence of positron range on image quality diminishes at lower positron energies as other resolution limiting effects (such as intrinsic scanner resolution) begin to dominate. As such, the worsening in resolution from utilizing ^{43}Sc over ^{18}F should be much less pronounced than the worsening in resolution from utilizing ^{68}Ga over ^{43}Sc [80, 82].

^{43}Sc also emits a 372.9 keV gamma ray with 22.1% intensity. As this gamma ray is characteristic to ^{43}Sc and is distinct from the emission of 511 keV gamma rays in positron annihilation, it can be utilized to verify the identity of ^{43}Sc during production, chemical separation, and radiolabeling procedures. Within the context of the radioscandiums, the energy of the ^{43}Sc gamma ray emission is also approximately an entire order of magnitude lower than that emitted by ^{44}Sc as will be discussed in the next section. This places ^{43}Sc as a distinctly better candidate for PET pharmaceutical development than ^{44}Sc from the perspective of its physical decay properties. By emitting a substantially lower energy gamma ray than ^{44}Sc, ^{43}Sc poses much lower risks with regards to internal dosimetry as well as radiation exposure risks to medical staff and a patient's proximal family members. Naturally, as the injected dose for PET is much lower than that of TRT, these dosimetric risks are minimal relative to those in the treatment phase of theranostic application; however, in adhering to "as low as reasonably achievable" (ALARA) principles, it should still be considered.

2.2.2 Scandium-44

Scandium-44 (^{44}Sc) is another positron-emitting radioscandium, therefore making it an additional candidate for PET imaging. ^{44}Sc decays by positron emission with 94.3% intensity with the remaining portion of the decay scheme being attributed to electron capture. The average kinetic energy of the ^{44}Sc positron emission is 630.2 keV with a corresponding CSDA

range of 0.241 cm. As a result, ^{44}Sc should have better intrinsic PET resolution than ^{68}Ga, but worse imaging resolution than ^{18}F and its sister isotope ^{43}Sc.

^{44}Sc also exhibits a 1157.0 keV prompt gamma ray emission with nearly 100% intensity. Because this emission is of relatively high energy, it has the capacity to contribute to the saturation and dead time of PET detectors (especially with pre-clinical small animal PET) by increasing the singles detection rate [78, 121]. Much like the increased dosimetric impact of this gamma ray mentioned in the previous section, this is a factor which should be considered when choosing which radioscandium to utilize for PET imaging. This gamma ray could also decrease system resolution through the detection of coincidences and multiples of prompt gamma rays and annihilation photons after Compton scattering; however, because its initial energy is well outside typical PET energy windowing this effect should be minimal if at all present [122, 123].

It is also worth mentioning that, although detrimental for standard PET imaging, the prompt gamma ray emission of ^{44}Sc also offers the unique possibility of positronium lifetime imaging (PLI) [124, 125]. Essentially, approximately 40% of emitted positrons form positronium, an orbital system composed of a positron and electron, prior to annihilation and thus the emission of the standard 511 keV gamma rays [126]. Because prompt gamma rays are emitted simultaneously with the emission of a positron in beta plus decay, the difference in time between the detection of the prompt gamma rays and the annihilation gamma rays can be used as a metric of the positronium lifetime [126]. The lifetime of positronium (specifically ortho-positronium where the electron and positron have parallel spin states) has been shown to be inversely correlated with oxygen concentration, thus meaning that PLI, and therefore ^{44}Sc, have potential applications in the imaging of tumor hypoxia [125, 126].

While ^{44}Sc already has significantly better transportability than ^{18}F and ^{68}Ga due to its 4-hour half-life, ^{44}Sc has an especially strong capacity for long-distance delivery through the ^{44}Ti/^{44}Sc generator [127, 128]. Even when compared to the ^{68}Ge/^{68}Ga generator ($t_{1/2}$ =

271 d) the ^{44}Ti/^{44}Sc generator is particularly remarkable because of ^{44}Ti's 59.1-y half life [129, 130]. The complete development of this generator system would provide a continuous, sustainable source of ^{44}Sc with the capacity for global distribution; however, at present, further development into potential exchange resins or post-elution processing methods to separate ^{44}Sc from the ^{44}Ti generator source whilst maintaining an environment suitable for downstream radiolabeling is required [127].

^{44}Sc can also be produced in two separate excitation states, the ground state ^{44g}Sc (referred to as ^{44}Sc throughout this thesis) as well as a metastable state ^{44m}Sc which decays back to the ground state through internal transition [131]. Because ^{44m}Sc has a half-life of 58.6 h, it can be utilized as an *in vivo* generator of ^{44g}Sc [69]. Under this lens, an injected ^{44m}Sc-PSMA-617 radiopharmaceutical would gradually decay to the positron emitting ^{44g}Sc-PSMA-617 as non-specific uptake washes out through the renal system. Consequently, the use of this *in vivo* generator would facilitate the PET imaging of mCRPC at later time points with improved tumor to background ratios and enable kinetic modeling on time-scales congruent with the half-life of therapeutic ^{47}Sc [69]. As mentioned in the previous section, extended kinetic modeling would greatly improve dosimetry estimates and enable highly aggressive treatment planning in theranostic mCRPC treatment. Unlike other proposed *in vivo* generators such as ^{140}Nd/^{140}Pr and ^{166}Dy/^{166}Ho which have been shown to dissociate from their respective ligands from the recoil of their decay emission and downstream radiolytic effects, Huclier-Markai et al. found the ^{44m}Sc-DOTA complex to be stable when decaying to ^{44g}Sc-DOTA, thus making it a strong candidate for *in vivo* applications [69, 132, 133].

2.2.3 Scandium-47

Scandium-47 (^{47}Sc) is the sole electron emitting radioscandium with a half-life and beta electron kinetic energy suitable for therapeutic applications [35]. With a half-life of 3.349 d, ^{47}Sc falls within the range of therapeutic radionuclides that are used clinically; however,

^{47}Sc does decay approximately twice as quickly as its clinically utilized analogue ^{177}Lu [134]. While this may limit the breadth of potential therapeutic applications of ^{47}Sc, the shorter half-life should not pose issues when utilized with rapidly clearing small peptides such as PSMA-617 in the targeting of mCRPC [135].

Radionuclide	$t_{1/2}$	β^- Intensity	$< E_{\beta-} >$	r^*_{CSDA}	E_γ	E_γ intensity
^{47}Sc	3.349 d	100%	162.0 keV	0.032 cm	159.4 keV	68.3%
^{177}Lu	6.644 d	100%	133.6 keV	0.023 cm	208.4 keV	10.4%
					112.9 keV	6.2%

Table 2.2: Radioactive decay information for electron-emitting radioscandiums and other radioisotopes used clinically for PSMA targeted radionuclide therapy. Gamma emissions below an energy of 100 keV or an intensity of 1% have been omitted for readability. *Electron range was linearly interpolated from the NIST published values for the energy dependent electron range in water according to the CSDA [136–138].

As is exhibited in Table 2.2, the beta electrons emitted by ^{47}Sc have an average kinetic energy of 162.0 keV which is comparable to ^{177}Lu, but does result in a 39.1% greater CSDA range than is observed with ^{177}Lu. From a dosimetric perspective, this may entail that ^{47}Sc is a better therapeutic candidate for larger tumors and tumors which exhibit a non-homogeneous expression of PSMA, whereas ^{177}Lu may be a better candidate for therapy in small, uniform tumors [95, 139]. Specifically, as some PSMA expressing tumors have been shown to have both spatial and temporal heterogeneities in PSMA expression, the additional range afforded by ^{47}Sc could yield a significant boost in therapeutic efficacy through the cross-fire and bystander effects when applied to tumors with non-homogeneous PSMA expression [139].

^{47}Sc also emits a 159.4 keV gamma ray with an intensity of 68.3%. Much like the gamma-rays described in the decay of ^{43}Sc and ^{44}Sc, this gamma ray can also be highly

useful for identity verification following production, separation, and radiolabeling procedures. More critically, this gamma ray can be utilized for SPECT imaging which will enable dose correlation with diagnostic imaging obtained with radioscandium PET. Of course, this type of imaging correlation is also feasible with the currently utilized pair of ^{177}Lu and ^{68}Ga; however, the approximately 6.6x greater intensity of ^{47}Sc's gamma ray should enable more accurate characterizations of dose distribution, albeit at a greater dose to the patient [135]. As a somewhat unique aspect of the decay scheme of ^{47}Sc, the presence of this gamma ray also means that ^{47}Sc can be utilized as a completely self-contained theranostic capable of real time kinetic distribution and dose monitoring which should facilitate even further refinements in dosimetry characterizations of ^{47}Sc TRT.

2.3 PSMA-617

Vipivotide tetraxetan, or as it is more commonly known PSMA-617, is a modified inhibitor of prostate-specific membrane antigen (PSMA), a transmembrane protein characteristic of prostatic tissue which is over-expressed in prostate carcinoma [140]. The PSMA-617 molecule (illustrated in Figure 2.5) consists of a DOTA (tetraxetan) chelation complex, 2-naphthyl-L-Ala and *trans*-(aminomethyl) cyclohexyl linker moieties, and a Lys-urea-Glu PSMA binding region, [64, 141].

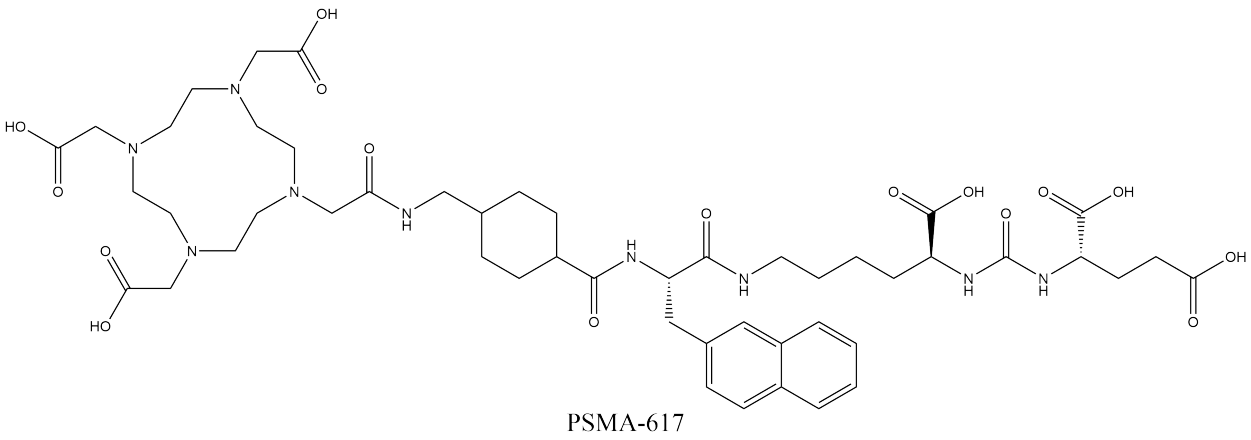

Figure 2.5: Chemical structure of PSMA-617.

Within its chemical structure, the DOTA chelation complex located at the head of the molecule is critical to PSMA-617's coordination chemistry as it enables the formation of aminopolycarboxylic acids with divalent, trivalent, and tetravalent cations [67, 142–144]. Essentially, each of the four nitrogen atoms within DOTA's macrocyclic ring contain a singular lone pair of electrons which can be shared with a central metal cation, forming four coordinated covalent bonds. The oxygen atoms on the three acetate side arms of DOTA, along with the amide oxygen, also have lone pairs of electrons which can be shared with the central ion, again forming coordinated covalent bonds [142, 145, 146]. Ultimately, this network of multiple coordinated covalent bonds provides additional thermodynamic stability relative to singular bonding between an organic molecule and a metal ion as the dissociation of the metal ion requires the breaking of all coordinate bonds which would require an unfavorable change in enthalpy [147, 148]. This binding is illustrated in Figure 2.6 with modified stereochemistry to improve visualization of the coordinate bonding to the central metal ion.

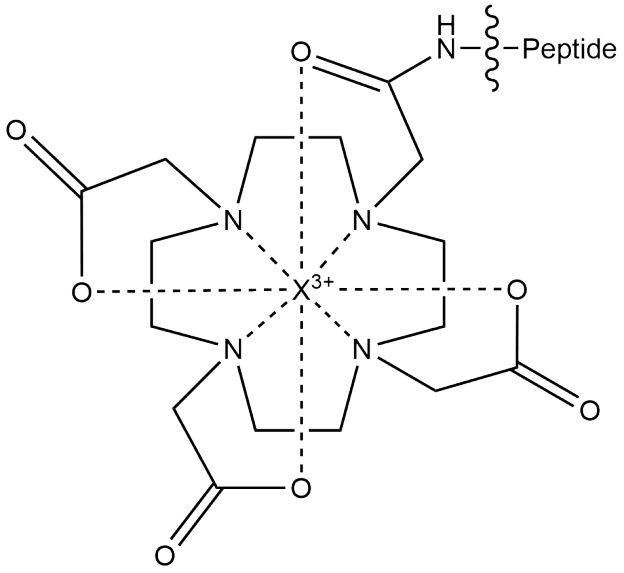

Figure 2.6: Chemical structure of the DOTA chelation complex bound to a trivalent cation.

As previously mentioned, this complex is able to form bonds with trivalent cations including scandium (Sc), lutetium (Lu), gallium (Ga), yttrium (Y), lanthanum (La), gadolinium (Gd), indium (In), thallium (Tl), bismuth (Bi), terbium (Tb), and actinium (Ac), facilitating immense potential for novel radiopharmaceutical applications [35, 145, 149]. However, the stability and formation rates of chelated complexes with these ions are highly variable, thus mandating that some ions are better suited for use in DOTA-based pharmaceuticals, especially with the added complexity of a targeting ligand such as PSMA-617 [149]. Multiple heavy metal ions such as iron (Fe), copper (Cu), and Zinc (Zn) also bind to DOTA chelators with often greater affinity than many of the trivalent cations mentioned above, thus mandating that precautions be taken to minimize metal contamination in the radiolabeling of DOTA-based ligands such as PSMA-617 [150, 151]. Moreover, the coordination geometry and conformation taken on by DOTA when chelating an ion is partially dependent on the characteristics of that ion such as with ion size [142]. This is particularly crucial within the lens of theranostic development as these conformational differences can yield different pharmacokinetic properties *in vivo* [142].

Examining the remainder of the molecule, the PSMA binding region of PSMA-617 exists at the terminal end of the molecule and is composed of a Lys-urea-Glu sequence. This binding region coordinates with the active site of the PSMA molecule which is composed of two Zn^{2+} ions that are coordinated to histidine and glutamate/aspartate as well as a water molecule [152]. Specifically, the terminal glutamate of PSMA-617 is drawn into a glutamate recognition pocket while the urea carbonyl group coordinates with the Zn^{2+} ion, and the rest of the binding motif interacts with the remaining charged amino acids in the active site [153, 154]. Moreover, the 2-naphthyl-L-Ala and *trans*-(aminomethyl) cyclohexyl linker moieties make the overall PSMA-617 molecule more lipophilic and facilitate further binding to PSMA's highly lipophilic arginine patch which sits just beyond the active site [153, 154]. As described, this deliberate design of the binding moiety and linker amounts to a highly coordinated series of enzyme-substrate bonds ultimately ensuring the specificity and sustained coordination of the PSMA-617 ligand to PSMA.

CHAPTER 3

NUCLEAR PRODUCTION OF RADIOSCANDIUMS

3.1 Introduction

The development of nuclear production methods is a critical facet of radiopharmaceutical development. Beyond the need for the radioactive material itself, the downstream implementation of radiopharmaceuticals in both the preclinical and clinical spaces necessitates production methods which are translatable to multiple facilities and, ideally, maintains accessibility through cost-efficiency [155, 156]. In essence, if a radioisotope is exceedingly difficult to obtain, its clinical impact will be diminished regardless of the prospective clinical benefits associated with it.

One must also consider the potential impurities generated in the bombardment of the selected target, as well as the decay products which are generated after the radionuclide has been produced. For radionuclides with substantial half-lives which are produced outside the primary reaction, this can create significant concerns in downstream dosimetry and the potential for long-term contamination of the chemical workspace [155]. While the production of undesired radionuclides can be partially mitigated by using highly enriched targetry, it is virtually impossible to develop targets with perfect isotopic enrichment and higher enrichment percentages also result in compounding costs.

The combination of these two production factors, along with decay characteristics, are therefore necessary considerations when selecting isotopes for radiopharmaceutical development [155]. As such, the present work examines the calcium-based production of ^{43}Sc, ^{44}Sc, and ^{47}Sc through the ^{42}Ca(d,n)^{43}Sc, ^{44}Ca(p,n)^{44}Sc, and ^{48}Ca(p,2n)^{47}Sc reactions; contextualizes the accessibility of each production route through the previously described characteristics; and provides an experimental proof-of-concept. Additionally, the yield of the ^{42}Ca(d,n)^{43}Sc reaction is examined across 22 separate productions and compared to

theoretically derived yields.

As production accessibility is a major consideration of this dissertation, this chapter also outlines a novel methodology to utilize the beam-stop of a biomedical cyclotron as a solid target holder. Through this innovation, radioscandium production, and solid target-based production in general, should become feasible for institutions which are equipped with cyclotrons only designed for use with liquid and gas targets.

3.1.1 Scandium-43

There are a multitude of proton and deuteron beam based nuclear reactions which can be utilized to produce ^{43}Sc including: ^{43}Ca(p,n)^{43}Sc; ^{44}Ca(p,2n)^{43}Sc; ^{46}Ti(p,α)^{43}Sc; and ^{42}Ca(d,n)^{43}Sc.

Within this set of potential production pathways, the ^{43}Ca(p,n)^{43}Sc reaction exhibits a favorable cross-section of up to 300 mb from 6-13 MeV; however, as shown in Carzaniga et al., this reaction also produces a significant fraction of ^{44}Sc which is problematic if pure ^{43}Sc is desired [117, 157]. Additionally, the ^{43}Ca target material necessary for this reaction only has a natural abundance of 0.135% [157]. Therefore, cost is a significant concern relative to other ^{43}Sc production routes.

The ^{44}Ca(p,2n)^{43}Sc reaction appears to be appealing due to its utilization of more abundant (2.09%) ^{44}Ca target material [157]. However, the cross-section for this reaction peaks at only approximately 170 mb from 18-27 MeV, so limited yields and a reduced proton stopping power ultimately mitigate the advantages of the material cost relative to other production methods [68]. Additionally, as many biomedical cyclotrons are only capable of a maximum proton beam energy of 18 MeV, the broad applications of this method are somewhat limited. In this regard, while it is possible to produce ^{43}Sc at energies below the peak cross-section, the ^{44}Ca(p,n)^{44}Sc cross-section also increases dramatically below 18 MeV thus yielding an impure, ^{44}Sc dominated product.

The ^{46}Ti(p,α)^{43}Sc production route is unique in its use of a titanium-based target; however, this route only has a peak cross-section of 45 mb across an energy range of 11-21 MeV thus resulting in low yields compared to the calcium-based routes [68, 157]. That being said, this production route has been demonstrated by Cingoranelli et al. to produce relatively high purity ^{43}Sc making it a viable option if only low quantities of ^{43}Sc are needed [158].

^{43}Sc also has a production route which utilizes an incident alpha particle beam on a ^{40}Ca (96.94% abundance) target to produce ^{43}Sc through the ^{40}Ca(α,n)^{43}Sc reaction. This particular method is highly appealing as the natural abundance of ^{40}Ca means that an enriched target is not needed. However, there exists a scarce number of cyclotrons equipped with alpha particle beams suitable for clinical production scale applications, thus widespread use is unfeasible at this time [68, 157].

Ultimately, these factors have led to our selection of the ^{42}Ca(d,n)^{43}Sc production route as the optimal methodology for producing ^{43}Sc. This production route has a peak cross-section of 200 mb with viable ^{43}Sc production being possible from 2-11 MeV with a high radionuclidic purity [157, 159]. Of course, this production route still does maintain some disadvantages such as requiring relatively expensive target material due to its low natural abundance (0.647%) and requiring a cyclotron equipped with deuteron beam capabilities.

3.1.2 Scandium-44

Although we have chosen to focus on ^{43}Sc as the primary diagnostic agent discussed in this thesis due to its lower average positron energy and lack of a high energy prompt gamma-ray, it is impossible to properly characterize the radioscandiums without any discussion of ^{44}Sc as it is the most prevalent scandium radioisotope in the nuclear medicine literature. This is particularly relevant within the context of nuclear production as much of ^{44}Sc's prominence derives from the distinct advantage of being more accessible and affordable to produce.

The isotopically enriched material used in the primary production route for ^{44}Sc, the

^{44}Ca(p,n)^{44}Sc reaction, has a natural abundance of 2.086% compared to a natural abundance of 0.647% for the ^{42}Ca used in the production of ^{43}Sc [68, 157]. This yields an approximately three to four times lower material cost for the production of ^{44}Sc relative to ^{43}Sc [68, 157]. This cost reduction is further compounded by the fact that the ^{44}Ca(p,n)^{44}Sc reaction has a peak cross-section of 700 mb making it easy to produce large quantities of ^{44}Sc. Moreover, because ^{43}Sc production with the ^{42}Ca(d,n)^{43}Sc requires a cyclotron capable of producing a deuteron beam, it is outside the scope of many facilities which exclusively utilize the more common single-particle medical cyclotrons. As such, there are difficult considerations to be made regarding whether the advantages of the decay properties of ^{43}Sc outweigh the more accessible and affordable production of ^{44}Sc.

Of course, while the ^{44}Ca(p,n)^{44}Sc reaction is the primary production route for ^{44}Sc, other production routes also exist. Among these is the ^{44}Ca(d,2n)^{44}Sc reaction. This production route is practically unfavorable as it has a smaller peak cross-section than the ^{44}Ca(p,n)^{44}Sc reaction while using the same target material [157]. Moreover, this reaction is only feasible from deuteron beam energies of 11-25 MeV which is beyond the energy range of most of the already scarce deuteron capable cyclotrons [157]. That being said, if the objective is to produce a larger fraction of ^{44m}Sc this production route is preferable to the proton-based route due to the higher incident particle energy; however, for this usage case, exotic production routes with higher energy incident particles such as alpha particles are most preferable [157, 160]. There is also a ^{47}Ti(p,α)^{44}Sc reaction which has a maximum cross-section of 70 mb and a viable production range between beam energies of 12-20 MeV, but this production route has not yet been explored with enriched titanium material so it is difficult to draw conclusions regarding its viability [68, 157].

3.1.3 Scandium-47

Relative to the production of ^{43}Sc and ^{44}Sc, the direct production of ^{47}Sc is somewhat unique in that there are multiple types of accelerators which can be utilized. Namely, ^{47}Sc can be produced through neutron-based interactions from thermal emission or nuclear reactors, photonuclear reactions with linear accelerators, or proton or deuteron based cyclotron irradiation [68, 157].

Indirect production methods also exist in which ^{47}Sc is produced through the decay of the directly produced radionuclide such as with the ^{46}Ca(n,γ)^{47}Ca$\rightarrow^{47}$Sc, ^{48}Ca(γ,n)^{47}Ca$\rightarrow^{47}$Sc, and ^{48}Ca(γ,p)^{47}K$\rightarrow^{47}$Ca$\rightarrow^{47}$Sc reactions [68]. As the isolation of ^{47}Sc from the target and generator materials in these methodologies is somewhat more complex, it is difficult to compare their practicality and scalability to the direct production routes.

The primary neutron based ^{47}Sc production route is the ^{47}Ti(n,p)^{47}Sc reaction. From a cost-efficiency perspective, this reaction is highly appealing as the ^{47}Ti target material has a relatively high natural abundance (7.44%), and the reaction cross-section is fairly large at approximately 250 mb [157]. As a neutron reaction, this production method does require a nuclear reactor which can produce fast neutrons thus limiting its scalability. Relative to accelerator selection in ^{43}Sc and ^{44}Sc production, however, this is a more minimal concern as the 3.35 day half-life of ^{47}Sc enables interstate and intrastate transport from large production sites. Conversely, the co-production of ^{46}Sc in this reaction is a major concern and likely the greatest limiting factor of this reaction as a consequence of its approximately 86 day half-life [157].

With regards to photonuclear reactions, ^{48}Ti(γ,p)^{47}Sc is the singular direct production route. This route uses relatively affordable enriched ^{48}Ti (73.72% natural abundance) targetry, but the reaction has a cross-section that peaks around only 28 mb from a beam energy of 16-28 MeV [157]. Much like with the nuclear reaction, the need of high-energy photons in this production route mandates specialized linear electron accelerators which are only

accessible to a handful of sites thus limiting scalability. Within the context of this work, this is the primary production route that was utilized by Argonne National Laboratory's Low Energy Accelerator Facility (LEAF) for the production of the majority of the ^{47}Sc used in this work; however, this production was done with a natural titanium target as described in Rotsch et al. and Meier et al. [161, 162].

There are also a multitude of cyclotron based reactions which are capable of producing ^{47}Sc from titanium and calcium based starting materials. Utilizing titanium targetry, ^{47}Sc can be produced with the following reactions: ^{50}Ti(p,α)^{47}Sc, ^{48}Ti(p,2p)^{47}Sc, ^{50}Ti(d,αn)^{47}Sc, ^{49}Ti(d,α)^{47}Sc, and ^{47}Ti(d,2p)^{47}Sc [157]. Among these reactions, ^{50}Ti(p,α)^{47}Sc and ^{48}Ti(p,2p)^{47}Sc are the two that have been primarily utilized in the literature.

^{50}Ti(p,α)^{47}Sc requires an expensive target material in ^{50}Ti (5.18% natural abundance) and has a relatively small peak cross-section of approximately 25 mb that peaks around 19-20 MeV thus excluding production with many biomedical cyclotrons [157]. This method also produces a non-negligible fraction of ^{48}V mandating additional separation chemistry prior to radiolabeling [158]. For the portions of this work which utilized ^{47}Sc produced by the University of Alabama at Birmingham, this was the production method utilized.

The ^{48}Ti(p,2p)^{47}Sc reaction is appealing due to its use of highly abundant ^{48}Ti (73.72% natural abundance); however, its small peak cross-section of 30 mb at incident beam energies ranging from 30-100 MeV is highly limiting with regards to facilities which can actually utilize this route to produce an appreciable quantity of ^{47}Sc [157]. Moreover, this production route also co-produces long-lived ^{46}Sc which is a major detriment to its practical application in the production of clinically driven radiopharmaceuticals [157].

As is the focus of ^{47}Sc production in this chapter, the radionuclide can be produced utilizing calcium targetry with the ^{48}Ca(p,2n)^{47}Sc reaction. This reaction has a very large peak cross-section of 800 mb and a viable production range from 12-26 MeV making it the primary ^{47}Sc production route which is accessible to standard biomedical cyclotrons and thus

a wide range of radionuclide production facilities [157]. The major downside of this reaction is the fact that it requires enriched ^{48}Ca (0.187% natural abundance) target material [157]. Beyond its high cost, ^{48}Ca also has extremely limited commercial availability due to the existence of very few facilities which are actively separating calcium isotopes from natural calcium sources. This reaction also co-produces ^{48}Sc; however, because ^{48}Sc is also a beta-electron emitter with a comparable half-life to ^{47}Sc ($t_{1/2} = 43.71$h), this byproduct is likely of minimal detriment especially when compared to the long-lived byproducts of other ^{47}Sc production methods.

3.2 Methods

3.2.1 Development of a Solid Target Holder for a Biomedical Cyclotrons

As most biomedical cyclotrons exclusively focus on the production of short-lived, classically used β^+ emitting radioisotopes such as ^{18}F and ^{11}C for PET, biomedical cyclotrons are often only equipped with the appropriate targetry for the irradiation of liquid or gas compounds [163, 164]. Although this was previously not an issue as most clinical radioisotopes requiring solid target irradiation were long-lived and could thus be transported nationally from dedicated production facilities with larger accelerators, the expanse of radioisotopes that are being utilized clinically, and even more so investigated preclinically, has greatly expanded to include a wealth of radioisotopes that can be produced only through the use of solid targetry. Notably, there now exists a multitude of PET isotopes within the theranostic space that require the use of solid targetry with the two prominent examples being ^{68}Ga and ^{89}Zr [163, 165]. Although the production routes achievable by a standard medical cyclotron are limited for many therapeutic isotopes, most therapeutic isotopes also require solid targetry to produce. Within the context of the radioscandiums, ^{43}Sc, ^{44}Sc, and ^{47}Sc exclusively have production routes that utilize solid titanium and calcium targets thus meaning they

are not producible with a standard biomedical cyclotron without modification. This includes the IBA Cyclone 18/9 dual beam cyclotron utilized at the University of Chicago Cyclotron facility where this research was conducted.

In this regard, the accessibility of radiopharmaceutical development, and especially theranostic research, is highly limited given that the standard methodology of converting a biomedical cyclotron to accommodate solid targetry involves financially and spatially expensive modifications such as an external beam line and a pneumatic tube system for target retrieval. While these modifications are undoubtedly necessary to support the full load of clinical production, we have proposed a more simplistic solution to promote the investigation of radiopharmaceuticals which require solid targetry enabling yields and activity concentrations suitable for development up to preclinical experiments. To accomplish this, we have designed a disc-shaped target holder which tightly slots into the cooling cone of one of the two beam-stops on the IBA Cyclone 18/9 thus converting it into a solid target irradiation port. A schematic of the target holder and its location within the beam-stop is presented in Figure 3.1.

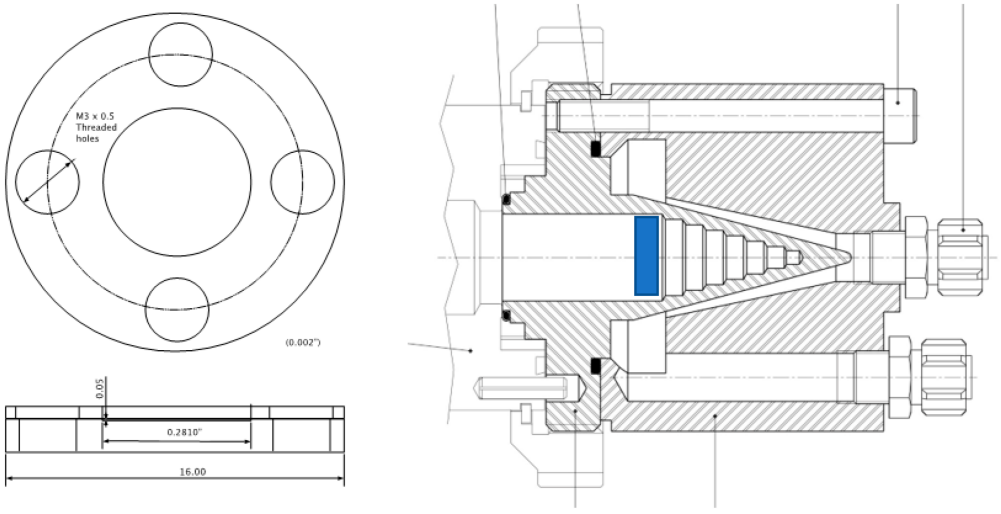

Figure 3.1: A schematic of the solid target holder conversion system along with its placement location within the cyclotron's beam-stop as is indicated by the blue rectangle. This figure was reused from Meier et al. [162].

Within this framework, the solid target holder consisted of a 5 mm thick aluminum backing disc with a diameter of 16 mm. A shallow 0.05 mm deep circular well with a diameter of 7.1 mm was machined into this backing disk to hold the solid target material. Four radially spaced threaded M3 screw holes were also machined into the backing disk. Using two titanium M3 screws, a 1.5 mm thick aluminum retaining ring with an inner diameter of 7.1 mm and an outer diameter of 16 mm was fastened to the backing disk using clear holes at identical positions to the M3 screw holes. When loading a target, pre-cored 25 μm thick graphite foils were placed on each side of the target material prior to placement into the backing disk. A photo of the fully assembled target holder loaded with CaO target material is shown in Figure 3.2.

Figure 3.2: The beam-stop conversion solid target holder loaded with CaO target material which is sandwiched between two graphite foils.

Once the holder was loaded with the target material and assembled, diffusion pump oil was applied to the assembled holder and it was loaded into the beam-stop where it rested into the first stepped section of the cooling cone. Because the target holder only makes contact with the cooling cone along its lateral surface, the diffusion pump oil was necessary to promote thermal transfer and prevent the target material from charring.

After the irradiation of the target holder, it was necessary to allow the holder to cool for approximately one hour after the end of bombardment. This delay in retrieval allowed the short-lived radionuclides generated in the target material, aluminum target holder, and titanium screws to decay out thus minimizing the dose to the staff responsible for target retrieval. While the target holder was deliberately designed such that the titanium screws were not in the beam spot, ^{46}Ti, ^{47}Ti, ^{48}Ti, ^{49}Ti, and ^{50}Ti all have the potential of generating long-lived vanadium and scandium isotopes through the reactions described in Table 3.1. As such, the target holder should be stored in a radioactive vault at all times, and handling times should be kept to a minimum even in the absence of irradiated target material.

Isotope	Abundance	Reaction	$t_{1/2}$	σ (mb)
^{46}Ti	8.25%	^{46}Ti(d,n)^{47}V	32.6 m	110.40
^{47}Ti	7.44%	^{47}Ti(p,n)^{47}V	32.6 m	47.95
		^{47}Ti(p,2p)^{46}Sc	83.808 d	4.53
		^{47}Ti(p,n+p)^{46}Ti	184.8 m	198.20
		^{47}Ti(d,n)^{48}V	15.974 d	162.25
		^{47}Ti(d,2n)^{47}V	32.6 m	166.78
^{48}Ti	73.72%	^{48}Ti(p,n)^{48}V	15.974 d	129.28
		^{48}Ti(p,2n)^{47}V	32.6 m	9.13
		^{48}Ti(d,n)^{49}V	330 d	224.41
		^{48}Ti(d,2n)^{48}V	15.974 d	138.78
^{49}Ti	5.41%	^{49}Ti(p,n)^{49}V	330 d	82.44
		^{49}Ti(p,2n)^{48}V	15.974 d	376.05
		^{49}Ti(d,2n)^{49}V	330 d	863.93
^{50}Ti	5.18%	^{49}Ti(p,2n)^{49}V	330 d	665.73

Table 3.1: Potential radioactive byproducts produced in the titanium screws of the solid target holder. For the calculation of cross-section, a beam energy of 18 Mev was utilized for proton-based reactions and 9 MeV was utilized for deuteron-based reactions. Reactions with a cross-section below one mB, produced products with half-lives less than one minute, or produced stable radionuclides were omitted for clarity [166, 167].

As this conversion system lacks an automated methodology for transferring the target, retrieval was performed manually with proper personal protective equipment to minimize contamination risk. To decrease the dose to personnel, two long M3 screws were screwed into the two unoccupied threaded holes in the target holder and utilized as distancing handles to remove the target holder from the beam-stop. Following this, the target holder must be disassembled to remove the target material which requires direct contact; however, the holder is designed to be quickly and easily disassembled to minimize dose as much as possible.

Even with these precautions, relative to a standard pneumatic tube system for solid target retrieval, this system obviously has disadvantages with regards to the radiation dose received by the personnel tasked with receiving the target; however, this dose can still be kept well within safe occupational limits with proper training and yield estimation. Utilizing the production of ^{43}Sc as an example, the dose rate was approximately 1-2 R/h at contact with the beam-stop, and the personnel retrieving the target received whole body doses ranging from 10-25 mR after the removal and disassembly of the target holder [162].

3.2.2 Scandium-43

Isotopically enriched $^{42}CaCO_3$ powder was purchased from the National Isotope Development Center (NIDC) of the Department of Energy (DOE) and ISOFLEX USA. The isotopic composition of each target along with their derivative nuclear reactions under bombardment are presented in Table 3.2. This powder was placed in a furnace at 800°C resulting in the

boiling off of carbon dioxide thus resulting in ^{42}CaO. This calcination process was performed because the higher density of CaO results in greater nuclear yields than $CaCO_3$, and the absence of carbon dioxide eliminates any concerns of the target degassing during the irradiation procedure [157].

Isotope	Abundance (NIDC)	Abundance (ISOFLEX)	Reaction	$t_{1/2}$	σ (mb)
^{40}Ca	5.01%	3.03%	^{40}Ca(d,p)^{41}Ca	9.94e+4 y	369.00
			^{40}Ca(d,2p)^{40}K	1.25e+9 y	218.44
			^{40}Ca(d,n)^{41}Sc	596.3 ms	30.64
			^{40}Ca(d,α)^{38}K	924.4 ms	54.51
			^{40}Ca(d,p+α)^{37}Ar	35.01 d	30.89
^{42}Ca	94.37%	96.30%	^{42}Ca(d,p)^{43}Ca	Stable	250.45
			^{42}Ca(d,n)^{43}Sc	**3.891 h**	**116.94**
			^{42}Ca(d,α)^{40}K	1.25e+9 y	62.51
			^{42}Ca(d,n+α)^{39}K	Stable	24.75
^{43}Ca	0.06%	0.10%	^{43}Ca(d,p)^{44}Ca	Stable	99.67
			^{43}Ca(d,n)^{44}Sc	4.042 h	135.49
			^{43}Ca(d,2n)^{43}Sc	**3.891 h**	**234.74**
			^{43}Ca(d,α)^{41}K	Stable	67.51
			^{43}Ca(d,p+α)^{40}Ar	Stable	3.73
			^{43}Ca(d,n+α)^{40}K	1.25e+9	15.14
^{44}Ca	0.55%	0.55%	^{44}Ca(d,p)^{45}Ca	162.61 d	84.61
			^{44}Ca(d,n)^{45}Sc	Stable	259.93
			^{44}Ca(d,2n)^{44}Sc	4.042 h	264.86
			^{44}Ca(d,α)^{42}K	12.359 h	24.39

^{46}Ca	0.001%	<0.01%	^{46}Ca(d,p)^{47}Ca	4.536 d	53.24
			^{46}Ca(d,n)^{47}Sc	3.349 d	190.46
			^{46}Ca(d,2n)^{46}Sc	83.808 d	903.26
			^{46}Ca(d,α)^{44}K	22.130 m	10.33
^{48}Ca	0.01%	0.02%	^{48}Ca(d,p)^{49}Ca	8.718 m	39.35
			^{48}Ca(d,n)^{49}Sc	57.200 m	95.77
			^{48}Ca(d,2n)^{48}Sc	43.710 h	1134.02
			^{48}Ca(d,α)^{46}K	96.310 s	2.21

Table 3.2: The isotopic composition and nuclear reactions of the enriched ^{42}Ca target material from both NIDC and ISOFLEX. Cross-sections of the described nuclear reactions are provided at a beam energy of 9 MeV. Cross-sections below 1 mB were omitted to improve table readability [166, 167].

Once converted into the oxide form, the ^{42}CaO target material was loaded into a manual pellet press and formed into a cylindrical target with a 7 mm diameter and a mass-dependent thickness. Target mass ranged from 4.6 mg to 22.4 mg (3.3-16.2 mg ^{42}Ca), but most targets were approximately 15 mg (10.86 ^{42}Ca). This translated to a range of target thicknesses which spanned from 0.045-0.174 mm with an average thickness of 0.117 mm. A representative ^{42}CaO target is shown in Figure 3.3.

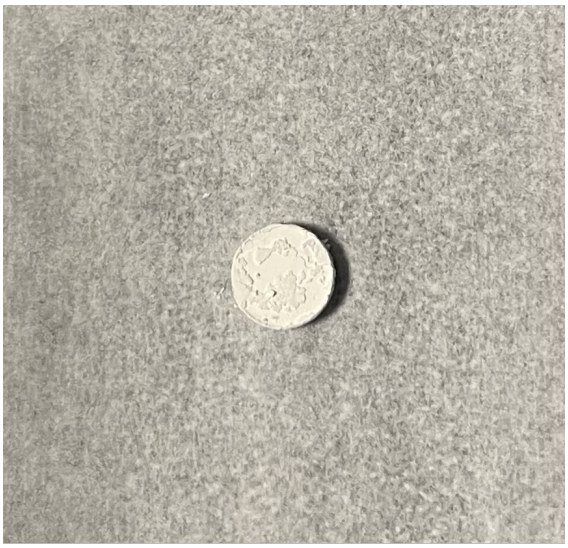

Figure 3.3: A standard ^{42}CaO target utilized in the production of ^{43}Sc throughout this work.

For each ^{43}Sc production, a ^{42}CaO target was loaded into the beam-stop of a standard compact biomedical cyclotron utilizing the novel solid target holder as was described in the previous section. Targets were irradiated for 7-10 h with a 9 MeV deuteron beam at beam currents ranging from 1-10 particle μA on target. Most irradiations were performed at beam currents of 8-10 μA to maximize yield. One hour after the end of each bombardment, the target was retrieved and the identity of ^{43}Sc was confirmed by identifying the characteristic 372.9 keV γ-ray with NaI spectroscopy. In order to better characterize the decay spectra of the radiated target, a cadmium zinc telluride (CZT) spectrum was obtained with a RayMon 10 handheld CZT detector for one select ^{43}Sc production. This CZT spectra is presented in Figure 3.4.

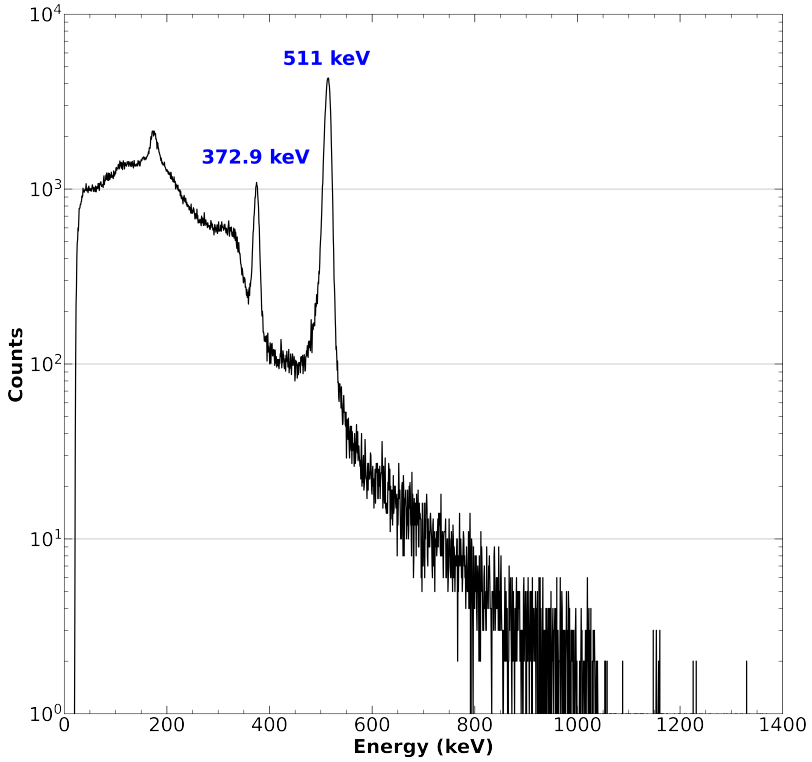

Figure 3.4: CZT spectrum of ^{43}Sc produced with the ^{42}Ca(d,n)^{43}Sc reaction.

In order to estimate ^{43}Sc yield, it was also necessary to employ an empirical equation which accounts for how beam energy, energy deposition, and reaction cross-section vary as the beam passes through a target of a given thickness. This was accomplished by using Equation 3.1 as described by Aikawa et al. to estimate the thick target yield of the ^{42}Ca(d,n)^{43}Sc reaction [168].

$$Yield = \frac{N_A I}{A_T}(1 - e^{-\lambda t}) \int_{E_e}^{E_0} \sigma(E) \frac{dE}{S(E)} \tag{3.1}$$

Within this equation, N_A is Avogadro's number, I is the incident particle flux, A_T is the atomic mass of the target atom, λ is the decay constant of the desired radionuclide, t is the beam time, E is the beam energy, E_o is the initial beam energy at the target's surface, E_e is the beam energy after being transmitted through the target, $\sigma(E)$ is the energy dependent cross-section, and $S(E)$ is the energy dependent mass stopping power.

Equation 3.1 was solved numerically utilizing simulated cross-sections generated in TENDL

and mass stopping powers generated from the ATIMA particle simulation program [167]. The utilization of these simulated quantities was necessary as there is currently an absence of cross-section data in the relevant energy range for the ^{42}Ca(d,n)^{43}Sc reaction as well as an absence of experimental stopping power data for deuterons in calcium or calcium oxide [162].

3.2.3 Scandium-44

^{44}Sc can be produced via the ^{44}Ca(p,n)^{44}Sc reaction utilizing an isotopically enriched ^{44}CaO target. Relative to the production of ^{43}Sc utilizing the ^{42}Ca(d,n)^{43}Sc reaction, the production and downstream chemical processing of ^{44}Sc from an isotopically enriched calcium target required only minor differences in the production protocol, notably the use of a proton beam in the nuclear reaction. Consequently, the same procedures described in Section 3.2.2 were utilized to prepare an isotopically enriched 15.8 mg ^{44}CaO (11.6 mg ^{44}Ca) target utilizing $^{44}CaCO_3$ material purchased from ISOFLEX USA. The composition of this target and all the relevant nuclear reactions at a proton beam energy of 14 MeV are described in Table 3.3. The same solid target holder conversion system described in the Section 3.2.1 was utilized for this proof-of-concept production of ^{44}Sc.

Isotope	Abundance	Reaction	$t_{1/2}$	σ (mb)
^{40}Ca	0.92%	^{40}Ca(p,2p)^{39}K	Stable	279.01
		^{40}Ca(p,α)^{37}K	1.24 s	22.05
		^{40}Ca(p,p+α)^{36}Ar	Stable	1.87
^{42}Ca	0.02%	^{42}Ca(p,n)^{42}Sc	680.79 ms	125.55
		^{42}Ca(p,n+p)^{41}Ca	9.94e4 y	58.98
		^{42}Ca(p,d)^{41}Ca	9.94e4 y	2.90
		^{42}Ca(p,2p)^{41}K	Stable	2.36
		^{42}Ca(p,α)^{39}K	Stable	76.43

		^{42}Ca(p,p+α)^{38}Ar	Stable	55.73
^{43}Ca	0.01%	^{43}Ca(p,n)^{43}Sc	3.891 h	130.15
		^{43}Ca(p,n+p)^{42}Ca	Stable	388.26
		^{43}Ca(p,d)^{42}Ca	Stable	13.05
		^{43}Ca(p,α)^{40}K	1.25e9 y	67.94
		^{43}Ca(p,n+α)^{39}K	Stable	13.11
^{44}Ca	99.04%	**^{44}Ca(p,n)^{44g}Sc**	**4.042 h**	**388.89**
		^{44}Ca(p,n)^{44m}Sc	58.6 h	66
		^{44}Ca(p,n+p)^{43}Ca	Stable	125.17
		^{44}Ca(p,d)^{43}Ca	Stable	4.19
		^{44}Ca(p,α)^{41}K	Stable	34.30
^{46}Ca	<0.01%	^{46}Ca(p,n)^{46}Sc	83.808 d	355.17
		^{46}Ca(p,2n)^{45}Sc	Stable	482.50
		^{46}Ca(p,n+p)^{45}Ca	162.61 d	14.96
		^{46}Ca(p,d)^{45}Ca	162.61 d	3.56
		^{46}Ca(p,α)^{43}K	22.28 h	16.85
^{48}Ca	0.01%	^{48}Ca(p,n)^{48}Sc	43.71 h	220.63
		^{48}Ca(p,2n)^{47}Sc	3.349 d	729.23
		^{48}Ca(p,n+p)^{47}Ca	4.536 d	8.30
		^{48}Ca(p,d)^{47}Ca	4.536 d	4.38
		^{48}Ca(p,α)^{45}K	17.81 m	1.30

Table 3.3: The isotopic composition and nuclear reactions of the enriched ^{44}Ca target material from ISOFLEX. Cross-sections of the described nuclear reactions are provided at a beam energy of 14 MeV. Cross-sections below 1 mB were omitted to improve table readability [166, 167, 169, 170].

The target was irradiated with a 14 MeV proton beam with 10 μA particle current on target for one hour. As most biomedical cyclotrons have a standard proton beam energy of 18 MeV (including the cyclotron utilized in this study), the degradation of the beam energy through the use of carbon foils was critical to maximize the cross-section of the ^{44}Ca(p,n)^{44}Sc reaction which has a large peak between approximately 5-15 MeV [166, 167, 169]. One hour after the end of bombardment, the target was retrieved and the identity of ^{44}Sc was confirmed by identifying the characteristic 1157.0 keV γ-ray with NaI spectroscopy.

3.2.4 Scandium-47

The overwhelming majority of the ^{47}Sc material utilized for the experiments described in this thesis came from production at Argonne National Laboratory's Low Energy Accelerator Facility (LEAF) and the University of Alabama Birmingham's Cyclotron Facility utilizing the ^{Nat}Ti(γ,p)^{47}Sc (driven by ^{48}Ti(γ,p)^{47}Sc) and ^{50}Ti(p, α)^{47}Sc reactions respectively which are described in Rotsch et al and Cingoranelli et al [158, 161]. However, a proof-of-concept production of ^{47}Sc utilizing the ^{48}Ca(p,2n)^{47}Sc reaction was also performed utilizing the same target holder described in Section 3.2.1 at the University of Chicago Cyclotron Facility.

As the natural abundance and commercial availability of ^{48}Ca is minuscule, the target synthesis procedure outlined for ^{43}Sc and ^{44}Sc production in Sections 3.2.2 and 3.2.3. had to be modified slightly to accommodate a significantly lower amount of starting material. Notably, additional exfoliated graphite filler material had to be mixed into the calcium target material prior to pellet formation to ensure the structural integrity of the ^{48}Ca target. Unlike with ^{43}Sc and ^{44}Sc production, the starting isotopically enriched $^{48}CaCO_3$ material did not undergo calcination as it was deemed that the material losses from transferring the target in and out of a ceramic boat for heating would outweigh the potential of slightly increased yields from the boiling off of carbon dioxide. A representative target composed of thoroughly mixed $CaCO_3$ and exfoliated graphite is presented in Figure 3.5.

Figure 3.5: $^{48}CaCO_3$ and graphite target for the production of ^{47}Sc.

Under this context, 97.10% isotopically enriched $^{48}CaCO_3$ produced by Trace Sciences International (provided by Argonne National Laboratory) was utilized to synthesize a homogenized target consisting of 6.09 mg of $^{48}CaCO_3$ (2.63 mg ^{48}Ca mass) and 7.91 mg of exfoliated graphite. The isotopic breakdown of the enriched calcium material along with all associated nuclear reactions under proton irradiation at 18 MeV are described in Table 3.4. As the final target was composed of a large amount of exfoliated graphite, it is likely that incident beam underwent significant degradation as it passed through the target. Consequently, the nuclear reactions described in Table 3.4 may not be fully representative of the full spectrum of nucleic products that were produced in this irradiation.

Isotope	Abundance	Reaction	$t_{1/2}$	σ (mb)
^{40}Ca	2.72%	$^{40}Ca(p,n)^{40}Sc$	182.4 ms	2.33
		$^{40}Ca(p,d)^{39}Ca$	860.3 ms	1.64
		$^{40}Ca(p,2p)^{39}K$	Stable	645.21
		$^{40}Ca(p,\alpha)^{37}K$	1.24 s	8.83

		^{40}Ca(p,p+α)^{36}Ar	Stable	61.91
^{42}Ca	0.02%	^{42}Ca(p,n)^{42}Sc	680.79 ms	35.91
		^{42}Ca(p,n+p)^{41}Ca	9.94e4 y	428.40
		^{42}Ca(p,d)^{41}Ca	9.94e4 y	25.80
		^{42}Ca(p,2p)^{41}K	Stable	46.16
		^{42}Ca(p,α)^{39}K	Stable	26.86
		^{42}Ca(p,p+α)^{38}Ar	Stable	130.56
		^{42}Ca(p,2α)^{35}Cl	Stable	1.05
^{43}Ca	0.01%	^{43}Ca(p,n)^{43}Sc	3.891 h	37.25
		^{43}Ca(p,2n)^{42}Sc	680.79 ms	6.17
		^{43}Ca(p,n+p)^{42}Ca	Stable	673.85
		^{43}Ca(p,d)^{42}Ca	Stable	25.76
		^{43}Ca(p,2p)^{42}K	12.539 h	5.55
		^{43}Ca(p,α)^{40}K	1.25e9 y	28.22
		^{43}Ca(p,n+α)^{39}K	Stable	39.33*
		^{43}Ca(p,p+α)^{39}Ar	268.0 y	7.19
^{44}Ca	0.15%	^{44}Ca(p,n)^{44}Sc	4.042 h	125.59
		^{44}Ca(p,2n)^{43}Sc	3.891 h	96.46
		^{44}Ca(p,n+p)^{43}Ca	Stable	371.80
		^{44}Ca(p,d)^{43}Ca	Stable	20.30
		^{44}Ca(p,α)^{41}K	Stable	19.90
		^{44}Ca(p,n+α)^{40}K	1.25e9 y	5.44
		^{44}Ca(p,p+α)^{40}Ar	Stable	2.28
^{46}Ca	<0.01%	^{46}Ca(p,n)^{46}Sc	83.808 d	102.94
		^{46}Ca(p,2n)^{45}Sc	Stable	649.11
		^{46}Ca(p,n+p)^{45}Ca	162.61 d	134.08

		^{46}Ca(p,d)^{45}Ca	162.61 d	16.97
		^{46}Ca(p,2p)^{45}K	17.79 m	7.58*
		^{46}Ca(p,α)^{43}K	22.28 h	23.88
		^{46}Ca(p,n+α)^{42}K	12.359 h	5.02
^{48}Ca	97.10%	^{48}Ca(p,n)^{48}Sc	43.71 h	118.66
		^{48}Ca(p,2n)^{47}Sc	**3.349 d**	**785.97**
		^{48}Ca(p,n+p)^{47}Ca	4.536 d	73.60*
		^{48}Ca(p,d)^{47}Ca	4.536 d	19.44
		^{48}Ca(p,α)^{45}K	17.81 m	3.73

Table 3.4: The isotopic composition and nuclear reactions of the enriched ^{48}Ca target material from Trace Sciences International. Cross-sections of the described nuclear reactions are provided at a beam energy of 18 MeV. Cross-sections below 1 mB were omitted to improve table readability. An asterisk (*) Indicates a linear interpolation of TENDL data [166, 167].

The $^{48}CaCO_3$ target was irradiated for 12 hours at a proton beam energy of 18 MeV and a beam current of 10 μA. One hour after the end of bombardment, the target was retrieved and the identity of ^{47}Sc was confirmed by identifying the characteristic 159.4 keV γ-ray with NaI spectroscopy.

3.3 Results

3.3.1 Scandium-43

^{43}Sc was successfully produced from ^{42}CaO targetry across over 30 different irradiations with EOB yields ranging from 144.67-1513.20 MBq depending on target mass, beam current, and irradiation time. The target normalized yields of these irradiations are presented as a

function of μA hours of beam on target in Figure 3.6.

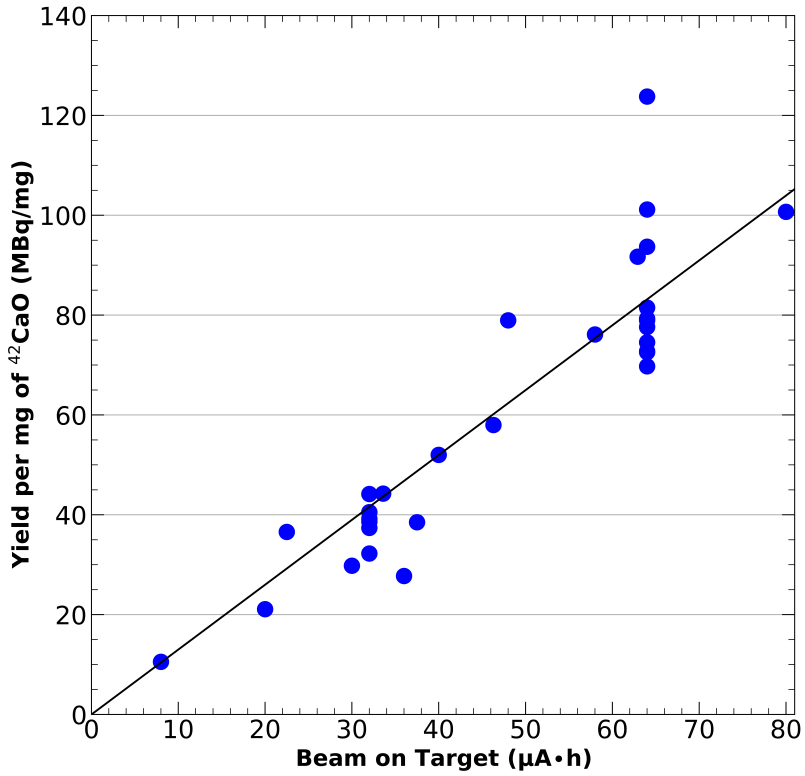

Figure 3.6: Yield of ^{43}Sc produced with the ^{42}Ca(d,n)^{43}Sc reaction.

As expected, the relationship between target normalized yield and beam on target is approximately linear and can be fit with a linear regression as shown in Equation 3.2 where the yield of ^{43}Sc per mg of ^{42}Ca is proportional to the beam current and irradiation time. In order to emulate experimental boundary conditions, this regression was forced through the origin resulting in a net correlation coefficient of $r = 0.914$.

$$Yield\ (MBq/mg) = 1.299 \cdot I\ (\mu A) \cdot t\ (h) \tag{3.2}$$

This regression can be utilized for making crude predictions of the end of bombardment yield based on target mass, beam current, and irradiation time; however, due to its simplistic nature, it does not account for variations in the experimental setup. Most notably, this

methodology fails to factor in how changes in target thickness (which linearly increases with target mass as the target diameter is fixed) can alter beam degradation throughout the target thus yielding derivative changes in cross-section and stopping power. This resulted in large variations in ^{43}Sc yield per mg of ^{42}Ca with identical beam parameters and irradiation times.

Utilizing the more sophisticated yield estimation method presented in Equation 3.1 which accounts for those variations in beam energy, yield estimates were found to overestimate experimental yield by an average of 20.7% across 22 irradiations. Experimental and theoretical yield is presented for each ^{42}Ca(d,n)^{43}Sc production in Figure 3.8. Although in a different energy range, these results are congruent with the results presented in Carzaniga et al. by which the TENDL simulated cross-section for the ^{42}Ca(d,n)^{43}Sc reaction was found to overestimate the experimentally derived cross-section from the entire measured beam energy range of 2.8-7.1 MeV [159].

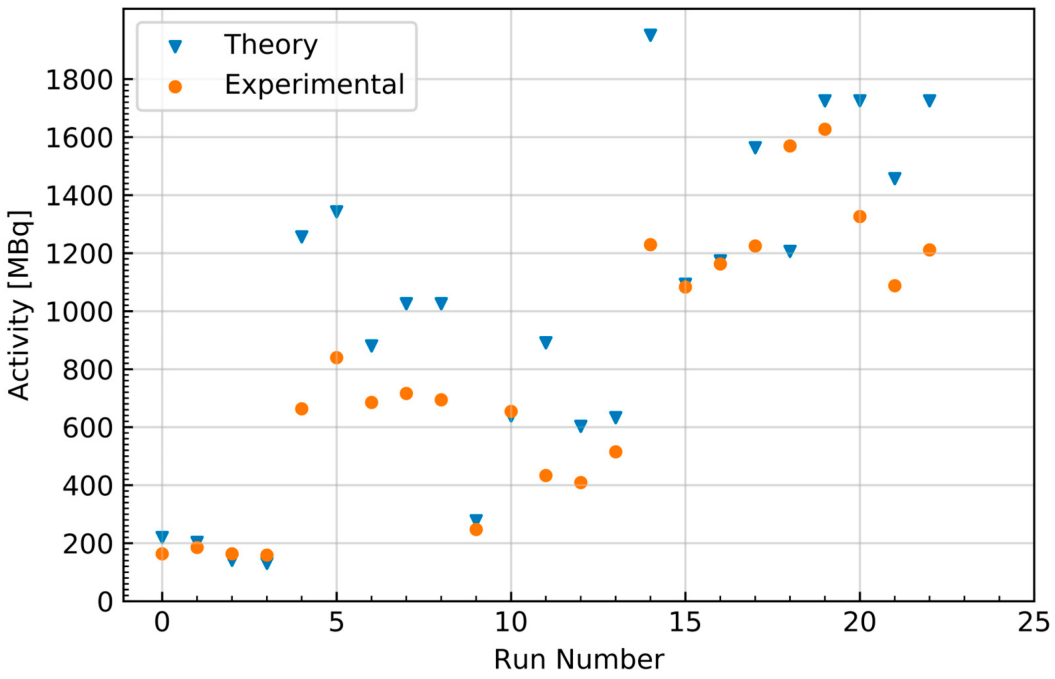

Figure 3.7: Experimental and theoretically derived yield of ^{43}Sc produced with the ^{42}Ca(d,n)^{43}Sc reaction. This figure was taken from Meier et al. [162].

The observed differences between experimental and theoretical yields were also analyzed as a function of target mass as is illustrated in Figure 3.8 where it is demonstrated that theoretical yield inaccuracy increases with more massive targets. Not dissimilar to the simple model of yield estimation, this mass-dependent discrepancy likely originates from an incomplete characterization of mass stopping power for deuterons in calcium and the cross-section of the overall ^{42}Ca(d,n)^{43}Sc reaction. Moreover, because the stopping power is crucial in how the degradation of the beam is modeled as it passes through the target, and cross-section is energy dependent, the inaccuracy of these simulated parameters likely compounds resulting in inaccurate estimates of yield.

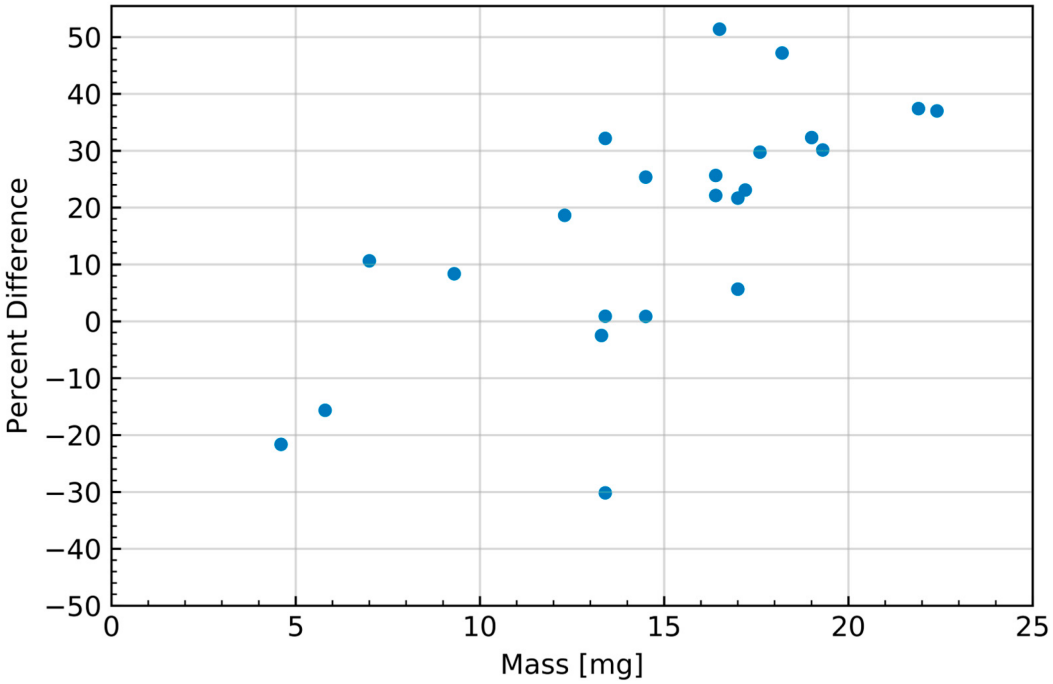

Figure 3.8: Percent difference of experimental and theoretical yield of ^{43}Sc produced with the ^{42}Ca(d,n)^{43}Sc reaction as a function of target mass. This figure was taken from Meier et al. [162].

Beyond the possible uncertainty introduced through the use of entirely simulated quantities, there were also a multitude of other unevaluated uncertainties that may have contributed to the discrepancy of theoretical and experimental yields. Notably, the loss of target material

and activity during the loading and unloading of the target into the makeshift target holder, well-counter inaccuracy, and scale inaccuracy could all have been contributing factors. Unfortunately, it was not possible to evaluate each of these potential sources of uncertainty individually as a result of the current workflow requirements of the daily operation of the University of Chicago Cyclotron Facility.

3.3.2 Scandium-44

Despite the short irradiation time, the proton irradiation of the ^{44}CaO target resulted in an EOB yield of 754.1 MBq. Although quantification was not possible due to the lack of a high-resolution spectrometer (e.g. an HPGE detector), the presence of long-lived ^{44m}Sc ($t_{1/2}$=58.6 h) was also confirmed in the irradiated target. Ultimately, this suggests that further beam degradation may be necessary if the synthesis of pure ^{44g}Sc is desired. Ideally, one could degrade the beam even further to <12 MeV to minimize the cross-section of ^{44m}Sc which peaks at 13 MeV [131, 166, 169, 170].

This target was able to successfully undergo the chemical separation and radiolabeling procedures described in Chapter 4, ultimately being synthesized into purified ^{44}Sc-PSMA-617 with a molar activity of 28.8 MBq/nmol of PSMA-617. This level of activity and radiochemical purity were more than sufficient to support a downstream murine injection, the biodistribution results of which are presented in Chapter 5.

3.3.3 Scandium-47

The proton irradiation of the homogenized $^{48}CaCO_3$ and exfoliated graphite target resulted in an EOB yield of 1498.5 MBq. The addition of the exfoliated graphite within the target did not affect any downstream chemical processing or recovery efforts, and the resulting activity was able to be radiolabeled at an efficiency of 7.4 MBq/nmol. This activity was utilized to synthesize a therapeutic dose of ^{47}Sc-PSMA-617 which was administered to two mice as is

described in Chapter 5. While this is a substantial yield for such a small target, the produced activity levels may be insufficient to support a true characterization of ^{47}Sc therapeutic effect in the absence of a more massive ^{48}Ca target because therapeutic effect is intimately connected to high molar activity and reaction activity. This relationship between starting activity and molar activity is further explored in Chapter 4. As this was the greatest yield of any radioscandium produced in this work and was primarily limited by the distribution of activity between aliquots during separation, the improvement of molar activity through the continued refinement of chemical separation may also be a promising avenue towards synthesizing therapeutically useful doses.

3.4 Recovery of Enriched Calcium Materials

The recycling of enriched calcium targets following the chemical separation from produced radioscandium material is a quintessential aspect of the production procedure which partially mitigates the material cost of radioscandium applications. This process is particularly crucial in ensuring the economic feasibility of calcium based productions of ^{43}Sc and ^{47}Sc given the high cost and natural scarcity of ^{42}Ca and ^{48}Ca, especially under the future aspiration of more widespread application in the clinical space.

As such, the recovery of calcium based targetry can be performed through the slight modification of a procedure described in US Patent Application 20170087260 [171]. Under this methodology, the branched ethylhexyldiglycolamide (DGA) column used in the separation of radioscandium from the calcium target materials is washed with 10 mL of 3 M HCl with the washings being collected in a large beaker and combined with the DGA pass through and washings from the separation procedure described in Section 4.2.1. Any conical tubes or beakers utilized in the separation procedure are also washed with 3 M HCl with the washings being added to the aforementioned beaker. This collection of washings is then placed on a hotplate set to 150 °C and evaporated to complete dryness under gentle stir-

ring. The evaporated solution is then redissolved in 5 mL of 3 M HCl and re-evaporated to complete dryness. After this, the evaporated solution is again redissolved with 20 mL of water, and the pH is adjusted with 2.5% ammonium hydroxide and 1 M HCl until a pH of 4-4.5 is obtained. Once the desired pH is reached, 20 mL of 0.3 M ammonium oxalate is added resulting in a opaque, cloudy white liquid. Once all particulates have settled to the bottom of the beaker, the solution is filtered through two 8 μm pore size ashless filter papers using a Buchner funnel under vacuum. The solution is then re-ran through this filtration process until the resulting filtrate is completely clear and colorless. Finally, the filter papers are placed in a ceramic boat or crucible and calcinated in a furnace at 800 °C for one hour. After removal from the furnace, the ceramic boat or crucible should contain the recovered enriched CaO material.

The recovery rate we have observed for this recovery procedure has been highly variable with results ranging from 65%-90% recovery of the starting CaO material. While it is difficult to pinpoint an exact explanation for the variability of recovery rate or what factors result in sub-optimal recovery rates, potential explanations could include the loss of material during container transfers throughout the separation and recovery processes, as well as the inability to characterize the material loss which occurs during target loading, extraction, and irradiation as a result of our utilization of the makeshift target holder described in Section 3.2.1. As such, to minimize material loss, it is recommended to recover multiple batches of irradiated calcium targets simultaneously to minimize the number of material transfers. In this regard, there is also an intrinsic tradeoff between maximizing recovery yield and obtaining ideal quantification and characterization of the yields obtained in this recovery process to which we have always prioritized maximizing yield. It is for this reason that we state a range of experimentally determined recovery yields here as opposed to explicit rates.

3.5 Discussion

The methodology and novel beam-stop conversion system that was developed as a solid target holder throughout this chapter can be more broadly applied to any biomedical cyclotron which has a removable beam-stop. To that end, the production of ^{44}Sc and ^{47}Sc through the ^{44}Ca(p,n)^{44}Sc and ^{48}Ca(p,2n)^{47}Sc reactions should be accessible to any biomedical cyclotron through the use of this system. While slightly less accessible, the production of ^{43}Sc through the ^{42}Ca(d,n)^{43}Sc reaction can also be replicated with any biomedical cyclotron which is equipped with a deuteron beam. As will be expanded upon in Chapters 4 and 5, the level of radioscandium activity produced with this methodology was sufficient to support downstream radiolabeling and pre-clinical evaluation in all cases except for therapeutic evaluation with ^{47}Sc. In accordance with Aim 1, this provides a pathway for the expansion of radioscandium development across other institutions while mitigating the high-barriers of cost and development time typically associated with the investigation of solid target derived radionuclides.

Of course, as radioscandium development progresses to the clinical stage, the need for dedicated solid targetry systems will still be necessary. At that stage of radiopharmaceutical development, the levels of radioactivity necessary to consistently output diagnostic and therapeutic doses will simply exceed that which is achievable without better target cooling, and, more importantly, a remote method of target retrieval that minimizes personnel dose. However, minimizing the financial investment for the initial stages of development is still immensely valuable.

Examining each reaction individually, the production of ^{43}Sc through the ^{42}Ca(d,n)^{43}Sc reaction resulted in yields of up to 1513.20 MBq with an 8-hour irradiation time at a deuteron beam energy of 9 MeV and beam current of 8 μA with yield varying with target mass. From a standpoint of activity level, this amount of ^{43}Sc should be sufficient for even clinical usage as it exceeds the activity prescribing guidelines for LOCAMETZ PET diagnostics (111-259

MBq), ^{43}Sc-PSMA-617's clinically utilized analogue [172]. The proof-of-concept production of ^{44}Sc through the ^{44}Ca(p,n)^{43}Sc reaction yielded 754.06 MBq which was also sufficient activity for a hypothetical clinical dose despite the irradiation requiring only a single hour of beam on target time at a beam energy of 14 MeV and a beam current of 10 μA.

Although it is still our opinion that ^{43}Sc is a superior diagnostic isotope than ^{44}Sc due to its lower positron kinetic energy and lack of a high energy gamma emission, the availability and cost of enriched isotopic materials, along with the feasibility of target recovery, will likely dictate which isotope is more extensively utilized in the preclinical and clinical spaces. Given the current state of the field, ^{44}Sc will likely remain the isotope of choice in radioscandium diagnostics due to its production necessitating a more accessible proton-based nuclear reaction, greater production rate, and the more abundant ^{44}Ca material. However, in the absence of ^{47}Sc therapeutics, it would seem the clinical application of ^{44}Sc may be limited seeing as ^{18}F labeled PSMA targeting agents are already preferred over ^{68}Ga-PSMA-11 due to the similar drawbacks of ^{68}Ga such as poor resolution due to a high positron energy.

The production of ^{47}Sc with the ^{48}Ca(p,2n)^{47}Sc reaction only resulted in 1498.5 MBq of activity after a 12 hour irradiation at a beam energy of 18 MeV and a of beam current of 10 μA which is well below that necessary to render a clinical dose when compared to the single dosing instructions for PLUVICTO radionuclide therapy (7400 MBq), the clinically utilized ^{177}Lu labeled analogue of ^{47}Sc-PSMA-617 [173]. Similarly, as discussed in Chapter 4, the starting activity produced in this experiment was too low to support radiolabeling at a therapeutically meaningful efficiency. However, this was likely a consequence of the low target mass as opposed to a poor reaction pathway as the ^{48}Ca(p,2n)^{47}Sc cross-section is approximately 6.7x greater than that utilized in ^{43}Sc production and 2.0x greater than that of ^{44}Sc production. As such, with an improved supply of ^{48}Ca target material, yields should be even larger than observed for the other radioscandiums.

To that end, it will be necessary to bolster the supply of isotopically enriched calcium to

make ^{47}Sc production, and thus radioscandium theranostics, a viable venture as ^{48}Ca is in limited enough supply that it is not commercially available in the United States and can only be purchased from the Department of Energy through a case-by-case application process. The development of the infrastructure necessary to produce a greater supply of isotopically enriched calcium would also ease practical concerns regarding the recommendation of ^{43}Sc over ^{44}Sc for diagnostic purposes as ^{42}Ca supplies would also increase. This issue can also be resolved through the continued development of calcium recovery techniques which could reduce material costs by as much as 95% as is seen with target recovery techniques for other radionuclide productions. While this would still entail high initial investment costs, through the repeated use of singular batches of target materials, beginning radioscandium research or even clinical production would become accessible to a wide span of institutions.

A thick target yield estimation method was also applied to ^{43}Sc production with the ^{42}Ca(d,n)^{43}Sc reaction resulting in an overestimate of experimental yields by an average of 20.7%. As the percent difference between theoretical and experimental yields was shown to increase with target mass, and thus target thickness, it is suspected that the underlying source of this discrepancy is likely rooted in the use of simulated stopping powers due to the absence of experimental data characterizing the interactions of deuterons in calcium or calcium oxide. As stopping power describes the energy degradation of the incident beam as it passes through a target, any mischaracterization of the stopping power would result in an evaluation of reaction cross-section at incorrect energies when utilizing Equation 3.1.

It is also a strong possibility that the simulation derived cross-sections utilized for yield estimation are also not fully accurate as experimental characterizations of the ^{42}Ca(d,n)^{43}Sc reaction have been shown to deviate from those obtained in TENDL. However, it is impossible to state this with absolute certainty as no experimental characterization has been performed at the deuteron beam energy used in this work. As such, these results would suggest that greater emphasis should be placed on the development of experimental cross-section for the

^{42}Ca(d,n)^{43}Sc reaction and, by extension, the ^{44}Ca(p,n)^{44}Sc and ^{48}Ca(p,2n)^{47}Sc reactions. A proposed methodology to achieve this characterization is discussed in Chapter 7.

3.6 Conclusion

This chapter described the development of a novel target holder which enabled the utilization of the beam-stop of a standard biomedical cyclotron for solid target irradiation. This solid target holder was successfully utilized to produce ^{43}Sc, ^{44}Sc, and ^{47}Sc from isotopically enriched calcium oxide and calcium carbonate targetry. Ultimately, the demonstrated viability of this beam-stop conversion system for radioscandium production stands to improve the accessibility of radioscandium pharmaceutical development. This is particularly evident when the successful production of these radioscandiums are considered alongside the successful radiolabeling and downstream pre-clinical evaluation of radioscandium PSMA-617 as is described in Chapters 4 and 5.

Utilizing this system, the production of ^{43}Sc via the ^{42}Ca(d,n)^{43}Sc reaction was shown to produce sufficient activity to sustain several pre-clinical experiments with an 8 h irradiation time. Similar results were obtained with the ^{44}Ca(p,n)^{44}Sc production route while only necessitating a 1 h irradiation time, adding to the practical advantages of ^{44}Sc over its sister isotope. In this regard, it is clear that ^{44}Sc production is more accessible than ^{43}Sc production with regards to material cost, irradiation time, and production route. However, ^{43}Sc is still a superior isotope with regards to its relatively contaminant free production route, superior imaging resolution, and lack of a high energy gamma ray. As such, future developments in enriched calcium supply and calcium target recycling will likely dictate which isotope is more viable in the clinical space. ^{47}Sc production using the ^{48}Ca(p,2n)^{47}Sc reaction was shown to produce sufficient activity to generate two therapeutic murine doses of ^{47}Sc-PSMA-617 with a 12 h irradiation time. However, this production was limited by the relatively small amount of ^{48}Ca available to our facility, and the achieved radiolabeling efficiency was below

therapeutically useful levels in the absence of more starting activity. Consequently, the future viability of ^{47}Sc in the pre-clinical and clinical spaces is likely contingent on the further refinement of calcium recycling methodology as well as the introduction of a larger supply of ^{48}Ca to the commercial market.

A methodology for estimating the yield of ^{43}Sc production was also proposed resulting in theoretical yield estimates which were greater than corresponding experimental yields on average. While still useful for selecting production parameters based upon the needed yield for downstream experiments, this result demonstrates the need for the experimental quantification of the ^{43}Sc cross-section and deuteron stopping power in calcium. While outside the scope of this work due to the limited number of ^{44}Sc and ^{47}Sc productions, this methodology should also be applicable to the ^{44}Ca(p,n)^{44}Sc and ^{48}Ca(p,2n)^{47}Sc reactions. Within this context, yield estimation is likely to produce more accurate results due to the more thorough experimental characterization of proton interactions within the literature; however, the experimental characterization of these cross-sections is still underdeveloped.

CHAPTER 4

CHEMICAL SYNTHESIS OF RADIOSCANDIUM PSMA-617 FROM IRRADIATED TARGET MATERIALS

4.1 Introduction

Although the separation of scandium from CaO and $CaCO_3$ targetry and the radiochemical synthesis of PSMA-617 based radiopharmaceuticals have each been vaguely described in the literature, the modular modification and refinement of these two chemical procedures has been necessary to facilitate the unique factors attributed to our choice of radionuclide, experimental setup, and downstream applications. Specifically, throughout the approximately 35 productions of radioscandium PSMA-617 that have been performed over the course of this work, there has been a continual need for the refinement and documentation of the chemical procedures utilized to separate radioscandium from its CaO starting material, radiolabel radioscandium with PSMA-617, and both purify and reconstitute the final radioscandium PSMA-617 product such that it is suitable for *in vitro* and *in vivo* utilization.

The motivation for the radiochemical aspects of this work is therefore multifaceted. With regards to documentation and ensuring the reproducibility of radioscandium PSMA-617 synthesis, we aimed to produce a detailed, step-by-step protocol for the complete synthesis of radioscandium PSMA-617 from calcium targetry. Ultimately this proposed protocol was drafted and published in *Methods and Protocols* with the inclusion of procedural information for the production of ^{43}Sc and the recovery of calcium target materials as described in the previous chapter.

Conversely, the refinement of these procedures has been primarily motivated by the notion that the molar activity—the ratio of radioactivity to the moles of ligand in the final radiopharmaceutical product—is critical to radiopharmaceutical specificity and thus its viable *in vitro* and *in vivo* applications. Essentially, when a mixture of labeled and unlabeled ligand

is administered *in vitro* or *in vivo*, the unlabeled ligand binds to the target molecule thus reducing the number of active sites available for binding by the labeled radiopharmaceutical thus acting as a classical competitive inhibitor [174].

Consistently maintaining high molar activity may also yield additional challenges in true theranostics as the molar activity greatly alters pharmacokinetics and thus could have significant impact in ensuring accurate dose correlation between diagnostic and therapeutic radiopharmaceuticals. While therapeutic radioisotopes require greater molar activity for treatment efficacy, diagnostic radioisotopes may actually pose a greater challenge in this regard. This is because, given samples of the same activity of a diagnostic and therapeutic radionuclide (e.g. 10 MBq), there will be much fewer radioactive atoms in the diagnostic sample due to the shorter half-life of diagnostic agents. This is illustrated in Equation 4.1 where the number of radioactive nuclei (N) in a sample of given activity (R) is linearly proportional to the half-life of those radioactive nuclei ($t_{1/2}$).

$$N = \frac{R \cdot t_{1/2}}{0.693} \tag{4.1}$$

Within the context of this work, given two samples of ^{43}Sc and ^{47}Sc of equal activity and volume, the sample of ^{47}Sc would have approximately 20 times the concentration and number of active nuclei available for radiolabeling than the ^{43}Sc. The reaction conditions are therefore much more favorable for the synthesis of ^{47}Sc than that of ^{43}Sc barring any prominent difference in contaminants between the samples. As such, the improvement of molar activity throughout this work has mostly been with regards to ^{43}Sc-PSMA-617.

Reducing the amount of unlabeled ligand present in the final radiopharmaceutical product is therefore critical. Beyond reducing competitive contaminants such as metals in the reaction mixture, this is primarily achieved by reducing the number of ligand molecules which must be added to the radioactivity to achieve a desired level of molar activity. According to "Le Chatelier's principle" and collision theory, the amount of ligand it is necessary to add to the

reaction mixture can be reduced by increasing the concentration of the radionuclide as the other key reactant [175]. For this reason, production yield can actually serve as a limiting factor in the chemical purity of radiopharmaceuticals.

Given this context, this chapter will describe the most up to date iteration of the chemical procedure we have generated for the synthesis of radioscandium PSMA-617 including any "experimental pearls" we have devised through our longstanding experience in synthesizing radioscandium PSMA-617. Although it is difficult to directly correlate refinements to this procedure to increases in molar activity, the experimental increase in molar activity throughout this work will also be shown and contextualized to production factors.

4.2 Methods

As is outlined in Figure 4.1, the entire chemical processing procedure utilized to synthesize an injectable dose of radioscandium PSMA-617 from an irradiated CaO or $CaCO_3$ target involves the separation of radioscandium from CaO, the synthesis of radioscandium PSMA-617, the purification and quality control of radioscandium PSMA-617, and the reformulation of radioscandium PSMA-617.

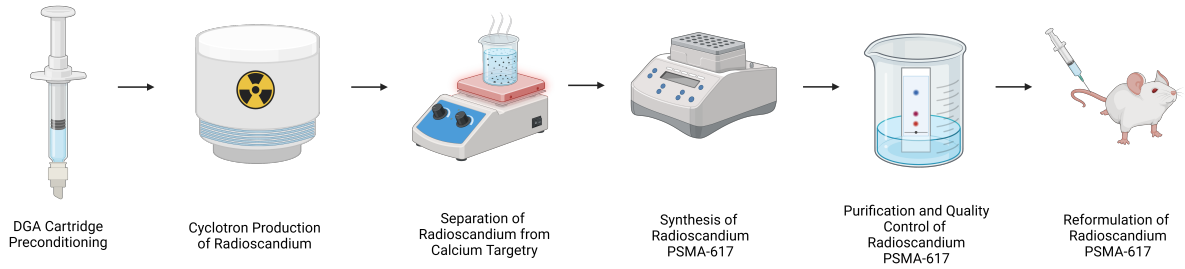

Figure 4.1: Radioscandium PSMA-617 synthesis from irradiated calcium targetry. This figure is a simplified version adopted from Meier et al. [176, 177].

As a high ratio of conjugated radioscandium PSMA-617 to cold PSMA-617 products is desirable, everything in this procedure prior to the formation of radioscandium PSMA-617 utilizes trace analysis grade metal free reagents to minimize the competitive binding of metal

contaminants to the PSMA-617 chelation complex.

4.2.1 Separation of Radioscandium from Calcium Targetry

Following the retrieval of an irradiated CaO or $CaCO_3$ target as described in the previous chapter, the target was transferred to a PFA beaker and placed on a hot plate set to 70 °C. 2 mL of 16 M HNO_3 was added to the target to facilitate dissolution. After 8 minutes elapsed, 1 mL of water was added to the nitric acid solution to promote protonation. This step was repeated every 8 minutes until a total of 4 mL of water was added. After 8 minutes elapsed from the final addition of water, the target was removed from the hot plate.

After the dissolution, the calcium and radioscandium mixture was loaded into an Eichrom DGA cartridge which had been pre-conditioned with 2 full column volumes (FCV) of 2.5 M HNO_3 followed by 2 FCV of 5 M HNO_3. The loaded DGA cartridge was then washed with 2 FCV of 5 M HNO_3 followed by 1 FCV of 1 M HCl. As the DGA cartridge has a high binding affinity for trivalent cations, the radioscandium remained trapped in the resin throughout the loading and washing steps while the dissolved calcium target material was removed. The trapped radioscandium was then ultimately eluted into approximately ten 0.5 mL aliquots of radioscandium $ScCl_3$ by passing heated 95 °C 0.1 M HCl through the DGA column. These aliquots were then assayed to determine the fractions with the highest activity concentrations for radiolabeling in the following step.

The pass through and washing solutions from this portion of the protocol were saved for the recovery of the enriched calcium target material as was described in the previous chapter. The DGA cartridge was also preserved for this purpose.

4.2.2 Radiosynthesis of Radioscandium PSMA-617

An equal volume of 1 M ammonium acetate (pH 5.5) was added to each aliquot of eluted radioscandium $ScCl_3$ that was taken for radiolabeling. Thinly cut strips of disposable pH

paper were utilized to confirm that the pH of the buffered solution was between 4 and 5 in order to ensure that the reaction mixture had favorable conditions for the complexation of radioscandium with the chelation complex of PSMA-617.

Utilizing the activity data obtained from the aliquots of radioscandium $ScCl_3$, a target molar activity was chosen and the volume of aqueous PSMA-617 (1 μg/μL H_2O) that needed to be added to achieve that target molar activity was calculated according to Equation 4.2 where V_{aq} is the volume of aqueous PSMA-617 that needed to be added to the reaction mixture, r is the activity, M_{ligand} is the molecular weight of PSMA-617, ρ_{aq} is the density of the aqueous PSMA-617 solution, and S_{target} is the target molar activity.

$$V_{aq} = \frac{r \cdot M_{ligand}}{\rho_{aq} \cdot S_{target}} \tag{4.2}$$

The determined quantity of PSMA-617 (e.g., 8.0 μg) was pipetted into each aliquot (e.g., 111.0 MBq in 1.0 mL buffer solution). The resultant reaction mixture was then placed onto a preheated thermal mixer set to 95 °C and a mixing frequency of 500 RPM. The radiolabeling reaction was allowed to proceed for 40 minutes.

Once the reaction was completed, 2 μL of the reaction mixture was spotted onto an instant thin-layer chromatography paper with a silica gel (iTLC-SG) which was then developed in a 1:1 ratio of methanol and 1M ammonium formate and analyzed with radio iTLC. On the resulting chromatogram, free radioscandium remained near the origin whereas radioscandium PSMA-617 migrated with the solvent front thus enabling a measurement of radiolabeling efficiency. If the radiolabeling efficiency was determined to be $\geq$85% the radiolabeled compound was taken for purification. At radiolabeling efficiencies below 85%, the reaction mixture was returned to the thermal mixer with additional cold PSMA-617 compound to react for an additional 40 minutes; however, this typically did not yield any meaningful increase in radiolabeling efficiency. That being said, for the overwhelming majority of the experiments performed throughout this work, radiolabeling efficiency was $\geq$95%.

4.2.3 Purification and Quality Control of Radioscandium PSMA-617

In order to remove any unlabeled radioscandium and reformulate the radioscandium PSMA-617 solvent from a buffered acid to ethanol, the reaction mixture was slowly passed through a Waters Oasis HLB light cartridge (30 mg sorbent) which was pre-conditioned with 3 mL of ethanol followed by 6 mL of water. The cartridge was then washed with 2 mL of water, and both the pass through and washings were assayed in a well counter. As the Oasis cartridge traps the radioscandium PSMA-617 (and cold PSMA-617) while allowing the unlabeled radioscandium to pass through, the ratio of the combined activity in the assayed solution to the total activity was confirmed to be approximately equal to the percentage of unlabeled radioscandium that was seen on radio iTLC prior to proceeding.

The radioscandium PSMA-617 was then eluted from the Oasis cartridge with approximately 300 μL of ethanol. 2 μL of this eluted fraction was utilized to prepare another iTLC plate which was again developed with a 1:1 ratio of methanol and 1M ammonium formate and then analyzed with radio iTLC. As the purification processed should have removed all unlabeled radioscandium, the resulting chromataogram should exhibit a singular peak which travels with the solvent front.

As most *in vitro* assays require the radiopharmaceutical solution to be diluted in cellular media, the final product within this step should be suitable for cellular studies. Within these cases, an additional quality control step was performed to calculate the true molar activity of the final product. 25 μL of the purified solution was transferred to a V-vial. Five μL of the solution within the V-vial was then injected into an HPLC system and analyzed utilizing both radio HPLC and UV HPLC methods. The resultant chromatogram was compared to a standard curve that was generated with the UV trace obtained from the HPLC chromatogram of a reference sample of unlabeled PSMA-617.

For *in vivo* utilization, further reformulation must be performed to ensure that the radiopharmaceutical dose is dissolved within a solvent that is non-toxic and of a physiologically

tolerable pH. As such, in these cases, the quality control steps described in the previous paragraph were instead performed after reformulation.

4.2.4 Reformulation of Radioscandium PSMA-617

In order to reformulate the solvent of radioscandium PSMA-617 from ethanol to a physiologically compatible media, it was necessary to first reduce the ethanol content through evaporative techniques. The preferred method for removing ethanol was to transfer the radioscandium PSMA-617 solution into a screw-top septum vial and place it onto a hot plate set to 60 °C. An 18-gauge needle was then pushed into the septum of the vial to create a port for the venting of evaporated ethanol. A nitrogen line was then attached to a 20 gauge needle and also inserted into the septum of the vial. A gentle flow of nitrogen was applied to the radioscandium PSMA-617 solution thus speeding up the evaporative process. This resulted in a complete evaporation of ethanol within 10 minutes.

In the absence of a nitrogen line, ethanol can also be removed by transferring the radioscandium PSMA-617 solution to a round bottom flask and placing it in a rotary evaporator which is held under vacuum and set to a temperature of at least 60 °C and a rotation rate of 120 RPM. With this experimental setup, the ethanol also evaporated within 10 minutes; however, it also posed significantly more concerns with regards to activity loss and the contamination of laboratory equipment due to the large surface area of the round bottom flask and the potential for violent boiling.

Once the ethanol was evaporated, phosphate buffered saline (PBS) was added to the radioscandium PSMA-617 at a ratio of 1.0 μL per 0.074 MBq for ^{43}Sc-PSMA-617 and ^{44}Sc-PSMA-617, or at a constant 300 μL for ^{47}Sc-PSMA-617. After PBS was added, a thin strip of universal pH paper was utilized to ensure that the final radioscandium solution had a physiological pH between 7-7.4. If the pH was found to be too acidic, additional PBS was added until the pH fell into the acceptable range.

4.3 Results

4.3.1 Separation of Radioscandium from Calcium Targetry

The separation of radioscandium from the calcium starting material was demonstrably effective with decay corrected activity losses typically ranging from 5-10% for the entire dissolution and separation processes. The majority of these losses occurred from radioactivity sticking to the PFA beaker and DGA column, as well as premature elution in the HCl wash.

Radioscandium was successfully eluted from the DGA column with the activity typically being concentrated in three to four 500 μL fractions. A representative elution curve from one instance of this processes utilizing a starting ^{43}Sc activity of 1040.74 MBq is presented in Figure 4.2a. A version of this elution curve which was normalized to the starting activity is also presented in Figure 4.2b.

Despite minimal losses, because the highly concentrated aliquots of eluted radioscandium are the only fractions which are viable for radiolabeling with high molar activity, only approximately 50-60% of the decay corrected activity is actually usable for radiolabeling. As such, future efforts to reduce the number of aliquots needed in the separation processes or to combine and concentrate the elution fractions may be valuable when trying to increase the maximum achievable molar activity.

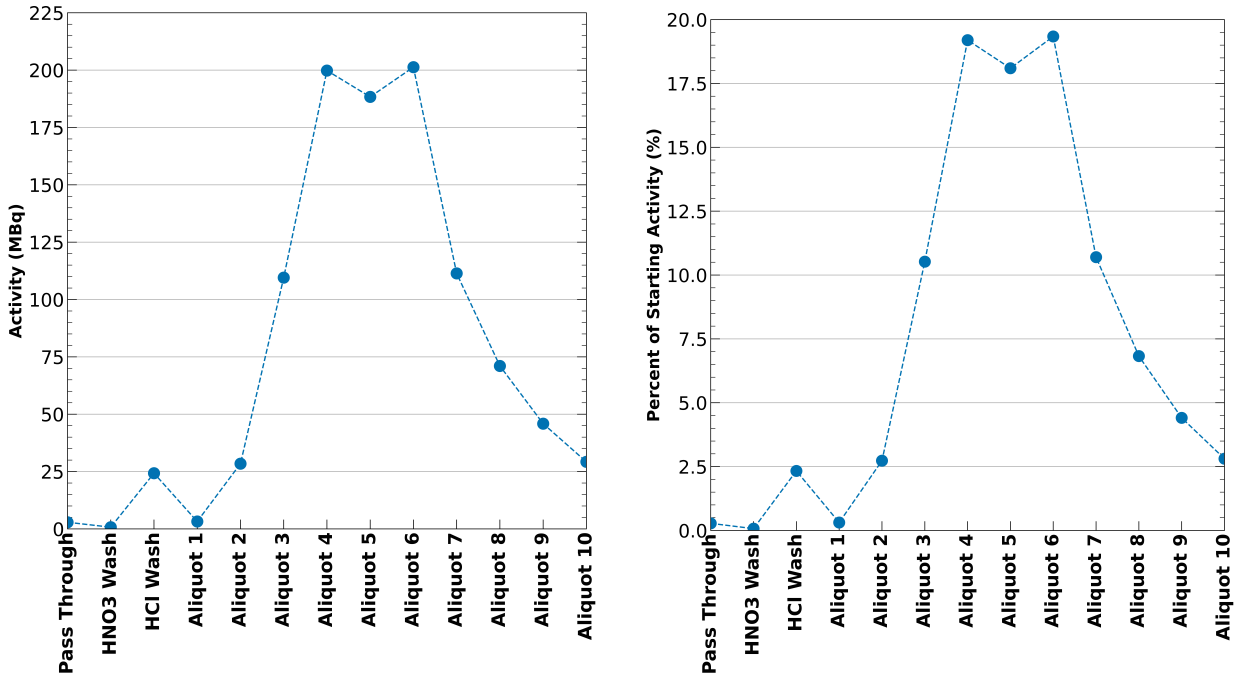

(a) Raw activity

(b) Normalized to starting activity

Figure 4.2: The activity elution curve from the separation of radioscandium from calcium target material utilizing a DGA column. This figure was adapted from the data presented in Table 1 of Meier et al [176].

4.3.2 Radiosynthesis of Radioscandium PSMA-617

Using the radiolabeling procedure described above, radioscandium PSMA-617 was successfully synthesized in 34 out of 41 total radiolabeling experiments yielding a success rate of 82.9%. Of the unsuccessful radiolabeling attempts, 57.1% occurred when attempting to radiolabel ^{47}Sc that was either of a very low starting activity (<74 MBq) or was separated from titanium targetry utilizing reagents that were not metal free or trace analysis grade. Of the remaining failed labeling attempts, three involved the labeling of ^{43}Sc which was also separated from its starting target material using reagents that were not metal free or trace analysis grade. The origin of the remaining radiolabeling failure is unclear; however, it occurred after the dissolution mixture was heated for an unprecedented amount of time (>2 hours). The molar activity values obtained from the radiolabeling of ^{43}Sc-PSMA-617,

^{44}Sc-PSMA-617, ^{47}Sc-PSMA-617 across the radioscandium PSMA-617 syntheses performed throughout this work are exhibited in Figure 4.3a. Molar activity is also presented as a function of ^{43}Sc end of bombardment (EOB) yield in Figure 4.3b.

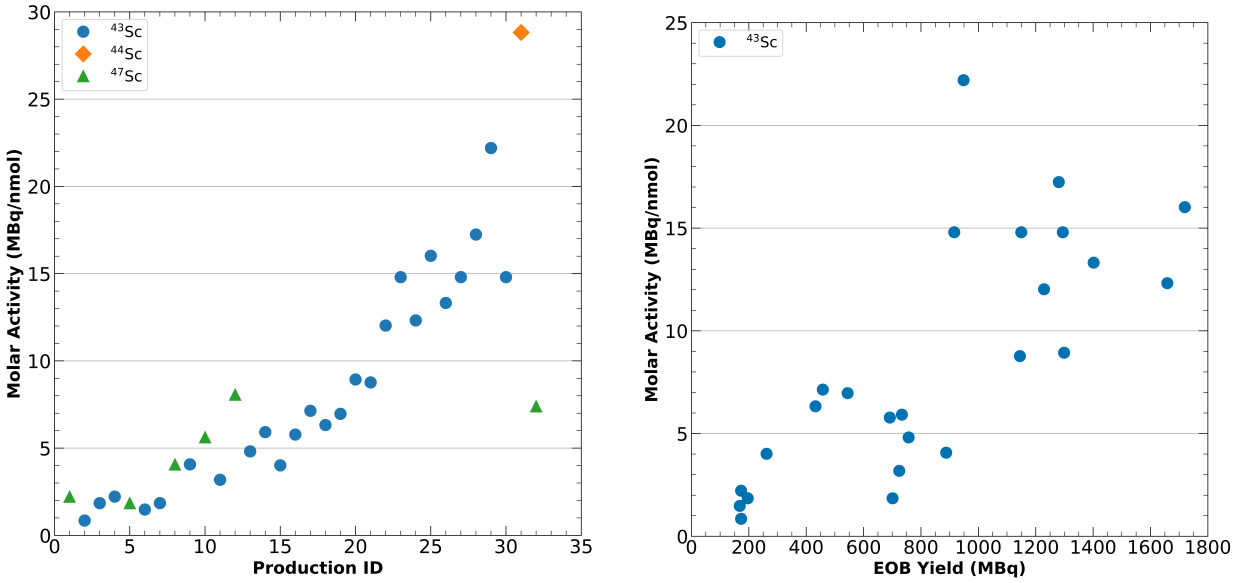

(a) Molar activity throughout this work

(b) Molar activity vs. starting activity

Figure 4.3: Molar activity of radiolabeled scandium PSMA-617.

As was shown in Figure 4.3a, there has been a general upward trend in the obtained molar activity from radioscandium synthesis throughout the duration of this work. As previously stated, it is difficult to directly assign causal factors for this gradual increase; however, our capacity to improve radioscandium PSMA-617 purity likely stems from a combination of increased experience with the protocol and small procedural changes such as switching to metal free reagents or diluting the ligand in buffer prior to adding it to the reaction mixture.

Figure 4.3b also clearly exhibits that the increase in radiolabeling efficiency does generally coincide with increasing production yields and thus increasing starting activity concentrations which enabled the utilization of less ligand according to collision theory and Le Chatelier's principle as previously mentioned. However, this data does not exhibit a tight upward trend with a high degree of variance in the resulting molar activity in close ranges

of EOB yields. This is most likely because other experimental variables were not held constant throughout the radiolabeling process as the main focus of the radiochemical portion of this work was improving radioscandium PSMA-617 radiolabeling efficiency as opposed to characterizing what factors improve radiolabeling efficiency.

4.3.3 Purification and Quality Control of Radioscandium PSMA-617

The purification of radioscandium PSMA-617 has also been highly successful with a complete removal of free radioscandium with negligible losses of labeled radioactivity being evident for all experiments throughout this work. An extreme example of the change in iTLC chromatograms resulting from the purification process performed on a reaction mixture with a high percentage of unlabeled radioscandium is presented in Figure 4.4a and Figure 4.4b.

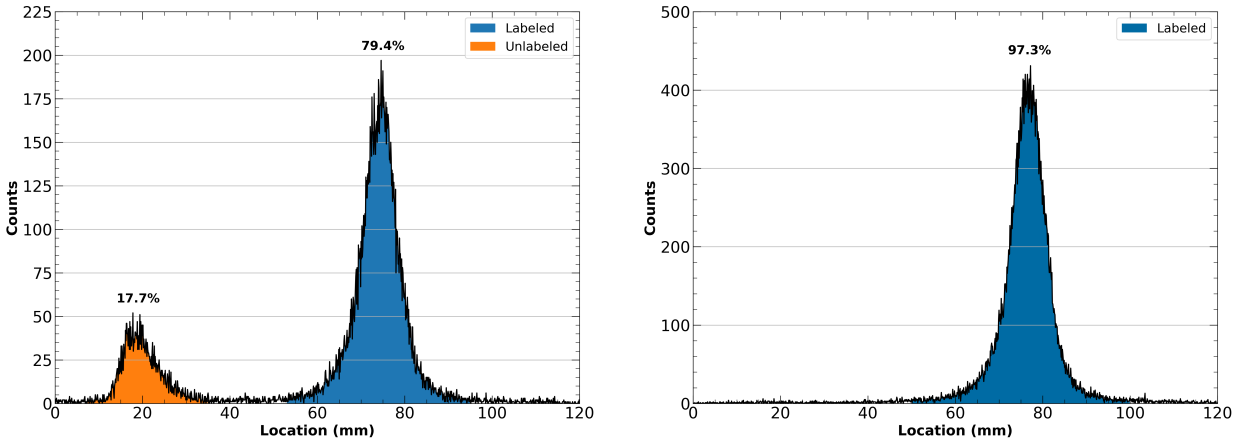

(a) Crude ^{43}Sc-PSMA-617 (b) Purified ^{43}Sc-PSMA-617

Figure 4.4: Radio iTLC chromatograms before and after purification. This figure was adopted from Meier et al. [176].

Given that this purification process is so highly effective, and because any excess ethanol from the elution can be removed through evaporative methods, there is no need to further refine this portion of the protocol. That being said, it is worth noting that this purification process removes free radioscandium but not unlabeled PSMA-617 ligand. As such, the development of additional purification procedures which can purify radioscandium PSMA-

617 from unlabeled PMSA-617 would be highly valuable especially in scenarios where it is not feasible to modify the production parameters to increase the starting activity. This idea is explored in greater depth in the Future Directions section of Chapter 7.

4.4 Discussion

In accordance with Aim 1, the radiochemical protocol which was developed throughout this work was successfully utilized for the synthesis of ^{43}Sc-PSMA-617, ^{44}Sc-PSMA-617, ^{47}Sc-PSMA-617 from calcium-based targetry. Within this protocol, the separation of radioscandium from calcium oxide or calcium carbonate, the purification and quality control of radioscandium PSMA-617, and the reformulation of radioscandium PSMA-617 were conducted seamlessly with minimal complications or activity losses. The proposed methodology of radiolabeling radioscandium with PSMA-617 was also highly successful; however, in 17.1% of experiments radioscandium did not conjugate with PSMA-617. The overwhelming majority of these failures occurred prior to our standardized use of metal free or trace analysis reagents throughout the entire radiochemical procedure, or in circumstances where the starting activity was less than 74 MBq. As such, the majority of these failures occurred in the early phases of this work and are not concerning in the broader development of radioscandium pharmaceuticals.

Conversely, the development of radioscandium pharmaceuticals will likely be contingent on the improvement of the maximum achievable molar activity in scandium radiolabeling. At present, the highest molar activity obtained with was 22.2 MBq/nmol for ^{43}Sc-PSMA-617, 28.8 MBq/nmol for ^{44}Sc-PSMA-617, and 8.1 MBq/nmol for ^{47}Sc-PSMA-617. Based on the current literature on PSMA targeted PET imaging, the molar activity presently obtainable with ^{43}Sc-PSMA-617 and ^{44}Sc-PSMA-617 is likely sufficient for diagnostic applications, but the molar activity obtainable with ^{47}Sc-PSMA-617 is insufficient for therapeutic applications.

In this regard, Langbein et al. noted only minimal changes on PET-derived biodistri-

bution when utilizing PSMA targeting ^{18}F flotufolastat with high molar activity (263.09 MBq/nmol) or low molar activity (28.38 MBq/nmol) for the imaging of prostate cancer [178]. Moreover, differences in tumor uptake of ^{18}F flotufolastat between these two groups was even less pronounced than in non-target structures [178]. Similarly, Radzina et al. noted the unimpeded use of ^{68}Ga-PSMA-11 for the clinical characterization of prostate cancer in PET/MRI with molar activity ranging from 10-50 MBq/nmol [179]. Consequently, the maximum observed molar activity of ^{43}Sc-PSMA-617 and ^{44}Sc-PSMA-617 are on the same approximate order of these two studies. As such, from the perspective of chemical specificity, ^{43}Sc-PSMA-617 and ^{44}Sc-PSMA-617 are definitively viable for pre-clinical diagnostic imaging and could potentially even be serviceable in clinical imaging as that was the context of the two aforementioned studies. This conclusion is congruent with the results we have obtained for the pre-clinical imaging of PSMA positive mice as will be discussed in Chapter 5.

While diagnostic imaging quality likely does degrade to some extent with reduced molar activity, molar activity is especially critical in radionuclide therapy given the large amounts of administered activity and the typically longer radioactive half-lives of therapeutically useful radionuclides [174, 180]. Within the context of PSMA-617 based therapeutics, Fendler et al. has shown that the molar activity of a therapeutic dose of ^{177}Lu-PSMA-617 (PLUVICTO) influences therapeutic response in syngeneic mice [181]. Within this framework, Fendler et al. found ^{177}Lu-PSMA-617 doses with specific activities of 15 MBq/nmol and 31 Mbq/nmol to produce suboptimal results in regard to the ratio of tumor to kidney uptake, DNA double strand break induction, and tumor growth inhibition when compared to a dose with a molar activity of 62 Mbq/nmol [181]. Particularly relevant to aspects of this work described in Chapter 5, Fendler et al. also did not observe any significant induction of DNA double strand breaks in the tumors of mice treated with the low molar activity ^{177}Lu-PSMA-617 when evaluated with the γ-H2AX immunohistochemistry assay, although the sample size for

this evaluation was relatively small (n=6) [181].

As even the low molar activity utilized in Fender et al. is still approximately double that of the highest molar activity achieved with ^{47}Sc-PSMA-617 in this work, it is clear that further development of ^{47}Sc-PSMA-617 synthesis is necessary. When compared to a typical clinical dose of ^{177}Lu-PSMA-617 which ranges from 100-212 MBq/nmol, the need for improved molar activity is even more evident [182]. Ideally, the poor radiochemical yield of this reaction would be overcome through the production of greater activity amounts such that the starting activity concentration in the reaction mixture would be higher; however, this is not necessarily a feasible solution due to the scarcity of the calcium material necessary to produce ^{47}Sc and the low yields of other titanium based production routes as described in Chapter 3. Consequently, for the radiosynthesis of ^{47}Sc-PSMA-617, it may be necessary to develop methods to increase activity concentration by reducing the volume of the reaction mixture or separating the radiolabeled and cold PSMA-617 compounds with precision chromatography.

4.5 Conclusion

This chapter outlined a protocol that was developed to synthesize usable doses of radioscandium PSMA-617 starting from irradiated enriched calcium targetry including reformulation for application in *in vitro* and *in vivo* experiments. Activity elution curves generated from the loading, washing, and elution of a DGA resin column indicated the successful separation of radioscandium from calcium starting materials with minimal activity loss. Radio iTLC chromatograms indicated the successful conjugation of radioscandium to PSMA-617 and also served as a quality control measure to validate the removal of remnant free scandium through the use of a polymeric separation cartridge. The molar activity obtained in this procedure was seen to increase throughout the course of this work and also generally increase as a function of starting activity; however, due to the experimental design it was not possible to directly identify singular factors with causal effects on maximum achievable molar activity.

When contextualized through the literature, the molar activity values obtained in this work were shown to likely be sufficient for diagnostic imaging with ^{43}Sc-PSMA-617 and ^{44}Sc-PSMA-617, but insufficient for the pre-clinical evaluation of therapeutic effect with ^{47}Sc-PSMA-617. This analysis is congruent with the *in vitro* and *in vivo* results obtained in Chapter 5. Given this deficiency, further steps must be taken to improve the maximum achievable molar activity in radioscandium radiolabeling in order to enable the application and evaluation of radioscandium true theranostics. Beyond simply producing more activity to improve the starting activity concentration of the reaction, molar activity could potentially be improved through the development of HPLC methods to separate cold PSMA-617 and radioscandium PSMA-617, or by reducing the volume of the radiolabeling reaction through the evaporation of the HCl eluent following the separation of radioscandium from the calcium target materials.

CHAPTER 5

IN VITRO AND *IN VIVO* ANALYSIS OF RADIOSCANDIUM CONJUGATED PSMA-617

5.1 Introduction

Following the establishment of production and radiochemical methods, pre-clinical evaluation is the next natural step in radiopharmaceutical development and arguably the most crucial for evaluating the practical viability of a radiopharmaceutical at the early stages of development. In that sense, this work is highly motivated by the promising clinical results which have been obtained with ^{177}Lu-PSMA-617 and ^{68}Ga-PSMA-11 in the mCRPC space. Moreover, because both of these isotopes have been adopted clinically, their respective pre-clinical evaluations have left behind a blueprint for the pre-clinical development of peptide-based PSMA targeting radiopharmaceuticals which include evaluations of target specificity, image-based tumor detection, pharmacokinetics, and therapeutic effectiveness. Within this broad scope, this chapter will focus on: *in vitro* uptake and internalization, static and dynamic PET imaging with ^{43}Sc-PSMA-617, static SPECT imaging with ^{47}Sc-PSMA-617, *ex vivo* biodistribution with ^{43}Sc-PSMA-617 and ^{44}Sc-PSMA-617, and DNA double strand break (DSB) and PSMA immunohistochemistry in excised tumors treated with ^{47}Sc-PSMA-617. As a novel element of this work motivated by the true theranostic potential of the radioscandiums, a dual modality imaging study will also be presented in which singular mice were imaged with both ^{43}Sc-PSMA-617 PET and ^{47}Sc-PSMA-617 SPECT.

Under that lens, the complete duration of this work has involved the conduction of over 10 radioscandium PSMA-617 specificity assays, the imaging of more than 70 individual mice with radioscandium PSMA-617, and the subsequent *ex vivo* biodistribution of a large fraction of those imaged animal models. As such, it is not possible to present the entire congregation of these results within this work. Moreover, because these experiments have coincided with

over 4 years of development in the production and radiochemical aspects of this work, as described in Chapter 3 and Chapter 4, these experiments have occurred over a vast range of molar activity and therefore specificity to PSMA-617. Consequently, we have elected to present the most recent results for each section of this chapter. The singular exception to this is the SPECT imaging results obtained with ^{47}Sc-PSMA-617 where images taken with multiple molar activities are presented to communicate the need for improved radiochemical yield.

5.2 Methods

5.2.1 Enzalutamide Resistant Cellular and Animal Models

The application of targeted radionuclide therapy in metastatic castration prostate cancer typically follows the development of a resistance to enzalutamide (XTANDI) after already developing a resistance to other androgen deprivation therapies [183, 184]. Moreover, acquisition of this resistance can entail genetic mutations, alterations in androgen signaling pathways, and changes to the tumor microenvironment that ultimately result in more aggressive tumor behavior *in vivo* [185]. As such, the development of radioscandium PSMA-617 for mCRPC implementations necessitated the implementation of an enzalutamide resistant cell line to most accurately reflect clinically relevant conditions.

As such we selected the luciferase expressing LNCaP-EnzaR-Luc cell line as described in Kregel et al. for utilization in the entirety of the *in vitro* and *in vivo* experiments described in this work [185]. A non-PSMA expressing DU145 cell line was also utilized as a negative control throughout this work. This cell line was also modified to express luciferase and has natural enzalutamide resistance as it does not express androgen receptors [186].

For the development of murine models for *in vivo* experiments, 2×10^6 LNCaP-EnzaR-Luc or DU145 cells were suspended in 35 μL of Hanks balanced salt solution, mixed with 115

μL of Matrigel and inoculated subcutaneously into the flank. Subsequent tumor growth was monitored with luciferase bioluminescence imaging and caliper measurements. All animal models consisted of immunocompromised athymic nude mice.

5.2.2 In Vitro Specificity

LNCaP-EnzaR-Luc and DU145 cells were cultured at 37 °C in T25 flasks with RPMI 1640 medium supplemented with 10% FBS and 0.1% penicillin-streptomycin. LNCaP-EnzaR-Luc cells were additionally treated with 10 μM enzalutamide to maintain enzalutamide resistance. Cellular cultures were monitored biweekly with an optical microscope to ensure that no contamination developed. Media changes in these cultures were also performed on a biweekly basis.

Twenty-four hours prior to uptake/internalization assay, cell media was removed and 1 mL of trypsin was added to each cell culture. Trypsinized cells were allowed to incubate for 10 minutes to ensure a complete detachment from the T25 flask surface. Cell density was then measured with an Invitrogen Countess II automated cell counter to ensure a density of at least 2.5×10^6 cells/ml trypsin (the minimum density to perform the assay), although it was preferred for cultures to reach at least 50% confluence prior to this step.

Each solution of suspended cells was then diluted with RPMI 1640 (supplemented with 10% FBS) to produce a final 25 mL solution with a density of 1×10^5 cells/ml. Each cell suspension was then pipetted into a 24-well plate with 1 mL (1×10^5 cells) being dispersed into each well. Each plate was then incubated for 24-hours at 37 °C to ensure cell reattachment. As the application of antibiotics during this phase can influence downstream uptake and internalization results, it was imperative that this portion of the procedure was conducted with the utmost diligence to minimize potential contamination.

Following this incubation period, the media was removed from three wells of each 24-well plate and replaced with 200 μL of trypsin. The plate was then returned to the incubator for

5 minutes at 37 °C. The trypsinized cells from each well were then counted with the Countess II automated cell counter to obtain an accurate measurement of the cellular density in each well as is necessary for the downstream calculation of uptake and internalization.

The media was removed from 3 additional wells of each 24-well plate and replaced with 200 μL of RPMI 1640 (without FBS). 1 μg of cold PSMA-617 ($\rho = 1\ \mu g/\mu L$) was added to each of these wells and incubated for 30-minutes at 37 °C in preparation for the blocking assay.

During this incubation period, the radioscandium PSMA-617 treatment was prepared by adding the desired activity of the radiopharmaceutical to a 10 mL well of RPMI 1640 and then performing a serial dilution to produce a minimum of six concentrations of radioscandium PSMA-617. The remaining media in the 24-well plate was removed and replaced with 200 μL of the treatment solution (3 wells at each concentration and an additional 3 wells at the highest concentration for the blocking assay).

Following the application of the radioscandium PSMA-617 solution, an additional 1 μg of cold PSMA-617 ($\rho = 1\ \mu g/\mu L$) was added to the 3 blocking assay wells of each 24-well plate. Both plates were then returned to the incubator and allowed to incubate for 2-hours. After the incubation period, the radioactive treatment media was removed from each well of the 24-well plate and each well was washed twice with 1 mL of RPMI 1640. 200 μL of RPMI 1640 was then re-added to each well and both 24-well plates were returned to the incubator for 2 hours.

Upon completion of the second incubation period, the cell media was again removed from the 24-well plate and each well was washed with 1 mL of cold PBS. 200 μL of 0.05 M glycine buffer (pH 2.8) was then added into each well (except for the 3 blocking assay wells) and incubated for 10 minutes to dissociate radioscandium PSMA-617 conjugated to the cellular surface. As the cellular surface conjugated radioscandium PSMA-617 represents the portion of uptake that is not internalized, the glycine buffer in each well was then collected into

gamma counter tubes for assay. After glycine buffer collection, wells were washed with another 1 mL of cold PBS.

To initiate cell lysis, 200 μL of 1 M NaOH was added to each well. Lysates were then collected into gamma counter tubes for assay. Two hundred μL of each stock treatment solution was also collected into gamma counter tubes for assay such that counts for each well could be normalized by the administered activity of radioscandium PSMA-617.

Finally, all samples were loaded into a WIZARD2 automated gamma counter and assayed for the number of counts originating from each sample in a 10-minute measurement period. These gamma counter measurements were decay corrected to the start of the experiment and averaged across all three wells corresponding to each administered concentration of radioscandium PSMA-617.

With the resulting data, cellular uptake and internalization were calculated for each cell line according to Equation 5.1 and Equation 5.2 where N_{cells} is the mean number of cells per well, $Counts_{Gly}$ is the mean number of counts from the cell surface fraction of uptake at a given radioscandium PSMA-617 concentration, $Counts_{NaOH}$ is the mean number of counts from the internalized portion of uptake at a given radioscandium PSMA-617 concentration ($c = [^{4x}Sc - PSMA - 617]$), and $Counts_{AA}$ is the mean number of counts from the stock treatment solution of the corresponding radioscandium PSMA-617 concentration.

$$\text{Uptake}(c) = \frac{1 \times 10^5}{N_{Cells}} \frac{Counts_{Gly} + Counts_{NaOH}}{Counts_{AA}} \cdot 100\% \tag{5.1}$$

$$\%\ \text{Internalization}(c) = \frac{Counts_{NaOH}}{Counts_{Gly} + Counts_{NaOH}} \cdot 100\% \tag{5.2}$$

Scandium-43

An assay of cellular uptake and internalization was performed with LNCaP-EnzaR-Luc and DU145 cell lines with the administration of ^{43}Sc-PSMA-617 at concentrations of 0.010, 0.022,

0.043, 0.085, 0.17, and 0.35 nM. The molar activity of the administered ^{43}Sc-PSMA-617 was 16.02 MBq/nmol at the start of the assay. These results are presented in Figure 5.2, and Figure 5.3.

A blocking assay was also performed with a separate dose of ^{43}Sc-PSMA-617 in parental (non-enzalutamide resistant) LNCaP cells. For this assay, the concentration of ^{43}Sc-PSMA-617 was 54.42 nM, and the molar activity was 5.92 MBq/nmol. At this molar activity, the equivalent activity of the added cold PSMA-617 was 11.36 MBq. These results are presented in Figure 5.1.

Scandium-47

An assay of cellular uptake and internalization was performed with LNCaP-EnzaR-Luc and DU145 cell lines with the administration ^{47}Sc-PSMA-617 at concentrations of 0.016, 0.065, 0.260, 1.04, 4.16, 16.62, and 66.49 pM. The molar activity of the administered ^{47}Sc-PSMA-617 was 3.21 MBq/nmol at the start of the assay. A blocking assay was also performed with the highest concentration ^{47}Sc-PSMA-617 treatment. For the blocking assay, the added cold PSMA-617 was equivalent to 6.16 MBq of active ^{47}Sc-PSMA-617. These results are presented in Figure 5.4, Figure 5.5, and Figure 5.6.

5.2.3 In Vivo Imaging

For static imaging procedures, the radioscandium pharmaceutical was administered by tail vein injection while the murine model was held under anesthesia consisting of 1-2% isoflurane in 100% oxygen. Following the radiopharmaceutical injection, animals were typically held for 2-6 hours to allow for radiopharmaceutical uptake and distribution prior to the start of imaging. ^{43}Sc-PSMA-617 static PET scans were obtained with the MOLECUBES β-CUBE and were approximately 30-minutes in duration. ^{47}Sc-PSMA-617 SPECT scans were obtained with the MOLECUBES γ-CUBE and were approximately 90-minutes in duration.

The acquisition of dynamic PET imaging data required the implementation of a tail vein catheter for dose administration. Under this protocol, the anesthetized animal was placed into the MOLECUBES β-CUBE PET system prior to injection, and the delivery of ^{43}Sc-PSMA-617 through the tail vein catheter directly coincided with the initiation of the scan. Dynamic image acquisitions were approximately 2 hours in duration.

In order to co-register functional imaging data with anatomic imaging, PET or SPECT imaging was always followed by a CT image acquisition utilizing the MOLECUBES X-CUBE. CT acquisition time was typically 2-5 minutes, increasing with the scanned bed length.

Animals remained anesthetized with 1-2% isoflurane in 100% oxygen for the duration of all imaging procedures. Moreover, to ensure animal well-being, murine respiratory rate was monitored with a cardiac sensor built into the mouse bed, and core temperature was monitored with a rectal temperature probe for the entire duration of imaging.

All animal images generated in this work are maximum intensity projection (MIP) images presented in standardized uptake values (SUV) which were calculated according to Equation 5.3 below where M is mass of the injected animal model, A_c is the activity concentration within the image, A_{inj} is the total injected activity, and $e^{\frac{-ln(2)t}{t_{1/2}}}$ is a decay correcting factor which corrects the activity of the total injected dose to the time of the image acquisition.

$$SUV = \frac{M \cdot A_c}{(A_{inj}) \cdot e^{-ln(2)\frac{t}{t_{1/2}}}} \tag{5.3}$$

Scandium-43 Static Imaging

Two mice bearing LNCaP-ENZaR-Luc xenografts were injected with 5.15-5.21 MBq and imaged with static PET for 30-minutes at 4-hours post-injection. The molar activity of the dose given to these mice was 12.03 MBq/nmol. These two static PET images are shown in Figure 5.7. The mice presented in these images also correspond to the *ex vivo* biodistribution taken at 4 h post-injection as is shown in Figure 5.16.

To visually characterize the changes in biodistribution over time after the injection of ^{43}Sc-PSMA-617, an additional murine model bearing an LNCaP-ENZaR-Luc xenograft was injected with 6.85 MBq of ^{43}Sc-PSMA-617 and imaged with a 30-minute static PET scan at 1, 2, 4, and 6 hours post-injection. The molar activity of this injection was 12.32 MBq/nmol. The images at each of these time points are presented in Figure 5.8. The animal imaged in this portion of this work was also taken for biodistribution, the results of which contributed to the dataset shown in Figure 5.17.

Scandium-43 Dynamic Imaging

Two mice bearing LNCaP-ENZaR-Luc xenografts were injected with 4.28-4.32 MBq for dynamic imaging. The dose of ^{43}Sc-PSMA-617 utilized in this dynamic imaging experiment was radiolabeled with a yield of 8.94 MBq/nmol. The resulting images are shown at 15, 30, 60, and 120 minutes post-injection in Figure 5.9. Regions of interest (ROIs) were drawn around the brain, heart, liver, muscle, and tumor in the resulting PET image sequence and changes in standardized uptake value (SUV) were observed over the course of the scan as is presented in Figure 5.10.

To visually exhibit the specificity of ^{43}Sc-PSMA-617 to PSMA-expressing cells, an additional dynamic imaging experiment was conducted with a murine model bearing a PSMA expressing LNCaP-ENZaR-Luc xenograft on the right flank and a non-PSMA expressing DU145 xenograft on the left flank. 4.39 MBq of ^{43}Sc-PSMA-617 was administered via tail vein catheter. The injected radiopharmaceutical had a molar activity of 6.97 MBq/nmol. Just as in the single tumor dynamic imaging experiment, ROIs were drawn around tissues of interest and changes in SUV were measured over the scan duration as are presented in Figure 5.11. The animals imaged in this portion of this work were also taken for biodistribution the results of which comprised the dataset shown in Figure 5.15.

Scandium-47 SPECT Imaging

In order to illustrate how molar activity can influence image quality under the lens of ^{47}Sc-PSMA-617 development, two mice bearing LNCaP-ENZaR-Luc xenografts were administered ^{47}Sc-PSMA-617 via tail vein injection at two different molar activities and imaged with a 90-minute SPECT scan. The dose delivered to the mouse shown in Figure 5.12a was 23.24 MBq at a molar activity of 0.95 MBq/nmol. The dose delivered to the mouse shown in Figure 5.12b was 53.70 MBq at a molar activity of 8.06 MBq/nmol.

Beyond the higher activity demands of SPECT imaging, significantly larger doses were utilized in these experiments relative to ^{43}Sc-PSMA-617 PET imaging to reflect the scale of therapeutic dosing as would be utilized in TRT applications of ^{47}Sc-PSMA-617.

Scandium-43 PET and Scandium-47 SPECT Serial Imaging

To once again facilitate the importance of molar activity in the serial imaging applications of ^{43}Sc-PSMA-617 and ^{47}Sc-PSMA-617, two separate mice bearing LNCaP-ENZaR-Luc xenografts were imaged with both radiopharmaceuticals such that the resulting PET and SPECT images could be compared.

The first of these animals was administered 5.86 MBq of ^{43}Sc-PSMA-617 at a molar activity of 17.24 MBq/nmol and then imaged with a 30-minute static PET scan at 3 hours post-injection. Four days later, this same mouse as given a 28.53 MBq injection of ^{47}Sc-PSMA-617 at a molar activity of 0.59 MBq/nmol then imaged with a 90-minute SPECT scan again at 3 hours post-injection. These images are presented in Figure 5.13.

The second of these animals was administered a 81.03 MBq injection of ^{47}Sc-PSMA-617 at a molar activity of 7.40 MBq/nmol then imaged with a 90-minute static SPECT scan at 2-hours post injection. Approximately 24-hours later, this mouse was given a 5.56 MBq injection of ^{43}Sc-PSMA-617 and imaged with a 30-minute PET scan at 2-hours post-injection. These images are presented in Figure 5.14.

5.2.4 Ex Vivo Biodistribution

Ex vivo biodistribution was performed immediately following *in vivo* imaging. Animals were first placed into an anesthetizing box with a steady flow of 3-5% isoflurane and 100% oxygen. Once unconscious, mice were transferred to a nose cone anesthesia system, again under a steady flow of 3-5% isoflurane and 100% oxygen. In order to ensure a sufficient level of anesthesia, murine respiratory rate was observed and the loss of the pedal reflex was confirmed as is described in the procedure outlined by Oh et al. [187].

Once sufficiently anesthetized, a transcardiac perfusion was performed according to the procedure described in Wu et al. [188]. This additional step ensured the removal of any radioactive blood from the organs which will be harvested for gamma counting analysis thus ensuring that any measured radioactivity within those organs was reflective of tissue-specific uptake.

Following the perfusion, tissue samples of the blood, heart, lungs, salivary glands, liver, spleen, stomach, small intestine, kidney, bone, muscle, and tumor were collected and weights recorded. These tissue samples were then loaded into a WIZARD2 automatic gamma counter and assayed. Isolated samples of the associated radioscandium were also measured with a well counter to determine their activity and then subsequently loaded into the gamma counter for assay. These samples of known activity were used to generate a calibration curve which correlated counts per minute (CPM) in the gamma counter to radioactivity amount. Using this calibration curve, the resulting counts measured in tissue were converted into radioactivity and then normalized by the tissue weight and total injected activity to produce results in percent injected dose per gram (%ID/g).

Scandium-43

The dissection and subsequent gamma counter measurement of several mice described earlier in this section facilitated the measurement of the *ex vivo* biodistribution of ^{43}Sc-PSMA-617

at 2, 4, and 6 hour time points.

The 2-hour time point consisted of the two mice described in the ^{43}Sc dynamic imaging portion of this chapter (Figure 5.9) which were administered 4.28-4.32 MBq of ^{43}Sc-PSMA-617 at a molar activity of 8.94 MBq/nmol.

The 4-hour time point consisted of the two mice which were imaged statically with ^{43}Sc-PSMA-617 PET (Figure 5.7). These animals were administered 5.15-5.21 MBq of ^{43}Sc-PSMA-617 at a molar activity of 12.03 MBq/nmol.

The 6-hour time point partially consisted of the murine model which was imaged at multiple time points with ^{43}Sc-PSMA-617 PET (Figure 5.8). Two additional mice which were administered the same batch of radiotracer were also dissected. These animals appear in the biodistribution study but not the PET imaging study as they both urinated in the bed during scanning thus rendering the images mostly unreadable. The injections administered to this group of animals had a molar activity of 12.32 MBq/nmol and the dose ranged from 4.47-6.85 MBq per mouse.

Scandium-44

A singular animal injected with 9.55 MBq of ^{44}Sc-PSMA-617 via tail vein catheter while simultaneously being imaged with the MOLECUBES β-CUBE scanner for PET image acquisition. The molar activity of the injection was 28.8 MBq/nmol. Because of the high energy gamma emission (1,157 keV) of ^{44}Sc, the detectors quickly became saturated and the imaging was terminated by the PET system thus resulting in an absence of imaging data for ^{44}Sc-PSMA-617. However, this mouse was still dissected at 4-hours post-injection for *ex vivo* biodistribution. The resulting gamma counter measurements are presented in Figure 5.18. This data is uniquely presented in decay corrected megacounts per minute per gram as opposed to %ID/g as we have not yet established a calibration curve to convert ^{44}Sc decay counts to dose with the WIZARD2 gamma counter.

5.2.5 Scandium-47 Radionuclide Therapy

As an attempt to probe the therapeutic efficacy of ^{47}Sc-PSMA-617, one murine model bearing an LNCaP-EnzaR-Luc xenograft was injected with 23.27 MBq of ^{47}Sc-PSMA-617 at a molar activity of 1.00 MBq/nmol. An identical murine model was simultaneously injected with the equivalent cold mass of PSMA-617 to serve as a negative control.

Following injection, the radiopharmaceutical was given a 3-day incubation period which was immediately proceeded by the surgical removal of the tumors. Once removed, the tumors were fixed in formalin and then transferred to 70% EtOH once the tumor of the treatment group was no longer active (approximately 10 days). The tumors were then transferred to the University of Chicago Human Tissue Resource Center for sectioning and staining with anti-PSMA and anti-γH2A.X antibodies for immunohistochemical analysis.

After staining, the resulting slides were converted into digital images with an Aperio AT2 slide scanner at 20x magnification. The resulting images were visually inspected for any variation in PSMA expression or induced DNA DSBs between the treatment and control groups.

5.3 Results

5.3.1 In Vitro Specificity

Scandium-43

The results of the ^{43}Sc-PSMA-617 cellular blocking assay are presented below in Figure 5.1. As shown, when DU145 cells were pretreated with 2 μg of cold PSMA-617 ($\rho = 1\ \mu g/\mu L$), cellular uptake was decreased by only 5.75% relative to the unblocked trial. Conversely, parental LNCaP cells were observed to block all uptake with the addition of cold PSMA-617. To that end, the negative uptake result observed in the LNCaP cells during blocking

is clearly non-physical and merely an artifact from background subtraction. As such, the uptake of ^{43}Sc-PSMA-617 in LNCaP cells can be taken to be effectively zero under blocking.

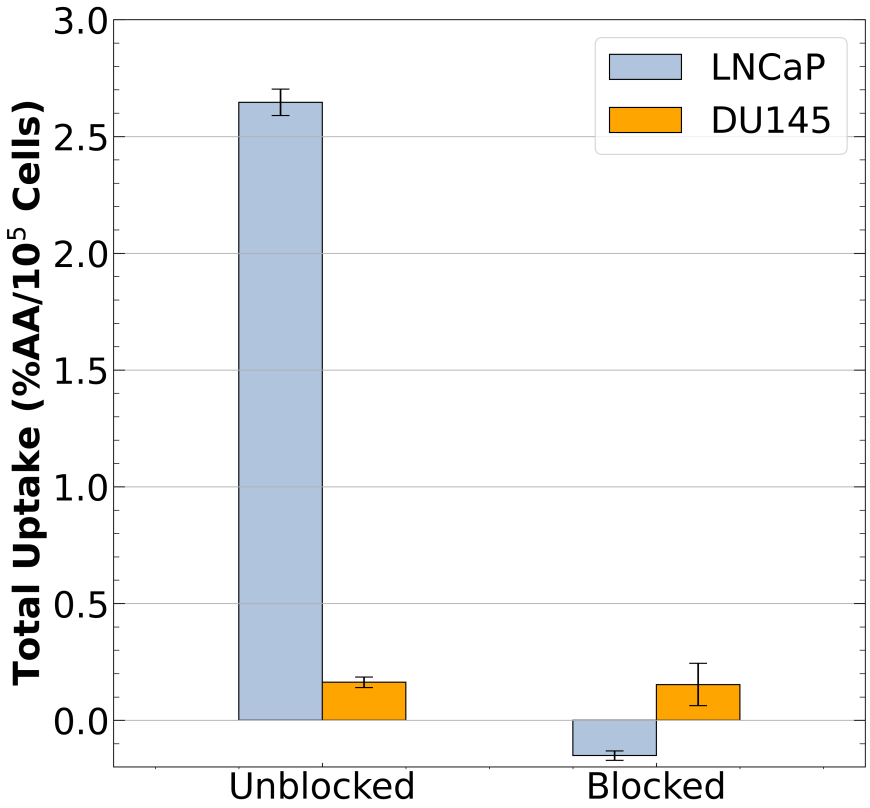

Figure 5.1: Cellular blocking assay in LNCaP and DU145 cell lines after 2-hours incubation at a ^{43}Sc-PSMA-617 concentration and molar activity of 54.42 nM and 5.92 MBq/nmol, respectively.

As LNCaP cells highly express the PSMA target whereas DU145 cells are non-PSMA expressing, this result indicates a clear specificity of ^{43}Sc-PSMA-617 to PSMA expression, even at moderate molar activity. While not conducted in the slightly modified LNCaP-EnzaR-LUC cell line, the blocking results obtained in the parental LNCaP cells should be translatable due to their high levels of PSMA expression.

This assay also provides a clear parallel as to why molar activity is critical in radiopharmaceutical preparation. Essentially, the blocked and unblocked states have different molar activities in the cell media as the amount of cold PSMA-617 is variable between the two

conditions. In the blocked state, we observe that the excess cold PSMA-617 acts as a competitive inhibitor to the PSMA binding sites in LNCaP cells such that ^{43}Sc-PSMA-617 is virtually unable to bind at all.

A similar result can be seen in the uptake assay shown in Figure 5.2 in which the percent of total cellular uptake decreases with increasing ^{43}Sc-PSMA-617 concentration due to receptor saturation. Although, this effect is significantly more pronounced in the LNCaP-EnzaR-LUC cell line than in DU145 thus indicating the expected specificity of ^{43}Sc-PSMA-617 uptake to PSMA expression. As expected, radiopharmaceutical uptake was also observed to be an average of 103.9% greater in LNCaP-EnzaR-LUC cells than DU145.

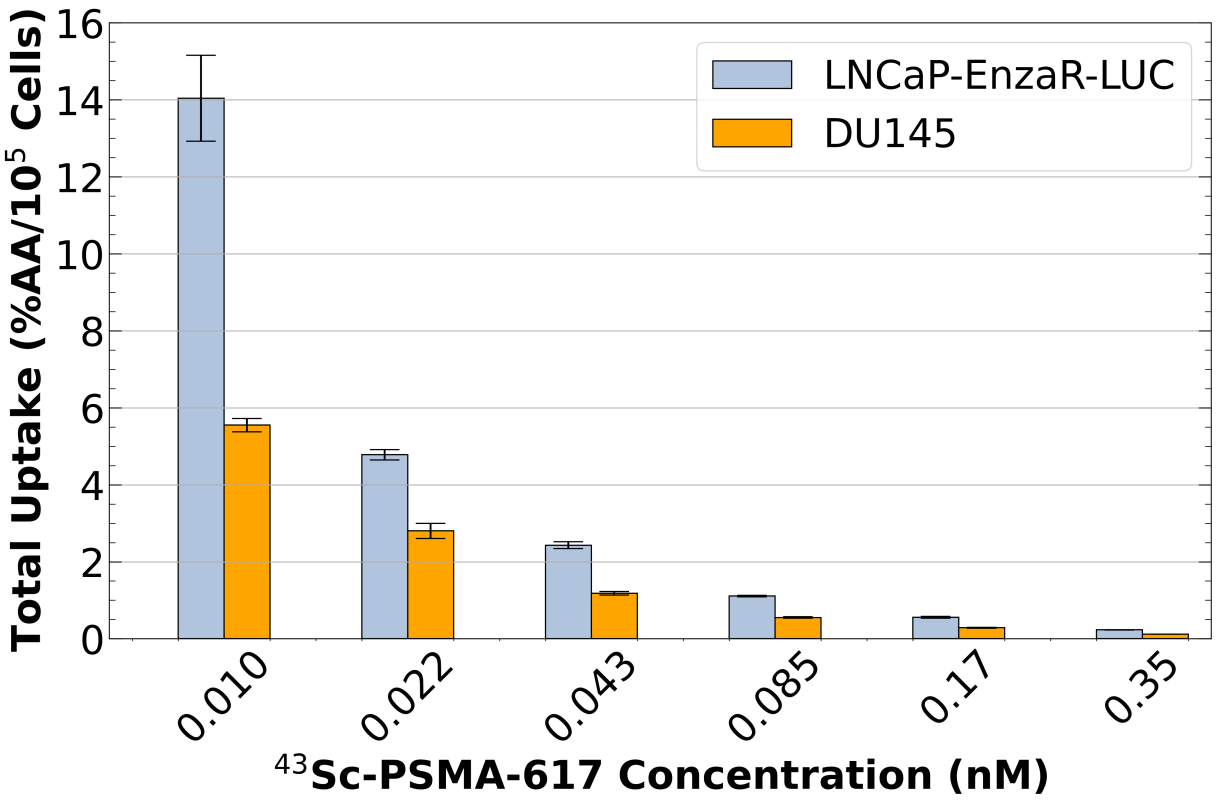

Figure 5.2: Cellular uptake assay in LNCaP-EnzaR-LUC and DU145 cell lines after 2-hours incubation at ^{43}Sc-PSMA-617 concentrations ranging from 0.01-0.35 nM and a molar activity of 16.02 MBq/nmol.

The observed uptake was one order of magnitude less than that stated for ^{177}Lu-PSMA-617 at a concentration of 1 nM (molar activity: 40 MBq/nmol) in LNCaP cells by Ruigrok

et al., and similarly two orders of magnitude less than observed in Tschan et al. (0.75 nM ^{177}Lu-PSMA-617; up to 150 MBq/nmol) [189, 190]. Uptake was approximately two orders of magnitude less than observed with ^{68}Ga-PSMA-617 at a radioligand concentration of 24 nM (molar activity: 6.17-12.34 GBq/nmol) by Duan et al., although this is expected given the approximately 1000 times greater molar activity [191].

Ultimately, while this uptake result indicates clear specificity towards PSMA, the context from the literature also indicates a clear pathway for improvement in uptake and specificity through the development of radiochemical methodology that yields greater molar activity.

As shown in Figure 5.3, the internalized fraction of ^{43}Sc-PSMA-617 within the aforementioned uptake study was observed to range from 43.9-54.0% in LNCaP cells (mean = 48.4%) and 38.2-52.9% in DU145 cells (mean = 46.9%).

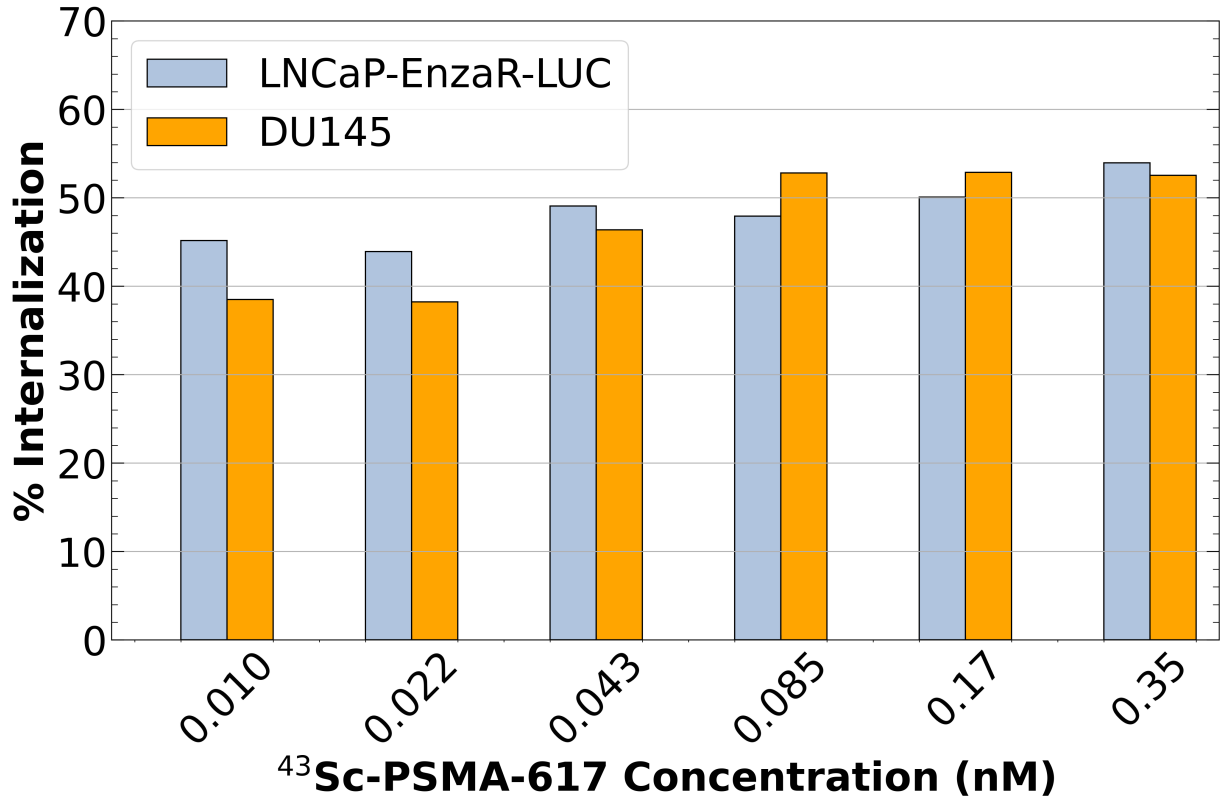

Figure 5.3: Cellular internalization assay in LNCaP-EnzaR-LUC and DU145 cell lines after 4-hours incubation at ^{43}Sc-PSMA-617 concentrations ranging from 0.01-0.35 nM and a molar activity of 16.02 MBq/nmol.

This result is on the same order of magnitude as that observed for the internalization of ^{177}Lu-PSMA-617 into LNCaP cells in Tschan et al. (>60.0%) and ^{68}Ga-PSMA-617 into LNCaP cells in Duan et al. (66.2%) [190, 191]. While these results do not indicate the stratification of internalization by target and non-target tissues, they are immensely helpful in the development and interpretation of simulated dosimetric data, indicating that approximately half of the radiotracer taken up by PSMA-positive cells will be bound to the cellular membrane with the other half being localized to the cytosol or cytoplasmic organelles. This idea will be explored further in the next chapter.

Scandium-47

As is shown in Figure 5.4, the blocking assay conducted with ^{47}Sc-PSMA-617 yielded a 37.9% decrease in cellular uptake in LNCaP-EnzaR-LUC cells relative to a 9% increase in DU145 cells with the addition of 2 μg of cold PSMA-617 at a concentration of 1 $\mu g/\mu L$.

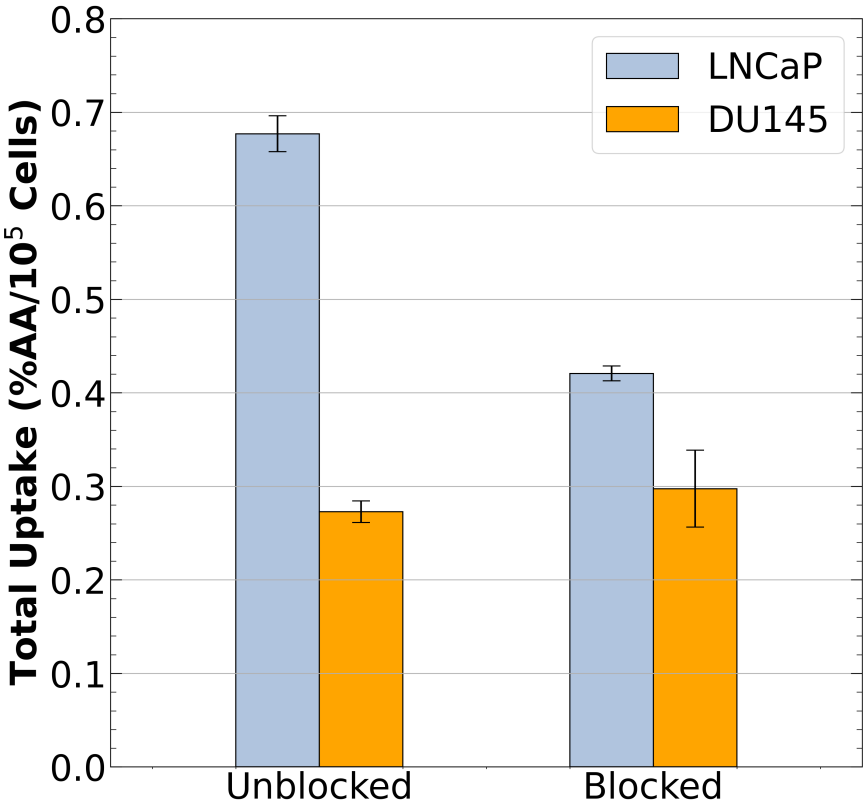

Figure 5.4: Cellular blocking assay in LNCaP-EnzaR-LUC and DU145 cell lines after 2-hours incubation at a ^{47}Sc-PSMA-617 concentration and molar activity of 66.49 pM and 3.21 MBq/nmol.

Much like in the previously described ^{43}Sc-PSMA-617 blocking assay, this experiment clearly indicated a specificity of ^{47}Sc-PSMA-617 to PSMA. However, the lower overall uptake and percent decrease in uptake with the addition of cold compound were also expectedly less drastic than that observed with ^{43}Sc-PSMA-617 due to the almost two times difference in molar activity. Ultimately, the more unlabeled compound present within the treatment dose, the greater the likelihood that radiolabeled PSMA-617 will be outcompeted by unlabeled PSMA-617 at the PSMA binding sites of tumor cells.

A similar result is also observed in the ^{47}Sc-PSMA-617 uptake assay shown in figure Figure 5.5. Within this assay, an average of 92.5% higher uptake was observed in the PSMA-expressing LNCaP-EnzaR-LUC cells relative to DU145 across all concentrations; however,

the disparity in uptake between these two cells lines, as well as the overall uptake percentage, is much lower than observed with ^{43}Sc-PSMA-617, even with picomolar concentrations of ^{47}Sc-PSMA-617 being utilized, as a result of the lower molar activity (3.21 MBq/nmol vs. 16.02 MBq/nmol).

Given the highly dilute nature of the administered ^{47}Sc-PSMA-617, it is difficult to appropriately contextualize these results to the literature; however, it is undoubtedly clear that these results indicate a need for improved molar activity prior to any meaningful characterization of ^{47}Sc-PSMA-617 binding or kinetics.

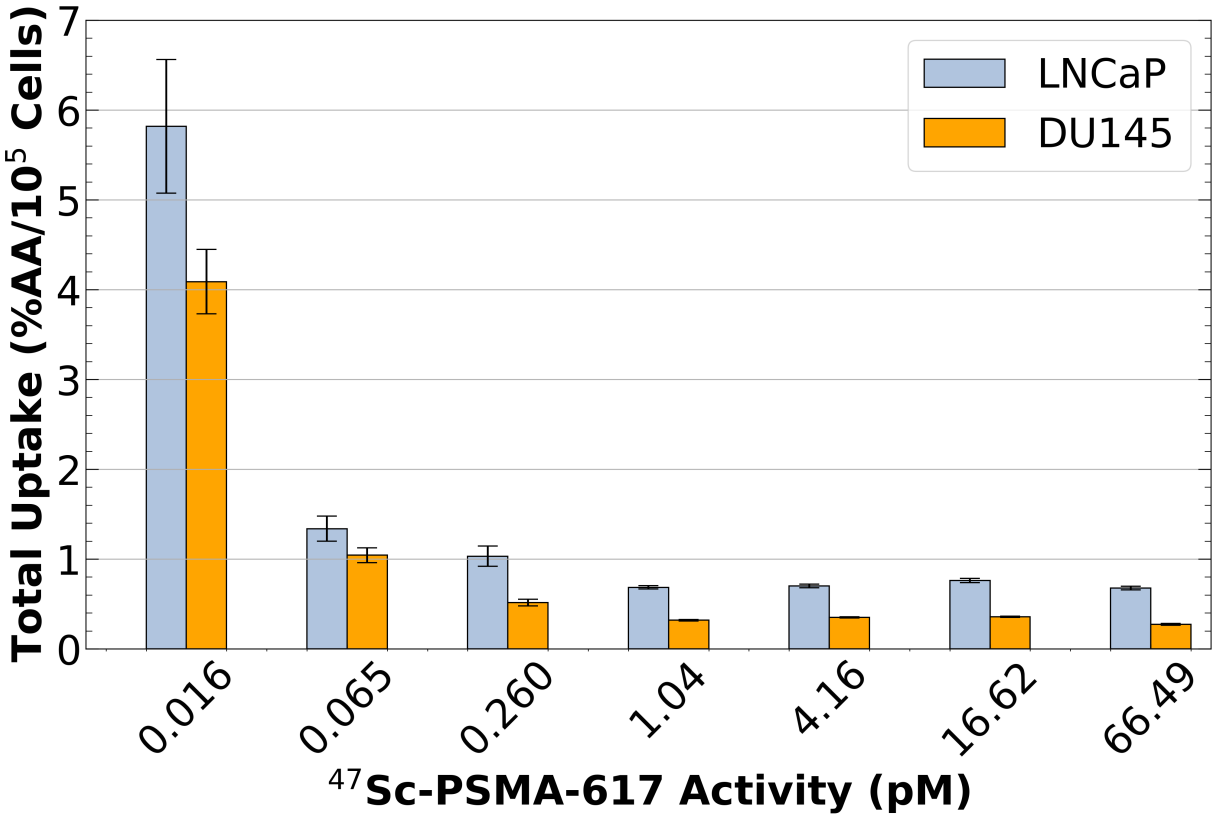

Figure 5.5: Cellular uptake assay in LNCaP-EnzaR-LUC and DU145 cell lines after 2-hours incubation with ^{47}Sc-PSMA-617 concentrations ranging from 0.260-66.49 pM and a molar activity of 3.21 MBq/nmol.

As is shown in Figure 5.6, cellular internalization of ^{47}Sc-PSMA-617 in LNCaP-EnzaR-LUC and DU145 cells was slightly higher than observed with ^{43}Sc-PSMA-617 at a mean

value of 61.3% and 62.2% respectively. Again, while the characterization of internalization is not informative with regards to specificity, it does provide context for later results in the simulation of unicellular dose and DNA DSBs as is discussed in the next chapter.

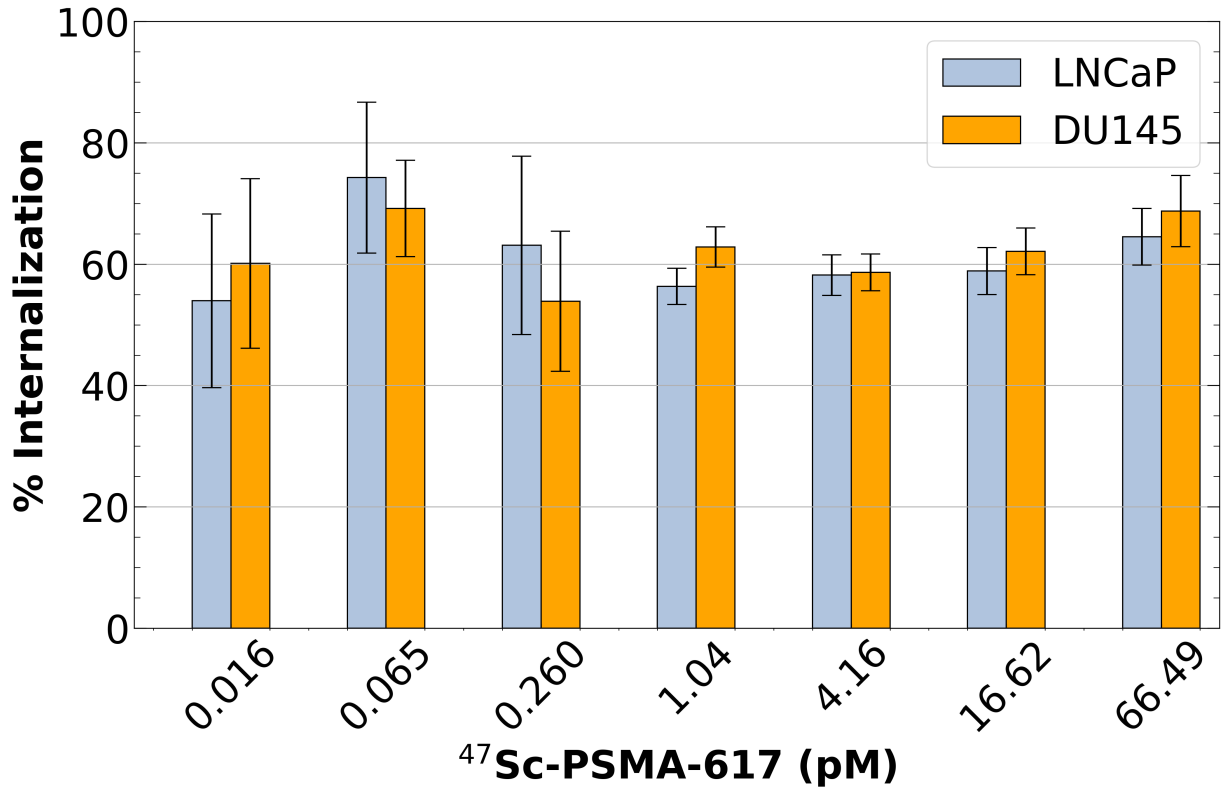

Figure 5.6: Cellular internalization assay in LNCaP-EnzaR-LUC and DU145 cell lines after 4-hours incubation at ^{47}Sc-PSMA-617 concentrations ranging from 0.260-66.49 pM and a molar activity of 3.21 MBq/nmol.

5.3.2 In Vivo Imaging

Scandium-43 Static Imaging

The resulting ^{43}Sc-PSMA-617 PET images from the injection of two LNCaP-EnzaR-Luc bearing mice at 4 hours post-injection are presented in Figure 5.7.

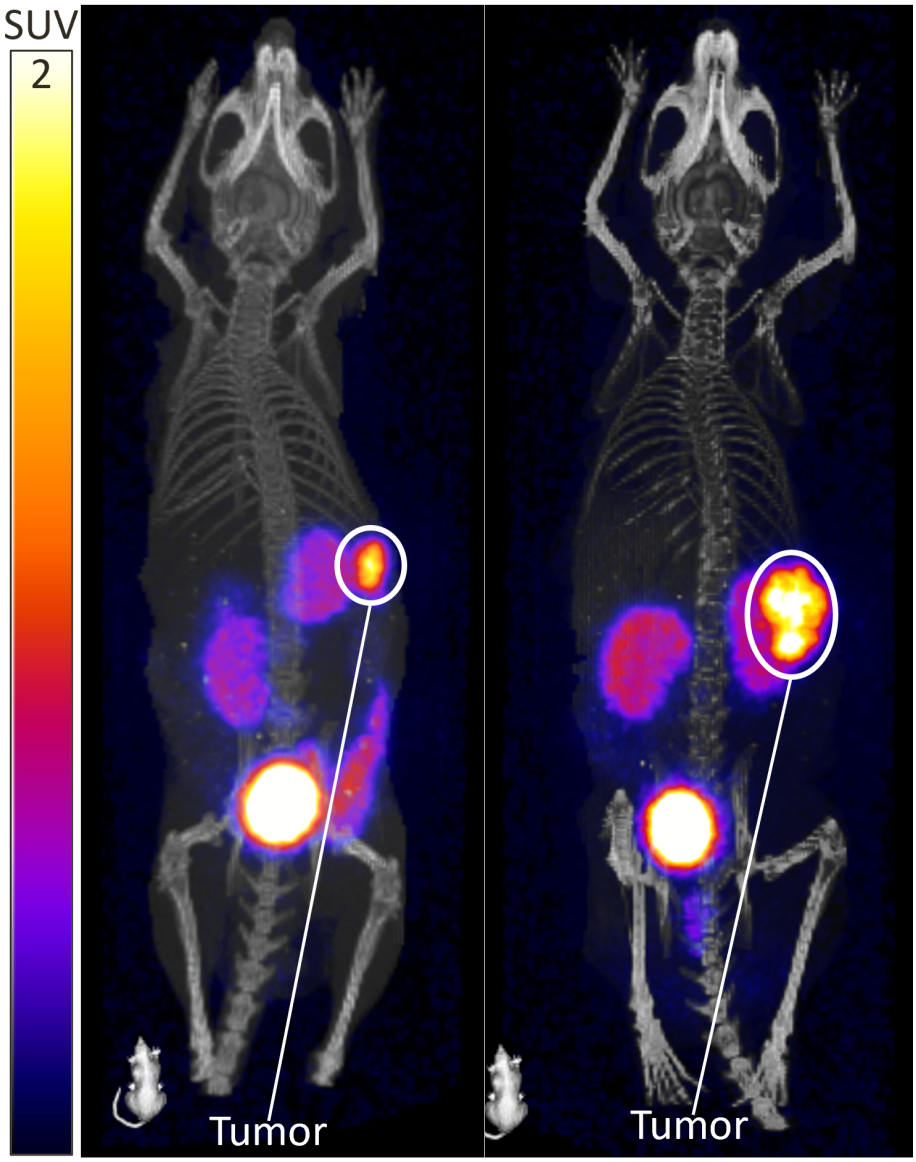

Figure 5.7: Static PET images of two LNCaP-EnzaR-Luc xenograft bearing mice injected with 5.15 MBq (left) and 5.21 MBq (right) of ^{43}Sc-PSMA-617 with a molar activity of 12.03 MBq/nmol. Images were acquired 4-hours post-injection This figure was adopted from Meier, et al. [176].

Tumor SUV was found to be 1.19 in the left image and 1.39 in the right image. By contrast, kidney SUV was found to be 0.38 in the left image and 0.5 in the right image. This suggests that, at the 4-hour time point, the specific uptake of ^{43}Sc-PSMA-617 is greater than the non-specific uptake of all tissues with the exception of the bladder. This is also

indicated visually by the detectability of the tumor in the right image in spite of it being superimposed on the right kidney. Naturally, this stands as a strong indicator of the tumor detection potential of ^{43}Sc-PSMA-617.

Examining a separate LNCaP-EnzaR-Luc bearing murine model, one can more broadly deduce the time dependence of the biodistribution of ^{43}Sc-PSMA-617 as is exhibited in the series of static PET images taken at 1, 2, 4, and 6 hours post injection as shown in Figure 5.8

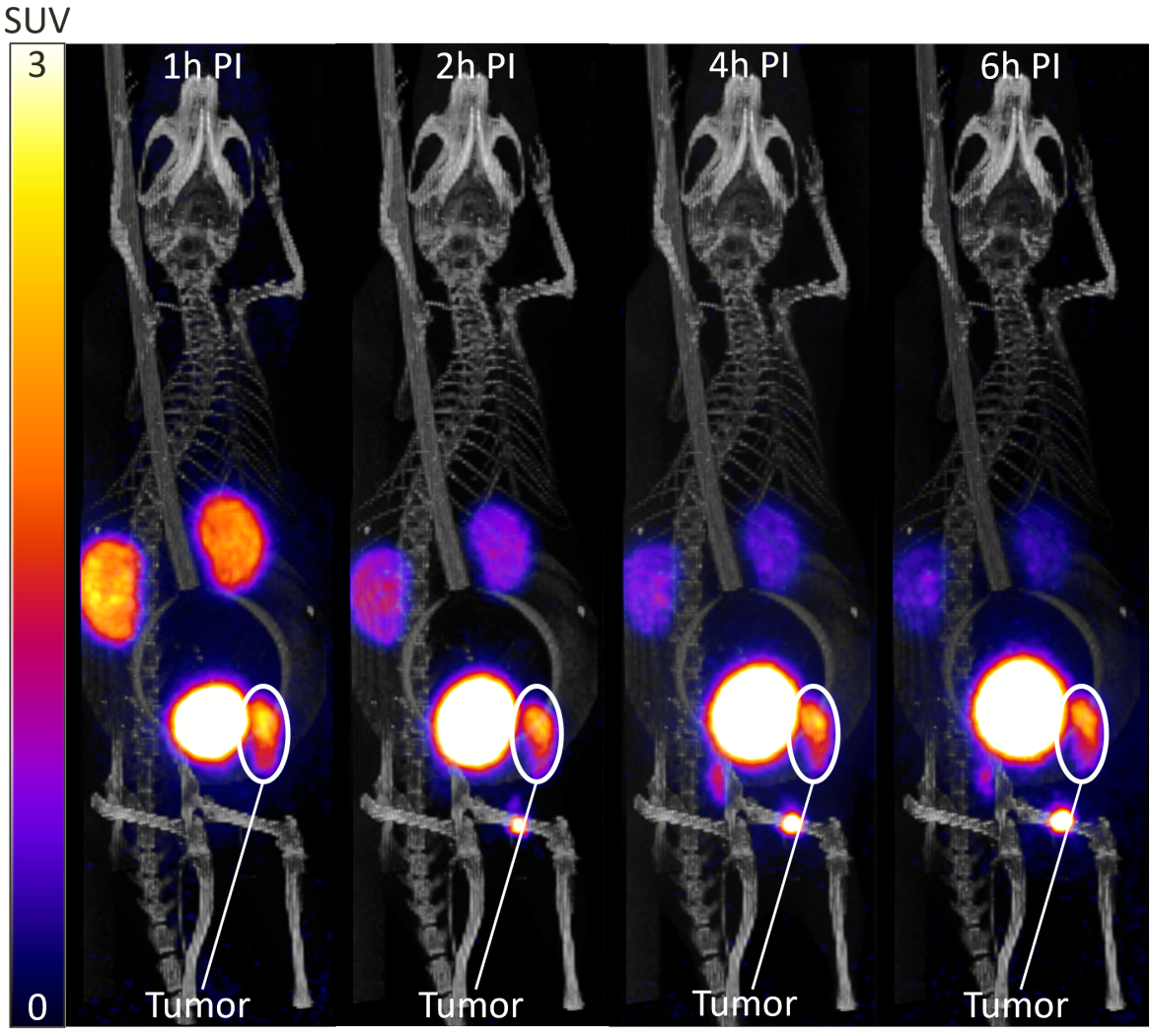

Figure 5.8: Decay corrected static PET/CT images of a LNCaP-EnzaR-Luc xenograft bearing murine model injected with 6.85 MBq of ^{43}Sc-PSMA-617 with a molar activity of 12.32 MBq/nmol. Images were acquired 1, 2, 4, and 6-hours post-injection

Through this imaging sequence, it becomes clear that ^{43}Sc-PSMA-617 is initially cleared into the kidneys (although there is some specific uptake as the renal medulla are slightly PSMA-expressing) and the PSMA-expressing tumor. Over time, however, the activity washes through the renal system into the bladder thus resulting in lower observed uptake in the kidneys with each progressing timepoint. Simultaneously, most uptake is retained in the PSMA-expressing tumor even at 6-hours post-injection.

Ultimately, this provides strong evidence for the hypothesized advantage of ^{43}Sc being capable of producing PET images at later time points relative to ^{68}Ga or ^{18}F. Simultaneously these images demonstrate the utility of imaging at later timepoints when there is a possibility of tumors or metastases near anatomic structures with background activity such as the renal system. Specifically, the tumor to kidney ratio was observed to increase from 0.72 at 1-hour post injection to 1.65 at 2-hours post injection, 2.69 at 4-hours post injection, and 3.82 at 6-hours post injection.

Scandium-43 Dynamic Imaging

The kinetics of ^{43}Sc-PSMA-617 can be further assessed through the dynamic PET imaging results presented in Figure 5.9 along with the corresponding SUV curves presented in Figure 5.10. As these images were acquired through dynamic imaging as opposed to static imaging, they provide a much more detailed characterization of ^{43}Sc-PSMA-617 biodistribution through the first two hours post-injection.

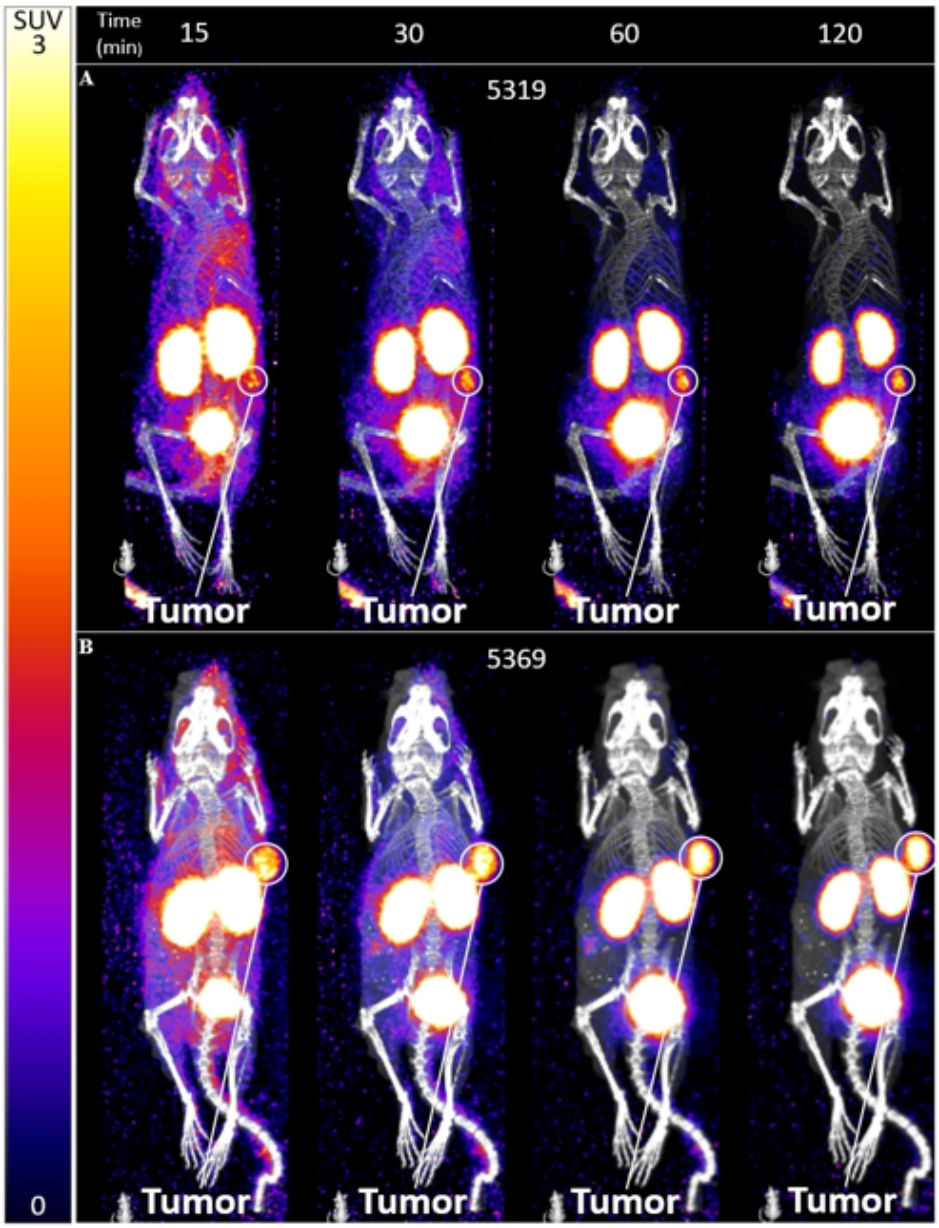

Figure 5.9: Dynamic PET/CT images of two LNCaP-EnzaR-Luc xenograft bearing mice injected with 4.28 (left) and 4.32 (right) MBq of ^{43}Sc-PSMA-617 with a molar activity of 8.94 MBq/nmol.

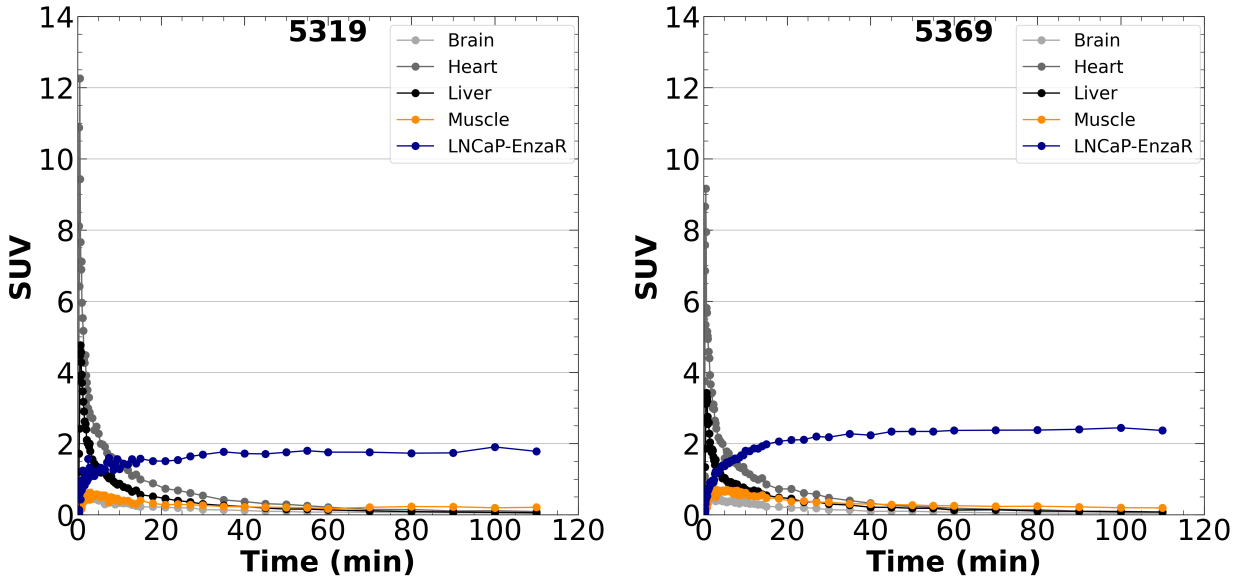

Figure 5.10: SUV curves derived from the dynamic PET imaging of two LNCaP-EnzaR-Luc xenograft bearing mice injected with 4.28 (left) and 4.32 (right) MBq of ^{43}Sc-PSMA-617 with a molar activity of 8.94 MBq/nmol. Organs with high non-specific uptake, such as the kidneys and bladder, were omitted from this curve to enhance legibility.

Although less pronounced since the scan duration was only two hours, ^{43}Sc-PSMA-617 rapidly accumulated in the kidneys and was gradually washed out into the bladder, as was observed in the multi-timepoint imaging results. Uptake in cardiac and hepatic tissue was initially very high, but this is expected for a tail vein injection as the injected radiopharmaceutical travels from the tail vein through the inferior vena cava to the heart with retrograde flow occurring in the hepatic veins [192]. As this initial "uptake" is primarily derivative of the physical delivery of the ^{43}Sc-PSMA-617, the observed activity rapidly decreased to match other background tissues (e.g. muscle) as the radiopharmaceutical dispersed into other tissues through the circulatory system. Although PSMA-617 is somewhat permeable to the blood brain barrier as was exhibited in Wei et al., brain uptake was negligible throughout the duration of the scan [193, 194].

Both mice exhibited tumor SUV values that exceeded all non-renal tissues by 9.5 minutes into the scan thus showing a high level of specificity towards PSMA expression. The mean

tumor to muscle SUV ratio from this point to the end duration of the scan was 6.47 in Mouse 5319 and 6.88 in Mouse 5369. The mean tumor SUV value for the entire scan length was 0.96 for Mouse 5319 and 1.10 for Mouse 5369, although these values are biased towards the beginning of the scan due to the higher sampling rate.

As exhibited in the SUV curve in Figure 5.11, when a similar experiment was repeated with a murine model bearing both a PSMA positive LNCaP-EnzaR-Luc xenograft and a PSMA negative DU145 xenograft, the overall pharmacokinetics of ^{43}Sc-PSMA-617 remained unchanged.

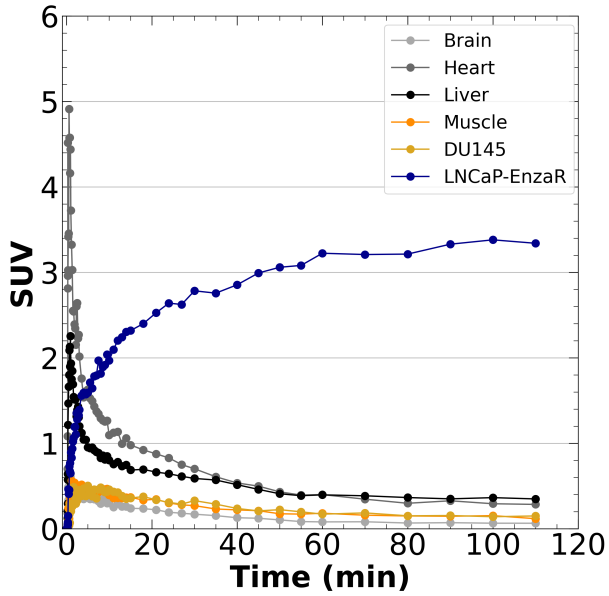

Figure 5.11: SUV curve derived from the dynamic PET imaging of an LNCaP-EnzaR-Luc and DU145 xenograft bearing murine model injected with 4.39 MBq of ^{43}Sc-PSMA-617 with a molar activity of 6.97 MBq/nmol. As high non-specific uptake organs, the kidneys and bladder were omitted from this curve to enhance legibility.

In this case, the LNCaP-EnzaR-LUC tumor maintained greater uptake than all other non-renal tissues by 5.5 minutes post-injection. The average tumor to muscle SUV ratio from this timepoint to the end of the scan was 10.45. The mean SUV value in the LNCaP-EnzaR-LUC tumor was found to be 1.35 when averaged through the entire duration of the scan. Conversely, the DU145 tumor exhibited virtually no uptake with a mean SUV value

of 0.232. The average ratio of LNCaP-EnzaR-LUC to DU145 SUV value was then 19.96 for the duration of the scan. Once again, this exemplifies that ^{43}Sc-PSMA-617 is highly specific to PSMA expression even in cancerous prostatic tissue.

Scandium-47 SPECT Imaging

The resulting ^{47}Sc-PSMA-617 SPECT images from the imaging of two LNCaP-EnzaR-Luc xenograft bearing mice at two hours post-injection with two separate molar activities are presented in Figure 5.12a (low molar activity) and Figure 5.12b (high molar activity).

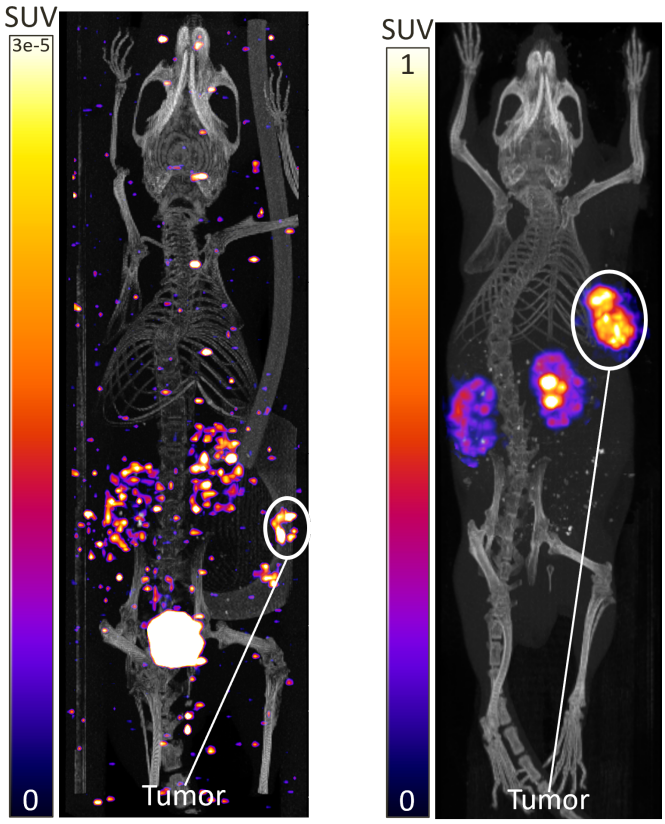

(a) MA = 0.95 Mbq/nmol

(b) MA = 8.06 Mbq/nmol

Figure 5.12: Static SPECT/CT images of two LNCaP-EnzaR-Luc xenograft bearing mice injected with 23.24 MBq (left) and 53.70 MBq (right) of ^{47}Sc-PSMA-617 with varying molar activity. This right hand portion of this figure was adopted from Meier, et al. [162].

While the tumor is partially resolvable in both of these images, they collectively make it exceedingly clear how critical molar activity is in the specificity of radioscandium PSMA-617 based radiopharmaceuticals. Beyond facilitating an improved depiction of tumor (and renal) morphology, the approximately 10-fold increase in molar activity resulted in an increase of maximum tumor SUV value of five orders of magnitude.

Scandium-43 PET and Scandium-47 SPECT Serial Imaging

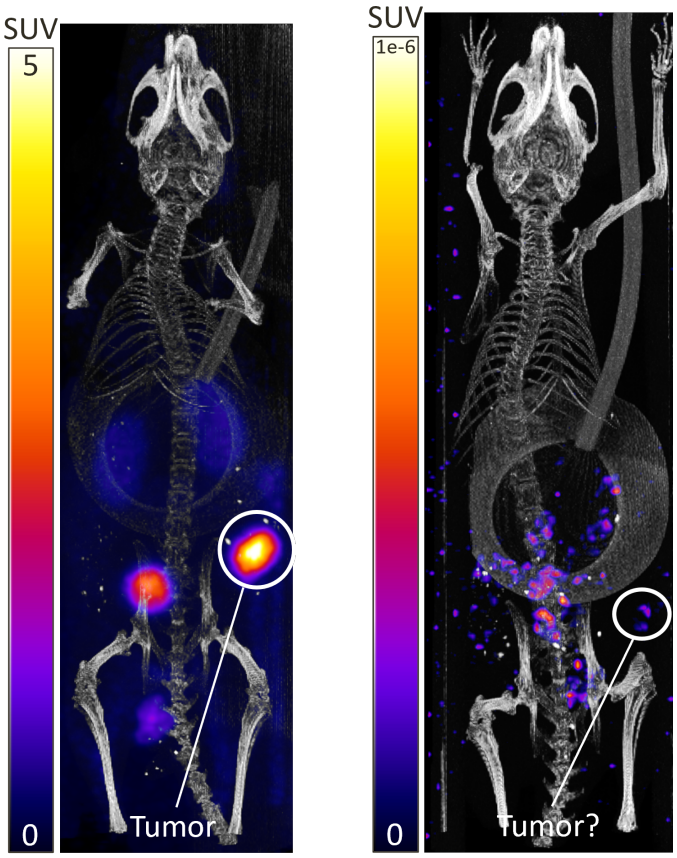

(a) ^{43}Sc (PET); MA = 17.24 MBq/nmol

(b) ^{47}Sc (SPECT); MA = 0.59 MBq/nmol

Figure 5.13: Static PET/CT and SPECT/CT images of a LNCaP-EnzaR-Luc xenograft bearing murine model injected with 5.86 MBq of ^{43}Sc-PSMA-617 and imaged with static PET (left) then injected with 28.53 MBq of ^{47}Sc-PSMA-617 four days afterwards and imaged with static SPECT (right).

Similar to the low molar activity SPECT image presented in the previous subsection, the dual imaging of two LNCaP-EnzaR-Luc xenograft bearing mice with both ^{43}Sc-PSMA-617 PET and ^{47}Sc-PSMA-617 SPECT, as presented in Figure 5.13 and Figure 5.14, facilitates a clear depiction of how molar activity influences radiopharmaceutical uptake in tumors and biodistribution in general. While the ^{43}Sc-PSMA-617 PET image shown in Figure 5.13a, clearly shows a PSMA expressing tumor on the right flank, the corresponding SPECT image shown in Figure 5.13b shows no meaningful uptake of ^{47}Sc-PSMA-617 within the same region. As such, the SPECT image shows no meaningful correlation to the PET image.

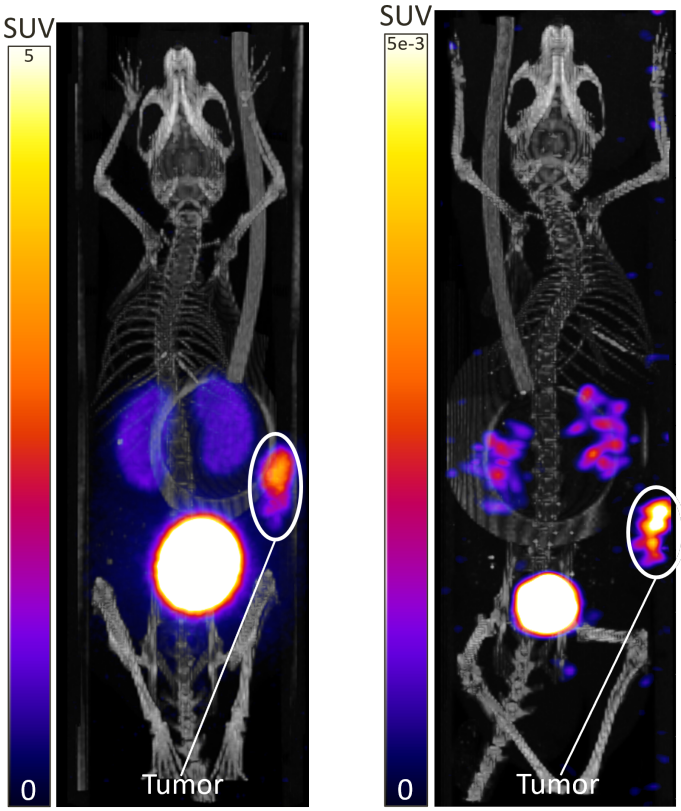

(a) ^{43}Sc; MA = 14.80 Mbq/nmol

(b) ^{47}Sc; MA = 7.40 Mbq/nmol

Figure 5.14: Static PET/CT and SPECT/CT images of a LNCaP-EnzaR-Luc xenograft bearing murine model injected with 81.03 MBq of ^{47}Sc-PSMA-617 and imaged with static SPECT (right) then injected with 5.56 MBq of ^{43}Sc-PSMA-617 one day later and imaged with static PET (left).

Conversely, in the second murine model which was imaged with an approximately 12.5 times greater molar activity of ^{47}Sc-PSMA-617, the tumor seen on the right flank with ^{43}Sc-PSMA-617 PET (Figure 5.14a) is also clearly resolved on ^{47}Sc-PSMA-617 SPECT (Figure 5.14b). Moreover, while it is not possible to fully register these two images as the change in mouse positioning resulted in significant changes in anatomical positioning, it is notable that both images seem to fully convey the complex morphology of the imaged tumor. Both images also exhibited similar tumor to kidney ratios with the PET image having a tumor to kidney ratio of 1.65, and the spect exhibiting a tumor to kidney ratio of 1.85.

5.3.3 Ex Vivo Biodistribution

Scandium-43

Ex vivo biodistribution results obtained from LNCaP-EnzaR-Luc bearing mice injected with ^{43}Sc-PSMA-617 are presented in Figure 5.15, Figure 5.16, and Figure 5.17.

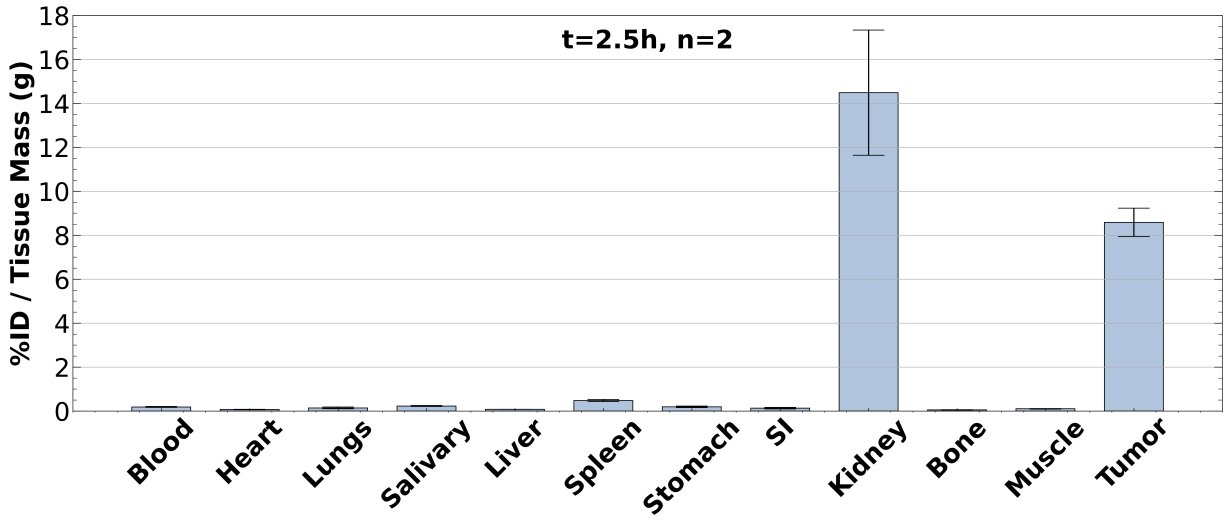

Figure 5.15: *Ex vivo* biodistribution corresponding to the mice shown in Figure 5.9 at 2.5 h post-injection.

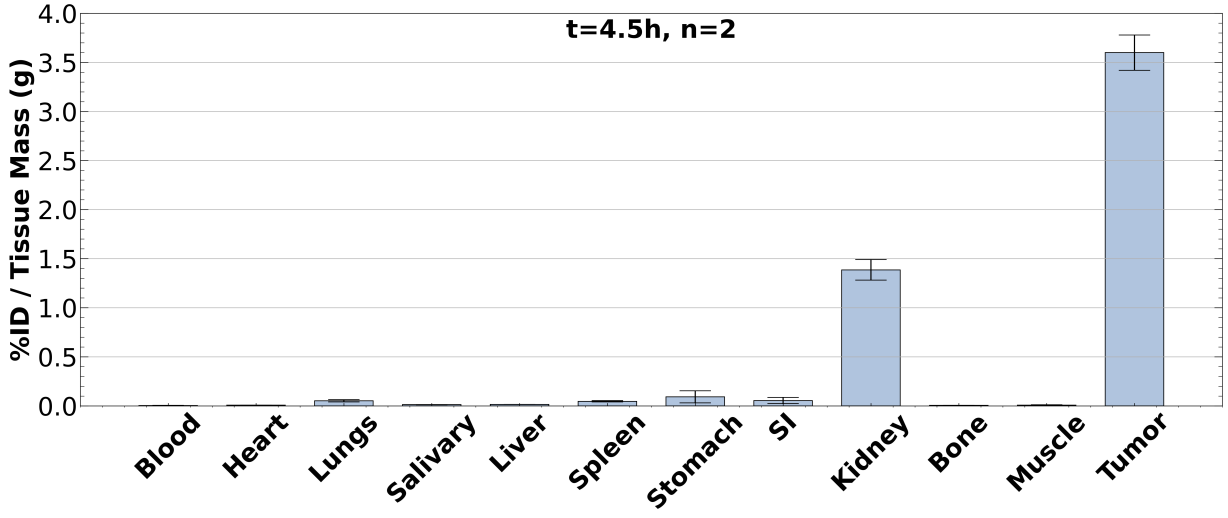

Figure 5.16: *Ex vivo* biodistribution corresponding to the mice shown in Figure 5.7 at 4.5 h post-injection.

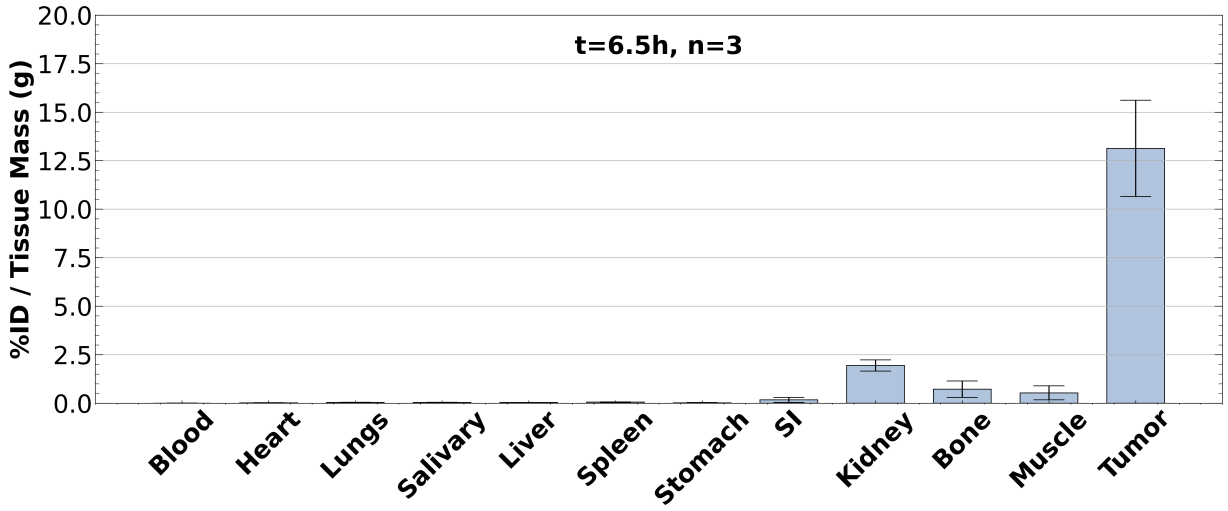

Figure 5.17: *Ex vivo* biodistribution corresponding to the mice shown in Figure 5.8 at 6.5 h post-injection.

Across these biodistributions, the mean tumor to kidney ratio of %ID/g was found to be 0.59, 2.60, and 6.76 at the 2.5, 4.5, and 6.5 hour timepoints respectively. In congruence with the images presented in the multi-timepoint and dynamic ^{43}Sc-PSMA-617 PET imaging experiments in the previous sections, these biodistributions indicate a gradual washout of non-specific uptake through the renal system while specific uptake is maintained within

PSMA positive tumors. This provides further credence to the hypothesis that the additional imaging timepoints afforded by the long half-life of ^{43}Sc could provide significant utility within the mCRPC space.

Moreover, these results were found to be within one order of magnitude of the biodistribution results presented in the literature for ^{68}Ga-PSMA-617 and ^{177}Lu-PSMA-617. Specifically, at the 2-hour timepoint, Duan et al. found the LNCaP tumor uptake of ^{68}Ga-PSMA-617 (molar activity: 6.16-7.0 MBq/nmol) to be 6.91 %ID/g and kidney uptake to be 3.57 %ID/g in comparison to the 8.58 and 14.48 %ID/g observed in this work [191]. At the 4-hour time-point, Tschan et al. found the uptake of ^{177}Lu-PSMA-617 (molar activity) to be 5.3 %ID/g in tumor and kidneys and 2.9 %ID/g relative to the 3.60 and 1.38 %ID/g observed in this work [190]. While the literature lacks of a biodistribution for these isotopes at 6-hours post-injection, the results presented here were within order of magnitude of the tumor to kidney ratio presented for the uptake of ^{177}Lu-PSMA-617 (molar activity: 100 MBq/nmol) 4-hours and 8-hours post-injection presented in Ruigrok et al. [195].

It is plausible that any variation in these results relative to those cited for ^{68}Ga-PSMA-617 and ^{177}Lu-PSMA-617 are the consequence of changes in PSMA binding affinity induced by the use of scandium in the radiopharmaceutical; however, it is more likely that these differences are the result of variance in animal models, injected activity amount, and molar activity.

Scandium-44

The *ex vivo* biodistribution results obtained from the LNCaP-EnzaR-Luc bearing mouse injected with ^{44}Sc-PSMA-617 at 4-hours post injection is presented in Figure 5.18. The resulting tumor to kidney ratio was found to be 1.16 which is approximately half of that observed with ^{43}Sc-PSMA-617 at 4-hours post-injection despite the higher molar activity.

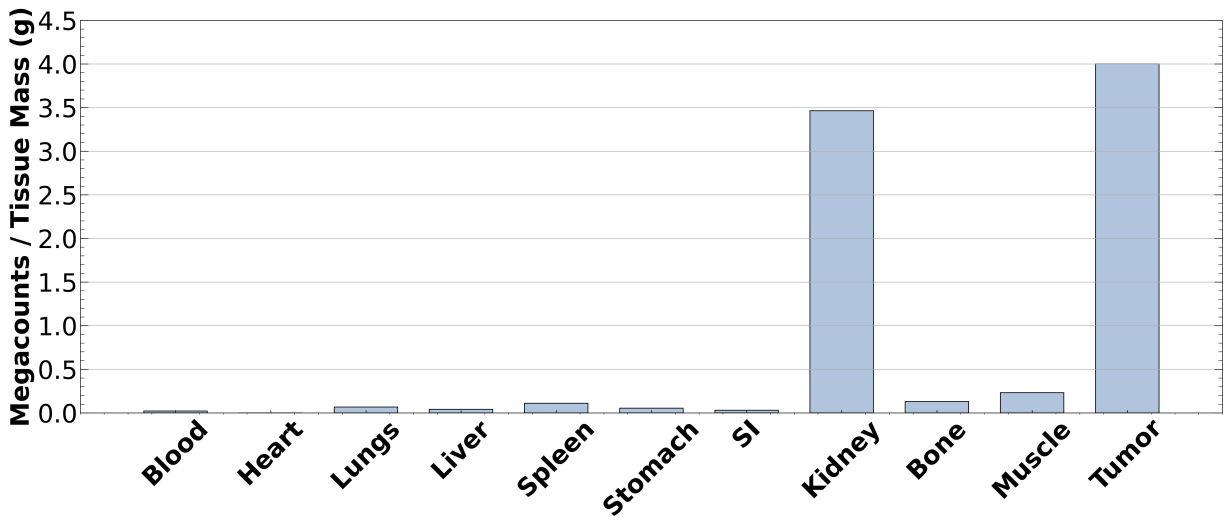

Figure 5.18: *Ex vivo* biodistribution corresponding to a LNCaP-EnzaR-LUC mouse injected with 9.55 MBq of ^{44}Sc-PSMA-617 at a molar activity of 28.8 MBq/nmol. Taken at 4 h post-injection.

5.3.4 Scandium-47 Radionuclide Therapy

As is shown in Figure 5.19, no notable difference was observed between the treatment and control groups under γ-H2Ax immunohistochemical staining thus indicating an absence of DNA DSBs from the administered dose of ^{47}Sc-PSMA-617. PSMA immunohistochemical staining also indicated no meaningful differences in PSMA expression between the treatment and control group thus indicating that the absence of a therapeutic effect was not a consequence of differences in tumor pathology. This result is consistent with the analysis of radiobiological effect with ^{177}Lu-PSMA-617 conducted by Fendler et al. in which DNA DSBs were not observed until molar activities of at least 31 MBq/nmol [181]. As such, this result is not a reflection of poor radiobiological effectiveness; rather, this result is a clear indication of the need for improved accelerator production and radiopharmaceutical purification methods (e.g., to separate the unlabeled PSMA-617 precursor) in order to produce doses of ^{47}Sc-PSMA-617 with therapeutically meaningful molar activity.

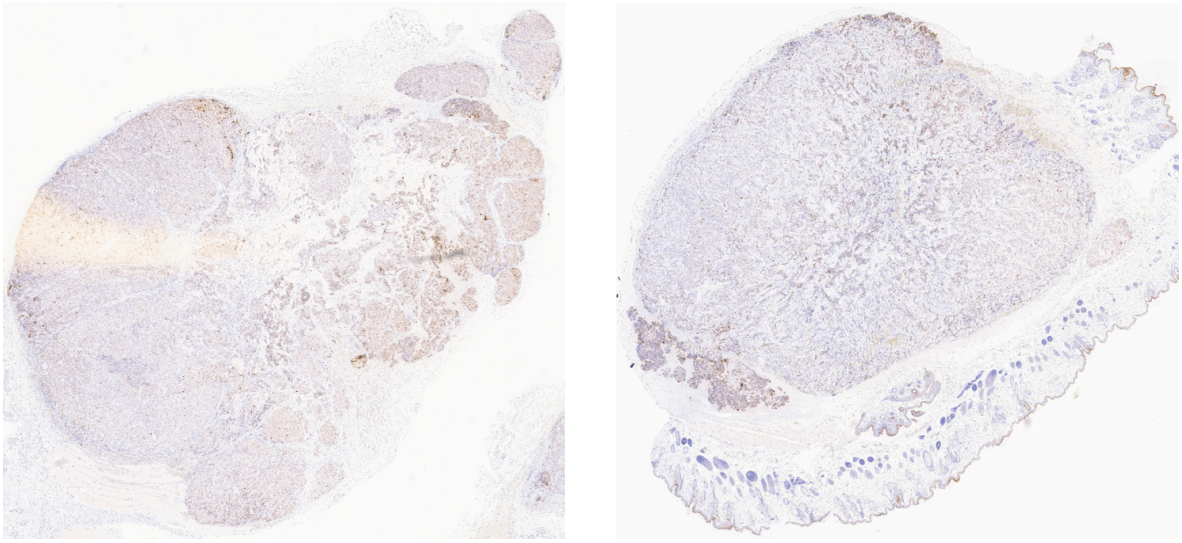

(a) Control (b) ID= 23.3 MBq; MA = 0.93 MBq/nmol

Figure 5.19: LNCaP-EnzaR-LUC tumor cross-sections stained with the γ-H2AX antibody and imaged with a 20x digital microscope. The left image corresponds to an excised tumor from a mouse which was not administered any activity, and the right image corresponds to an excised tumor obtained from a mouse that was injected with 23.3 MBq of ^{47}Sc-PSMA-617 at a molar activity of 0.93 MBq/nmol.

This experiment is currently being repeated with 5 additional pairs of mice that were injected with similar doses of ^{47}Sc-PSMA-617 (molar activity: 0.59-0.95 MBq/nmol) to ensure statistical significance of this result. One additional study is also being conducted with a ^{47}Sc-PSMA-617 injection of 7.4 MBq/nmol (the animal shown in Figure 5.14). Although these results will not be fully prepared by the conclusion of this work, we still do not anticipate any meaningful induction of DNA DSBs at this molar activity based upon the literature.

5.4 Discussion

In vitro uptake and blocking studies conducted with ^{43}Sc-PSMA-617 and ^{47}Sc-PSMA-617 exhibited greater uptake and successful competitive blocking with the addition of unlabeled PSMA-617 in PSMA-expressing parental LNCaP or LNCaP-EnzaR-Luc cells relative to non-

PMSA expressing DU145 cells. This indicates a clear specificity of radioscandium PSMA-617 towards PSMA, although ^{43}Sc-PSMA-617 exhibited a higher level of specificity relative to ^{47}Sc-PSMA-617 likely as a result of its superior molar activity. Internalization was shown to range from approximately 45%-60% for both cell lines thus providing context for the cellular simulations discussed in the next chapter with regards to the intracellular localization of radioscandium pharmaceuticals.

In vivo multi-timepoint static and dynamic PET imaging obtained with ^{43}Sc-PSMA-617 facilitated a broad characterization of the pharmacokinetics of radioscandium PSMA-617. Notably, both studies showed a gradual washout of non-specific uptake in the kidneys as time progressed post-injection whilst specific uptake in PSMA-expressing tumors was maintained. This observation provides evidence for the hypothesized benefits of long time-point imaging in mCRPC that can be provided by ^{43}Sc-PSMA-617 as a consequence of its approximately 4 h half-life. These results were corroborated by the ^{43}Sc-PSMA-617 *ex vivo* biodistribution data obtained at 2.5, 4.5, and 6.5-hour time points as they exhibited mean tumor to kidney ratios that increased from 0.59, to 2.60, and finally to 6.76 with each respective timepoint. Similar biodistribution data was observed at the 4-hour timepoint for ^{44}Sc-PSMA-617. Through the dynamic scan, it was also observed that PSMA positive tumor uptake exceeded uptake in all non-renal tissues in as little as 9.5 minutes thus indicating that PSMA positive tumors should be detectable with ^{43}Sc-PSMA-617 PET even at early timepoints.

Within the additional dynamic scan that was conducted with a murine model bearing both a PSMA positive and PSMA negative tumor, no notable difference in kinetic was observed relative to the two dynamic scans taken in mice bearing only PSMA positive tumors. No uptake was observed within the non-PSMA expressing DU145 tumor thus providing further evidence of the specificity of ^{43}Sc-PSMA-617.

While ^{43}Sc-PSMA-617 PET imaging was shown to consistently delineate PSMA-expressing tumors, the detection of LNCaP-EnzaR-Luc tumors with ^{47}Sc-PSMA-617 SPECT was in-

consistent as a consequence of its variable molar activity. In that sense, the difference in image clarity exhibited by the side-by-side SPECT images shown with an order of magnitude difference in molar activity provide evidence for the importance of molar activity in image accuracy.

A similar disparity in imaging results was observed in the multi-modality imaging of LNCaP-EnzaR-Luc bearing mice with ^{43}Sc-PSMA-617 PET and ^{47}Sc-PSMA-617 SPECT of low and moderate molar activity. Within this framework, the ^{47}Sc-PSMA-617 SPECT image obtained at a molar activity of 0.59 MBq/nmol was essentially unreadable; however the ^{47}Sc-PSMA-617 SPECT image obtained at 7.40 MBq/nmol actually exhibited the same tumor morphology shown on the much higher-resolution ^{43}Sc-PSMA-617 PET scan. This was also significant as, to our knowledge, this was the first example of dual modality imaging conducted with the radioscandiums in a single murine model.

Unfortunately, as a result of the limited availability of ^{47}Sc at the time of this study, all multi-modality imaging experiments were conducted with the ^{43}Sc-PMSA-617 PET and ^{47}Sc-PSMA-617 SPECT occurring at different time points with injections being 1-4 days apart as opposed to co-injecting both radiopharmaceuticals and sequentially imaging with PET and SPECT. As such, it was not possible to preserve the anatomic positioning of the animal for image co-registration thus limiting the scope of the multi-modality study.

Similarly, while the PET performance of the MOLECUBES β-CUBE has been rigorously characterized in Krishnamoorthy et al., no such characterization has been performed with MOLECUBES γ-CUBE SPECT system [196]. As such, it is uncertain if their system is well suited for quantitative SPECT applications as would be required for the development of predictive dosimetry through these multi-modality experiments.

An attempt to characterize the therapeutic efficacy of ^{47}Sc-PSMA-617 was also made through the application of γ-H2AX and PSMA immunohistochemistry to an excised LNCaP-EnzaR-Luc tumor in a murine model injected with ^{47}Sc-PSMA-617; however no meaningful

difference was observed between the treatment and control groups. This result is more than likely a consequence of the low molar activity of ^{47}Sc-PSMA-617. Within the context of the literature, it would appear that an approximately 5 to 10 times increase in molar activity will be required before the biological effect of ^{47}Sc-PSMA-617 can be measured in any meaningful way.

5.5 Conclusion

This chapter presented a multitude of *in vitro*, *in vivo*, and *ex vivo* experiments which were conducted with ^{43}Sc-PSMA-617, ^{44}Sc-PSMA-617, and ^{47}Sc-PSMA-617 to exemplify the specificity and diagnostic capabilities of the radioscandiums. Cellular uptake and blocking assay results exhibited the specificity of radioscandium PSMA-617 to PSMA expression. Static and dynamic PET imaging and *ex vivo* biodistribution conducted with ^{43}Sc-PSMA-617 exhibited the time-dependent washout of non-specific uptake through the renal system and the sustained specific uptake in PSMA expressing tissues therefore providing proof-of-concept of the extended timepoint imaging feasible with the relatively longer half-life of ^{43}Sc (3.89 h). A single biodistribution study was also conducted with ^{44}Sc-PSMA-617 showing similar results to that observed with ^{43}Sc-PSMA-617. Static ^{47}Sc-PSMA-617 SPECT images conducted at low and moderate molar activity demonstrated the need for improved production and/or radiopharmaceutical purification methods in the synthesis of ^{47}Sc-PSMA-617, a notion which was compounded by the null result obtained in the γ-H2AX immunohistochemical analysis of tumors treated with ^{47}Sc-PSMA-617. Most critically, single animal, dual modality imaging was conducted with ^{43}Sc-PSMA-617 PET and ^{47}Sc-PSMA-617 SPECT for the first time, exhibiting tumor detection and a congruent depiction of tumor morphology across both modalities.

The overwhelming majority of these experiments clearly focused on ^{43}Sc-PSMA-617. This is because, although several shipments of ^{47}Sc were provided by Argonne National

Laboratory and the University of Alabama Birmingham during the course of this work, in addition to the singular ^{47}Sc production described in Chapter 3, many of the *in vitro* and *in vivo* aspects of this work have been limited by the availability and producibility of ^{47}Sc making it difficult to directly probe the pharmacokinetics, diagnostic, and therapeutic properties of ^{47}Sc-PSMA-617. While this has undoubtedly limited the direct scope of this work with regards to pre-clinical evaluation, one of the novel benefits of evaluating a true theranostic pair is that the experimental results obtained from the other more easily produced forms of radioscandium PSMA-617 can still provide valuable information about ^{47}Sc-PSMA-617. Under this lens, the imaging capabilities and pharmacokinetic characterization of ^{43}Sc-PSMA-617 presented throughout this chapter presents ^{47}Sc-PSMA-617 as a highly promising isotope for SPECT imaging and targeted radionuclide therapy once readily producible with molar activity on par with other therapeutic radiopharmaceuticals.

CHAPTER 6

DOSIMETRIC AND RADIOBIOLOGICAL CHARACTERIZATION OF RADIOSCANDIUMS WITH TOPAS

6.1 Introduction

With the renaissance of nuclear medicine theranostics being a major facet in the development of true precision medicine, the necessity of evaluating the dosimetry and radiation physics of individual isotopes with an immensely precise control of systemic variables has become increasingly clear. Even more so, there has been an increased interest in evaluating the physical and biological interactions of radiopharmaceuticals at the subcellular scale, a level of precision which is beyond current experimental methods. As the emission and interactions of radiative particles with matter are stochastic processes, the random sampling methodology employed by Monte Carlo simulation methods is optimal for evaluating these otherwise unmeasurable parameters [197].

The application of Monte Carlo simulations to the nuclear medicine space poses to be an immensely valuable tool for radionuclide selection in radiopharmaceutical development as dosimetry and biological effect can be probed prior to the time-consuming and costly development of production methods, radiochemistry, or pre-clinical evaluation [198, 199]. Within this space, Monte Carlo can also prove useful for the contextualization and validation of experimental results, or contrasting the effectiveness of radionuclides in a vacuum by removing other experimental barriers such as molar activity or activity amount.

In this context, this chapter details the use of the Monte Carlo program TOol for PArticle Simulation (TOPAS) to investigate how the physical decay characteristics of the radioscandiums can influence dosimetry and radiobiology, particularly with reference to their clinically used analogues ^{68}Ga and ^{177}Lu. TOPAS serves as a wrapper for the more commonly known particle simulation toolkit, Geant4, improving its accessibility and ease of use within the con-

text of medical physics and, by extension, nuclear medicine [200]. This is particularly true when the capabilities of TOPAS are expanded with TOPAS-nBio, an extension for TOPAS which adds additional functionality for radiobiology including the modeling of cellular structure, radiochemical processes, and both DNA damage and repair mechanisms [201].

Specifically, TOPAS was utilized to characterize the energy deposition of ^{43}Sc, ^{44}Sc, ^{47}Sc, ^{68}Ga, and ^{177}Lu both within a large spherical water phantom and in various intracellular locations of a simple cellular geometry. TOPAS-nBio was utilized to evaluate the DNA damage induced by each of these radionuclides at various intracellular locations in a cellular geometry with a complete nuclear model. The motivation and significance of each of these simulations is detailed below.

6.1.1 Radially-Varying Radiation Dosimetry

Within the field of external beam radiation therapy, Monte Carlo has been a long-standing dosimetry tool for the validation of numerical and experimental dose estimation methods. While Monte Carlo methods are not typically used clinically due to their high computational cost, Monte Carlo is considered a highly valuable tool for dose characterization as it is able to precisely track the individual interactions of particles as they transcend a medium [202, 203]. This facilitates the generation of nuanced dosimetric information which accurately models the influence of radiation physics on dose distribution, especially in complex geometries such as at the interface of different media types [199].

While the complex interplay of radiation physics, biological geometry, dosimetry, and other involved factors is not exclusive to radiation oncology where these methods have historically been utilized, the generation and assessment of dosimetric curves within nuclear medicine is still somewhat underutilized. This is likely in part due to the fact that there are additional dependencies unique to internal radiation dosimetry such as pharmacokinetics and biological half-life [202]. However, the evaluation of the dosimetric profile of radionuclides

independent of those biological factors can still provide critical information for radionuclide selection especially when multiple radionuclides are compatible with a single targeting ligand, as is the case with PSMA-617.

Therefore, as an analogue to the percent depth dose curves utilized in both clinical and pre-clinical external beam radiation therapy, we have utilized TOPAS Monte Carlo to measure radionuclidic energy deposition within a spherical water phantom as a function of radial distance from an isotropic source at the center of the phantom. These simulations have enabled the creation of energy deposition curves which characterize how the individual decay physics of these radioisotopes influence their dosimetric properties as radiopharmaceuticals, encompassing both micro and macro scales. As the localization of the energy deposited by radiopharmaceuticals directly relates to efficacy in target tissues, toxicity in non-target tissues, and potential concerns of radiation safety with regards to hospital staff and the general public, is is our hope that the proposed energy deposition curves help inform what radioscandium pharmaceuticals are best suited to the clinical space.

6.1.2 Cellular S-Values

The cellular S-value formalism was proposed by Goddu et al. in 1994 as an extension to the Society of Nuclear Medicine's and Molecular Imaging's Medical Internal Radiation Dose (MIRD) Committee's approach to calculating the mean dose absorbed by organs and bulk tumors from administered radiopharmaceuticals [204]. Goddu postulated that, when assessing the efficacy of radiopharmaceuticals, it was more relevant to examine the dose absorbed by individual cells given that radiopharmaceuticals both concentrate in cellular compartments and often emit ionizing radiations with ranges on the cellular scale [204]. As such, to evaluate cellular dosimetry, the cell is modeled as the primary cellular compartments associated with varying levels of radiopharmaceutical accumulation (uptake, internalization, and nuclear localization) as well as those associated with meaningful radiosensitivity: nucleus,

cytoplasm, cell-surface, and whole cell. These cellular compartments then serve as source and target regions for the calculation of radiopharmaceutical induced radiation dose.

Within this schema, the dose ($\bar{D}$) in a target cellular compartment (R_T) from a source cellular compartment (R_S) is described in Equation 6.1 below where the S-value (S) describes the dose per unit of cumulated activity in a target cellular compartment and acts as a source location, target location, and radioisotope dependent coefficient which appropriately correlates dose to the accumulation of radioactivity in a source compartment (described by the integral of $A(t)$) during the time interval between t_1 and t_2 [204–206].

$$\bar{D} = S(R_T \leftarrow R_S) \int_{t1}^{t2} A(t)dt \tag{6.1}$$

By extension the cellular S-value is described in Equation 6.2 where n_i is the yield of radiation type i per decay, E_i is the energy of radiation type i, ϕ_i is the fraction of the radiative energy originating from the radiation of type i in the source compartment which is absorbed by the target cellular compartment, and m_T is that mass of the target compartment [204–206].

$$S(T \leftarrow S) = \sum_{i=1}^{n} \frac{n_i E_i \phi_i (R_T \leftarrow R_S)}{m_T} \tag{6.2}$$

This concept was quickly adapted by the Committee on MIRD in 1994, and eventually developed into MIRDcell, an open-source dosimetry tool designed for the calculation of cellular dosimetry in multiple configurations [205, 207]. While the MIRDcell toolkit and the compendium of S-values published by MIRD are immensely useful for assessing the dosimetry of commonly utilized or studied isotopes, they do not cover the entire breadth of radioisotope development. Notably, at the time of this thesis, there are not any published S-values for the positron-emitting radioscandiums, ^{43}Sc and ^{44}Sc, nor are they directly calculable in the MIRDcell software.

Additionally, MIRDcell does not account for the complete spectrum of radionuclidic emis-

sions, notably omitting some low energy interactions, such as those from Auger electrons, in its calculation of S-values ultimately yielding discrepancies as high as 50% with more comprehensive Monte Carlo derived S-values [208, 209]. Therefore, S-values calculated with Monte Carlo methods which explicitly simulate all radioactive decay particles and the subsequent interactions of decay radiation with cellular material should exhibit greater accuracy than those generated with the MIRDcell software.

6.1.3 DNA Double Strand Breaks

As described in Section 2.1.4, the creation of DNA double strand breaks (DSBs) through the direct interaction of ionizing radiation or radiation induced free radicals with the DNA double helix is the primary mechanism which induces cancer cell death in targeted radionuclide therapy. Quantifying the number of DSBs induced by different radionuclides can therefore provide highly valuable information regarding radiobiological effect and provide a point of contrast between novel and established radiopharmaceuticals [210]. As was seen in Chapter 5, this type of therapeutic evaluation is not always feasible in the early phases of radiopharmaceutical development as the refinement of production and chemical methodologies can lag behind the demands of *in vitro* and *in vivo* studies.

Within these scenarios, the application of Monte Carlo methods can provide a means of probing therapeutic efficacy prior to making time-consuming investments into the other aspects of radiopharmaceutical development thus streamlining radioisotope evaluation and selection. Even in cases where experimental evaluation is plausible, the controlled placement of radioactive sources, and the subcellular scales at which biological effect can be scored at, facilitate a precision assay of microdosimetry and radiobiological effect which would otherwise be impossible outside of a simulation space [211]. Beyond the comparison of radioisotopes, this precise level of control also enables the evaluation of other aspects of radiopharmaceutical selection which are difficult to validate experimentally such as how intracellular localization

influences biological effect [209, 212].

Based on these applications, we have utilized TOPAS Monte Carlo to measure the induction of DNA DSBs in a modeled nucleus with the radioactive source being distributed throughout various intracellular locations akin to this described in the previous section. This analysis of DNA DSBs through TOPAS has facilitated an additional perspective on the therapeutic efficacy of ^{47}Sc, a necessity given the limitations associated with producing a therapeutic dose of ^{47}Sc-PSMA-617 using the current methodology of the nuclear production and radiosynthesis. Moreover, these simulations have also facilitated a direct comparison to the biological effect of ^{177}Lu as such a comparison was not experimentally feasible in this work given that the majority of the pre-clinical aspects took place during the PLUVICTO shortage. The DNA damage induced by the diagnostic radioscandiums and ^{68}Ga was also investigated for completeness.

6.2 Methods

6.2.1 Radially-Varying Radiation Dosimetry

In order to probe the energy deposition profiles of the decay of ^{43}Sc, ^{44}Sc, ^{47}Sc, ^{68}Ga, and ^{177}Lu, a simulation was constructed in which an isotropic radioactive source was placed at the center of a water-filled sphere with a radius of 100 cm. This sphere was nested in a water filled cube with side lengths of 210 cm to ensure that the resultant energy deposition curves were purely characteristic of the decay schema of each isotope and not the result of particle scattering effects which occur at the interface between two heterogeneous media [213–215]. Each individual radioisotope underwent 10,000 decays (histories) and the total energy deposition within the sphere was scored in 10,000 radial compartments each with a radius of 0.01 cm, or roughly 10 mammalian cell diameters. Each of these simulations were repeated across 10 unique seeds and then presented as a mean of those results. The geometry

of this simulation, including the hemisphere approximation described later in this section, is illustrated in Figure 6.1a.

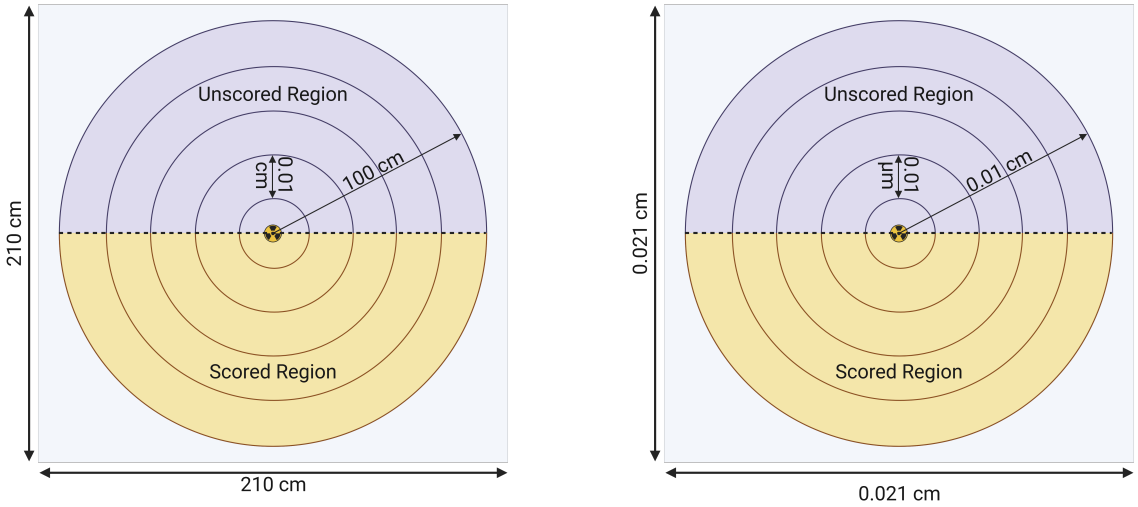

(a) Macroscale (b) Microscale

Figure 6.1: A graphical representation of the geometry of the simulation of energy deposited in radial bins including the hemisphere approximation in which only half of the sphere is scored to reduce computational demand [216, 217].

Prior to use with the radioscandiums, these simulation parameters were tested for congruence with the radially-varying radiation dosimetry simulations of ^{67}Cu, ^{131}I, ^{90}Y, ^{177}Lu, ^{166}Ho, and ^{186}Re described in Merrick et al, and were found to be in complete agreement. [218].

As the previously described simulation geometry has a bin size of 0.01 cm, it is unable to characterize any fluctuations in energy deposition across smaller distances than that sampling size. This is most notable in the region spanning from 0 to 0.01 cm which is dominated by positron and electron interactions. This region also best reflects the cellular biological scale which is of heightened importance due to the highly specific cell targeting nature of targeted radionuclide therapy. Quantifying the amount of energy deposited within that cellular scale is therefore critical as it enables the probing of how effectively an isotope

might be at delivering dose when successfully uptaken or internalized by target expressing cells [219, 220]. Moreover, by producing a curve exhibiting the range of energy transfer, one can deduce whether an isotope is better suited towards applications in ligands which are specific to heterogeneously or homogeneously expressed targets [94, 221, 222]. As such, the previously described simulation was repeated at a smaller scale with a sphere radius of 0.01 cm in radius, a cube with side length of 0.021 cm, and a radial bin width of 10 nm. This geometry is represented in Figure 6.1b. Just as in the large-scale implementation, each simulation consisted of 10,000 histories and was averaged over 10 different seeds.

Both of these macro and microscale radially-varying radiation dose simulations were analyzed through four separate interpretations of the energy being deposited within each bin. The first of these interpretations was to simply look at the energy deposited within each radial bin thus quantifying raw energy deposition as a function of radial distance from the origin of radioactivity. As presented in Equation 6.3, the energy at any radial (x) position within the plot is simply the energy deposited in the ith bin normalized by the total number of decays (N). The simulated data was then examined by looking at the cumulative energy deposited as the radial axis of the spherical phantom is traversed. This is represented as the summation of the energy per decay deposited from radial bin $i = 1$ to $i = k$ as is shown in Equation 6.4. Next, an interpretation analogueous to percent depth dose (PDD) curves was made by normalizing the energy deposited within each bin by the maximum energy deposited in a single bin. The formula for these percent depth energy or "PDE" curves is presented in Equation 6.5. Finally, the sum of the energy deposited from radial bin $i = 1$ to $i = k$ was normalized by the total energy deposited throughout the entire sphere as is exhibited in Equation 6.6.

$$E_i' = \frac{1}{N} E_i(x) \tag{6.3}$$

$$E'_k = \frac{1}{N}\sum_{i=1}^{k} E_i(x) \tag{6.4}$$

$$PDE_i = \frac{E_i(x)}{E_{Max}} \tag{6.5}$$

$$E_k = \frac{\sum_{i=1}^{k} E_i(x)}{\sum_{i=1}^{K} E_i(x)} = \frac{1}{E_{Tot}}\sum_{i=1}^{k} E_i(x) \tag{6.6}$$

Partial Volume Approximation

Because these simulations entail an immense number of particle interactions being tabulated within a large number of energy scoring bins, they are highly computationally expensive. As such, it was necessary to develop approximation methods to minimize computation time without sacrificing quantitative accuracy. The simplest method of truncating the necessary number of computations was to calculate the energy deposited over only a fraction of the spherical phantom by limiting the range of the spherical polar and azimuthal angles scored, then extrapolating the calculated energy deposition over the entire volume. This reduces computation time by reducing the volume over which the energy deposition of individual particle interactions must be tracked.

As such, the macroscale simulation described in the previous paragraphs was repeated with fractional volumetric scoring of 1/16, 1/8, 1/4, and 1/2 of the spherical phantom's total volume with all simulations utilizing the same seed in order to eliminate any potential inconsistencies between each simulation run. The ranges of polar and azimuthal angles utilized to generate the partial volume scorer are presented in Table 6.1.

Fractional Volume	θ Range	ϕ Range
1/1	$0 \leq \theta \leq 2\pi$	$0 \leq \phi \leq \pi$

$1/2$	$0 \leq \theta \leq 2\pi$	$0 \leq \phi \leq \pi/2$
$1/4$	$0 \leq \theta \leq \pi$	$0 \leq \phi \leq \pi/2$
$1/8$	$0 \leq \theta \leq \pi$	$0 \leq \phi \leq \pi/4$
$1/16$	$0 \leq \theta \leq \pi/2$	$0 \leq \phi \leq \pi/4$

Table 6.1: The range of polar and azimuthal angles utilized to generate the partial spherical volume of the energy deposition scorer according to the volumetric integral of a spherical object ($V = \iiint p^2 sin(\phi)\ dp\ d\theta\ d\phi$).

The extrapolated energy deposition curve generated for each of these partial spheres was calculated and compared to the same curves generated for a full volume sphere using Equation 6.3. These curves are presented by isotope in Figure 6.2.

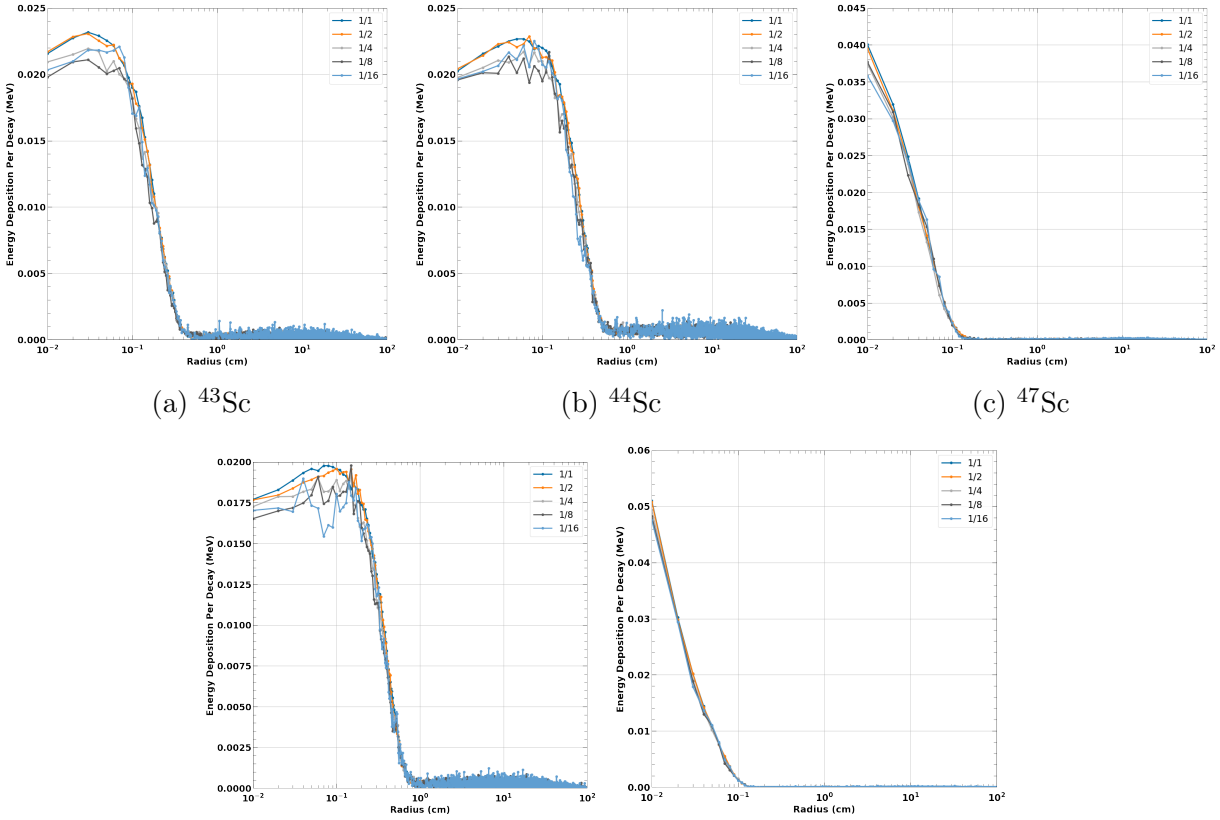

(a) ^{43}Sc (b) ^{44}Sc (c) ^{47}Sc

(d) ^{68}Ga (e) ^{177}Lu

Figure 6.2: Energy deposition in radially scored bins of various fractional spheres of water with r = 100 cm.

When treating the scoring of the entire sphere as ground-truth, it became clear that these simulations diminished in accuracy as less of the sphere is scored, particularly in the range of tortuous positron interactions from 0.01 to 0.5 cm in simulations of the positron-emitting ^{43}Sc, ^{44}Sc, and ^{68}Ga. However, it was difficult to quantify the variation between these curves when exclusively examining the energy deposited within each bin. This is because the small bin size results in highly variable energy deposition from bin to bin, particularly in the tail region where photon interactions dominate as they, unlike electrons, are not continually interacting.

In order to minimize the wrongful attribution of stochastic variances in particle interactions to errors introduced by a reduction in scoring volume, the energy deposited within

each bin was also summed along the radial compartment as described in Equation 6.4. The resultant summed energy deposition curves are thus presented in Figure 6.3. Through this summation representation, it becomes increasingly clear that the hemisphere scoring most accurately approximates the scoring over the entire sphere as expected, with a small drop in accuracy when choosing a smaller scoring volume.

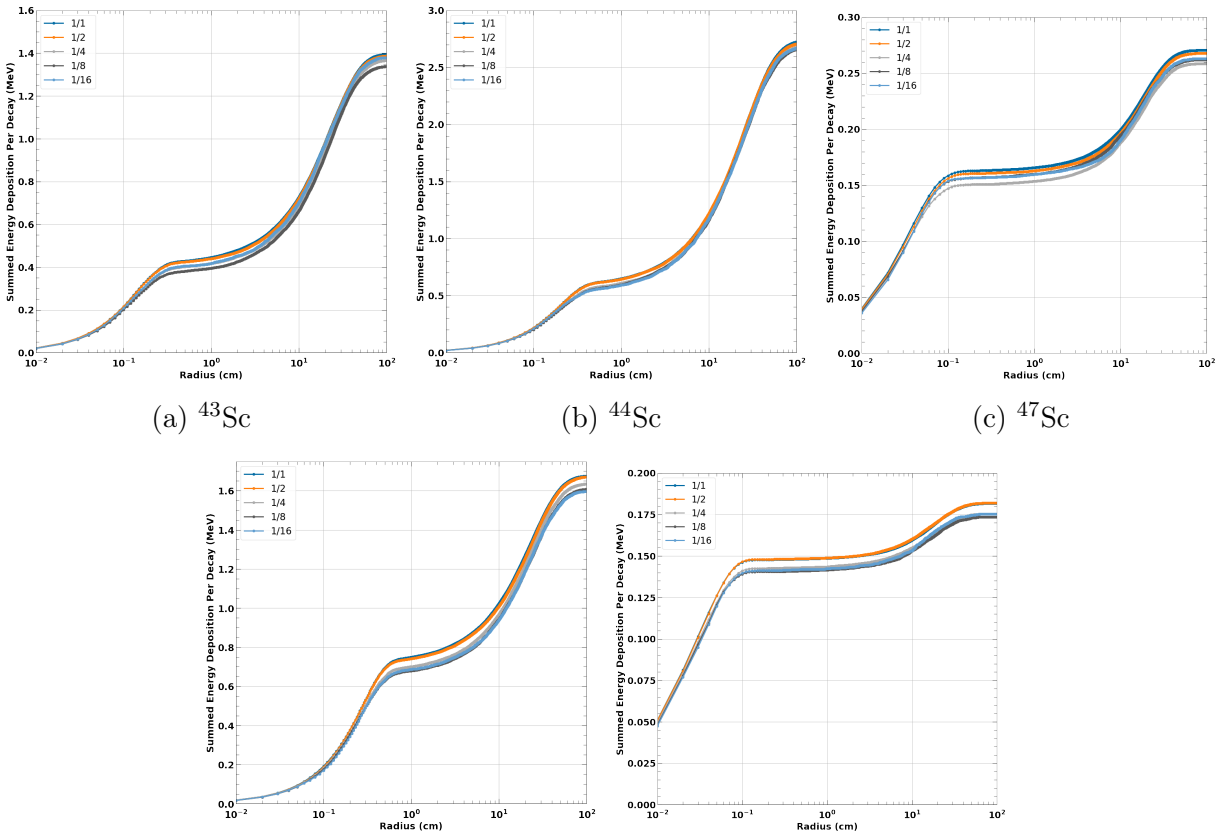

(a) ^{43}Sc (b) ^{44}Sc (c) ^{47}Sc

(d) ^{68}Ga (e) ^{177}Lu

Figure 6.3: Summed energy deposition in radially scored bins of various fractional spheres of water with r = 100 cm.

These results have been quantified in Table 6.2 which describes the mean and maximum percent error exhibited by each curve relative to the scoring of the full sphere, and also presented graphically in Figure 6.4.

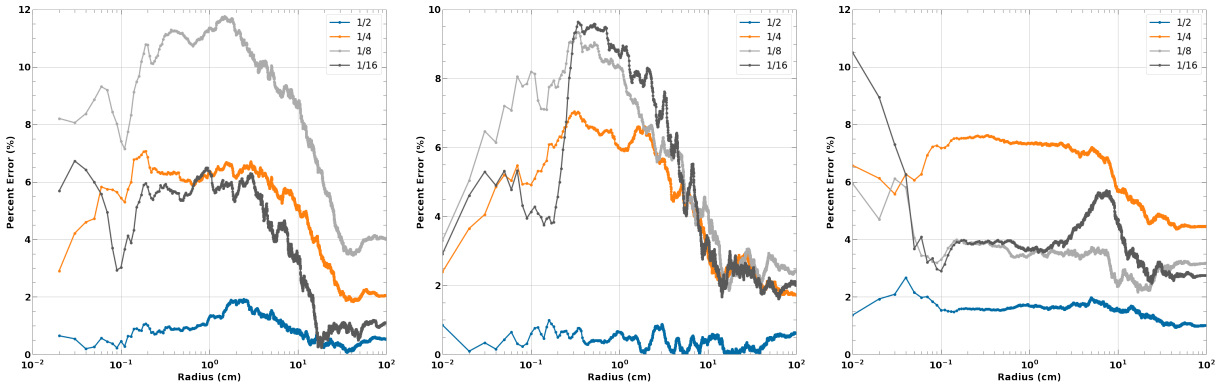

(a) ^{43}Sc (b) ^{44}Sc (c) ^{47}Sc

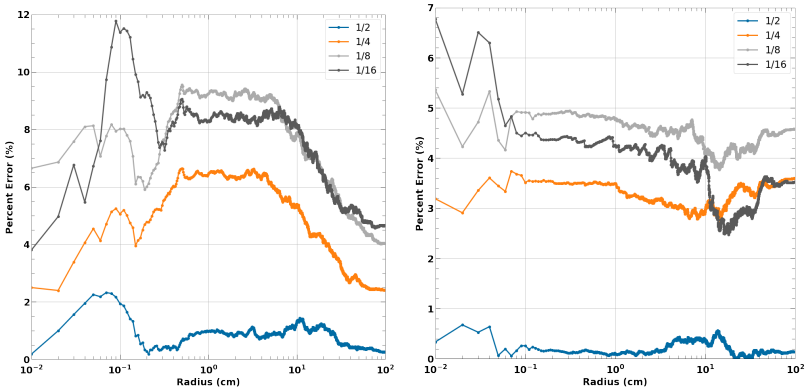

(d) ^{68}Ga (e) ^{177}Lu

Figure 6.4: Percent error of summed energy deposition in radially scored bins of various fractional spheres of water with r = 100 cm.

Isotope	Sphere Fraction	Mean Difference	Max Difference
^{43}Sc	1/2	0.518%	1.924%
	1/4	2.718%	7.070%
	1/8	4.924%	11.760%
	1/16	1.409%	6.730%
^{44}Sc	1/2	0.398%	0.988%
	1/4	2.345%	7.038%
	1/8	2.841%	9.343%
	1/16	2.445%	9.636%

^{47}Sc	1/2	1.168%	2.674%
	1/4	4.844%	7.628%
	1/8	3.054%	6.114%
	1/16	3.048%	10.507%
^{68}Ga	1/2	0.556%	2.326%
	1/4	3.242%	6.641%
	1/8	5.291%	9.557%
	1/16	5.357%	11.768%
^{177}Lu	1/2	0.159%	0.677%
	1/4	3.401%	3.741%
	1/8	4.411%	5.360%
	1/16	3.379%	6.773%

Table 6.2: Changes in computational accuracy with fractional spherical scoring in TOPAS.

Through these results it was clear that the hemisphere approximation is the only partial sphere geometry which did not result in a greater than 3% deviation in summed energy deposition from the full spherical volume. The hemisphere approximation was thus the only partial volume sphere deemed acceptable to utilize for reducing computational burden of these energy deposition simulations. As such, the hemisphere geometry was utilized for both the macroscale and microscale simulations described at the beginning of this section.

6.2.2 Cellular S-Values

The MIRD formalism models cellular geometry with a series of concentric spherical shells composed of a fluid with cytosol-like properties with the innermost sphere representing the

nucleus, the interior spherical shell representing the cytoplasm, and the thin outermost shell representing the cell surface [204, 223, 224]. This geometry was replicated in TOPAS with the nucleus having a radius of 4 μm and the cytoplasm having an inner and outer radii of 4 μm and 5 μm respectively. An additional 10 nm layer was added to this geometry spanning from 5 μm to 5.01 μm to represent the cellular membrane. Because TOPAS cannot distribute a radioactive source across an object without a volume, the cell surface was defined as the 1 nm thick region just outside the cellular membrane. All structures were composed of Geant4's G4_WATER which produces a fluid with cytosol like molecular properties. This geometry is presented graphically in Figure 6.5.

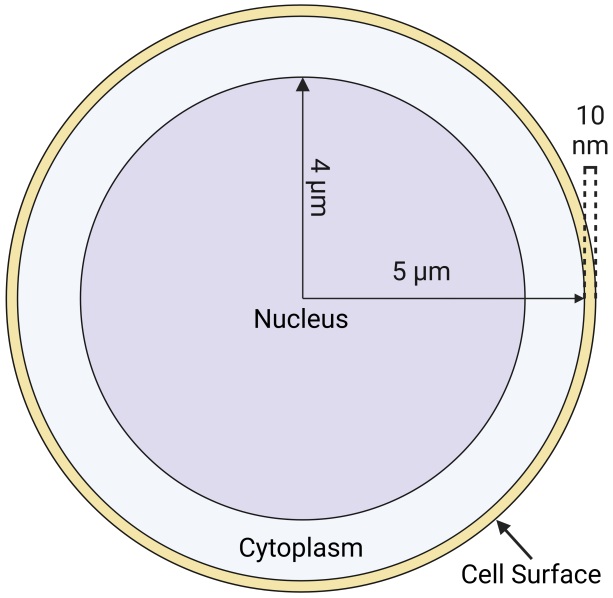

Figure 6.5: A graphical representation of the geometry used in the simulation of cellular S-values [225].

Simulations were conducted utilizing the same source to target configurations outlined in the MIRDCell formalism. These include: Cell to Cell, Cell Surface to Cell, Cell Surface to

Nucleus, Cytoplasm to Nucleus, and Nucleus to Nucleus. Within this construct, the source location is the cellular compartment where the radioactive source of ^{43}Sc, ^{44}Sc, ^{47}Sc, ^{68}Ga, or ^{177}Lu was volumetrically distributed. The target cellular compartment is where dose per radioactive decay was scored. As such, the cell surface and cytoplasm source components are of particular interest as these are the cellular compartments that PSMA-617 and PSMA-11 based radiopharmaceuticals localize to. Similarly, the nucleus target component is of the greatest relevant as it is dose deposited within the nucleus that yields direct DNA damage. For the purpose of these simulations, the whole cell volume was defined as the combined nucleus and cytoplasm compartments. Each simulation consisted of 10,000 histories and was repeated across 10 different seeds. The results presented in the next section are therefore the mean dose across all 10 seeds with error bars representing the standard error.

Validation with MIRDcell

As a point of validation and comparison, dosimetry calculations using an identical geometry (barring the cellular membrane) were also conducted in MIRDCell for ^{68}Ga, ^{177}Lu, and ^{47}Sc. MIRDCell Cellular dosimetry could not be obtained for ^{43}Sc and ^{44}Sc as these radionuclides do not presently exist within the MIRDCell database. The simulated S-values for ^{47}Sc, ^{68}Ga, and ^{177}Lu as calculated in TOPAS and MIRDcell are therefore presented in Figure 6.6, Figure 6.7, and Figure 6.8. These results are also presented in tabulated form in Table 6.3.

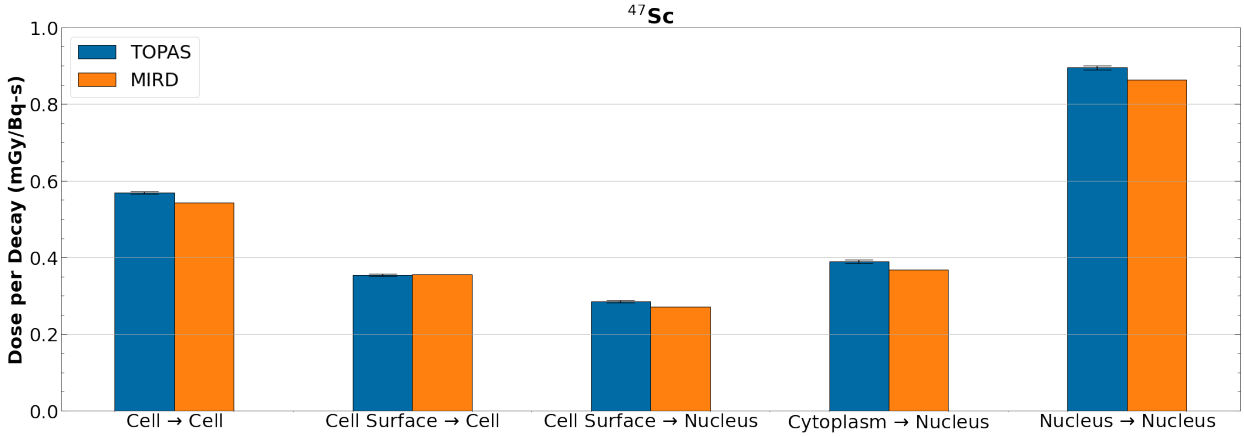

Figure 6.6: Radiobiological S-Values of ^{47}Sc calculated with TOPAS and MIRDcell

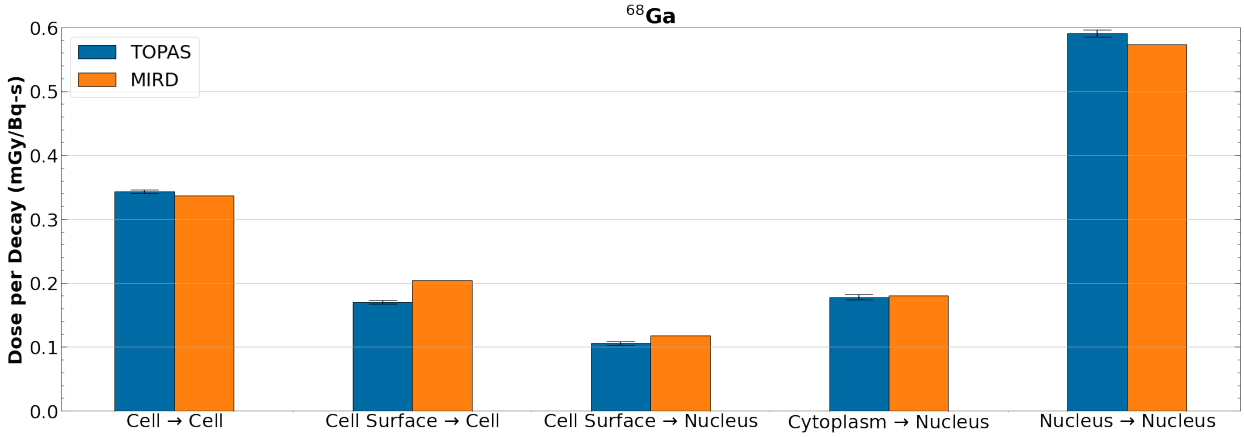

Figure 6.7: Radiobiological S-Values of ^{68}Ga calculated with TOPAS and MIRDcell

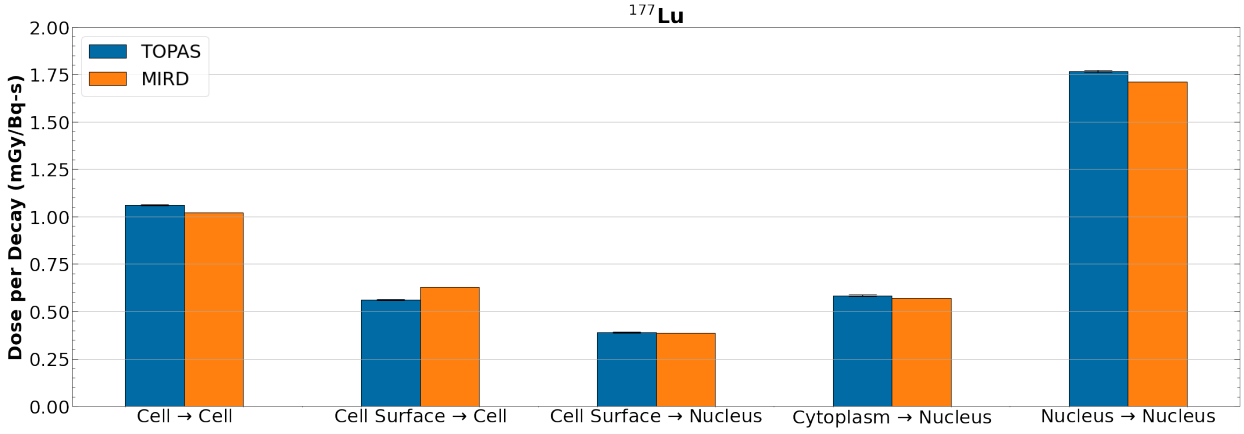

Figure 6.8: Radiobiological S-Values of ^{177}Lu calculated with TOPAS and MIRDcell

Isotope	Program	Cell → Cell (mGy/Bq-s)	Cell Surface → Cell (mGy/Bq-s)	Cell Surface → Nucleus (mGy/Bq-s)	Cytoplasm → Nucleus (mGy/Bq-s)	Nucleus → Nucleus (mGy/Bq-s)
^{47}Sc	TOPAS	0.568	0.354	0.284	0.389	0.895
	MIRDcell	0.543	0.356	0.271	0.368	0.863
	Difference	4.56%	0.554%	4.99%	5.78%	3.68%
^{68}Ga	TOPAS	0.343	0.170	0.106	0.178	0.590
	MIRDcell	0.337	0.204	0.118	0.180	0.573
	Difference	1.83%	18.2%	10.8%	1.19%	7.02%
^{177}Lu	TOPAS	1.06	0.561	0.390	0.583	1.76
	MIRDcell	1.02	0.628	0.386	0.570	1.71
	Difference	3.87%	11.3%	1.07%	2.42%	3.23%

Table 6.3: Radiobiological S-Values of ^{47}Sc, ^{68}Ga, and ^{177}Lu calculated in TOPAS and MIRDcell.

As is seen in Table 6.3, the mean percent difference between the TOPAS and MIRDcell calculation of S-values was 3.91% for ^{47}Sc, 7.02% for ^{68}Ga, and 4.38% for ^{177}Lu. The maximum percent difference was 5.78% for ^{47}Sc, 18.2% for ^{68}Ga, and 11.3% for ^{177}Lu. This is congruent with other Monte Carlo assessments of MIRDcell's S-value calculations and therefore facilitates confidence in the methodology and simulation geometry constructed within this section.

6.2.3 DNA Double Strand Breaks

To simulate DNA damage in TOPAS, a geometric model of the nucleus and its subsequent DNA contents were incorporated from the commonly used extension, TOPAS-nBio. The

DNA was modeled using the solenoid chromatin fiber model first proposed by Finch and Klug in 1976 and modeled in Geant4DNA by Henthorn et al. [226, 227]. As shown in Figure 6.9, this structure models DNA bases as 0.208 nm base spheres and the sugar-phosphate backbone as 0.240 nm spheres. A hydration shell of 0.16 nm was also modeled around the double helices to more accurately model ionizations that result in backbone breaks. This double helix DNA structure was then wrapped around cylindrical histone proteins of radius 3.3 nm and length 5.7 nm in 1.65 superhelical left-handed turns per histone. These histones were then arranged to form chromatin solenoids which contain 61 histones total [201, 227].

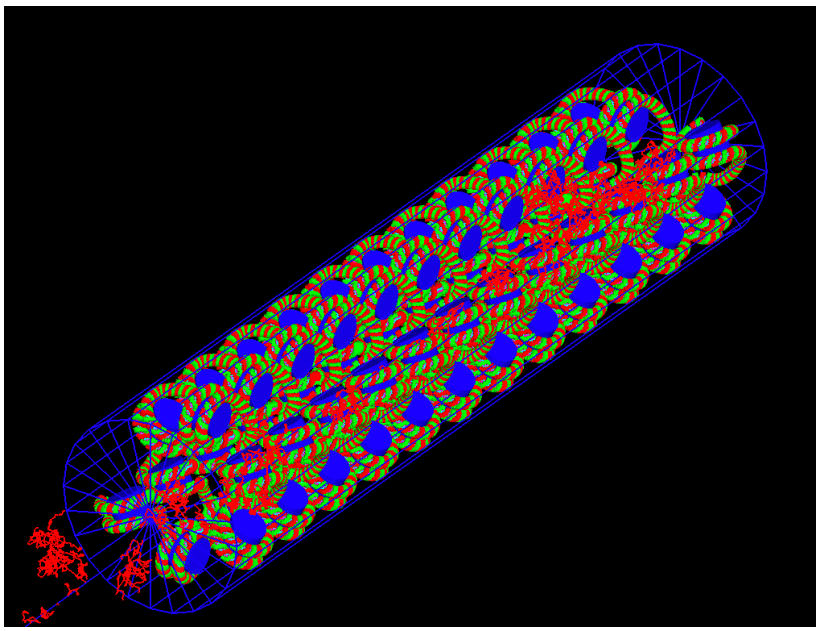

Figure 6.9: The TSSolenoidFiber structure modeled in TOPAS-nBio. This figure was adopted from the TOPAS-nBio documentation [201, 227].

Using the geometric model, TsNucleus, a sphere of radius 4.65 μm was uniformly filled with these chromatin solenoids which were then linked with a 4-layer Hilbert curve which was repeated 30 times in each dimension yielding 27,000 voxels and 6.078 gigabase pairs [201, 227]. To model DNA damage from different points of radioisotope localization, a cytoplasmic region was also modeled extending from the surface of the nucleus to a radius of 6.75 μm. Both the radii of the nucleus and cytoplasm were selected to be similar to

that of human LNCaP cells [228]. Similarly, a thin 10 nm cell surface region was modeled to mimic the plasma membrane of a typical cell enabling the estimation of DNA damage of radiopharmaceutical uptake to the transmembrane PSMA receptor without internalization [140, 229, 230]. This cellular model is presented in Figure 6.10. All materials in this simulation were composed of Geant4's G4_WATER. All materials were assigned a density of 1 g/cm^3 with the exception of histones which were assigned a density of 1.407 g/cm^3 [201, 227, 231, 232].

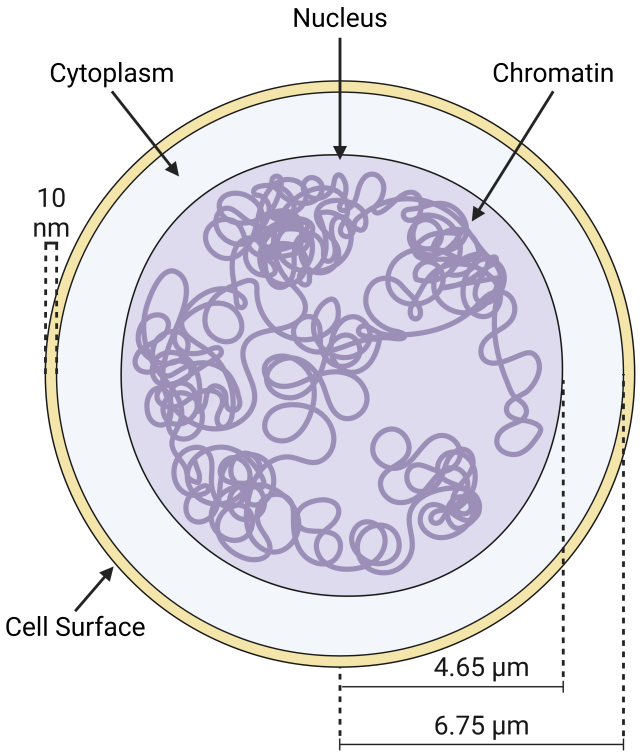

Figure 6.10: A graphical representation of the geometry of the simulation of DNA damage [233].

A DNA damage scorer specifically designed for use with the previously described nuclear DNA model was also incorporated from TOPAs-nBio. Within this framework, a DNA single strand break is scored when 11.75 eV or greater is deposited into the DNA backbone or the hydration shell. Double strand breaks are then scored when two single strand breaks occur

within 10 base pairs of each other. This scorer is also capable of evaluating DNA damage through the scavenging of radiation induced free radicals by DNA bases, the DNA backbone, hydration shells, and histones; however, this study was purely focused on the quantization of direct DNA damage by radioactive decay and thus those features were disabled in all the described simulations.

Within the described cellular geometry, individual simulations were conducted with the radioactive source being volumetrically distributed in the nucleus, cytoplasm, and cell surface. All simulations were conducted with 10,000 histories and repeated across 10 different seeds. As such, all reported results are the mean across these seeds.

6.3 Results

6.3.1 Radially-Varying Radiation Dosimetry

Diagnostic Isotopes

The simulated energy deposition curves for the diagnostic radioscandiums and their clinical analogue, ^{68}Ga, are presented in Figure 6.11. Each subplot within this figure represents a different method of examining the simulated data as was described in the equations presented in Section 6.2.1.

As positron-emitting isotopes, ^{43}Sc, ^{44}Sc, and ^{68}Ga all exhibit similarly shaped energy deposition profiles with the maximum energy deposition occurring at a distance that is on the same order as the positron range. As exhibited in Figure 6.11a and Figure 6.11c peak deposition shifts to further distances from the decay origin as the positron range increases. Therefore, as ^{43}Sc has the lowest positron energy of these isotopes, it is posed to deposit the lowest fraction of its decay energy into tissues which are localized to the target cells, such as in the case of mCRPC metastases near bone marrow. However, within this initial dose region, both ^{43}Sc and ^{44}Sc deposit 12.4% and 12.8% more energy per decay from the origin

point of decay to a radial distance of 0.1 cm.

When examining fractional summed energy deposition in Figure 6.11c, however, it becomes clear that the cumulative interactions of the gamma rays emitted by these diagnostic radionuclides composed the largest fraction of energy deposition. At radial distances greater than 1 cm, ^{43}Sc, ^{44}Sc, and ^{68}Ga were shown to deposit 68.3%, 76.1%, and 55.3% of their energy beyond the 1 cm threshold. These variations in dose profile are likely the consequence of the additional gamma emissions of these isotopes beyond the annihilation gamma rays. This is congruent with the fact that ^{68}Ga exhibits the least dose contribution by gamma rays, as it has no additional significant gamma emissions, and ^{44}Sc has the largest fractional deposition contribution on account of its 1,157 keV prompt gamma.

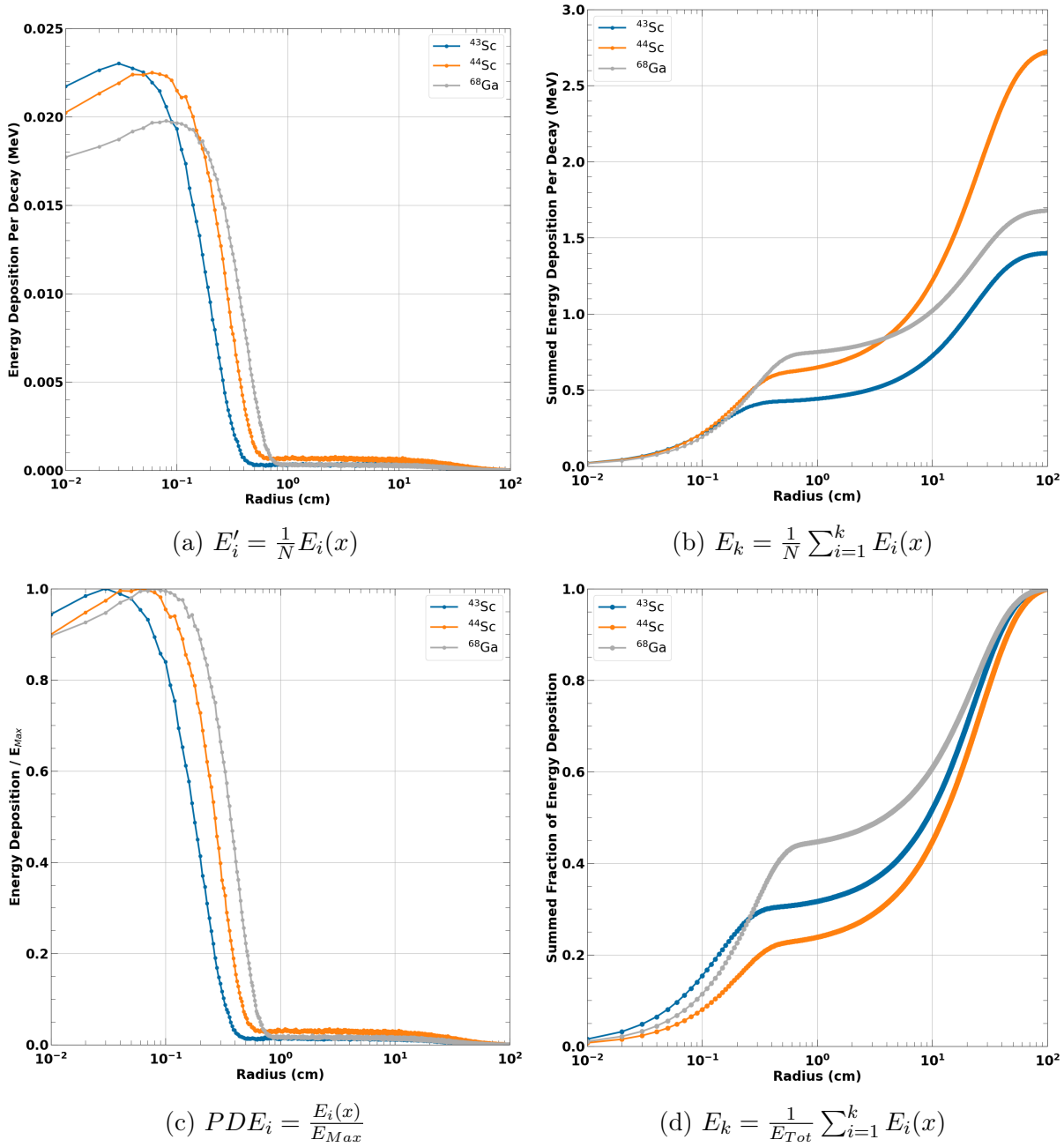

(a) $E'_i = \frac{1}{N} E_i(x)$

(b) $E_k = \frac{1}{N} \sum_{i=1}^{k} E_i(x)$

(c) $PDE_i = \frac{E_i(x)}{E_{Max}}$

(d) $E_k = \frac{1}{E_{Tot}} \sum_{i=1}^{k} E_i(x)$

Figure 6.11: Energy deposited by the diagnostic radioscandiums and their clinical analogue ^{68}Ga in spherical shells of increasing radius.

The contrast between these gamma ray derived features becomes more apparent when comparing the summed energy deposition of these radionuclides in Figure 6.11b. Notably, compared to ^{43}Sc and ^{68}Ga, ^{44}Sc exhibited an extremely steep increase in energy deposition

from radial distances of 1-100 cm due to its high energy gamma emission. This also translated to a significantly greater total energy deposition which was shown to total 2.72 MeV per decay compared to 1.40 MeV in ^{43}Sc decay and 1.68 MeV in ^{68}Ga decay.

Examining the same four interpretations for the subcellular scale simulations yielded the energy deposition curves shown in Figure 6.12. At this scale, the summed energy deposition (Figure 6.11b) and fractional summed energy deposition curves (Figure 6.11d) were nearly identical for these diagnostic isotopes. Some slight variation in energy deposition was observed in Figure 6.12a. Notably, within the first radial bin at the origin, ^{43}Sc was shown to deposit 0.099 keV per decay compared to 0.081 and 0.077 keV per decay with ^{44}Sc and ^{68}Ga respectively. Within Figure 6.11a and Figure 6.11c, each isotope was also shown to produce a small secondary peak in energy deposition between 0.1 to 1 μm. As this peak appeared to shift to further distances from the decay origin at higher mean positron kinetic energies, it is a feature likely derived from spur and blob formation in positron track structure [104, 234].

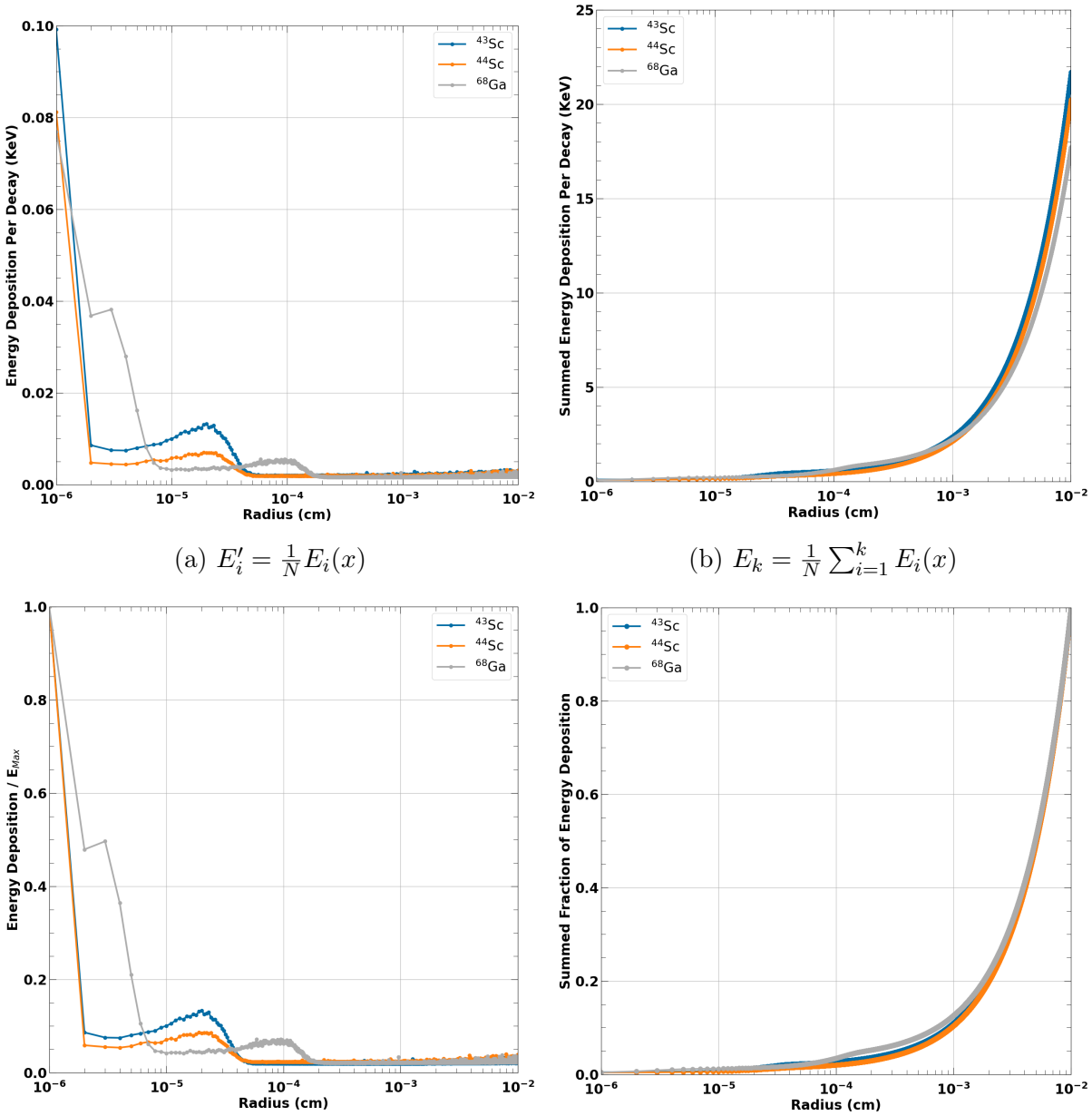

(a) $E_i' = \frac{1}{N} E_i(x)$

(b) $E_k = \frac{1}{N} \sum_{i=1}^{k} E_i(x)$

(c) $PDE_i = \frac{E_i(x)}{E_{Max}}$

(d) $E_k = \frac{1}{E_{Tot}} \sum_{i=1}^{k} E_i(x)$

Figure 6.12: Energy deposited by the diagnostic radioscandiums and their clinical analogue, ^{68}Ga, in spherical shells of increasing radius at the subcellular scale.

Therapeutic Isotopes

The macroscale energy deposition curves simulated for ^{47}Sc and ^{177}Lu are presented in Figure 6.13 below.

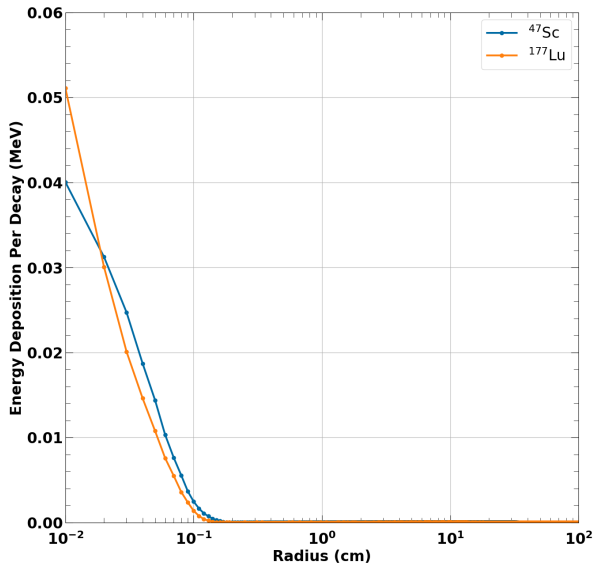

(a) $E_i' = \frac{1}{N} E_i(x)$

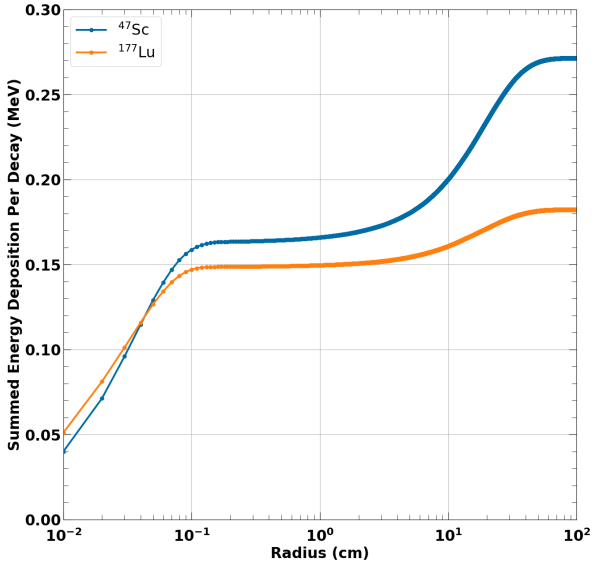

(b) $E_k = \frac{1}{N} \sum_{i=1}^{k} E_i(x)$

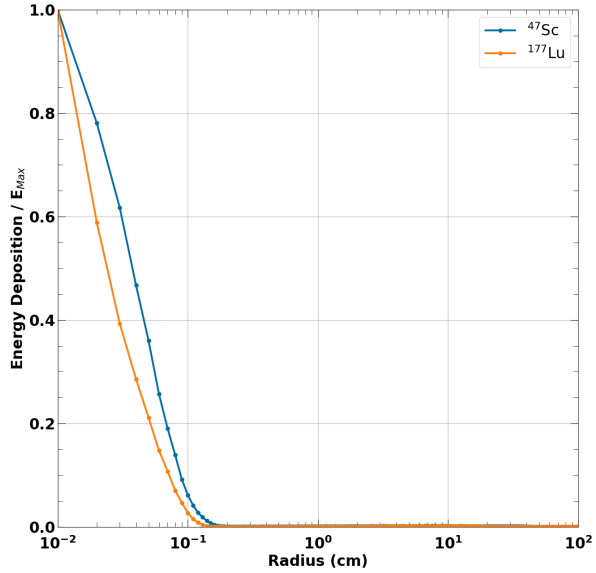

(c) $PDE_i = \frac{E_i(x)}{E_{Max}}$

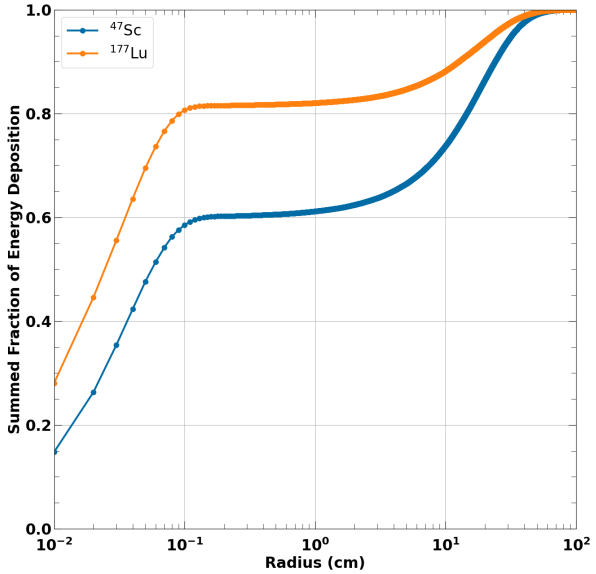

(d) $E_k = \frac{1}{E_{Tot}} \sum_{i=1}^{k} E_i(x)$

Figure 6.13: Energy deposited by the therapeutic isotopes ^{47}Sc and ^{177}Lu in spherical shells of increasing radius.

As shown in Figure 6.13a and Figure 6.13c, the maximum single bin energy deposition for both of these isotopes was shown to occur at the origin of decay; however, ^{47}Sc was shown to deposit approximately 21.7% less energy per decay than ^{177}Lu within that volume. Conversely, ^{47}Sc was shown to deposit more energy than ^{177}Lu in the radial bins ranging

from 0.02 cm to approximately 0.1 cm, an effect likely derivative of the higher kinetic energy of ^{47}Sc's beta electron emission. This is also reflected in the summed energy deposition curve shown in Figure 6.13b where ^{47}Sc is shown to deposit more total energy than ^{177}Lu from 0.05 cm to 100 cm. Within the portion of the curve spanning from 0.01 cm to 0.1 cm, where energy deposition is dominated by electron interactions, this translated to a 7.9% increase in total energy deposited by ^{47}Sc relative to ^{177}Lu.

These results suggest that ^{177}Lu likely has greater dose targeting precision than ^{47}Sc and thus would be preferential in the targeting of metastases which are very small or homogeneously express PSMA. Conversely, because ^{47}Sc has been shown to deposit energy across an extended distance, it is likely better suited for tumors and metastases that are heterogeneously PSMA expressing or of a slightly larger size as a consequence of the cross-fire effect.

Naturally, the greater mean electron range and subsequent extended energy deposition profile of ^{47}Sc poses greater concerns with regards to dose to organs at risk relative to ^{177}Lu, particularly when metastases are adjacent to bone-marrow, as is often the case in mCRPC. Moreover, because ^{47}Sc's gamma emission has an intensity of 68.3% compared to a combined intensity of 16.6% for the combined gamma emissions of ^{177}Lu decay, ^{47}Sc deposits significantly more of its decay energy past 0.1 cm. This is clearly exhibited in Figure 6.13d where ^{47}Sc is shown to deposit 41.5% of its total decay energy past 0.1 cm whereas ^{177}Lu deposits only 19.3% in the same range.

Simulating the decay of ^{47}Sc and ^{177}Lu on microdosimetric scales resulted in the four energy deposition curves presented in Figure 6.14.

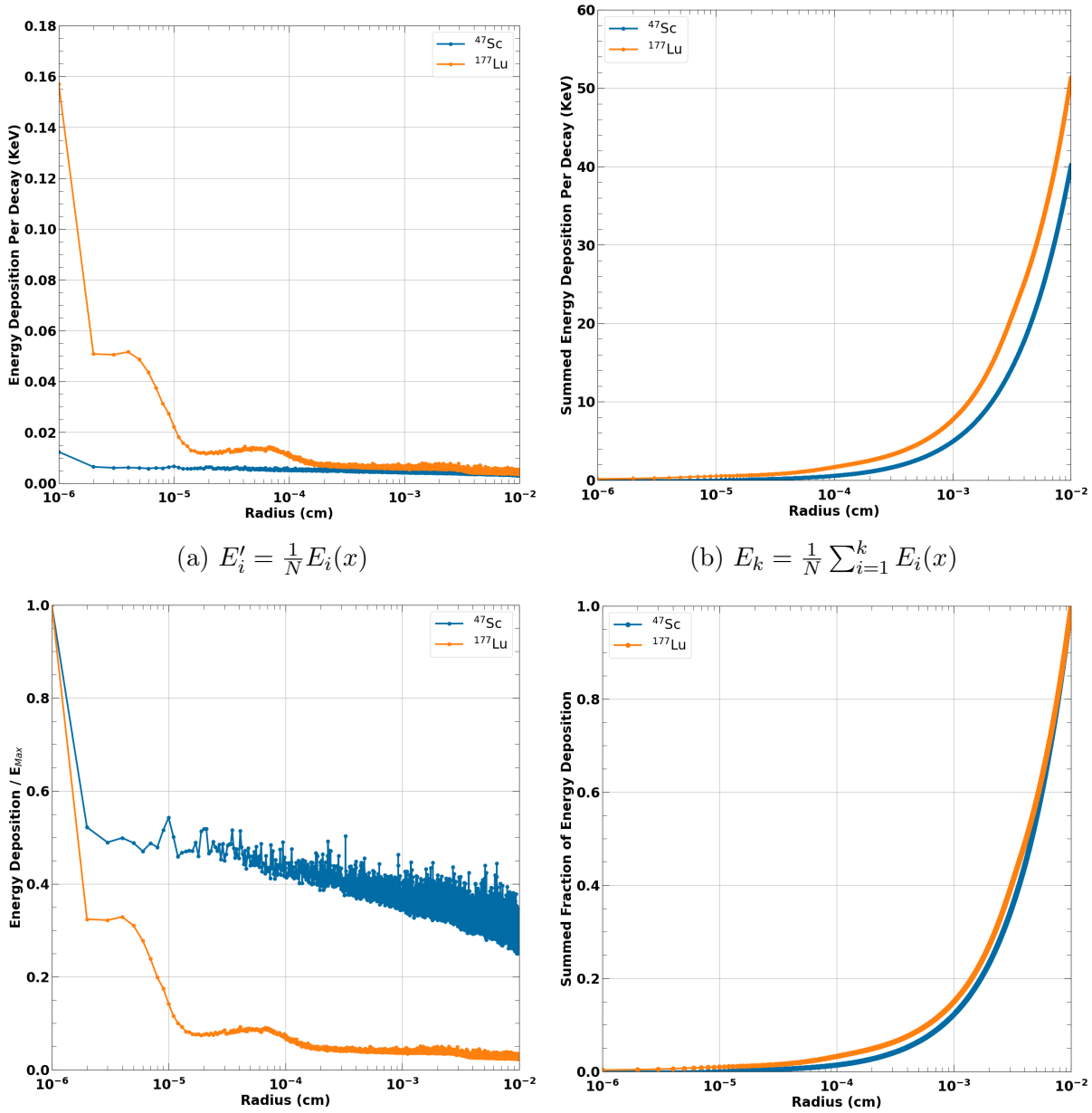

(a) $E_i' = \frac{1}{N} E_i(x)$

(b) $E_k = \frac{1}{N} \sum_{i=1}^{k} E_i(x)$

(c) $PDE_i = \frac{E_i(x)}{E_{Max}}$

(d) $E_k = \frac{1}{E_{Tot}} \sum_{i=1}^{k} E_i(x)$

Figure 6.14: Energy deposited by the therapeutic isotopes, ^{47}Sc and ^{177}Lu, in spherical shells of increasing radius at the subcellular scale.

The energy deposition observed in Figure 6.14a initially appears very striking as ^{47}Sc deposits 92.1% less energy than ^{177}Lu at the origin and 87.0% less over the range of 0.01 μm to 0.1 μm. However, because this occurs over a scale much smaller than that of the width of

a typical cytoplasm, the majority of this energy would be deposited in the cytosol or cellular membrane in the absence of a ligand capable of nuclear localization limiting the biological effect to indirect radiolytic reactions. As shown in Figure 6.14b, this region also composes a small portion of the total energy deposition (0.17% for ^{47}Sc and 1.01% for ^{177}Lu) as the interaction of beta electrons becomes more frequent as they lose energy [235].

Although the summed energy deposition curves shown in Figure 6.14b and Figure 6.14d exhibited similar profiles for ^{47}Sc and ^{177}Lu, the PDE curve in Figure 6.14c clearly shows that the continuous energy deposition of ^{47}Sc decay occurs over an extended range relative to ^{177}Lu. Of course, ^{177}Lu still deposited more energy than ^{47}Sc over the entire range from 0.01 μm to 100 μm; however, the increased energy deposition of ^{47}Sc relative to its max energy deposition from 0.1 μm to 100 μm may be exploitable by administering a greater activity amount than is presently used with ^{177}Lu in TRT. This is particularly relevant as this range encompasses several biologically relevant sizes including the diameter of typical circulating prostate cancer cells (∼6-10 μm) and LNCaP cells (∼18 μm) [236, 237].

6.3.2 Cellular S-Values

Diagnostic Isotopes

The TOPAS simulated S-values for the diagnostic radioscandiums and their clinically utilized analogue, ^{68}Ga, are presented in Figure 6.15 and Table 6.4.

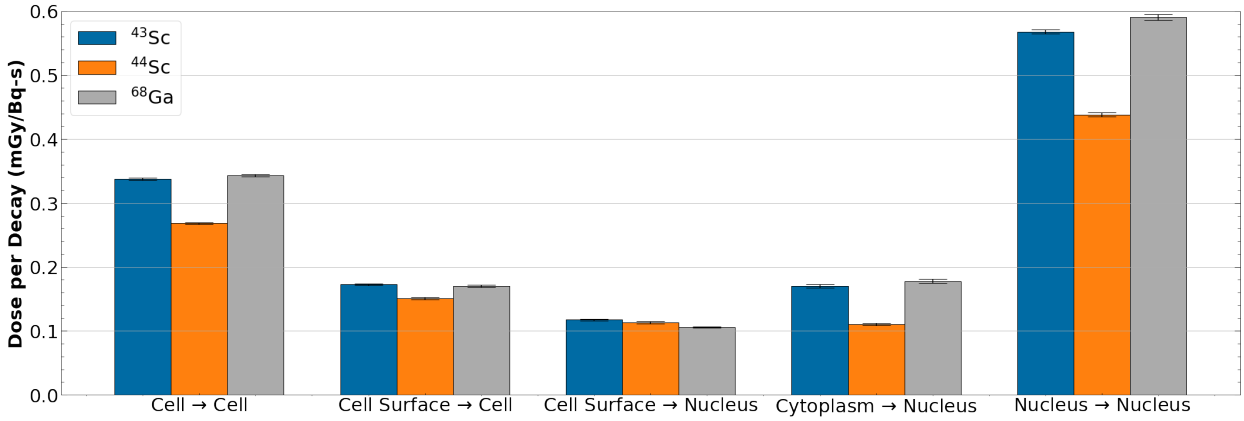

Figure 6.15: Radiobiological S-values of the diagnostic radioscandiums and ^{68}Ga.

Isotope	Cell → Cell (mGy/Bq-s)	Cell Surface → Cell (mGy/Bq-s)	Cell Surface → Nucleus (mGy/Bq-s)	Cytoplasm → Nucleus (mGy/Bq-s)	Nucleus → Nucleus (mGy/Bq-s)
^{43}Sc	0.338	0.172	0.117	0.170	0.568
^{44}Sc	0.268	0.151	0.113	0.110	0.438
^{68}Ga	0.343	0.170	0.106	0.178	0.590

Table 6.4: Radiobiological S-values of diagnostic radioscandiums and ^{68}Ga.

The cellular S-values simulated for ^{43}Sc and ^{68}Ga were found to be highly similar, differing by only 1.2%-10.4% depending on source to target configuration. As such, ^{43}Sc and ^{68}Ga deposit similar cellular doses, and thus deal similar levels of local biological damage, regardless of intracellular localization. Conversely, ^{44}Sc was found to almost universally have lower S-values than ^{43}Sc or ^{68}Ga in every source to target configuration except for cell surface to nucleus. Specifically, the ^{44}Sc S-values were 11.2%-38.2% lower than ^{68}Ga and 3.4%-35.3% lower than ^{43}Sc depending on source to target configuration. This would imply that ^{44}Sc deals less local cellular damage than ^{43}Sc or ^{68}Ga when internalized into a target

cell.

While provided for completeness, this is not a particularly insightful probe of dosimetric risk because the majority of the energy deposited by these isotopes is through their annihilation gamma rays and additional gamma emissions as was shown in the previous section. Moreover, as these isotopes are utilized diagnostically and thus would be administered at relatively low doses, any biological effect in target cells would be minimal relative to the downstream use of any therapeutic radiopharmaceuticals. As such, these values should not be heavily emphasized in diagnostic isotope selection during radiopharmaceutical development. Conversely, when compared to the S-values generated for the therapeutically intended isotopes below, it becomes immediately obvious that none of ^{43}Sc, ^{44}Sc, or ^{68}Ga are well suited for the theorized therapeutic application of positron emitting isotopes as postulated in Section 2.1.4.

Therapeutic Isotopes

As presented in Figure 6.16 and Table 6.5 cellular S-value simulations showed ^{47}Sc and ^{177}Lu to deposit cellular dose on approximately the same order of magnitude with greater divergence between the dose deposited by the two isotopes as source localization became more proximal to the nucleus.

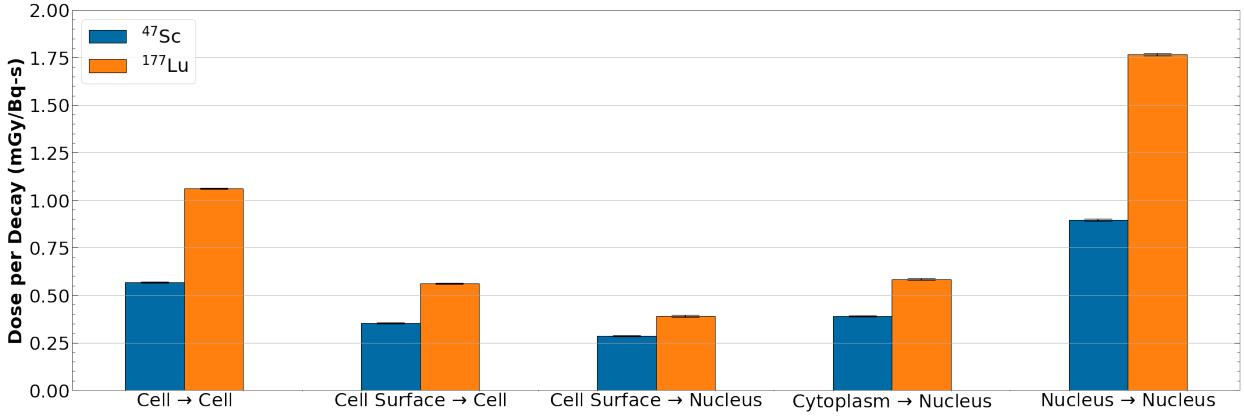

Figure 6.16: Radiobiological S-values of ^{47}Sc and ^{177}Lu.

Isotope	Cell → Cell (mGy/Bq-s)	Cell Surface → Cell (mGy/Bq-s)	Cell Surface → Nucleus (mGy/Bq-s)	Cytoplasm → Nucleus (mGy/Bq-s)	Nucleus → Nucleus (mGy/Bq-s)
^{47}Sc	0.568	0.354	0.284	0.389	0.895
^{177}Lu	1.060	0.561	0.390	0.583	1.766

Table 6.5: Radiobiological S-values of ^{47}Sc and ^{177}Lu.

Notably, ^{47}Sc only deposits 50.7% of the dose per decay as ^{177}Lu in the nucleus to nucleus source target configuration and 53.6% in the cell to cell configuration (which inherently assumes some level of nuclear uptake). However, these levels of radiopharmaceutical localization are not reflective of the current state of peptide based radiopharmaceutical development as it is very difficult to design compounds that are internalized by the cellular membrane and then translocated through the nuclear envelope. The cell surface to nucleus configuration therefore provides a scenario more reflective of PSMA-617 based TRT by emulating a radiopharmaceutical which is uptaken but not internalized. Within this configuration, ^{47}Sc deposits a much more viable 73.0% of the dose per decay of ^{177}Lu. Of course, as shown in Section 5.2.5, a significant portion of PSMA-617 based radiopharmaceuticals, are also internalized thus requiring an analysis of the cytoplasm to nucleus configuration. With this higher order of cellular localization, ^{47}Sc is shown to deposit 66.8% of the dose per decay as ^{177}Lu.

6.3.3 DNA Double Strand Breaks

Diagnostic Isotopes

The number of DSBs directly induced by ^{43}Sc, ^{44}Sc, and ^{68}Ga when localized to the nucleus, cytoplasm, and cell surface are presented in Figure 6.17 and Table 6.6. While not the primary focus of this section, the number of single strand breaks (SSBs) and damaged nucleobases within these simulations, along with the combined number of all direct DNA damage types, are also presented in Table 6.6.

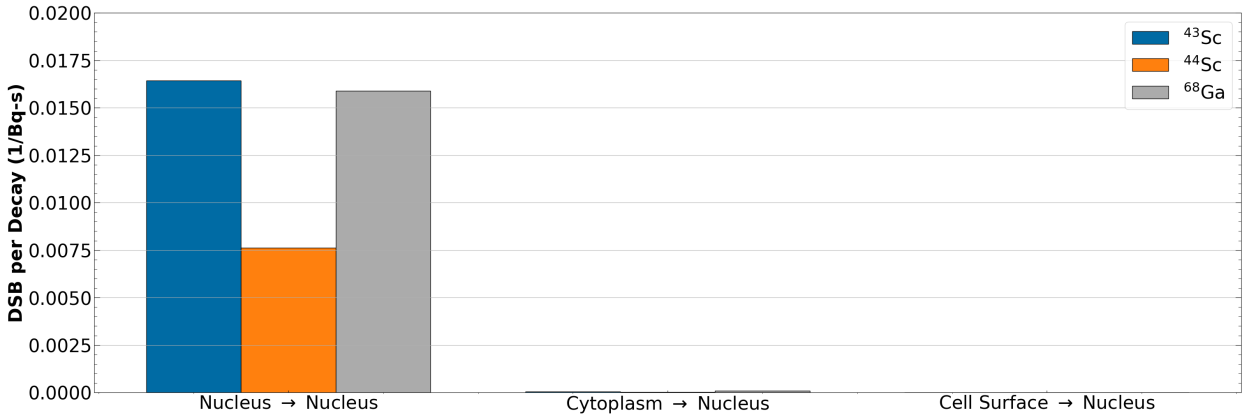

Figure 6.17: Simulated DNA DSBs of the diagnostic radioscandiums per radioactive decay.

Isotope	Lesion Type	Nucleus (1/Bq·s)	Cytoplasm (1/Bq·s)	Cell Surface (1/Bq·s)
^{43}Sc	DSB	0.0164	0.00004	0
	SSB	0.1489	0.0007	0.00008
	Base	0.2135	0.0007	0.00006
	Total	0.3789	0.0014	0.0001
^{44}Sc	DSB	0.0076	0.00002	0
	SSB	0.0729	0.0003	0.00004
	Base	0.1053	0.0004	0.00005

	Total	0.1858	0.0007	0.00009
^{68}Ga	DSB	0.0159	0.0001	0
	SSB	0.1638	0.0034	0.00003
	Base	0.2309	0.0038	0.00005
	Total	0.4106	0.0072	0.00008

Table 6.6: Simulated DNA damage induced by the diagnostic radioscandiums per radioactive decay.

Analogous to the simulation of cellular S-values, ^{43}Sc induced a similar number of DSBs as ^{68}Ga when localized to the nucleus while ^{44}Sc induced 60% less DSBs than ^{68}Ga. When localized to the cytoplasm, the number of induced DSBs was reduced by approximately three orders of magnitude for ^{43}Sc, ^{44}Sc, and ^{68}Ga thus rendering their biological effect negligible. This is particularly evident when one compares these values to those of the therapeutic isotopes presented in the following section, and considers the relatively minimal activity amounts administered in PET imaging relative to TRT. Furthermore, when simulating the cellular surface to nucleus source target geometry, none of these diagnostic isotopes induced any DNA DSBs when localized to the cell surface.

Much like the evaluation of cellular S-values for ^{43}Sc, ^{44}Sc, and ^{68}Ga in the prior section, the inclusion of simulated DNA DSB data is primarily for the sake of completeness. As these isotopes do not deposit a significant amount of dose locally, and are thus not well suited for therapeutic applications, DNA DSB data should have very minimal emphasis in the radionuclide selection process during radiopharmaceutical development.

Therapeutic Isotopes

As is shown in Figure 6.18 and Table 6.7, the vast disparity between the number of DNA DSBs directly induced by ^{47}Sc relative to ^{177}Lu when localized to the nucleus initially appears to be the most striking result of the DSB simulations with ^{47}Sc only inducing 14.4% of the number of DSBs as ^{177}Lu. However, as described in the previous section, the nucleus to nucleus source target configuration is not reflective of the level of cellular localization observed with PSMA-617 or any other DOTA-based ligand. As such, it is more relevant to examine the number of DNA DSBs induced when the radioligand is localized to the cytoplasm or cell surface as is congruent with cellular internalization and uptake.

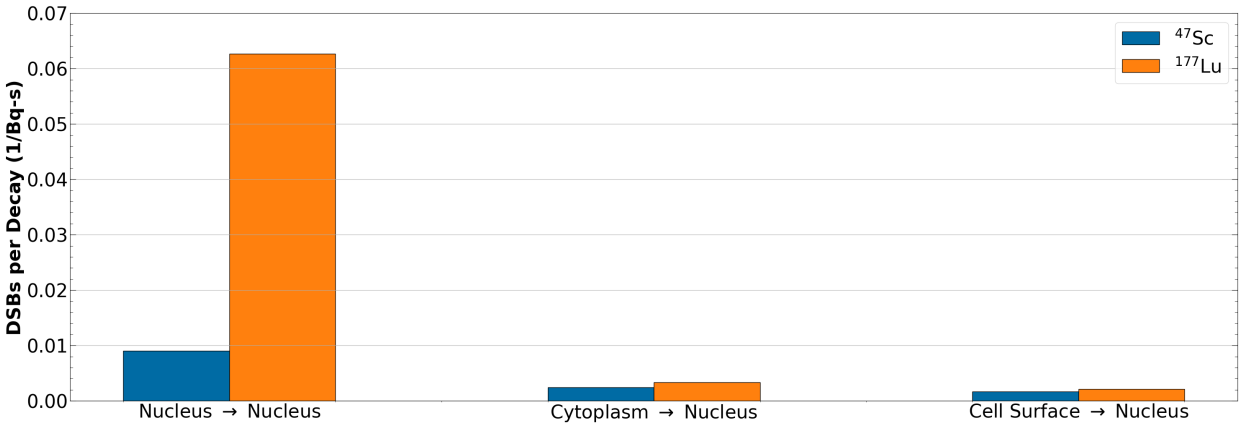

Figure 6.18: Simulated DNA DSBs directly induced by therapeutic ^{47}Sc and ^{177}Lu per radioactive decay.

Isotope	Lesion Type	Nucleus (1/Bq·s)	Cytoplasm (1/Bq·s)	Cell Surface (1/Bq·s)
^{47}Sc	DSB	0.0090	0.0024	0.0017
	SSB	0.2315	0.0729	0.0475
	Base	0.2968	0.0948	0.5907
	Total	0.5373	0.1701	0.1082
^{177}Lu	DSB	0.0627	0.0034	0.002

SSB	0.6365	0.1032	0.0600
Base	0.9072	0.1329	0.0783
Total	1.6064	0.1329	0.0783

Table 6.7: Simulated DNA damage induced by therapeutic ^{47}Sc and ^{177}Lu per radioactive decay.

To better visualize the relative number of DNA DSBs induced by ^{47}Sc and ^{177}Lu when localized to the cell surface and cytoplasm, the previous figure was rescaled to only these two source to target geometries and presented in Figure 6.19.

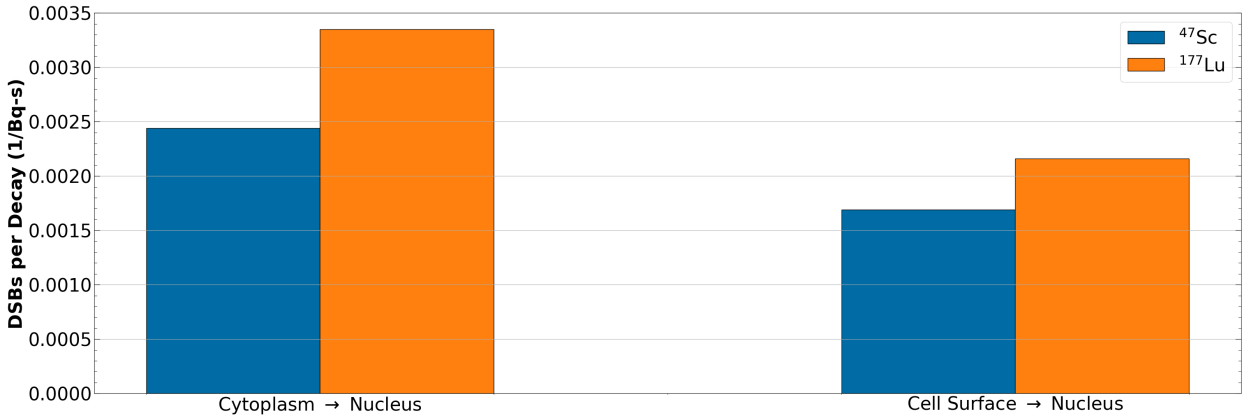

Figure 6.19: Simulated DNA DSBs of therapeutic radioscandiums per radioactive decay in non-nuclear uptake and internalization.

At these levels of cellular localization, the biological effect of ^{47}Sc was found to be much more comparable to ^{177}Lu, although ^{177}Lu still outperformed ^{47}Sc in both source target configurations. Specifically, ^{47}Sc was found to induce 72.8% of the number of DSBs as ^{177}Lu when distributed throughout the cytoplasm, and 78.2% of the number of DSBs as ^{177}Lu when distributed throughout the cell surface. While the simulated geometries were not perfectly identical due to the use of different radii for the nucleus and cytoplasm, these results are mostly congruent with the trends observed in the cellular S-value simulations in

the previous section. As such, this slight deficit in the biological effect of ^{47}Sc could likely be mitigated by administering more activity than would be used with ^{177}Lu.

6.4 Discussion

Through the radially-varying radiation dose simulations, ^{43}Sc and ^{44}Sc were shown to produce energy deposition curves of a similar shape and magnitude to that of the clinically utilized ^{68}Ga at both the macroscopic and microscopic scales. The initial portion of these curves where positron interactions dominate energy deposition was shown to shift further to the right with increased average positron energy, but this is more relevant with regards to spatial resolution as opposed to practical dosimetry. Conversely, the difference in simulated energy deposition from approximately 1-100 cm was notable with ^{44}Sc depositing approximately double the energy of ^{43}Sc and ^{68}Ga within this region. As the high energy gamma emission of ^{44}Sc is clearly deeply penetrating, the application of ^{44}Sc in the clinical setting will therefore require significant considerations in dosimetry and health physics with regards to patients, medical staff, and the general public. Although further experimental testing is required, this makes a compelling argument as to why ^{43}Sc may be a preferable diagnostic isotope in the development of radioscandium theranostics despite its more challenging and costly production.

Simulations of cellular S-values were also conducted with ^{43}Sc, ^{44}Sc, and ^{68}Ga. Within this framework, the cellular S-values of ^{43}Sc were shown to be comparable to that of ^{68}Ga at all levels of cellular localization; however, ^{44}Sc was shown to deposit less local dose per decay than both ^{43}Sc and ^{68}Ga at all localizations. Similar results were observed in the simulation of DNA DSBs in which ^{43}Sc and ^{68}Ga induced a similar number of DSBs when localized to the nucleus, but ^{44}Sc induced approximately half as many DSBs. When localized to the cytoplasm or nucleus, the number of DNA DSBs induced by these diagnostic isotopes became negligible. While these results facilitate the claim that none of these diagnostic isotopes

would be viable as therapeutics despite the hypothesized potential of positron emitters in TRT, they are not particularly relevant for the selection of radioisotopes for diagnostic use as the overwhelming majority of their energy deposition occurs on macroscopic scales.

Within the beta electron dominated range of the radially-varying radiation dose simulations of ^{47}Sc and ^{177}Lu, ^{47}Sc deposited approximately 21.7% less energy than ^{177}Lu within the first 0.01 cm (100 μm) radial bin, but 7.9% more energy than ^{177}Lu within the first 0.1 cm (1000 μm). As expected, this suggests that the higher kinetic energy of ^{47}Sc's positron emission results in a broadened dose profile relative to ^{177}Lu. Although this increased deposition was fairly minimal, this suggests that ^{47}Sc may have greater biological effect when targeting clusters of cancer cells due to the cross-fire effect. However, this slightly extended range may also yield further considerations when examining dose to any organs at risk which are proximal to the target metastases, especially when combined with the more frequent gamma emission of ^{47}Sc. While further investigation is required to make a definitive claim, this suggests that ^{47}Sc may be better suited for the treatment of larger metastases or tumors which do not exhibit uniform PSMA expression. Conversely, ^{177}Lu may be better suited for use with small metastases and homogeneous tumors.

The greater intensity of the gamma emission of ^{47}Sc relative to ^{177}Lu also resulted in a 72.6 keV greater energy deposition per decay from 1-100 cm. As the amount of activity administered in TRT is on the order of GBq, and the radioactive and biological half-life of therapeutic radiopharmaceuticals is considerable, this additional downstream dose would require significant consideration in the use of ^{47}Sc over ^{177}Lu. This is especially true as TRT for mCRPC often involves the treatment of metastases which are proximal to bone marrow, a highly radiosensitive organ.

While not visible on the macrodosimetric scale, the PDE curves produced from the microdosimetric radially-varying radiation dose simulation of ^{47}Sc and ^{177}Lu decay showed that, across each 10 nm radial bin from the origin to 0.01 cm, ^{47}Sc deposits its energy

much more uniformly than ^{177}Lu. It is not immediately clear if this might improve the radiobiological effect of ^{47}Sc since the bin width is on the approximate order of the DNA double helix (2 nm), as discussed in the presentation of linear energy transfer in Section 2.1.4., but it is a dosimetric feature worth investigating further. Of course, when examining the summed energy deposition of ^{47}Sc and ^{177}Lu across this range, it would seem that this effect does not translate to any meaningful differences in the shape of the summed energy deposition curve potentially implying that this observation is the result of the oversampling of energy deposition.

The cellular S-value simulations of ^{47}Sc and ^{177}Lu showed ^{177}Lu to universally deposit greater cellular dose per decay than ^{47}Sc with the stratification between the isotopes increasing with higher order cellular localization. As such, ^{47}Sc only deposited 50.7% of the nuclear dose per decay as ^{177}Lu when localized to the nucleus, but deposited 66.8% of the ^{177}Lu dose per decay when localized to the cytoplasm, and 73.0% when localized to the cell surface. While not identical, this pattern was mirrored in the DNA DSBs simulation results in which ^{47}Sc induced 14.4% of the number of DSBs when induced by ^{177}Lu when localized to the nucleus, 72.8% when localized to the cytoplasm, and 78.2% when localized to the cell surface.

At first glance these results give the appearance that ^{177}Lu is a vastly superior therapeutic isotope to ^{47}Sc because of the large difference in cellular dose deposition and induced DSBs under the nucleus to nucleus source target configuration. This would be true in the event that a DOTA-based ligand that readily localizes to the nucleus is designed; however, the current array of peptide radiopharmaceuticals are not capable of nuclear uptake or internalization, although this is currently a major area of study in radiopharmaceutical design. Moreover, with that level of localization, alpha particle or Auger electron emitting isotopes would be vastly superior choices for TRT thus rendering the debate between ^{47}Sc and ^{177}Lu moot.

When contextualized to PSMA-617, a ligand which undergoes both cellular uptake and

internalization but does not localize to the nucleus, the cellular S-value and DNA DSBs simulations indicate that ^{177}Lu has a slight edge over ^{47}Sc with regards to unicellular dosimetry and biological effect. As both of these deficiencies could be overcome by proportionally increasing the administered activity of ^{47}Sc beyond what would be utilized with ^{177}Lu, the capacity of ^{47}Sc to provide any therapeutic advantage over ^{177}Lu likely rests upon the capacity for predictive dosimetry with ^{43}Sc or ^{44}Sc. If the maximum dose of ^{47}Sc that can be safely administered to a given patient, as determined by predictive dosimetry for organs at risk with radioscandium PET, is greater than these thresholds, it is possible that the additional treatment aggressiveness afforded by radioscandium true theranostics would be sufficient to see improved outcomes relative to the ^{177}Lu standard.

6.5 Conclusion

Monte Carlo simulations were developed to analyze how the decay physics of the of the radioscandiums influence their dosimetric and radiobiological properties, and to facilitate a comparison between the radioscandiums and their clinically utilized analogues, ^{68}Ga and ^{177}Lu. This was achieved through the simulation of energy deposition curves, unicellular dosimetry based on the MIRDcell formalism, and the induction of DNA DSBs.

These simulations indicated that ^{43}Sc and ^{44}Sc have similar dosimetric distributions to the clinically utilized ^{68}Ga with the exception of the excess downstream energy deposition produced by the high energy gamma emission of ^{44}Sc. In this regard, the additional dosimetric and health physics considerations that must be taken with the potential clinical implementation of ^{44}Sc provide a strong argument for the preferential development of ^{43}Sc as the primary diagnostic radioscandium in spite of its less accessible production methodology.

Applying these same simulations to the therapeutic isotopes, while the ^{47}Sc beta electron emission was found to deposit less energy than ^{177}Lu at the origin, it was shown to deposit slightly more cumulative energy over its entire path as a consequence of its greater initial

kinetic energy. The energy deposition of the ^{47}Sc beta electron was therefore also found to deposit its energy over a slightly broader range than observed with ^{177}Lu decay. As such, it is likely that the therapeutic application of ^{47}Sc will yield some increased benefit over ^{177}Lu when used to treat larger metastases or non-homogeneously PSMA expressing tumors as a result of the cross-fire effect. However, the higher intensity gamma emission of ^{47}Sc was shown to result in a significant increase in non-local (>1 cm from the decay origin) energy deposition relative to ^{177}Lu thus indicating that ^{177}Lu may be more suitable in scenarios where the target cells are proximal to any dose limiting organs.

While maintaining the same order of magnitude, ^{47}Sc was shown to deposit less nuclear dose and induce less DNA DSBs per decay than ^{177}Lu when localized to the cytoplasm or cell surface. It remains to be seen if these dosimetric and radiobiological deficits can be overcome by the increased treatment aggressiveness that is hypothesized to be enabled with true theranostic dose correlation as such an evaluation will require extensive *in vivo* testing.

CHAPTER 7

CONCLUSIONS AND FUTURE DIRECTIONS

7.1 Summary of Work

The work presented in this dissertation was completed under the lens of three separate objectives rooted in the broad development of radioscandium pharmaceuticals spanning all the way from accelerator-based production to pre-clinical evaluation.

The first objective involved the development of radioscandium production methods using a compact biomedical cyclotron. In this regard, a novel beam-stop conversion system was constructed therefore enabling the utilization of solid targetry with an IBA Cyclone 18/9 dual beam cyclotron. This beam-stop conversion system was utilized for 30 productions of ^{43}Sc via the ^{42}Ca(d,n)^{43}Sc reaction; 1 production of ^{44}Sc via the ^{44}Ca(p,n)^{44}Sc; and 1 production of ^{47}Sc via the ^{48}Ca(p,2n)^{47}Sc reaction. These productions resulted in maximum end of bombardment yields of 1513.0 MBq of ^{43}Sc, 754.1 MBq of ^{44}Sc, and 1498.5 MBq of ^{47}Sc.

As an extension of the first objective, radiochemical separation and DOTA-based radiolabeling methodology was also developed in coincidence with production methodology. These methods facilitated the synthesis of ^{43}Sc-PSMA-617, ^{44}Sc-PSMA-617, and ^{47}Sc-PSMA-617 with peak molar activities of 22.2 MBq/nmol, 28.8 MBq/nmol, and 8.1 MBq/nmol respectively. The resulting radiolabeled compounds derived from these methods facilitated the pre-clinical evaluation which was the primary focus of the next objective. Moreover, as molar activity is an immensely critical factor in radiopharmaceutical specificity, and thus both diagnostic and therapeutic performance, the further refinement of these chemical methodologies will likely be the focal point of the continuation of this work.

The second objective focused on the preliminary pre-clinical evaluation of the radioscandiums with regards to specificity, diagnostic capabilities, and therapeutic effect. In this

regard, *in vitro* blocking and uptake assays were performed which clearly exhibited the specific uptake of radioscandium PSMA-617 in PSMA-expressing enzalutamide resistant LNCaP-EnzaR-Luc cells relative to non-PSMA expressing DU145 cells. Internalization assays characterized that approximately 45%-60% of radioscandium PSMA-617 uptake is internalized thus providing meaningful context for the level of cellular localization of radioscandium PSMA-617. Static ^{43}Sc-PSMA-617 PET images were obtained at 1, 2, 4, and 6-hour timepoints which successfully resolved LNCaP-EnzaR-Luc xenografts in mice, and exhibited the time dependent pharmacokinetics of radioscandium PSMA-617. Dynamic PET images were also acquired with ^{43}Sc-PSMA-617 thus providing even further characterization of radioscandium PMSA-617 pharmacokinetics. Notably, these dynamic scans showed that LNCaP-EnzaR-Luc tumor uptake becomes greater than the uptake in all non-renal tissues in as little as 9.5 minutes with an average tumor to muscle SUV ratio of 6.47-10.45. *Ex vivo* biodistribution studies were also conducted with ^{43}Sc-PSMA-617 at 2, 4, and 6 hours post-injection. Much like the multi-timepoint imaging, these biodistribution studies exhibited a rapid clearance of radioactivity from the renal system whilst maintaining tumor uptake. Specifically, the ratio of percent injected dose per gram of tissue (%ID/g) in the tumor relative to kidney was observed to increase from to 0.59, to 2.60, to 6.76 from the 2, 4, and 6-hour time points. This indicates that the exploitation of the longer half-life of ^{43}Sc-PSMA-617 should facilitate improved diagnostic capabilities near regions of non-specific uptake as was hypothesized.

While the characterization of ^{47}Sc-PSMA-617 was much less thorough than that of ^{43}Sc-PSMA-617 due to the market scarcity of both the isotope itself and its calcium target material, SPECT images were also obtained with highly variable levels of tumor resolvability that coincided with the highly variable molar activity of ^{47}Sc-PSMA-617. Notably, serial imaging of individual mice with both ^{43}Sc-PSMA-617 PET and ^{47}Sc-PSMA-617 SPECT were also acquired. While these experiments also had mixed results that were contingent on

molar activity, a set of images were produced which highlighted similar tumor morphology on PET and SPECT. Although co-registration of these images and correlative dose prediction was unfortunately not plausible for logistical reasons, the clear similarities between these two images are still a major leap in the development of radioscandium theranostics. As ^{47}Sc-PSMA-617 is primarily intended for use as a therapeutic radiopharmaceutical, an attempt was made to characterize its induction of DNA double strand breaks with γ-H2AX immunohistochemistry in excised LNCaP-EnzaR-Luc xenografts. Unfortunately, the maximum achievable molar activity of ^{47}Sc-PSMA-617 at the time of this work was simply too low for any observable biological effect to be achieved.

Although we selected ^{43}Sc-PSMA-617 as our diagnostic radioscandium of focus at the beginning of this work, one imaging experiment was attempted utilizing ^{44}Sc-PSMA-617. As a result of the high energy gamma emission of ^{44}Sc-PSMA-617, the detectors of our PET system quickly became saturated thus confirming some of our concerns with the isotope and reaffirming our selection of ^{43}Sc-PSMA-617 based upon its decay profile. Despite this, an *ex vivo* biodistribution study was able to be performed with ^{44}Sc-PSMA-617 at 4-hours post-injection thus yielding a similar biodistribution of activity to ^{43}Sc-PSMA-617 and a tumor to kidney ratio of detected counts per gram tissue of 1.15.

The final objective of this dissertation was to utilize the Monte Carlo simulation program TOPAS to define the dosimetric and radiobiological properties of the radioscandiums and contextualize those results to their clinically utilized analogues, ^{68}Ga and ^{177}Lu. In this regard, simulations of radially-varying radiation dosimetry showed similar energy deposition patterns between ^{43}Sc, ^{44}Sc, and ^{68}Ga with the exception of an elevated deposition of energy at 1-100 cm from the decay origin in ^{44}Sc decay as a result of its high energy gamma emission. ^{47}Sc was shown to have a slightly extended energy deposition profile relative to ^{177}Lu with ^{177}Lu depositing more energy at the origin of decay but ^{47}Sc depositing more energy from 0.02-0.1 cm. As such, it was hypothesized that ^{47}Sc may be more suitable than ^{177}Lu for

utilization with larger metastases due to the cross-fire effect. The higher intensity of the ^{47}Sc gamma ray emission relative to the gamma ray emission of ^{177}Lu also resulted in an approximately two times larger fraction of its overall energy deposition occurring beyond 0.1 cm, therefore suggesting that ^{47}Sc may require considerations beyond the standard practice with ^{177}Lu when predicting non-target organ dose.

Unicellular S-values and DNA double strand break induction were also simulated in a concentric shell geometry modeled after the main cellular compartments considered in radiopharmaceutical development (cell surface, cytoplasm, nucleus). Mimicking the physical conditions observed in the uptake and internalization of radioscandium PSMA-617, ^{47}Sc was observed to deliver 66.8% of the nuclear dose per decay as ^{177}Lu when localized to the cytoplasm and 73.0% when localized to the cell surface. Similarly, the DNA DSB simulation results indicated that ^{47}Sc delivered 72.8% of the DNA DSBs as ^{177}Lu when localized to the cytoplasm and 78.2% when localized to the cell surface. As such, these two simulations provided evidence that ^{47}Sc is slightly inferior to ^{177}Lu at inducing cellular damage when localized to the cytoplasm or cell surface as is the case when conjugated with PMSA-617. However, as these results were still fairly comparable, the capacity of ^{47}Sc to be clinically relevant likely lies within its capacity to be utilized more aggressively than ^{177}Lu as a result of true theranostic predictive dosimetry with ^{43}Sc or ^{44}Sc.

7.2 Conclusions

Under the context of radioscandium radiopharmaceutical development, this work has provided a holistic perspective on the broader pipeline of true theranostic development including: simulation based dosimetric modeling, radiobiology, accelerator-based radioisotope production, radiochemistry, and pre-clinical assessment both *in vitro* and *in vivo*. The methodology and results developed throughout this work have therefore also provided a novel outlook on the viability of the true theranostic application of the radioscandiums along with the sequen-

tial developments which must be undergone for that viability to reach realization.

In this regard, the proof-of-concept calcium based cyclotron irradiations which were showcased for the production of ^{43}Sc, ^{44}Sc, and ^{47}Sc have provided proof of the technical feasibility of producing the compendium of medically relevant radioscandium isotopes. This development was aided by the creation of a novel beam-stop conversion system which enabled solid target based production on a standard biomedical cyclotron equipped with only liquid and gas targetry, a development which stands to improve the accessibility to radioscandium production if adopted by other production facilities.

Despite this, it is still impossible to ignore the challenges of radioscandium production when put into practical and economic context. Most notably, the incredible scarcity of the enriched ^{48}Ca material needed to produce ^{47}Sc via the ^{48}Ca(p,2n)^{47}Sc reaction poses an immense problem for the further development of ^{47}Sc therapeutics, especially under the context that the activity produced in our proof-of-concept production was of insufficient concentration to synthesize ^{47}Sc-PSMA-617 at a therapeutically meaningful molar activity in spite of the yield being highly promising. Similarly, the high expense of the ^{42}Ca material needed to produce ^{43}Sc via the ^{42}Ca(d,n)^{43}Sc reaction, along with its less accessible deuteron based production route, makes it difficult to recommend over the much cheaper to produce ^{44}Sc in spite of its objectively inferior high positron kinetic energy and high energy gamma ray emission.

Naturally, these issues can be partially mitigated through the improvement of calcium recycling methodology and the refinement of radiolabeling techniques, especially for the preclinical phases of development; however, it also becomes increasingly clear that for scandium true theranostics to ever become accessible enough to have any clinical relevancy, significant focus will need to be placed on improving the commercial availability of isotopically enriched calcium.

Under the lens of pre-clinical evaluation, it has been made abundantly clear through the

myriad of cellular specificity assays, static and dynamic PET images, and *ex vivo* biodistribution data presented in this work that ^{43}Sc-PSMA-617 exhibits clear specificity towards PSMA-expressing tissue and is highly capable in the identification of PSMA-expressing tumors. However, all of these evaluations were also done in the absence of comparative testing with ^{68}Ga-PSMA-617, ^{18}F piflufolastat, or ^{18}F flotufolastat thus making it impossible to draw direct comparisons with current clinical standards. As such, while ^{43}Sc-PSMA-617 stands as an immensely promising diagnostic radiopharmaceutical with highly favorable decay physics relative to ^{68}Ga and ^{18}F, further testing will be necessary to determine its viability in a clinical space which already boasts several options for PSMA PET imaging.

Conversely, the pre-clinical evaluation of ^{47}Sc-PSMA-617 still necessitates significant developments as an unfortunate consequence of the commercial scarcity of both the ^{47}S radionuclide itself and the underlying ^{48}Ca material needed to produce it. This is further exacerbated by the fact that much of the pre-clinical evaluation necessary in this aspect of radioscandium true theranostic development is therapeutic and thus requires large activity amounts that can be radiolabeled at appreciable molar activities. With the limited supply of ^{47}Sc available for this work, it was still however possible to exhibit the specificity of ^{47}Sc-PSMA-617 to PSMA expression and develop proof-of-concept SPECT images which showed clear detection of PSMA expressing tumors with sufficient molar activity. While far from true theranostic predictive dosimetry, this work also produced the first images of individual mice imaged with both ^{43}Sc-PSMA-617 PET and ^{47}Sc-PSMA-617 SPECT with the images associated with the highest molar activity of ^{47}Sc-PSMA-617 showing particularly strong agreement in tumor morphology.

Given the insufficient supply of ^{47}Sc, TOPAS based Monte Carlo simulations were utilized to probe the therapeutic efficacy of ^{47}Sc relative to the ^{177}Lu clinical standard independent of production or radiochemical limitations. In this regard, ^{47}Sc was shown to have a slightly more extended energy deposition profile relative to ^{177}Lu thus indicating a possible advantage

in therapeutic effect when targeting larger metastases or inhomogeneously PSMA expressing tumors due to the cross-fire effect. When examining unicellular dose and the induction of DNA double strand breaks, ^{47}Sc was found to be marginally inferior to ^{177}Lu when localized to the cell membrane or cytoplasm; however, this trend could potentially reverse in cellular clusters due to the dosimetric profile previously described.

When applying this same set of simulations to the diagnostic radioscandiums and ^{68}Ga, the heightened non-local dose deposited by ^{44}Sc relative to ^{68}Ga was particularly notable thus validating our selection of ^{43}Sc as the most viable diagnostic radioscandium in spite of its production challenges. In this context, the dose profile of ^{43}Sc was comparable to ^{68}Ga thus providing further evidence to its potential as a diagnostic agent, especially with the added context of its longer half-life and hypothesized superior PET resolution over ^{68}Ga.

Ultimately, this work has created a foundation for the continued development of radioscandium true theranostics from the perspective of the entire pipeline of radiopharmaceutical development whilst most critically providing evidence for the immense potential of ^{43}Sc-PSMA-617, ^{44}Sc-PSMA-617, and ^{47}Sc-PSMA-617 within the mCRPC and broader nuclear medicine spaces. Although, significant work remains to fully realize the potential of radioscandium true theranostics, it is therefore our hope that this dissertation serves as a suitable starting point. In that regard, potential future directions for the continued development of radioscandium true theranostics are discussed below.

7.3 Future Directions

7.3.1 Production of Radioscandiums

Although it has been clearly exhibited in Chapter 4 that our design of the beam-stop conversion system for solid target irradiations was more than capable of generating enough activity to support the multitude of preclinical experiments described in this work, the present design

fails to maximize the amount of radioactivity that can be produced due to its inadequate contact with the cooling cone of the beam-stop. That is to say, in the experiments described in this work, we have limited the deuteron current on target to ensure that the target would not overheat and thus char or combust as a precaution. Consequently, it would be beneficial to design an improved beam-stop conversion system which has thermal contact with the entire stepped cooling cone of the beam-stop thus facilitating significantly greater heat dissipation. Such a design is exhibited in Figure 7.1.

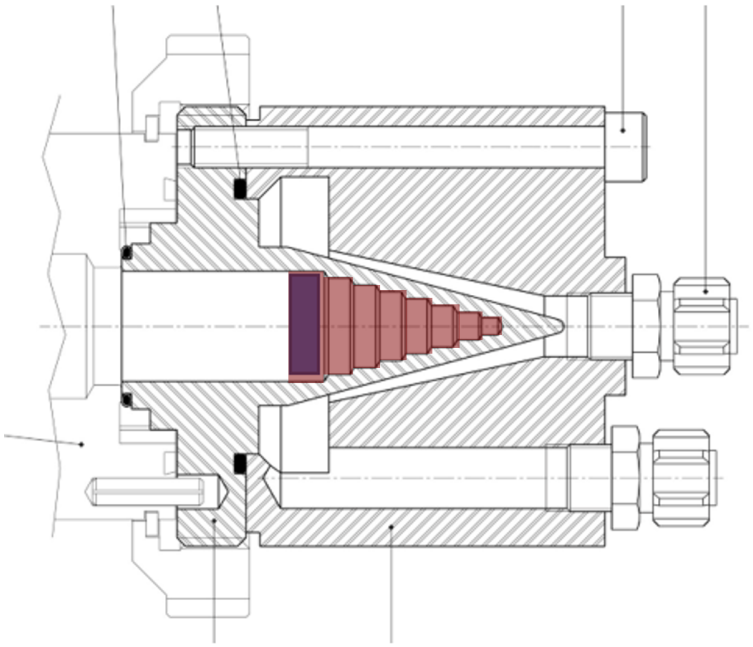

Figure 7.1: A proposed improved design of the solid target holder conversion system which would enable greater thermal contact with the beam-stop. The purple shading indicates the current solid target holder design whereas the red shading indicates the proposed design.

While much of this thesis has discussed the actual production methodology of the radioscandiums from a practical perspective, further work must be done to systematically characterize the ^{42}Ca(d,n)^{43}Sc; ^{44}Ca(p,n)^{44}Sc; and ^{48}Ca(p,2n)^{47}Sc reactions such that general, accurate yield estimates can be made. While several elements of such a characterization, such as measuring the deuteron stopping power in CaO, would require highly specialized laboratory equipment, it would be feasible to use the exact cyclotron setup described in this

work to generate an experimental estimate of each of those cross-sections. This could be accomplished by subtracting the end of bombardment yields for two productions with a nominal difference in incident beam energy as per Equation 7.1 where σ describes the cross section, E is the beam energy, Y is the end of bombardment yield, and S is the stopping power [238, 239].

$$\sigma(E; E + \Delta E) = \frac{[Y(E + \Delta E) - Y(E)] \cdot S(E; E + \Delta E)}{\Delta E} \tag{7.1}$$

In this equation the lack of experimental information about the stopping power of deuterons in CaO is still a significant limitation; however, this methodology would still provide more experimental information about the ^{42}Ca(d,n)^{43}Sc; ^{44}Ca(p,n)^{44}Sc; and ^{48}Ca(p,2n)^{47}Sc cross-sections than presently exist in the literature.

By extension, while any yield estimation methodology will be limited by the lack of experimental cross-section and stopping power data, the implementation of TOPAS based Monte Carlo simulations as predictors of yield could prove immensely useful in the planning of radioscandium productions and could serve as a second comparison to the yield estimation method exhibited in Chapter 4. As we look to practical implementation of the radioscandiums in the pre-clinical and clinical space, the development of yield estimation tools such as this is critical when the amount of activity needed for downstream use is a known quantity. One potential methodology for this yield estimation would be to emulate experimental cross-section measurement methodology and thus simulate the irradiation of a stack of thin targets within the TOPAS ecosystem as has been illustrated by Broder et al [240, 241].

7.3.2 Further Refinement of Radiochemistry

Because the molar activity or radiochemical purity of radiopharmaceuticals is pivotal to their specificity and thus effectiveness in *vitro* and *in vivo*, continued efforts must also be made

to improve these quantities especially if we look to potential in-human use in the future [242]. This is principally true for ^{47}Sc-PSMA-617 which is more difficult to produce in large quantities (limiting its concentration during radiosynthesis with PSMA-617) and mandates higher molar activity to maintain its intended therapeutic effect while limiting dose to the renal system from non-specific retention. Barring the development of new production sites using large accelerators to produce ^{47}Sc, or an increase in ^{48}Ca availability and affordability, rather than looking to improve the radiochemical yield of the radiosynthesis, the most feasible way to improve the molar activity of ^{47}Sc-PSMA-617 would be to chemically separate the unlabeled PSMA-617 precursor from the radiolabeled compound. Naturally, the separation of a radiolabeled and unlabeled ligand is difficult because the addition of a chelated metal to a large ligand results in little change to its chemical properties; however, such a separation is possible through the extensive development of HPLC methodology as there is slight separation between the two compounds in an HPLC chromatogram [243, 244].

7.3.3 Radioscandium PET and SPECT Imaging

While we have focused on *in vivo* imaging throughout this work to emphasize the tumor detection capabilities of ^{43}Sc-PSMA-617 and ^{47}Sc-PSMA-617, it would also be advantageous to measure detectability across isotopes utilizing a Derenzo phantom. When imaged on the same imaging system with identical levels of administered activity, this would enable the quantification of how the full-width at half-maximum (FWHM) imaging resolution of radioscandium PET varies between ^{43}Sc and ^{44}Sc, or even the clinically used ^{68}Ga [245]. By extension, similar data could be obtained comparing ^{47}Sc and ^{177}Lu SPECT to facilitate a full comparison of radioscandium imaging performance to the current standard of care.

It would also be greatly useful to further characterize the imaging quality of ^{43}Sc with other PET phantoms. Particularly, as we look towards initiating a first in-human study of ^{43}Sc-PSMA-617 in the near future, it would be highly useful to image a humanoid phantom

such as the NEMA IEC body phantom with a PET/CT system designed for human use, especially if repurposed specifically to assess prostate PET performance [246]. As an extension of this, it would also be valuable to assess the detectability of small lesions (<5 mm) with ^{43}Sc-PSMA-617 PET as smaller tumors are a potential indicator of high-risk prostate cancer and also prominent in metastatic disease [247, 248]. This could potentially be accomplished through the imaging of alternative body phantoms such as the Data Spectrum Jaszczak ECT Phantom or the National Institute of Metrology body PET/CT phantom [248, 249].

7.3.4 Murine Metastases Model

While the mice employed in this work have been optimal for the exhibition of radioscandium-PSMA-617 specificity to PSMA-expressing tumors, they are not necessarily an ideal characterization of the metastatic disease for which these models are intended to emulate by nature of being ectopic tumors [250]. Specifically, orthotopic models of prostate cancer have been shown to better emulate the tumor microenvironment of clinically observed prostate cancers with regards to vascular perfusion, microvasculature density, and hypoxic burden [251, 252].

For radiopharmaceutical applications in mCRPC, the analysis of metastatic sites is of particular importance as these sites can be proximal to organs with heightened risks of hematologic toxicity [60]. One such risk is that of bone metastasis which are often a dose limiting factor in TRT with ^{177}Lu-PSMA-617 due to the adverse effects of radiation induced damage to bone marrow [60–62].

One viable method of inducing and modeling these bone metastases in mice is through intracardiac injection, particularly when using ultrasound guidance [253–256]. Essentially, by precisely injecting cancer cells into the left ventricle, it is possible to bypass the pulmonary capillaries and reliably produce bone metastasis despite skeletal blood-flow being a minimal portion of cardiac output [254, 257].

By using this technique to create mice with enzalutamide resistant LNCaP bone metas-

tases it would therefore be possible to evaluate the performance of radioscandium theranostics in a model which closely parallels the clinical realities of mCRPC, a natural next-step in the development of radioscandium theranostics prior to proposal of in-human studies.

7.3.5 Multicellular S-Values

As previously alluded to in the discussions of radially-varying radiation dose and unicellular S-values in Chapter 6, it would be incredibly useful to adopt the multicellular geometry utilized by MIRDcell to expand the cellular dosimetry simulations conducted in this work to include cellular clusters thus producing cross-dose S-values as described in Goddu et al. [204]. While outside the scope of the formalism set forth by MIRD, this multicellular geometry could also be applied to the simulation of DNA DSBs to fully characterize how the cross-fire effect influences radiobiological effect and cross-cellular dose in the comparison of ^{47}Sc and ^{177}Lu. Given the slightly extended dose profile that was observed for ^{47}Sc in the simulations of radially-varying radiation dose, we anticipate that such a simulation would definitively illustrate that ^{47}Sc is capable of inducing an increased level of cellular damage relative to ^{177}Lu in cellular clusters thus solidifying its viability as a potential therapeutic for large metastases or tumors with inhomogeneous PSMA expression. As Monte Carlo is characterized by its unique capacity for precise adjustments within experimental simulation geometry, it might also be feasible to perform these simulations with variable cellular cluster size to precisely define the point, if any, at which ^{47}Sc becomes therapeutically superior to ^{177}Lu.

7.3.6 Radiobiology in TOPAS Monte Carlo

While the Monte Carlo-based characterization of the radioscandiums described in Chapter 4 has included evaluations of both physical and radiobiological characteristics, TOPAS offers a wealth of tools that could allow for a more holistic characterization. Notably, our radio-

biological simulations only considered direct damage caused to DNA by ionizing radiation whereas indirect radiochemical effects play a significant role in the creation of DNA double strand breaks in real biological systems [258, 259]. In this regard, TOPAS is capable of simulating the production of free radical species in cytosol-like fluid through the TOPAS-nBIO extension [201, 260]. Utilizing this information, it is possible to generate G-value which describes the yield of reactive species generated per 100 eV of energy deposited into the cellular environment by ionizing radiation [261]. This data could also be compared to *in vitro* measurements of free radical production with electron paramagentic resonsance (EPR) thus providing the framework for a robust comparison of the radioscandiums to ^{68}Ga-PSMA-11 and ^{177}Lu when conjugated to PMSA-617 and administered to a cellular system [262–264].

7.3.7 Translation to the Clinical Space

The penultimate goal of radiopharmaceutical development is almost always the translation of a novel drug into the clinical space. In this regard, a minimal amount of clinical testing has been conducted with the radioscandiums within the literature. Neither ^{43}Sc or ^{47}Sc have ever been utilized in-human while ^{44}Sc has been the subject of two first-in-human studies. The first of these studies successfully exhibited the suitability of ^{44}Sc-DOTANOC for neuroendocrine neoplasm PET imaging, and the other exhibited that ^{44}Sc-PSMA-617 could be suitably used for the PET imaging of mCRPC [115, 265]. These two highly promising results provide great optimism for the clinical viability of the other radioscandiums due to their shared pharmacokinetics; however, each radioscandium still must be individually tested given that each scandium isotope has unique decay properties which influence dosimetry, biological effect, and image quality as was outlined in Chapters 2 and 6. Moreover, while these first-in-human results are promising, there is still a pressing need for a larger scale clinical evaluation with the radioscandiums to truly grasp their suitability to the clinical space and their performance relative to current clinical standards. Within that context, it

is our hope that the breadth of pre-clinical results that we have generated for ^{43}Sc-PSMA-617 will soon facilitate the first-in-human use of ^{43}Sc as a stepping stone for the eventual development of a clinical trial. Naturally, it is our hope to eventually develop sufficient data to also move forward with the first-in-human utilization of ^{47}Sc-PSMA-617; however, such translation will require significant advances in ^{48}Ca availability and radiochemical labeling or purification techniques as was mentioned earlier in this chapter.

7.3.8 Translation to other Cancer Targets

The implementation of radioscandium theranostics with PSMA-617 is just one example of the utility potentially achievable with true theranostic radionuclide treatment planning and therapy. Even within the space of mCRPC there is vast potential for the use of radioscandiums with other experimental ligands that utilize a different chelation complex, such as DOTAGA, or alter the linker between the chelation complex and the PSMA binding moiety in an effort to reduce uptake into radiosensitive organs such as the renal system and salivary glands [72, 266, 267]. Among these, PSMA-I&T particularly stands out as an optimal ligand for radioscandium theranostics as, when utilized in ^{177}Lu based TRT, it has been shown to exhibit half the whole body half-life of PSMA-617 with comparable absorbed dose in tumors in humans, induce minimal nephrotoxicity in pre-clinical murine experiments, and act as a suitable neoadjuvant therapy in conjunction with radical prostatectomy [268–270].

Contrary to its namesake, in recent years, PSMA has also been found to be over-expressed in several other cancers providing potential pathways for future innovations beyond prostate cancer. Specifically, PSMA expression has also been observed in select forms of breast, ovarian, endometrial, lung, colorectal, bladder, and pancreatic cancers, as well as renal cell carcinoma and multiple myeloma among other oncologic diseases [271–273]. Given the already immense prominence of PSMA-targeting radiopharmaceuticals in the nuclear medicine space, it is unsurprising that PSMA-targeting ligands, including PSMA-617, are presently

being tested in case reports and clinical trials for the targeting of non-prostatic cancers such as those mentioned above [274]. The broadening potential of PSMA-617 beyond prostate cancer gives further credence to the notion that there is value in re-purposing presently utilized ligands with novel radionuclides given the increasing number of morphologies and pathologies that may benefit from having multiple options in radionuclide selection.

Beyond the diagnosis, staging, and treatment of mCRPC with ^{68}Ga-PSMA-617 and ^{177}Lu-PSMA-617, the ^{68}Ga and ^{177}Lu pseudo theranostic pair is also utilized clinically for the treatment of neuroendocrine tumors (NETs) when conjugated with DOTATATE, a ligand which targets the expression of somatostatin receptor type 2 (SSTR2). Analogous to the utilization of ^{68}Ga and ^{177}Lu for mCRPC theranostics, ^{177}Lu-DOTATATE (LUTATHERA) TRT has been shown to greatly improve mean survival time and progression-free survival time in patients with NETs; however, estimation of therapeutic dose with ^{68}Ga-DOTATATE (NETSPOT) PET still requires further refinement, exhibiting a mean absolute percent error of up to 18.0% when estimating renal dose [275–278].

Naturally, the demonstrated difficulty in correlating the physiological distribution of ^{68}Ga-DOTATATE to downstream ^{177}Lu-DOTATATE dosimetry limits the capacity to which ^{68}Ga and ^{177}Lu based DOTATATE theranostics can be utilized to increase treatment aggressiveness, particularly as the kidneys are a dose limiting organ in ^{177}Lu-DOTATATE TRT [279]. Consequently, the development of other DOTATATE radiopharmaceuticals which utilize true theranostic isotopes could enable a more ideal correlation between diagnostic imaging and therapeutic dose.

As implied by the name, DOTATATE utilizes a DOTA chelation complex to bind to ^{68}Ga and ^{177}Lu thus meaning that the DOTATATE ligand is also compatible with the radioscandiums [280]. To that end, the PSMA-617 and DOTATATE ligands are similar enough that the entire radiochemistry procedure described in Chapter 4 does not need any alteration aside from the substitution of PSMA-617 for DOTATATE in radiolabeling. Consequently,

the development of ^{43}Sc-DOTATATE, ^{44}Sc-DOTATATE, and ^{47}Sc-DOTATATE theranostics is a natural progression of this work, and, in fact, has been a parallel endeavor within this group as is illustrated in Zhang et al. [281, 282].

Our group has also identified and begun investigation of other novel targets for radioscandium application. For example, as is shown in Bhuiyan et al., ^{47}Sc can be conjugated with humanized monoclonal antibody 3D1 (mAb 3D1) and utilized to target the MUC1-C oncoprotein as is overexpressed in a multitude of cancers [283]. Similarly, our group has also successfully conjugated the radioscandiums with DOTA-linked triphenylphosphonium (TPP^+) and tetraphenylphosphonium ($TetPP^+$) for the targeting of mitochondrial disorders [284]. With this diverse array of potential radioscandium pharmaceuticals, it is our hope that versatility of the radioscandiums permeates throughout the nuclear medicine space and finds applications across various ligands and biological targets with radioscandium PSMA-617 being the mere starting point in true theranostic development.

REFERENCES

[1] Jean-Luc Urbain, Andrew M Scott, Sze Ting Lee, John Buscombe, Charlotte Weston, Jun Hatazawa, Seigo Kinuya, Baljinder Singh, Mohamad Haidar, Andrew Ross, Francois Lamoureux, Jolanta Kunikowska, Wolfgang Wadsak, Rudi Dierckx, Diana Paez, Francesco Giammarile, Kyung-Han Lee, Joo Hyun O, Modiselle Moshe, Lizette Louw, Stuart More, Helen Nadel, Daniel Lee, and Richard Wahl. Theranostic radiopharmaceuticals: A universal challenging educational paradigm in nuclear medicine. *J. Nucl. Med.*, 64(6):986–991, June 2023.

[2] Jean-Marc Idée, Stéphanie Louguet, Sébastien Ballet, and Claire Corot. Theranostics and contrast-agents for medical imaging: a pharmaceutical company viewpoint. *Quant. Imaging Med. Surg.*, 3(6):292–297, December 2013.

[3] I Gilham. Theranostics: An emerging tool in drug discovery and commercialisation. *Drug Discov World*, 6:24–32, 2002.

[4] John Funkhouser. Reinventing pharma: the theranostic revolution. *Curr Drug Discov*, 2:17–19, 2002.

[5] PharmaNetics Inc. Securities and exchange commission form s-3. `https://www.sec.gov/Archives/edgar/data/1072546/000095016803002126/ds3.htm`, June 2003.

[6] Shahid Karim, Nasir Ali Siddiqui, Mohammad Imran Khan, Muhammad Wahajuddin, and Shariq Syed. Editorial: Novel theranostic agents for precision therapeutics. *Front. Pharmacol.*, 15:1407366, April 2024.

[7] Sneha S Kelkar and Theresa M Reineke. Theranostics: combining imaging and therapy. *Bioconjug. Chem.*, 22(10):1879–1903, October 2011.

[8] José Flávio Gomes Marin, Rafael F Nunes, Artur M Coutinho, Elaine C Zaniboni, Larissa B Costa, Felipe G Barbosa, Marcelo A Queiroz, Giovanni G Cerri, and Carlos A Buchpiguel. Theranostics in nuclear medicine: Emerging and re-emerging integrated imaging and therapies in the era of precision oncology. *Radiographics*, 40(6):1715–1740, October 2020.

[9] Thomas Langbein, Wolfgang A Weber, and Matthias Eiber. Future of theranostics: An outlook on precision oncology in nuclear medicine. *J. Nucl. Med.*, 60(Suppl 2):13S–19S, September 2019.

[10] Anna Yordanova, Elisabeth Eppard, Stefan Kürpig, Ralph Bundschuh, Stefan Schönberger, Maria Gonzalez-Carmona, Georg Feldmann, Hojjat Ahmadzadehfar, and Markus Essler. Theranostics in nuclear medicine practice. *Onco. Targets. Ther.*, 10:4821–4828, October 2017.

[11] Brian J Burkett, David J Bartlett, Patrick W McGarrah, Akeem R Lewis, Derek R Johnson, Kezban Berberoğlu, Mukesh K Pandey, Annie T Packard, Thorvardur R Halfdanarson, Carrie B Hruska, Geoffrey B Johnson, and A Tuba Kendi. A review of theranostics: Perspectives on emerging approaches and clinical advancements. *Radiol. Imaging Cancer*, 5(4):e220157, July 2023.

[12] Geoffrey M Currie and Eric M Rohren. Sharpening the blade of precision theranostics. *Semin. Nucl. Med.*, February 2025.

[13] Eric O Aboagye, Tara D Barwick, and Uwe Haberkorn. Radiotheranostics in oncology: Making precision medicine possible. *CA Cancer J. Clin.*, 73(3):255–274, May 2023.

[14] Edward B Silberstein. Radioiodine: the classic theranostic agent. *Semin. Nucl. Med.*, 42(3):164–170, May 2012.

[15] Frederik A Verburg, Alexander Heinzel, Heribert Hänscheid, Felix M Mottaghy, Markus Luster, and Luca Giovanella. Nothing new under the nuclear sun: towards 80 years of theranostics in nuclear medicine. *Eur. J. Nucl. Med. Mol. Imaging*, 41(2):199–201, February 2014.

[16] C T Sawin and D V Becker. Radioiodine and the treatment of hyperthyroidism: the early history. *Thyroid*, 7(2):163–176, April 1997.

[17] Carl K Hoh. Clinical use of FDG PET. *Nucl. Med. Biol.*, 34(7):737–742, October 2007.

[18] Sharmila Banerjee, Maroor Raghavan Ambikalmajan Pillai, and Natesan Ramamoorthy. Evolution of tc-99m in diagnostic radiopharmaceuticals. *Semin. Nucl. Med.*, 31(4):260–277, October 2001.

[19] Wenjie Zhang, Weiwei Zhao, Zhiyun Jia, and Houfu Deng. Strontium-89 therapy for the treatment of huge osseous metastases in prostate carcinoma: A case report. *Exp. Ther. Med.*, 5(2):608–610, February 2013.

[20] C K Lee, D M Aeppli, J Unger, R J Boudreau, and S H Levitt. Strontium-89 chloride (metastron) for palliative treatment of bony metastases. the university of minnesota experience. *Am. J. Clin. Oncol.*, 19(2):102–107, April 1996.

[21] Oliver Sartor. Overview of samarium sm 153 lexidronam in the treatment of painful metastatic bone disease. *Rev. Urol.*, 6 Suppl 10:S3–S12, 2004.

[22] Antonio J Grillo-López. Zevalin: the first radioimmunotherapy approved for the treatment of lymphoma. *Expert Rev. Anticancer Ther.*, 2(5):485–493, October 2002.

[23] Stanley J Goldsmith. Radioimmunotherapy of lymphoma: Bexxar and zevalin. *Semin. Nucl. Med.*, 40(2):122–135, March 2010.

[24] Julie M Vose. Bexxar®: Novel radioimmunotherapy for the treatment of low-grade and transformed low-grade non-hodgkin's lymphoma. *Oncologist*, 9(2):160–172, April 2004.

[25] Pedro Brugarolas, Jessica Comstock, David W. Dick, Teresa Ellmer, Jonathan W. Engle, Suzanne E. Lapi, Steven H. Liang, Ephraim E. Parent, Naga Vara Kishore Pillarsetty, Svetlana Selivanova, Xiankai Sun, Amy Vavere, and Peter J.H. Scott. Fifty years of radiopharmaceuticals. *Journal of Nuclear Medicine Technology*, 48(Supplement 1):34S–39S, 2020.

[26] Siqi Zhang, Xingkai Wang, Xin Gao, Xueyao Chen, Linger Li, Guoqing Li, Can Liu, Yuan Miao, Rui Wang, and Kuan Hu. Radiopharmaceuticals and their applications in medicine. *Signal Transduct. Target. Ther.*, 10(1):1, January 2025.

[27] Andreas G Wibmer, Hedvig Hricak, Gary A Ulaner, and Wolfgang Weber. Trends in oncologic hybrid imaging. *Eur. J. Hybrid Imaging*, 2(1), December 2018.

[28] Hossein Jadvar and Patrick M Colletti. 18F-NaF/223RaCl2 theranostics in metastatic prostate cancer: treatment response assessment and prediction of outcome. *Br. J. Radiol.*, 91(1091):20170948, November 2018.

[29] Ken Herrmann, Markus Schwaiger, Jason S Lewis, Stephen B Solomon, Barbara J McNeil, Michael Baumann, Sanjiv S Gambhir, Hedvig Hricak, and Ralph Weissleder. Radiotheranostics: a roadmap for future development. *Lancet Oncol.*, 21(3):e146–e156, March 2020.

[30] Othman Al Musaimi. Peptide therapeutics: Unveiling the potential against cancer-a journey through 1989. *Cancers (Basel)*, 16(5):1032, March 2024.

[31] Cesare Berton, Simon Klingler, Stanislav Prytuliak, and Jason P Holland. New tactics in the design of theranostic radiotracers. *npj Imaging*, 2(1), August 2024.

[32] Matteo Bauckneht, Chiara Ciccarese, Riccardo Laudicella, Claudia Mosillo, Francesca D'Amico, Annunziato Anghelone, Alessandro Strusi, Viria Beccia, Sergio Bracarda, Giuseppe Fornarini, Giampaolo Tortora, and Roberto Iacovelli. Theranostics revolution in prostate cancer: Basics, clinical applications, open issues and future perspectives. *Cancer Treat. Rev.*, 124(102698):102698, March 2024.

[33] Melanie Senior. Fresh from the biotech pipeline: fewer approvals, but biologics gain share. *Nat. Biotechnol.*, 41(2):174–182, February 2023.

[34] Thorvardur Ragnar Halfdanarson, Diane Lauren Reidy, Namrata Vijayvergia, Daniel M Halperin, Grace Goldstein, Grace Kong, Michael Michael, Simone Leyden, Simona Grozinsky-Glasberg, Halfdan Sorbye, Kjell E Oberg, Cristina Sierras, and Philip Harris. Pivotal phase III COMPOSE trial will compare ^{177}Lu-edotreotide with best standard of care for well-differentiated aggressive grade 2 and grade 3 gastroenteropancreatic neuroendocrine tumors. *J. Clin. Oncol.*, 40(4_suppl):TPS514–TPS514, February 2022.

[35] Cristina Müller, Katharina A Domnanich, Christoph A Umbricht, and Nicholas P van der Meulen. Scandium and terbium radionuclides for radiotheranostics: current state of development towards clinical application. *Br. J. Radiol.*, 91(1091):20180074, November 2018.

[36] Katherine A Morgan, Stacey E Rudd, Asif Noor, and Paul S Donnelly. Theranostic nuclear medicine with gallium-68, lutetium-177, copper-64/67, actinium-225, and lead-212/203 radionuclides. *Chem. Rev.*, 123(20):12004–12035, October 2023.

[37] Emily B Ehlerding, Carolina A Ferreira, Eduardo Aluicio-Sarduy, Dawei Jiang, Hye Jin Lee, Charles P Theuer, Jonathan W Engle, and Weibo Cai. $^{86/90}$Y-based theranostics targeting angiogenesis in a murine breast cancer model. *Mol. Pharm.*, 15(7):2606–2613, July 2018.

[38] Outi Keinänen, Kimberly Fung, James M Brennan, Nicholas Zia, Matt Harris, Ellen van Dam, Colin Biggin, Amos Hedt, Jon Stoner, Paul S Donnelly, Jason S Lewis, and Brian M Zeglis. Harnessing 64Cu/67Cu for a theranostic approach to pretargeted radioimmunotherapy. *Proc. Natl. Acad. Sci. U. S. A.*, 117(45):28316–28327, November 2020.

[39] Nasim Vahidfar, Elisabeth Eppard, Saeed Farzanehfar, Anna Yordanova, Maryam Fallahpoor, and Hojjat Ahmadzadehfar. An impressive approach in nuclear medicine: Theranostics. *PET Clin.*, 16(3):327–340, July 2021.

[40] Geoff Currie. Theranostics. In *Nuclear medicine and molecular imaging: Technology and techniques*, pages 621–642. Elsevier, 2022.

[41] Xiao Li, Mingming Yu, Jian Yang, Danni Li, Rou Li, Juanli Mao, Changjing Zuo, Zeying Liang, Qiang Li, and Chao Cheng. [18F]AlF-PSMA-11 PET in diagnosing prostate cancer: a head-to-head comparison with [68Ga]Ga-PSMA-11 PET and an exploration of dual-phase scanning. *EJNMMI Rep*, 8(1):28, September 2024.

[42] Partha S Choudhury and Manoj Gupta. Differentiated thyroid cancer theranostics: radioiodine and beyond. *Br. J. Radiol.*, 91(1091):20180136, November 2018.

[43] James R Ballinger. Theranostic radiopharmaceuticals: established agents in current use. *Br. J. Radiol.*, 91(1091):20170969, November 2018.

[44] Rebecca L Siegel, Tyler B Kratzer, Angela N Giaquinto, Hyuna Sung, and Ahmedin Jemal. Cancer statistics, 2025. *CA Cancer J. Clin.*, 75(1):10–45, January 2025.

[45] Katrine L Wallace, Adrienne Landsteiner, Scott H Bunner, Nicole M Engel-Nitz, and Amy N Luckenbaugh. Increasing prevalence of metastatic castration-resistant prostate cancer in a managed care population in the united states. *Cancer Causes Control*, 32(12):1365–1374, December 2021.

[46] Oliver Sartor, Johann de Bono, Kim N Chi, Karim Fizazi, Ken Herrmann, Kambiz Rahbar, Scott T Tagawa, Luke T Nordquist, Nitin Vaishampayan, Ghassan El-Haddad, Chandler H Park, Tomasz M Beer, Alison Armour, Wendy J Pérez-Contreras, Michelle DeSilvio, Euloge Kpamegan, Germo Gericke, Richard A Messmann, Michael J Morris, Bernd J Krause, and VISION Investigators. Lutetium-177-PSMA-617 for metastatic castration-resistant prostate cancer. *N. Engl. J. Med.*, 385(12):1091–1103, September 2021.

[47] Renu S Eapen, James P Buteau, Price Jackson, Catherine Mitchell, Sheng F Oon, Omar Alghazo, Lachlan McIntosh, Nattakorn Dhiantravan, Mark J Scalzo, Jonathan O'Brien, Shahneen Sandhu, Arun A Azad, Scott G Williams, Gaurav Sharma, Mohammad B Haskali, Mathias Bressel, Kenneth Chen, Pocharapong Jenjitranant, Aoife McVey, Daniel Moon, Nathan Lawrentschuk, Paul J Neeson, Declan G Murphy, and Michael S Hofman. Administering [177Lu]Lu-PSMA-617 prior to radical prostatectomy in men with high-risk localised prostate cancer (LuTectomy): A single-centre, single-arm, phase 1/2 study. *Eur. Urol.*, 85(3):217–226, March 2024.

[48] Fda expands pluvicto's metastatic castration resistant prostate cancer indication. `https://www.fda.gov/drugs/resources-information-approved-drugs/fda-expands-pluvictos-metastatic-castration-resistant-prostate-cancer-indication`, March 2025.

[49] Christian Uprimny, Alexander Stephan Kroiss, Clemens Decristoforo, Josef Fritz, Elisabeth von Guggenberg, Dorota Kendler, Lorenza Scarpa, Gianpaolo di Santo, Llanos Geraldo Roig, Johanna Maffey-Steffan, Wolfgang Horninger, and Irene Johanna Virgolini. 68Ga-PSMA-11 PET/CT in primary staging of prostate cancer: PSA and gleason score predict the intensity of tracer accumulation in the primary tumour. *Eur. J. Nucl. Med. Mol. Imaging*, 44(6):941–949, June 2017.

[50] Ida Sonni, Matthias Eiber, Wolfgang P Fendler, Rejah M Alano, Sitaram S Vangala, Amar U Kishan, Nicholas Nickols, Matthew B Rettig, Robert E Reiter, Johannes Czernin, and Jeremie Calais. Impact of 68Ga-PSMA-11 PET/CT on staging and management of prostate cancer patients in various clinical settings: A prospective single-center study. *J. Nucl. Med.*, 61(8):1153–1160, August 2020.

[51] Phillip H Kuo, Michael J Morris, Jacob Hesterman, A Tuba Kendi, Kambiz Rahbar, Xiao X Wei, Bruno Fang, Nabil Adra, Rohan Garje, Jeff M Michalski, Kim Chi, Johann de Bono, Karim Fizazi, Bernd Krause, Oliver Sartor, Scott T Tagawa, Samson Ghebremariam, Marcia Brackman, Connie C Wong, Ana M Catafau, Taylor Benson, Andrew J Armstrong, and Ken Herrmann. Quantitative 68Ga-PSMA-11 PET and clinical outcomes in metastatic castration-resistant prostate cancer following 177Lu-PSMA-617 (VISION trial). *Radiology*, 312(2):e233460, August 2024.

[52] Phillip Kuo, Jacob Hesterman, Kambiz Rahbar, Ayse T Kendi, Xiao X Wei, Bruno Fang, Nabil Adra, Andrew J Armstrong, Rohan Garje, Jeff M Michalski, Samson

Ghebremariam, Marcia Brackman, Connie Wong, Taylor Benson, and Nicholas J Vogelzang. [^{68}Ga]Ga-PSMA-11 PET baseline imaging as a prognostic tool for clinical outcomes to [^{177}Lu]Lu-PSMA-617 in patients with mCRPC: A VISION substudy. *J. Clin. Oncol.*, 40(16_suppl):5002–5002, June 2022.

[53] Daniel Groener, Sina Schneider, Justus Baumgarten, Christian Happel, Konrad Klimek, Nicolai Mader, Christina Nguyen Ngoc, Jennifer Wichert, Philipp Mandel, Nikolaos Tselis, Frank Grünwald, and Amir Sabet. Baseline [68Ga]Ga-PSMA-11 PET/CT before [177Lu]Lu-PSMA-617 radioligand therapy: Value of PSMA-uptake thresholds in predicting targetable lesions. *Cancers (Basel)*, 15(2):473, January 2023.

[54] Andrew F Voter, Rudolf A Werner, Kenneth J Pienta, Michael A Gorin, Martin G Pomper, Lilja B Solnes, and Steven P Rowe. Piflufolastat F-18 (18F-DCFPyL) for PSMA PET imaging in prostate cancer. *Expert Rev. Anticancer Ther.*, 22(7):681–694, July 2022.

[55] Young-A Heo. Flotufolastat F 18: Diagnostic first approval. *Mol. Diagn. Ther.*, 27(5):631–636, September 2023.

[56] Ruohua Chen, Yining Wang, Yinjie Zhu, Yiping Shi, Lian Xu, Gang Huang, and Jianjun Liu. The added value of 18F-FDG PET/CT compared with 68Ga-PSMA PET/CT in patients with castration-resistant prostate cancer. *J. Nucl. Med.*, 63(1):69–75, January 2022.

[57] Surekha Yadav, Sarasa T Kim, Abuzar Moradi Tuchayi, Fei Jiang, Amanda Morley, Rachelle Saelee, Yingbing Wang, Roxanna Juarez, Courtney Lawnh-Heath, Vadim S Koshkin, and Thomas A Hope. Comparison of 18F-DCFPyL and 68Ga-PSMA-11 for 177Lu-PSMA-617 therapy patient selection. *Front. Oncol.*, 14:1382582, June 2024.

[58] Steffie M B Peters, Regina Hofferber, Bastiaan M Privé, Maarten de Bakker, Martin Gotthardt, Marcel Janssen, Frank de Lange, Constantijn H J Muselaers, Niven Mehra, J Alfred Witjes, Pedro F Costa, James Nagarajah, Mark W Konijnenberg, and Walter Jentzen. [68Ga]Ga-PSMA-11 PET imaging as a predictor for absorbed doses in organs at risk and small lesions in [177Lu]Lu-PSMA-617 treatment. *Eur. J. Nucl. Med. Mol. Imaging*, 49(4):1101–1112, March 2022.

[59] Levent Kabasakal, Mohammad AbuQbeitah, Aslan Aygün, Nami Yeyin, Meltem Ocak, Emre Demirci, and Turkay Toklu. Pre-therapeutic dosimetry of normal organs and tissues of 177Lu-PSMA-617 prostate-specific membrane antigen (PSMA) inhibitor in patients with castration-resistant prostate cancer. *Eur. J. Nucl. Med. Mol. Imaging*, 42(13):1976–1983, December 2015.

[60] Ute Hennrich and Matthias Eder. [177Lu]Lu-PSMA-617 (PluvictoTM): The first FDA-approved radiotherapeutical for treatment of prostate cancer. *Pharmaceuticals (Basel)*, 15(10):1292, October 2022.

[61] Léa Vazquez and Antoine Arnaud. Hematological toxicity induced by bone metastasis radiation therapy. In *Metastasis*, pages 109–116. Exon Publications, May 2022.

[62] Amanda Kristiansson, Oskar Vilhelmsson Timmermand, Mohamed Altai, Joanna Strand, Sven-Erik Strand, Bo Åkerström, and Anders Örbom. Hematological toxicity in mice after high activity injections of 177Lu-PSMA-617. *Pharmaceutics*, 14(4):731, March 2022.

[63] Sangeeta Ray Banerjee, Zhengping Chen, Mrudula Pullambhatla, Ala Lisok, Jian Chen, Ronnie C Mease, and Martin G Pomper. Preclinical comparative study of (68)ga-labeled DOTA, NOTA, and HBED-CC chelated radiotracers for targeting PSMA. *Bioconjug. Chem.*, 27(6):1447–1455, June 2016.

[64] Fanny Lundmark, Gustav Olanders, Sara Sophie Rinne, Ayman Abouzayed, Anna Orlova, and Ulrika Rosenström. Design, synthesis, and evaluation of linker-optimised PSMA-targeting radioligands. *Pharmaceutics*, 14(5):1098, May 2022.

[65] K S Ajish Kumar and Anupam Mathur. Total chemical synthesis of PSMA-11: API for 68Ga-PSMA-11 used for prostate cancer diagnosis. *Eur. J. Med. Chem. Rep.*, 3(100014):100014, December 2021.

[66] Frédéric Bois, Camille Noirot, Sébastien Dietemann, Ismini C Mainta, Thomas Zilli, Valentina Garibotto, and Martin A Walter. [68Ga]Ga-PSMA-11 in prostate cancer: a comprehensive review. *Am. J. Nucl. Med. Mol. Imaging*, 10(6):349–374, December 2020.

[67] Mitsuyoshi Yoshimoto, Yukie Yoshii, Hiroki Matsumoto, Mitsuhiro Shinada, Masashi Takahashi, Chika Igarashi, Fukiko Hihara, Tomoko Tachibana, Ayano Doi, Tatsuya Higashi, Hirofumi Fujii, and Kohshin Washiyama. Evaluation of aminopolycarboxylate chelators for whole-body clearance of free 225ac: A feasibility study to reduce unexpected radiation exposure during targeted alpha therapy. *Pharmaceutics*, 13(10):1706, October 2021.

[68] Margarita Chernysheva, Shaun C Loveless, Tom Brossard, Kaelyn Becker, Shelbie Cingoranelli, Eduardo Aluicio-Sarduy, Jeongseong Song, Paul Ellison, Jerry Nolen, David A Rotsch, Suzanne E Lapi, and Jonathan W Engle. Accelerator production of scandium radioisotopes: Sc-43, sc-44, and sc-47. *Curr. Radiopharm.*, 14(4):359–373, 2021.

[69] S Huclier-Markai, R Kerdjoudj, C Alliot, A C Bonraisin, N Michel, F Haddad, and J Barbet. Optimization of reaction conditions for the radiolabeling of DOTA and DOTA-peptide with (44m/44)sc and experimental evidence of the feasibility of an in vivo PET generator. *Nucl. Med. Biol.*, 41 Suppl:e36–43, May 2014.

[70] Ukihide Tateishi. Prostate-specific membrane antigen (PSMA)-ligand positron emission tomography and radioligand therapy (RLT) of prostate cancer. *Jpn. J. Clin. Oncol.*, 50(4):349–356, April 2020.

[71] Jason Meier. Radiometal components and targeting, 2025. Made in Biorender: https://BioRender.com/ppwyu5g.

[72] Lukas Greifenstein, Nils Engelbogen, Hanane Lahnif, Jean-Philippe Sinnes, Ralf Bergmann, Michael Bachmann, and Frank Rösch. Synthesis, labeling and preclinical evaluation of a squaric acid containing PSMA inhibitor labeled with 68 ga: A comparison with PSMA-11 and PSMA-617. *ChemMedChem*, 15(8):695–704, April 2020.

[73] Vibhu Kapoor, Barry M McCook, and Frank S Torok. An introduction to PET-CT imaging. *Radiographics*, 24(2):523–543, March 2004.

[74] Ernest V Garcia. Physical attributes, limitations, and future potential for PET and SPECT. *J. Nucl. Cardiol.*, 19 Suppl 1(S1):S19–29, February 2012.

[75] Jason Meier. Graphical depiction of pet imaging, 2025. Made in Biorender: https://BioRender.com/ww3xjwr.

[76] Jason Meier. Scatter coincidence, 2025. Made in Biorender: https://BioRender.com/kzaiytz.

[77] Jason Meier. Random coincidence, 2025. Made in Biorender: https://BioRender.com/fp8srr4.

[78] C C Martin, B T Christian, M R Satter, L H Nickerson, and R J Nickles. Quantitative PET with positron emitters that emit prompt gamma rays. *IEEE Trans. Med. Imaging*, 14(4):681–687, 1995.

[79] M E Daube-Witherspoon and R E Carson. Unified deadtime correction model for PET. *IEEE Trans. Med. Imaging*, 10(3):267–275, 1991.

[80] William W Moses. Fundamental limits of spatial resolution in PET. *Nucl. Instrum. Methods Phys. Res. A*, 648 Supplement 1:S236–S240, August 2011.

[81] G F Gribakin. Mechanisms of positron annihilation on molecules. *Phys. Rev. A*, 61(2), January 2000.

[82] L M Carter, Adam Leon Kesner, E C Pratt, V A Sanders, A V F Massicano, C S Cutler, S E Lapi, and Jason S Lewis. The impact of positron range on PET resolution, evaluated with phantoms and PHITS monte carlo simulations for conventional and non-conventional radionuclides. *Mol. Imaging Biol.*, 22(1):73–84, February 2020.

[83] Simon R Cherry, James A Sorenson, and Michael E Phelps. *Physics in Nuclear Medicine*. W B Saunders, London, England, 3 edition, August 2003.

[84] Ichiro Matsunari. New generation SPECT cameras based on cadmium-zinc telluriide technology. *Ann. Nucl. Cardiol.*, 10(1):59–63, October 2024.

[85] Atsuro Suzuki, Wataru Takeuchi, Takafumi Ishitsu, Katsutoshi Tsuchiya, Yuichi Morimoto, Yuichiro Ueno, Keiji Kobashi, Naoki Kubo, Tohru Shiga, and Nagara Tamaki. High-sensitivity brain SPECT system using cadmium telluride (CdTe) semiconductor detector and 4-pixel matched collimator. *Phys. Med. Biol.*, 58(21):7715–7731, November 2013.

[86] Jason Meier. Spect imaging, 2025. Made in Biorender: `https://BioRender.com/g5bmg8l`.

[87] Mahsa Noori-Asl. Investigation of different factors affecting the quality of SPECT images: A simulation study. *J. Med. Phys.*, 45(1):44–51, January 2020.

[88] ZongJian Cao, Lawrence E. Holder, and Charles C. Chen. Optimal number of views in 360° spect imaging. *Journal of Nuclear Medicine*, 37(10):1740–1744, 1996.

[89] Philipp Ritt and Torsten Kuwert. Quantitative SPECT/CT—technique and clinical applications. In *Recent Results in Cancer Research*, Recent results in cancer research. Fortschritte der Krebsforschung. Progres dans les recherches sur le cancer, pages 565–590. Springer International Publishing, Cham, 2020.

[90] Dennis Kupitz, Heiko Wissel, Jan Wuestemann, Stephanie Bluemel, Maciej Pech, Holger Amthauer, Michael C Kreissl, and Oliver S Grosser. Optimization of SPECT/CT imaging protocols for quantitative and qualitative 99mtc SPECT. *EJNMMI Phys.*, 8(1):57, July 2021.

[91] Michael Ljungberg. *Quantitative SPECT Imaging*, pages 473–500. Springer International Publishing, Cham, 2021.

[92] Yousef Khazaei Monfared, Pedram Heidari, Samuel J Klempner, Umar Mahmood, Aparna R Parikh, Theodore S Hong, Matthew R Strickland, and Shadi A Esfahani. DNA damage by radiopharmaceuticals and mechanisms of cellular repair. *Pharmaceutics*, 15(12), December 2023.

[93] Anika Trenner and Alessandro A Sartori. Harnessing DNA double-strand break repair for cancer treatment. *Front. Oncol.*, 9:1388, December 2019.

[94] Caroline Stokke, Monika Kvassheim, and Johan Blakkisrud. Radionuclides for targeted therapy: Physical properties. *Molecules*, 27(17):5429, August 2022.

[95] Giorgio Baiocco, Stefan Bartzsch, Valeria Conte, Thomas Friedrich, Burkhard Jakob, Adrianna Tartas, Carmen Villagrasa, and Kevin M Prise. A matter of space: how the spatial heterogeneity in energy deposition determines the biological outcome of radiation exposure. *Radiat. Environ. Biophys.*, 61(4):545–559, November 2022.

[96] George Sgouros. Radiopharmaceutical therapy. *Health Phys.*, 116(2):175–178, February 2019.

[97] S A Enger, T Hartman, J Carlsson, and H Lundqvist. Cross-fire doses from beta-emitting radionuclides in targeted radiotherapy. a theoretical study based on experimentally measured tumor characteristics. *Phys. Med. Biol.*, 53(7):1909–1920, April 2008.

[98] Nicolaas A P Franken, Rosemarie ten Cate, Przemek M Krawczyk, Jan Stap, Jaap Haveman, Jacob Aten, and Gerrit W Barendsen. Comparison of RBE values of high-LET α-particles for the induction of DNA-DSBs, chromosome aberrations and cell reproductive death. *Radiat. Oncol.*, 6(1):64, June 2011.

[99] Amin I Kassis. Therapeutic radionuclides: biophysical and radiobiologic principles. *Semin. Nucl. Med.*, 38(5):358–366, September 2008.

[100] Narges K Tafreshi, Michael L Doligalski, Christopher J Tichacek, Darpan N Pandya, Mikalai M Budzevich, Ghassan El-Haddad, Nikhil I Khushalani, Eduardo G Moros, Mark L McLaughlin, Thaddeus J Wadas, and David L Morse. Development of targeted alpha particle therapy for solid tumors. *Molecules*, 24(23):4314, November 2019.

[101] Stephen Tronchin, Jake C Forster, Kevin Hickson, and Eva Bezak. Dosimetry in targeted alpha therapy. a systematic review: current findings and what is needed. *Phys. Med. Biol.*, 67(9), April 2022.

[102] Roger W Howell. Advancements in the use of auger electrons in science and medicine during the period 2015-2019. *Int. J. Radiat. Biol.*, 99(1):2–27, 2023.

[103] Anthony Ku, Valerie J Facca, Zhongli Cai, and Raymond M Reilly. Auger electrons for cancer therapy - a review. *EJNMMI Radiopharm. Chem.*, 4(1):27, October 2019.

[104] Takanori Hioki, Yaser H Gholami, Kelly J McKelvey, Alireza Aslani, Harry Marquis, Enid M Eslick, Kathy P Willowson, Viive M Howell, and Dale L Bailey. Overlooked potential of positrons in cancer therapy. *Sci. Rep.*, 11(1):2475, January 2021.

[105] Singh Balraj and Chen Jun. Nuclear data sheets 126, 1. 2015.

[106] Chen Jun and Singh Balraj. Nuclear data sheets 190, 1. 2023.

[107] E.A. Mccutchan. Nuclear data sheets 113, 1735. 2012.

[108] Weller Tilley and Chasteler Chives. Nuclear physics a595, 1. 1995.

[109] M. J. Berger and S. M. Seltzer. Stopping powers and ranges of electrons and positrons, December 1982.

[110] Nicholas P van der Meulen, Maruta Bunka, Katharina A Domnanich, Cristina Müller, Stephanie Haller, Christiaan Vermeulen, Andreas Türler, and Roger Schibli. Cyclotron production of (44)sc: From bench to bedside. *Nucl. Med. Biol.*, 42(9):745–751, September 2015.

[111] Cristina Müller, Maruta Bunka, Josefine Reber, Cindy Fischer, Konstantin Zhernosekov, Andreas Türler, and Roger Schibli. Promises of cyclotron-produced 44sc as a diagnostic match for trivalent β–emitters: in vitro and in vivo study of a 44Sc-DOTA-folate conjugate. *J. Nucl. Med.*, 54(12):2168–2174, December 2013.

[112] Maarten de Bakker, Noa Dominicus, Antoi Meeuwis, Marcel Janssen, Mark W Konijnenberg, James Nagarajah, and Steffie M B Peters. Urinary excretion kinetics of [177Lu]Lu-PSMA-617. *Eur. J. Nucl. Med. Mol. Imaging*, 50(12):3572–3575, October 2023.

[113] Nicholas P van der Meulen, Roger Hasler, Zeynep Talip, Pascal V Grundler, Chiara Favaretto, Christoph A Umbricht, Cristina Müller, Gaia Dellepiane, Tommaso S Carzaniga, and Saverio Braccini. Developments toward the implementation of 44sc production at a medical cyclotron. *Molecules*, 25(20):4706, October 2020.

[114] Ken Herrmann, Kambiz Rahbar, Matthias Eiber, Richard Sparks, Nicholas Baca, Bernd J Krause, Michael Lassmann, Walter Jentzen, Jun Tang, Daniela Chicco, Patrick Klein, Lars Blumenstein, Jean-René Basque, and Jens Kurth. Renal and multiorgan safety of 177Lu-PSMA-617 in patients with metastatic castration-resistant prostate cancer in the VISION dosimetry substudy. *J. Nucl. Med.*, 65(1):71–78, January 2024.

[115] Elisabeth Eppard, Ana de la Fuente, Martina Benešová, Ambreen Khawar, Ralph A Bundschuh, Florian C Gärtner, Barbara Kreppel, Klaus Kopka, Markus Essler, and Frank Rösch. Clinical translation and first in-human use of [44Sc]Sc-PSMA-617 for PET imaging of metastasized castrate-resistant prostate cancer. *Theranostics*, 7(18):4359–4369, September 2017.

[116] Rafał Walczak, Seweryn Krajewski, Katarzyna Szkliniarz, Mateusz Sitarz, Kamel Abbas, Jarosław Choiński, Andrzej Jakubowski, Jerzy Jastrzębski, Agnieszka Majkowska, Federica Simonelli, Anna Stolarz, Agnieszka Trzcińska, Wiktor Zipper, and Aleksander Bilewicz. Cyclotron production of (43)sc for PET imaging. *EJNMMI Phys.*, 2(1):33, December 2015.

[117] Tommaso Stefano Carzaniga, Martin Auger, Saverio Braccini, Maruta Bunka, Antonio Ereditato, Konrad Pawel Nesteruk, Paola Scampoli, Andreas Türler, and Nicholas van der Meulen. Measurement of 43sc and 44sc production cross-section with an 18 MeV medical PET cyclotron. *Appl. Radiat. Isot.*, 129:96–102, November 2017.

[118] Wouter A P Breeman and Alfons M Verbruggen. The 68ge/ 68ga generator has high potential, but when can we use 68ga-labelled tracers in clinical routine? *Eur. J. Nucl. Med. Mol. Imaging*, 34(7):978–981, July 2007.

[119] Sho Tomita, Kei Higashikawa, Satoshi Ueno, Yuki Mizuno, Shusaku Tazawa, and Yuji Kuge. Long-term quality control test of a 68Ge/68Ga generator. *Kaku Igaku*, 58(1):47–58, 2021.

[120] C S Levin and E J Hoffman. Calculation of positron range and its effect on the fundamental limit of positron emission tomography system spatial resolution. *Phys. Med. Biol.*, 44(3):781–799, March 1999.

[121] Thomas Lewellen, Joel Karp, Miles Wernick, and John Aarsvold. *Emission tomography: the fundamentals of PET and SPECT*, chapter 10, pages 179–194. Elsevier Academic Press, 01 2004.

[122] Stéphan Walrand, François Jamar, Isabelle Mathieu, Joëlle De Camps, Max Lonneux, Mérence Sibomana, Daniel Labar, Christian Michel, and Stanislas Pauwels. Quantitation in PET using isotopes emitting prompt single gammas: application to yttrium-86. *Eur. J. Nucl. Med. Mol. Imaging*, 30(3):354–361, March 2003.

[123] Mark Lubberink and Hans Herzog. Quantitative imaging of 124I and 86Y with PET. *Eur. J. Nucl. Med. Mol. Imaging*, 38 Suppl 1(S1):S10–8, May 2011.

[124] Zhuo Chen, Chien-Min Kao, Hsiun-Hsiung Huang, and Lingling An. Enhanced positronium lifetime imaging through two-component reconstruction in time-of-flight positron emission tomography. *Frontiers in Physics*, 12, 2024.

[125] Sodai Takyu, Fumihiko Nishikido, Hideaki Tashima, Go Akamatsu, Ken-Ichiro Matsumoto, Miwako Takahashi, and Taiga Yamaya. Positronium lifetime measurement using a clinical PET system for tumor hypoxia identification. *Nucl. Instrum. Methods Phys. Res. A*, 1065(169514):169514, August 2024.

[126] Jinyi Qi and Bangyan Huang. Positronium lifetime image reconstruction for TOF PET. *IEEE Trans. Med. Imaging*, 41(10):2848–2855, October 2022.

[127] Christine E Schmidt, Leah Gajecki, Melissa A Deri, and Vanessa A Sanders. Current state of 44Ti/44Sc radionuclide generator systems and separation chemistry. *Curr. Radiopharm.*, 16(2):95–106, 2023.

[128] Nadia Benabdallah, Hanwen Zhang, Ryan Unnerstall, Amanda Fears, Lucy Summer, Michael Fassbender, Buck E Rodgers, Diane Abou, Valery Radchenko, and Daniel L J Thorek. Engineering a modular 44Ti/44Sc generator: eluate evaluation in preclinical models and estimation of human radiation dosimetry. *EJNMMI Res.*, 13(1):17, February 2023.

[129] E.A. Mccutchan. Nuclear data sheets 113, 1735. 2012.

[130] Chen Jun and Singh Balraj. Nuclear data sheets 190, 1. 2023.

[131] M Teresa Durán, Frédéric Juget, Youcef Nedjadi, Claude Bailat, Pascal V Grundler, Zeynep Talip, Nicholas P van der Meulen, Pierluigi Casolaro, Gaia Dellepiane, and Saverio Braccini. Half-life measurement of 44sc and 44msc. *Appl. Radiat. Isot.*, 190(110507):110507, December 2022.

[132] K P Zhernosekov, D V Filosofov, Syed M Qaim, and Frank Rösch. A 140Nd/140Pr radionuclide generator based on physico-chemical transitions in 140pr complexes after electron capture decay of 140Nd-DOTA. *Radiochim. Acta*, 95(6):319–327, June 2007.

[133] J R Zeevaart, Z Szücs, S Takács, N V Jarvis, and D Jansen. Recoil and conversion electron considerations of the 166Dy/166Ho in vivo generator. *Radiochim. Acta*, 100(2):109–113, February 2012.

[134] Sergey V Gudkov, Natalya Yu Shilyagina, Vladimir A Vodeneev, and Andrei V Zvyagin. Targeted radionuclide therapy of human tumors. *Int. J. Mol. Sci.*, 17(1):33, December 2015.

[135] Klaudia Siwowska, Patrycja Guzik, Katharina A Domnanich, Josep M Monné Rodríguez, Peter Bernhardt, Bernard Ponsard, Roger Hasler, Francesca Borgna, Roger Schibli, Ulli Köster, Nicholas P van der Meulen, and Cristina Müller. Therapeutic potential of 47sc in comparison to 177lu and 90y: Preclinical investigations. *Pharmaceutics*, 11(8):424, August 2019.

[136] T.W. Burrows. Nuclear data sheets 108, 923. 2007.

[137] F.G. Kondev. Nuclear data sheets 159, 1. 2019.

[138] Stephen Seltzer. Stopping-powers and range tables for electrons, protons, and helium ions, NIST standard reference database 124, 1993.

[139] Martin K Bakht and Himisha Beltran. Biological determinants of PSMA expression, regulation and heterogeneity in prostate cancer. *Nat. Rev. Urol.*, 22(1):26–45, January 2025.

[140] Sam S Chang. Overview of prostate-specific membrane antigen. *Rev. Urol.*, 6 Suppl 10:S13–8, 2004.

[141] Martin Schäfer, Ulrike Bauder-Wüst, Mareike Roscher, Lucia Motlová, Zsófia Kutilová, Yvonne Remde, Karel D Klika, Jürgen Graf, Cyril Bařinka, and Martina Benešová-Schäfer. Structure-activity relationships and biological insights into PSMA-617 and its derivatives with modified lipophilic linker regions. *ACS Omega*, 10(7):7077–7090, February 2025.

[142] Luis M De León-Rodríguez and Zoltan Kovacs. The synthesis and chelation chemistry of DOTA-peptide conjugates. *Bioconjug. Chem.*, 19(2):391–402, February 2008.

[143] Eugeny N Zapolotsky, Yanyang Qu, and Sergey P Babailov. Lanthanide complexes with polyaminopolycarboxylates as prospective NMR/MRI diagnostic probes: peculiarities of molecular structure, dynamics and paramagnetic properties. *J. Incl. Phenom. Macrocycl. Chem.*, 102(1-2):1–33, 2022.

[144] Serge K Lyashchenko, Tuan Tran, Steffen Happel, Hijin Park, David Bauer, Kali Jones, Tullio V Esposito, Nagavarakishore Pillarsetty, and Jason S Lewis. [89Zr]ZrCl4 for direct radiolabeling of DOTA-based precursors. *Nucl. Med. Biol.*, 136-137(108943):108943, September 2024.

[145] Artem R Khabibullin, Aleksandra Karolak, Mikalai M Budzevich, Mark L McLaughlin, David L Morse, and Lilia M Woods. Structure and properties of DOTA-chelated radiopharmaceuticals within the 225ac decay pathway. *Medchemcomm*, 9(7):1155–1163, July 2018.

[146] Azhar Pasha, Mai Lin, Gyula Tircsó, Cynthia L Rostollan, Mark Woods, Garry E Kiefer, A Dean Sherry, and Xiankai Sun. Synthesis and evaluation of lanthanide ion DOTA-tetraamide complexes bearing peripheral hydroxyl groups. *J. Biol. Inorg. Chem.*, 14(3):421–438, March 2009.

[147] Chris Schaller. Chelation, October 2022.

[148] Robert J. Lancashire. Stability of Metal Complexes and Chelation, June 2023.

[149] Zsolt Baranyai, Gyula Tircsó, and Frank Rösch. The use of the macrocyclic chelator DOTA in radiochemical separations. *Eur. J. Inorg. Chem.*, 2020(1):36–56, January 2020.

[150] Dirk Mueller, Wouter A P Breeman, Ingo Klette, Michael Gottschaldt, Andreas Odparlik, Manfred Baehre, Izabela Tworowska, and Michael K Schultz. Radiolabeling of DOTA-like conjugated peptides with generator-produced 68ga and using NaCl-based cationic elution method. *Nat. Protoc.*, 11(6):1057–1066, June 2016.

[151] Can Cui, Masayuki Hanyu, Akiko Hatori, Yiding Zhang, Lin Xie, Tomoya Ohya, Masami Fukada, Hisashi Suzuki, Kotaro Nagatsu, Cuiping Jiang, Rui Luo, Guoqiang Shao, Mingrong Zhang, and Feng Wang. Synthesis and evaluation of [64Cu]PSMA-617 targeted for prostate-specific membrane antigen in prostate cancer. *Am. J. Nucl. Med. Mol. Imaging*, 7(2):40–52, April 2017.

[152] Mindy I Davis, Melanie J Bennett, Leonard M Thomas, and Pamela J Bjorkman. Crystal structure of prostate-specific membrane antigen, a tumor marker and peptidase. *Proc. Natl. Acad. Sci. U. S. A.*, 102(17):5981–5986, April 2005.

[153] Klaus Kopka, Martina Benešová, Cyril Bařinka, Uwe Haberkorn, and John Babich. Glu-ureido–based inhibitors of prostate-specific membrane antigen: Lessons learned during the development of a novel class of low-molecular-weight theranostic radiotracers. *J Nucl Med*, 58(Supplement 2):17S–26S, September 2017.

[154] Mohamed El Fakiri, Nicolas M Geis, Nawal Ayada, Matthias Eder, and Ann-Christin Eder. PSMA-targeting radiopharmaceuticals for prostate cancer therapy: Recent developments and future perspectives. *Cancers (Basel)*, 13(16):3967, August 2021.

[155] J J Cuaron, J A Hirsch, D C Medich, B S Rosenstein, C B Martel, and A E Hirsch. A proposed methodology to select radioisotopes for use in radionuclide therapy. *AJNR Am. J. Neuroradiol.*, 30(10):1824–1829, November 2009.

[156] Jeroen J M de Goeij. Nuclear, physical and chemical aspects in cyclotron production of radionuclides. *Nucl. Instrum. Methods Phys. Res. B*, 139(1-4):91–97, April 1998.

[157] R Mikolajczak, S Huclier-Markai, C Alliot, F Haddad, D Szikra, V Forgacs, and P Garnuszek. Production of scandium radionuclides for theranostic applications: towards standardization of quality requirements. *EJNMMI Radiopharm. Chem.*, 6(1):19, May 2021.

[158] Shelbie J Cingoranelli, Jennifer L Bartels, Pavithra H A Kankanamalage, C Shaun Loveless, David A Rotsch, and Suzanne E Lapi. Production and purification of 43sc and 47sc from enriched [46Ti]TiO2 and [50Ti]TiO2 targets. *Sci. Rep.*, 13(1):22683, December 2023.

[159] Tommaso Stefano Carzaniga, Nicholas P van der Meulen, Roger Hasler, Christian Kottler, Peter Peier, Andreas Türler, Etienne Vermeulen, Christof Vockenhuber, and Saverio Braccini. Measurement of the 43sc production cross-section with a deuteron beam. *Appl. Radiat. Isot.*, 145:205–208, March 2019.

[160] Katarzyna Szkliniarz, Mateusz Sitarz, Rafał Walczak, Jerzy Jastrzębski, Aleksander Bilewicz, Jarosław Choiński, Andrzej Jakubowski, Agnieszka Majkowska, Anna Stolarz, Agnieszka Trzcińska, and Wiktor Zipper. Production of medical sc radioisotopes with an alpha particle beam. *Appl. Radiat. Isot.*, 118:182–189, December 2016.

[161] David A Rotsch, M Alex Brown, Jerry A Nolen, Thomas Brossard, Walter F Henning, Sergey D Chemerisov, Roman G Gromov, and John Greene. Electron linear accelerator production and purification of scandium-47 from titanium dioxide targets. *Appl. Radiat. Isot.*, 131:77–82, January 2018.

[162] Jason P Meier, Hannah J Zhang, Richard Freifelder, Mohammed Bhuiyan, Phillip Selman, Megan Mendez, Pavithra H A Kankanamalage, Thomas Brossard, Antonino Pusateri, Hsiu-Ming Tsai, Lara Leoni, Sagada Penano, Kaustab Ghosh, Brittany A Broder, Erica Markiewicz, Amy Renne, Walter Stadler, Ralph Weichselbaum, Jerry Nolen, Chien-Min Kao, Satish K Chitneni, David A Rotsch, Russell Z Szmulewitz, and Chin-Tu Chen. Accelerator-based production of scandium radioisotopes for applications in prostate cancer: Toward building a pipeline for rapid development of novel theranostics. *Molecules*, 28(16):6041, August 2023.

[163] S. Spellerberg, B. Scholten, I. Spahn, W. Bolten, M. Holzgreve, H.H. Coenen, and S.M. Qaim. Target development for diversified irradiations at a medical cyclotron. *Applied Radiation and Isotopes*, 104:106–112, 2015.

[164] Richard L Wahl, Joseph M Herman, and Eric Ford. The promise and pitfalls of positron emission tomography and single-photon emission computed tomography molecular imaging-guided radiation therapy. *Semin. Radiat. Oncol.*, 21(2):88–100, April 2011.

[165] Diane S Abou, Mark Longtine, Amanda Fears, Nadia Benabdallah, Ryan Unnerstall, Hannah Johnston, Kyuhwan Shim, Abbie Hasson, Hanwen Zhang, David Ulmert, Floriane Mangin, Serife Ozen, Laurent Raibaut, Stéphane Brandès, Michel Meyer, Jean-Claude Chambron, David S Tatum, Darren Magda, Richard L Wahl, and Daniel L J Thorek. Evaluation of candidate theranostics for 227Th/89Zr paired radioimmunotherapy of lymphoma. *J. Nucl. Med.*, 64(7):1062–1068, July 2023.

[166] M.B. Chadwick, P. Obložinský, M. Herman, N.M. Greene, R.D. McKnight, D.L. Smith, P.G. Young, R.E. MacFarlane, G.M. Hale, S.C. Frankle, A.C. Kahler, T. Kawano, R.C. Little, D.G. Madland, P. Moller, R.D. Mosteller, P.R. Page, P. Talou, H. Trellue, M.C. White, W.B. Wilson, R. Arcilla, C.L. Dunford, S.F. Mughabghab, B. Pritychenko, D. Rochman, A.A. Sonzogni, C.R. Lubitz, T.H. Trumbull, J.P. Weinman, D.A. Brown, D.E. Cullen, D.P. Heinrichs, D.P. McNabb, H. Derrien, M.E. Dunn, N.M. Larson, L.C. Leal, A.D. Carlson, R.C. Block, J.B. Briggs, E.T. Cheng, H.C. Huria, M.L. Zerkle, K.S. Kozier, A. Courcelle, V. Pronyaev, and S.C. Van Der Marck. ENDF/B-VII.0: Next Generation Evaluated Nuclear Data Library for Nuclear Science and Technology. *Nuclear Data Sheets*, 107(12):2931–3060, December 2006.

[167] A J Koning, D Rochman, J-Ch Sublet, N Dzysiuk, M Fleming, and S van der Marck. TENDL: Complete nuclear data library for innovative nuclear science and technology. *Nucl. Data Sheets*, 155:1–55, January 2019.

[168] Naohiko Otuka and Sandor Takács. Definitions of radioisotope thick target yields. *Radiochim. Acta*, 103(1):1–6, January 2015.

[169] C Duchemin, A Guertin, F Haddad, N Michel, and V Métivier. Production of scandium-44 m and scandium-44 g with deuterons on calcium-44: cross section measurements and production yield calculations. *Phys. Med. Biol.*, 60(17):6847–6864, September 2015.

[170] Tommaso Stefano Carzaniga and Saverio Braccini. Cross-section measurement of 44Sc,47Sc, 48sc and 47ca for an optimized 47sc production with an 18 MeV medical PET cyclotron. *Appl. Radiat. Isot.*, 143:18–23, January 2019.

[171] Andreas Tuerler, Meulen Nicholas Van Der, and Maruta Bunka. Production of 43sc Radionuclide and Radiopharmaceuticals Thereof for Use in Positron Emission Tomography, March 2017.

[172] Locametz dosing and administration. `https://www.locametz-hcp.com/psma-pet-ct/dosing-and-administration`.

[173] Pluvicto dosing and administration. `https://www.pluvicto-hcp.com/psma-positive-mcrpc/dosing-and-administration`.

[174] Gert Luurtsema, Verena Pichler, Salvatore Bongarzone, Yann Seimbille, Philip Elsinga, Antony Gee, and Johnny Vercouillie. EANM guideline for harmonisation on molar activity or specific activity of radiopharmaceuticals: impact on safety and imaging quality. *EJNMMI Radiopharm. Chem.*, 6(1):34, October 2021.

[175] Jason P Holland. Chemical kinetics of radiolabelling reactions. *Chemistry*, 24(62):16472–16483, November 2018.

[176] Jason P. Meier, Mohammed Bhuiyan, Richard Freifelder, Hannah J. Zhang, Lucas Gonzalez, Antonino Pusateri, Hsiu-Ming Tsai, Lara Leoni, Kaustab Ghosh, Erica Markiewicz, Christopher Henning, Yuhan Zhang, Ralph Weichselbaum, Jerry Nolen, David A. Rotsch, Chien-Min Kao, Russell Z. Szmulewitz, Chin-Tu Chen, and Satish K. Chitneni. Synthesis of dota-based 43sc radiopharmaceuticals using cyclotron-produced 43sc as exemplified by [43sc]sc-psma-617 for psma pet imaging. *Methods and Protocols*, 8(3), 2025.

[177] Jason Meier. Radioscandium psma-617 synthesis from irradiated calcium targetry, 2025. Made in Biorender: `https://BioRender.com/bpol8dn`.

[178] Thomas Langbein, Alexander Wurzer, Andrei Gafita, Andrew Robertson, Hui Wang, Ayça Arçay, Michael Herz, Hans-Juergen Wester, Wolfgang A. Weber, and Matthias Eiber. The influence of specific activity on the biodistribution of 18f-rhpsma-7.3: A retrospective analysis of clinical pet data. *Journal of Nuclear Medicine*, 63(5):742–745, 2022.

[179] Maija Radzina, Mara Tirane, Lilita Roznere, Liene Zemniece, Laura Dronka, Marika Kalnina, Edgars Mamis, Juergen Biederer, Vilnis Lietuvietis, Arvis Freimanis, and Egils Vjaters. Accuracy of 68Ga-PSMA-11 PET/CT and multiparametric MRI for the detection of local tumor and lymph node metastases in early biochemical recurrence of prostate cancer. *Am. J. Nucl. Med. Mol. Imaging*, 10(2):106–118, April 2020.

[180] Suzanne E Lapi and Michael J Welch. A historical perspective on the specific activity of radiopharmaceuticals: what have we learned in the 35 years of the ISRC? *Nucl. Med. Biol.*, 39(5):601–608, July 2012.

[181] Wolfgang P Fendler, Andreea D Stuparu, Susan Evans-Axelsson, Katharina Lückerath, Liu Wei, Woosuk Kim, Soumya Poddar, Jonathan Said, Caius G Radu, Matthias Eiber, Johannes Czernin, Roger Slavik, and Ken Herrmann. Establishing 177Lu-PSMA-617 radioligand therapy in a syngeneic model of murine prostate cancer. *J Nucl Med*, 58(11):1786–1792, November 2017.

[182] Ivan E. Wang, Allen F. Brooks, Peter J. Scott, and Benjamin L. Viglianti. Determining psma-617 mass and molar activity in pluvicto doses. *Journal of Nuclear Medicine*, 2025.

[183] Marcello Tucci, Clizia Zichi, Consuelo Buttigliero, Francesca Vignani, Giorgio V Scagliotti, and Massimo Di Maio. Enzalutamide-resistant castration-resistant prostate cancer: challenges and solutions. *Onco. Targets. Ther.*, 11:7353–7368, October 2018.

[184] Alexandra Vander Ark, Jingchen Cao, and Xiaohong Li. Mechanisms and approaches for overcoming enzalutamide resistance in prostate cancer. *Front. Oncol.*, 8, May 2018.

[185] Steven Kregel, James L Chen, Westin Tom, Venkatesh Krishnan, Jacob Kach, Hannah Brechka, Tim B Fessenden, Masis Isikbay, Gladell P Paner, Russell Z Szmulewitz, and Donald J Vander Griend. Acquired resistance to the second-generation androgen receptor antagonist enzalutamide in castration-resistant prostate cancer. *Oncotarget*, 7(18):26259–26274, May 2016.

[186] A Chlenski, K Nakashiro, K V Ketels, G I Korovaitseva, and R Oyasu. Androgen receptor expression in androgen-independent prostate cancer cell lines. *Prostate*, 47(1):66–75, April 2001.

[187] Sang Su Oh and Heather L Narver. Mouse and rat anesthesia and analgesia. *Curr. Protoc.*, 4(2):e995, February 2024.

[188] Jinyun Wu, Yuqi Cai, Xiaoyang Wu, Yue Ying, Yilin Tai, and Miao He. Transcardiac perfusion of the mouse for brain tissue dissection and fixation. *Bio Protoc.*, 11(5):e3988, March 2021.

[189] Eline A M Ruigrok, Nicole van Vliet, Simone U Dalm, Erik de Blois, Dik C van Gent, Joost Haeck, Corrina de Ridder, Debra Stuurman, Mark W Konijnenberg, Wytske M van Weerden, Marion de Jong, and Julie Nonnekens. Extensive preclinical evaluation of lutetium-177-labeled PSMA-specific tracers for prostate cancer radionuclide therapy. *Eur. J. Nucl. Med. Mol. Imaging*, 48(5):1339–1350, May 2021.

[190] Viviane J Tschan, Francesca Borgna, Roger Schibli, and Cristina Müller. Impact of the mouse model and molar amount of injected ligand on the tissue distribution profile of PSMA radioligands. *Eur. J. Nucl. Med. Mol. Imaging*, 49(2):470–480, January 2022.

[191] Xiaojiang Duan, Zhen Cao, Hua Zhu, Chen Liu, Xiaojun Zhang, Jinming Zhang, Ya'nan Ren, Futao Liu, Xuekang Cai, Xiaoyi Guo, Zhen Xi, Martin G Pomper, Zhi Yang, Yan Fan, and Xing Yang. 68ga-labeled ODAP-Urea-based PSMA agents in prostate cancer: first-in-human imaging of an optimized agent. *Eur. J. Nucl. Med. Mol. Imaging*, 49(3):1030–1040, February 2022.

[192] Tsutomu Kanefuji, Takeshi Yokoo, Takeshi Suda, Hiroyuki Abe, Kenya Kamimura, and Dexi Liu. Hemodynamics of a hydrodynamic injection. *Mol. Ther. Methods Clin. Dev.*, 1(14029):14029, July 2014.

[193] Xiao Wei, Carl Schlenkhoff, Bettina Schwarz, Markus Essler, and Hojjat Ahmadzadehfar. Combination of 177Lu-PSMA-617 and external radiotherapy for the treatment of cerebral metastases in patients with castration-resistant metastatic prostate cancer. *Clin. Nucl. Med.*, 42(9):704–706, September 2017.

[194] Janik Puttemans, Tony Lahoutte, Matthias D'Huyvetter, and Nick Devoogdt. Beyond the barrier: Targeted radionuclide therapy in brain tumors and metastases. *Pharmaceutics*, 11(8):376, August 2019.

[195] Eline A M Ruigrok, Nicole van Vliet, Simone U Dalm, Erik de Blois, Dik C van Gent, Joost Haeck, Corrina de Ridder, Debra Stuurman, Mark W Konijnenberg, Wytske M van Weerden, Marion de Jong, and Julie Nonnekens. Extensive preclinical evaluation of lutetium-177-labeled PSMA-specific tracers for prostate cancer radionuclide therapy. *Eur. J. Nucl. Med. Mol. Imaging*, 48(5):1339–1350, May 2021.

[196] Srilalan Krishnamoorthy, Eric Blankemeyer, Pieter Mollet, Suleman Surti, Roel Van Holen, and Joel S Karp. Performance evaluation of the MOLECUBES β-CUBE-a high spatial resolution and high sensitivity small animal PET scanner utilizing monolithic LYSO scintillation detectors. *Phys. Med. Biol.*, 63(15):155013, July 2018.

[197] H Zaidi. Relevance of accurate monte carlo modeling in nuclear medical imaging. *Med. Phys.*, 26(4):574–608, April 1999.

[198] Wesley E Bolch. The monte carlo method in nuclear medicine: current uses and future potential. *J. Nucl. Med.*, 51(3):337–339, March 2010.

[199] Frederic H Fahey, Kira Grogg, and Georges El Fakhri. Use of monte carlo techniques in nuclear medicine. *J. Am. Coll. Radiol.*, 15(3):446–448, March 2018.

[200] J Perl, J Shin, J Schumann, B Faddegon, and H Paganetti. TOPAS: an innovative proton monte carlo platform for research and clinical applications. *Med. Phys.*, 39(11):6818–6837, November 2012.

[201] J Schuemann, A L McNamara, J Ramos-Méndez, J Perl, K D Held, H Paganetti, S Incerti, and B Faddegon. TOPAS-nBio: An extension to the TOPAS simulation toolkit for cellular and sub-cellular radiobiology. *Radiat. Res.*, 191(2):125–138, February 2019.

[202] S. Muraro, G. Battistoni, and A.C. Kraan. Challenges in monte carlo simulations as clinical and research tool in particle therapy: A review. *Frontiers in Physics*, Volume 8 - 2020, 2020.

[203] Harald Paganetti, Hongyu Jiang, Katia Parodi, Roelf Slopsema, and Martijn Engelsman. Clinical implementation of full monte carlo dose calculation in proton beam therapy. *Phys. Med. Biol.*, 53(17):4825–4853, September 2008.

[204] S M Goddu, D V Rao, and R W Howell. Multicellular dosimetry for micrometastases: dependence of self-dose versus cross-dose to cell nuclei on type and energy of radiation and subcellular distribution of radionuclides. *J Nucl Med*, 35(3):521–530, 1994.

[205] S.M. Goddu and T.F. Budinger. *MIRD Cellular S. Values: Self-absorbed Dose Per Unit Cumulated Activity for Selected Radionuclides and Monoenergetic Electron and Alpha Particle Emitters Incorporated Into Different Cell Compartments*. A publication of the Society of Nuclear Medicine. Society of Nuclear Medicine, 1997.

[206] E L Rojas-Calderón, O Ávila, and G Ferro-Flores. Monte carlo calculations of the cellular S -values for α-particle-emitting radionuclides incorporated into the nuclei of

cancer cells of the MDA-MB231, MCF7 and PC3 lines. *Appl. Radiat. Isot.*, 135:1–6, May 2018.

[207] R. W. Howell. The MIRD Schema: from organ to cellular dimensions. *Journal of Nuclear Medicine: Official Publication, Society of Nuclear Medicine*, 35(3):531–533, March 1994.

[208] Martin Šefl, Sébastien Incerti, George Papamichael, and Dimitris Emfietzoglou. Calculation of cellular s-values using Geant4-DNA: The effect of cell geometry. *Appl. Radiat. Isot.*, 104:113–123, October 2015.

[209] J Carrasco-Hernández, J Ramos-Méndez, B Faddegon, A R Jalilian, M Moranchel, and M A Ávila-Rodríguez. Monte carlo track-structure for the radionuclide copper-64: characterization of s-values, nanodosimetry and quantification of direct damage to DNA. *Phys. Med. Biol.*, 65(15):155005, July 2020.

[210] Maikol Salas-Ramirez, Michael Lassmann, and Uta Eberlein. In silico analysis of radiation-induced double-strand breaks by internal ex vivo irradiation of lymphocytes for 45 alpha- and beta/gamma-emitting radionuclides. *EJNMMI Res.*, 15(1):21, March 2025.

[211] Ramak Salim and Payvand Taherparvar. Monte carlo single-cell dosimetry using Geant4-DNA: the effects of cell nucleus displacement and rotation on cellular S values. *Radiat. Environ. Biophys.*, 58(3):353–371, August 2019.

[212] Jhonatan Carrasco-Hernandez, José Ramos-Méndez, Elizabeth Padilla-Rodal, and Miguel A Avila-Rodriguez. Cellular lethal damage of 64cu incorporated in mammalian genome evaluated with monte carlo methods. *Front. Med. (Lausanne)*, 10:1253746, September 2023.

[213] James C L Chow and Amir M Owrangi. Dosimetric dependences of bone heterogeneity and beam angle on the unflattened and flattened photon beams: A monte carlo comparison. *Radiat. Phys. Chem. Oxf. Engl. 1993*, 101:46–52, August 2014.

[214] A S Jagtap, B J Patil, S S Dahiwale, V N Bhoraskar, and S D Dhole. Electron depth dose curves in inhomogeneous medium for radiation therapy: A simulation approach. *Phys. Med.*, 32:266–267, September 2016.

[215] Ananda Giri Babu Alagar, Ganesh Kadirampatti Mani, and Kaviarasu Karunakaran. Percentage depth dose calculation accuracy of model based algorithms in high energy photon small fields through heterogeneous media and comparison with plastic scintillator dosimetry. *J. Appl. Clin. Med. Phys.*, 17(1):132–142, January 2016.

[216] Jason Meier. Energy deposition simulation geometry, 2025. Made in Biorender: `https://BioRender.com/kqi0pca`.

[217] Jason Meier. Energy deposition simulation geometry small, 2025. Made in Biorender: `https://BioRender.com/t8znm0n`.

[218] Michael Joseph Merrick, David A Rotsch, Ashok Tiwari, Jerry Nolen, Thomas Brossard, Jeongseog Song, Thaddeus J Wadas, John Sunderland, and Stephen Graves. Imaging and dosimetric characteristics of67cu. *Phys. Med. Biol.*, 66(3):035002, November 2020.

[219] P A K Oliver and Rowan M Thomson. A monte carlo study of macroscopic and microscopic dose descriptors for kilovoltage cellular dosimetry. *Phys. Med. Biol.*, 62(4):1417–1436, February 2017.

[220] Martin P Martinov, Elizabeth M Fletcher, and Rowan M Thomson. Multiscale monte carlo simulations of gold nanoparticle dose-enhanced radiotherapy i: Cellular dose enhancement in microscopic models. *Med. Phys.*, 50(9):5853–5864, September 2023.

[221] Zachary S Morris, Andrew Z Wang, and Susan J Knox. The radiobiology of radiopharmaceuticals. *Semin. Radiat. Oncol.*, 31(1):20–27, January 2021.

[222] Emma Mellhammar, Magnus Dahlbom, Oskar Vilhelmsson-Timmermand, and Sven-Erik Strand. Tumor control probability and small-scale monte carlo dosimetry: Effects of heterogenous intratumoral activity distribution in radiopharmaceutical therapy. *J. Nucl. Med.*, 64(10):1632–1637, October 2023.

[223] Behrooz Vaziri, Han Wu, Atam P. Dhawan, Peicheng Du, and Roger W. Howell. Mird pamphlet no. 25: Mirdcell v2.0 software tool for dosimetric analysis of biologic response of multicellular populations. *The Journal of Nuclear Medicine*, 55:1557 – 1564, 2014.

[224] Sumudu Katugampola, Jianchao Wang, Alex Rosen, Roger W. Howell, and SNMMI MIRD committee. MIRD Pamphlet No. 27: MIRDcell V3, a Revised Software Tool for Multicellular Dosimetry and Bioeffect Modeling. *Journal of Nuclear Medicine: Official Publication, Society of Nuclear Medicine*, 63(9):1441–1449, September 2022.

[225] Jason Meier. Cellular s-value geometry, 2025. Made in Biorender: `https://BioRender.com/xus8trq`.

[226] J T Finch and A Klug. Solenoidal model for superstructure in chromatin. *Proc. Natl. Acad. Sci. U. S. A.*, 73(6):1897–1901, June 1976.

[227] N T Henthorn, J W Warmenhoven, M Sotiropoulos, R I Mackay, K J Kirkby, and M J Merchant. Nanodosimetric simulation of direct ion-induced DNA damage using different chromatin geometry models. *Radiat. Res.*, 188(6):770–783, December 2017.

[228] Cassandra Miller, Guillaume Chausse, Julia Brosch-Lenz, Francois Benard, Arman Rahmim, and Carlos Uribe. Comparison of s-values and absorbed dose rates at the cellular level in prostate cancer cells irradiated with 177lu and 225ac labelled compounds. *Journal of Nuclear Medicine*, 62(supplement 1):1574–1574, 2021.

[229] Magnus von Knebel Doeberitz and Nicolas Wentzensen. Chapter 1 - the cell: Basic structure and function. In Marluce Bibbo and David Wilbur, editors, *Comprehensive*

Cytopathology (Third Edition), pages 3–22. W.B. Saunders, Edinburgh, third edition edition, 2008.

[230] Donald B. McMillan and Richard J. Harris. Chapter a - the animal cell. In Donald B. McMillan and Richard J. Harris, editors, *An Atlas of Comparative Vertebrate Histology*, pages 3–25. Academic Press, San Diego, 2018.

[231] Hongyu Zhu, Aimee L McNamara, Stephen J McMahon, Jose Ramos-Mendez, Nicholas T Henthorn, Bruce Faddegon, Kathryn D Held, Joseph Perl, Junli Li, Harald Paganetti, and Jan Schuemann. Cellular response to proton irradiation: A simulation study with TOPAS-nBio. *Radiat. Res.*, 194(1):9–21, July 2020.

[232] Małgorzata A Śmiałek, Nykola C Jones, Søren Vrønning Hoffmann, and Nigel J Mason. Measuring the density of DNA films using ultraviolet-visible interferometry. *Phys. Rev. E Stat. Nonlin. Soft Matter Phys.*, 87(6):060701, June 2013.

[233] Jason Meier. Dna dsb simulation geometry, 2025. Made in Biorender: `https://BioRender.com/7c0f6ha`.

[234] Sergey V. Stepanov, Vsevolod M. Byakov, and Tetsuya Hirade. To the theory of ps formation. new interpretation of the e+ lifetime spectrum in water. *Radiation Physics and Chemistry*, 76(2):90–95, 2007. Proceedings of the 8th International Workshop on Positron and Positronium Chemistry.

[235] Frank H Attix. *Charged-Particle Interactions in Matter*, chapter 8, pages 160–202. John Wiley Sons, Ltd, 1986.

[236] Sunyoung Park, Richard R Ang, Simon P Duffy, Jenny Bazov, Kim N Chi, Peter C Black, and Hongshen Ma. Morphological differences between circulating tumor cells from prostate cancer patients and cultured prostate cancer cells. *PLoS One*, 9(1):e85264, January 2014.

[237] Pauline A J Mendelaar, Jaco Kraan, Mai Van, Leonie L Zeune, Leon W M M Terstappen, Esther Oomen-de Hoop, John W M Martens, and Stefan Sleijfer. Defining the dimensions of circulating tumor cells in a large series of breast, prostate, colon, and bladder cancer patients. *Mol. Oncol.*, 15(1):116–125, January 2021.

[238] Gy Gyürky, M Vakulenko, Zs Fülöp, Z Halász, G G Kiss, E Somorjai, and T Szücs. Cross section and reaction rate of determined from thick target yield measurements. *Nucl. Phys. A*, 922:112–125, February 2014.

[239] T Szücs, G G Kiss, Gy Gyürky, Z Halász, Zs Fülöp, and T Rauscher. Cross section of α-induced reactions on iridium isotopes obtained from thick target yield measurement for the astrophysical γ process. *Phys. Lett. B*, 776:396–401, January 2018.

[240] Brittany A Broder, Richard Freifelder, Anna Kucharski, and Chin-Tu Chen. Modelling cyclotron-based production of radioisotopes via TOPAS. *Phys. Med. Biol.*, 68(1):015017, December 2022.

[241] F. Tárkányi, F. Szelecsényi, and S. Takács. Determination of effective bombarding energies and fluxes using an improved stacked foil technique. *Acta Radiologica. Supplementum*, 376:72, 1991.

[242] Shankar Vallabhajosula, Ronan P Killeen, and Joseph R Osborne. Altered biodistribution of radiopharmaceuticals: role of radiochemical/pharmaceutical purity, physiological, and pharmacologic factors. *Semin. Nucl. Med.*, 40(4):220–241, July 2010.

[243] Bryce J B Nelson, Jan D Andersson, Frank Wuest, and Sarah Spreckelmeyer. Good practices for 68ga radiopharmaceutical production. *EJNMMI Radiopharm. Chem.*, 7(1):27, October 2022.

[244] Sajjad Molavipordanjani, Vladimir Tolmachev, and Seyed Jalal Hosseinimehr. Basic and practical concepts of radiopharmaceutical purification methods. *Drug Discov. Today*, 24(1):315–324, January 2019.

[245] F J Beekman, C Kamphuis, S Koustoulidou, R M Ramakers, and M C Goorden. Positron range-free and multi-isotope tomography of positron emitters. *Phys. Med. Biol.*, 66(6):065011, March 2021.

[246] Frank DiFilippo. Repurposing the iec/nema phantom for prostate pet performance assessment. *Journal of Nuclear Medicine*, 65(supplement 2):241346–241346, 2024.

[247] Zhen Zhou, Feng Yue, Liang Jin, Xiang Liu, Ting-Shuai Zhai, Jia-Xin Zhang, Wen-Yu Gu, Sheng-Hua Liu, Ming Luo, Bo Peng, Xu-Dong Yao, and Lin Ye. Characteristics and risk differences of different tumor size on localized prostate cancer: A retrospective cohort study in the SEER database. *Cancer Med.*, 10(8):2763–2773, April 2021.

[248] Stephen Adler, Jurgen Seidel, Peter Choyke, Michael V Knopp, Katherine Binzel, Jun Zhang, Craig Barker, Shielah Conant, and Roberto Maass-Moreno. Minimum lesion detectability as a measure of PET system performance. *EJNMMI Phys.*, 4(1):13, December 2017.

[249] Shujie Lu, Peng Zhang, Chengwei Li, Jie Sun, Wenli Liu, and Pu Zhang. A NIM PET/CT phantom for evaluating the PET image quality of micro-lesions and the performance parameters of CT. *BMC Med. Imaging*, 21(1):165, November 2021.

[250] Karyn S Ho, Peter C Poon, Shawn C Owen, and Molly S Shoichet. Blood vessel hyperpermeability and pathophysiology in human tumour xenograft models of breast cancer: a comparison of ectopic and orthotopic tumours. *BMC Cancer*, 12(1):579, December 2012.

[251] Wenting Zhang, Wei Fan, Satyanarayana Rachagani, Zhengyuan Zhou, Subodh M Lele, Surinder K Batra, and Jered C Garrison. Comparative study of subcutaneous and orthotopic mouse models of prostate cancer: Vascular perfusion, vasculature density, hypoxic burden and BB2r-targeting efficacy. *Sci. Rep.*, 9(1):11117, July 2019.

[252] Laura Gómez-Cuadrado, Natasha Tracey, Ruoyu Ma, Binzhi Qian, and Valerie G Brunton. Mouse models of metastasis: progress and prospects. *Dis. Model. Mech.*, 10(9):1061–1074, September 2017.

[253] Sun Hee Park, Matthew Robert Eber, and Yusuke Shiozawa. Models of prostate cancer bone metastasis. *Methods Mol. Biol.*, 1914:295–308, 2019.

[254] Jong Hyun Tae and In Ho Chang. Animal models of bone metastatic prostate cancer. *Investig. Clin. Urol.*, 64(3):219–228, May 2023.

[255] Junli Chang, Xingyuan Sun, Xiaoping Ma, Peng Zhao, Binhao Shi, Yongjun Wang, Xianghui Han, and Yanping Yang. Intra-cardiac injection of human prostate cancer cells to create a bone metastasis xenograft mouse model. *J. Vis. Exp.*, (189), November 2022.

[256] Coralie Genevois, Arnaud Hocquelet, Claire Mazzocco, Emilie Rustique, Franck Couillaud, and Nicolas Grenier. In vivo imaging of prostate cancer tumors and metastasis using non-specific fluorescent nanoparticles in mice. *Int. J. Mol. Sci.*, 18(12):2584, December 2017.

[257] M. Haq, D. Goltzman, G. Tremblay, and P. Brodt. Rat prostate adenocarcinoma cells disseminate to bone and adhere preferentially to bone marrow-derived endothelial cells. *Cancer Research*, 52(17):4613–4619, September 1992.

[258] S. S. Wallace. Enzymatic processing of radiation-induced free radical damage in DNA. *Radiation Research*, 150(5 Suppl):S60–79, November 1998.

[259] J-L Ravanat, J Breton, T Douki, D Gasparutto, A Grand, W Rachidi, and S Sauvaigo. Radiation-mediated formation of complex damage to DNA: a chemical aspect overview. *Br. J. Radiol.*, 87(1035):20130715, March 2014.

[260] J Ramos-Méndez, J A LaVerne, N Domínguez-Kondo, J Milligan, V Štěpán, K Stefanová, Y Perrot, C Villagrasa, W-G Shin, S Incerti, A McNamara, H Paganetti, J Perl, J Schuemann, and B Faddegon. TOPAS-nBio validation for simulating water radiolysis and DNA damage under low-LET irradiation. *Phys. Med. Biol.*, 66(17):175026, September 2021.

[261] J Ramos-Méndez, J Perl, J Schuemann, A McNamara, H Paganetti, and B Faddegon. Monte carlo simulation of chemistry following radiolysis with TOPAS-nBio. *Phys. Med. Biol.*, 63(10):105014, May 2018.

[262] Barry Halliwell and Matthew Whiteman. Measuring reactive species and oxidative damage in vivo and in cell culture: how should you do it and what do the results mean? *Br. J. Pharmacol.*, 142(2):231–255, May 2004.

[263] A E Holley and K H Cheeseman. Measuring free radical reactions in vivo. *Br. Med. Bull.*, 49(3):494–505, July 1993.

[264] Michael P Murphy, Hülya Bayir, Vsevolod Belousov, Christopher J Chang, Kelvin J A Davies, Michael J Davies, Tobias P Dick, Toren Finkel, Henry J Forman, Yvonne Janssen-Heininger, David Gems, Valerian E Kagan, Balaraman Kalyanaraman, Nils-Göran Larsson, Ginger L Milne, Thomas Nyström, Henrik E Poulsen, Rafael Radi, Holly Van Remmen, Paul T Schumacker, Paul J Thornalley, Shinya Toyokuni, Christine C Winterbourn, Huiyong Yin, and Barry Halliwell. Guidelines for measuring reactive oxygen species and oxidative damage in cells and in vivo. *Nat. Metab.*, 4(6):651–662, June 2022.

[265] Aviral Singh, Nicholas P van der Meulen, Cristina Müller, Ingo Klette, Harshad R Kulkarni, Andreas Türler, Roger Schibli, and Richard P Baum. First-in-human PET/CT imaging of metastatic neuroendocrine neoplasms with cyclotron-produced 44Sc-DOTATOC: A proof-of-concept study. *Cancer Biother. Radiopharm.*, 32(4):124–132, May 2017.

[266] Thomas M Jeitner, John W Babich, and James M Kelly. Advances in PSMA theranostics. *Transl. Oncol.*, 22(101450):101450, August 2022.

[267] Martina Weineisen, Jakub Simecek, Margret Schottelius, Markus Schwaiger, and Hans-Jürgen Wester. Synthesis and preclinical evaluation of DOTAGA-conjugated PSMA ligands for functional imaging and endoradiotherapy of prostate cancer. *EJNMMI Res.*, 4(1):63, December 2014.

[268] Christiane Schuchardt, Jingjing Zhang, Harshad R Kulkarni, Xiaoyuan Chen, Dirk Müller, and Richard P Baum. Prostate-specific membrane antigen radioligand therapy using 177Lu-PSMA I&T and 177Lu-PSMA-617 in patients with metastatic castration-resistant prostate cancer: Comparison of safety, biodistribution, and dosimetry. *J. Nucl. Med.*, 63(8):1199–1207, August 2022.

[269] Kristell L S Chatalic, Sandra Heskamp, Mark Konijnenberg, Janneke D M Molkenboer-Kuenen, Gerben M Franssen, Marian C Clahsen-van Groningen, Margret Schottelius, Hans-Jürgen Wester, Wytske M van Weerden, Otto C Boerman, and Marion de Jong. Towards personalized treatment of prostate cancer: PSMA I&T, a promising prostate-specific membrane antigen-targeted theranostic agent. *Theranostics*, 6(6):849–861, 2016.

[270] Shay Golan, Michael Frumer, Yarden Zohar, Eli Rosenbaum, Maxim Yakimov, Daniel Kedar, David Margel, Jack Baniel, Adam P Steinmetz, David Groshar, Liran Domachevsky, and Hanna Bernstine. Neoadjuvant 177Lu-PSMA-I&T radionuclide treatment in patients with high-risk prostate cancer before radical prostatectomy: A single-arm phase 1 trial. *Eur. Urol. Oncol.*, 6(2):151–159, April 2023.

[271] Roberto A Salas Fragomeni, Tali Amir, Sara Sheikhbahaei, Susan C Harvey, Mehrbod S Javadi, Lilja B Solnes, Ana P Kiess, Mohamad E Allaf, Martin G Pomper, Michael A Gorin, and Steven P Rowe. Imaging of nonprostate cancers using PSMA-targeted

radiotracers: Rationale, current state of the field, and a call to arms. *J Nucl Med*, 59(6):871–877, June 2018.

[272] Alla G Wernicke, Sae Kim, He Liu, Neil H Bander, and Edyta C Pirog. Prostate-specific membrane antigen (PSMA) expression in the neovasculature of gynecologic malignancies: Implications for PSMA-targeted therapy. *Appl. Immunohistochem. Mol. Morphol.*, 25(4):271–276, April 2017.

[273] Clara Unger, Peter Bronsert, Kerstin Michalski, Anna Bicker, and Ingolf Juhasz-Böss. Expression of prostate specific membrane antigen (PSMA) in breast cancer. *Geburtshilfe Frauenheilkd.*, 82(1):50–58, January 2022.

[274] Jarey H Wang and Ana P Kiess. PSMA-targeted therapy for non-prostate cancers. *Front. Oncol.*, 13:1220586, August 2023.

[275] Jonathan R Strosberg, Martyn E Caplin, Pamela L Kunz, Philippe B Ruszniewski, Lisa Bodei, Andrew Eugene Hendifar, Erik Mittra, Edward M Wolin, James C Yao, Marianne E Pavel, Enrique Grande, Eric Van Cutsem, Ettore Seregni, Hugo Duarte, Germo Gericke, Amy Bartalotta, Arnaud Demange, Sakir Mutevelic, Eric Krenning, and on behalf of the NETTER-1 study group. Final overall survival in the phase 3 NETTER-1 study of lutetium-177-DOTATATE in patients with midgut neuroendocrine tumors. *J. Clin. Oncol.*, 39(15_suppl):4112–4112, May 2021.

[276] Simron Singh, Daniel Halperin, Sten Myrehaug, Ken Herrmann, Marianne Pavel, Pamela L Kunz, Beth Chasen, Salvatore Tafuto, Secondo Lastoria, Jaume Capdevila, Amparo García-Burillo, Do-Youn Oh, Changhoon Yoo, Thorvardur R Halfdanarson, Stephen Falk, Ilya Folitar, Yufen Zhang, Paola Aimone, Wouter W de Herder, Diego Ferone, and all the NETTER-2 Trial Investigators. [177Lu]Lu-DOTA-TATE plus long-acting octreotide versus high-dose long-acting octreotide for the treatment of newly diagnosed, advanced grade 2-3, well-differentiated, gastroenteropancreatic neuroendocrine tumours (NETTER-2): an open-label, randomised, phase 3 study. *Lancet*, 403(10446):2807–2817, June 2024.

[277] Habibollah Dadgar, Esmail Jafari, Hojjat Ahmadzadehfar, Seyed Javad Rekabpour, Mohammad Reza Ravanbod, Mohammadreza Kalantarhormozi, Iraj Nabipour, and Majid Assadi. Feasibility and therapeutic potential of the 68Ga/177Lu-DOTATATE theranostic pair in patients with metastatic medullary thyroid carcinoma. *Ann. Endocrinol. (Paris)*, 84(1):45–51, February 2023.

[278] Avery B Peterson, Chang Wang, Ka Kit Wong, Kirk A Frey, Otto Muzik, Matthew J Schipper, and Yuni K Dewaraja. 177Lu-DOTATATE theranostics: Predicting renal dosimetry from pretherapy 68Ga-DOTATATE PET and clinical biomarkers. *Clin. Nucl. Med.*, 48(5):393–399, May 2023.

[279] Bilal Kovan, Zeynep Gözde Özkan, Bayram Demir, Duygu Tunçman, Emine Göknur Işik, Duygu Has Şimşek, Fikret Büyükkaya, Cüneyt Türkmen, and Yasemin Şanli.

An analysis for therapeutic doses of patients with neuroendocrine tumor treated with lutetium 177 (177Lu)-DOTATATE. *Cancer Biother. Radiopharm.*, 37(1):17–22, February 2022.

[280] Carlos Vinícius Gomes, Bruno Melo Mendes, Lucas Paixão, Silvano Gnesin, Cristina Müller, Nicholas P van der Meulen, Klaus Strobel, Telma Cristina Ferreira Fonseca, and Thiago Viana Miranda Lima. Comparison of the dosimetry of scandium-43 and scandium-44 patient organ doses in relation to commonly used gallium-68 for imaging neuroendocrine tumours. *EJNMMI Phys.*, 11(1):61, July 2024.

[281] Hannah Zhang, Mohammed Bhuiyan, Jason Meier, Olga Lakiza, Pavithra Kankanamalage, Thomas Brossard, Hsiu-Ming Tsai, Lara Leoni, Anna Kucharski Raubic, Richard Freifelder, Chih-Yi Liao, Yonglin Pu, Daniel Appelbaum, Ralph Weichselbaum, Jerry Nolen, Chien-Min Kao, David Rotsch, Xavier Keutgen, and Chin-Tu Chen. Preliminary investigation of 43sc/47sc-dotatate for theranostic applications. *Journal of Nuclear Medicine*, 63(supplement 2):2893–2893, 2022.

[282] Hannah Zhang, Antonino Pusateri, Jason Meier, Olga Lakiza, Mohammed Bhuiyan, Hsiu-Ming Tsai, Lara Leoni, Kaustab Ghosh, Richard Freifelder, Liao Andy, Yonglin Pu, Daniel Appelbaum, Ralph Weichselbaum, Jerry Nolen, Chien-Min Kao, David Rotsch, Chin-Tu Chen, and Xavier Keutgen. Scandium-43-dotatate, a novel positron emission tomography (pet) tracer for neuroendocrine tumor imaging. *Endocrine Abstracts*, 12 2023.

[283] Mohammed Bhuiyan, Chin-Tu Chen, Richard Freifelder, Hannah Zhang, Jason Meier, Hsiu-Ming Tsai, Chien-Min Kao, Anna Kucharski Raubic, Jerry Nolen, David Rotsch, Pavithra Kankanamalage, Lara Leoni, Nami Yamashita, Thomas Brossard, Ralph Weichselbaum, and Donald Kufe. Targeting muc1-c for cancer theranostics using humanized 47sc-mab 3d1. *Journal of Nuclear Medicine*, 63(supplement 2):2357–2357, 2022.

[284] Mohammed Bhuiyan, Kaustab Ghosh, Hannah Zhang, Jeffrey Souris, Brian Roman, Yonglin Pu, Daniel Appelbaum, Jason Meier, Richard Freifelder, and Chin-Tu Chen. Novel lipophilic-cationic molecular probes for enhanced imaging of mitochondria. *Journal of Nuclear Medicine*, 64(supplement 1):P504–P504, 2023.